Synthesis, Coordination and Properties of Porphyrins with Various Vinylene-Bridges and Porphyrin Nanobelt

(様々なビニレン架橋部位を持つ共役拡張ポルフィリンとポルフィリンナノベルトの合成と物性)

Dissertation

Xue Songlin

2018

Laboratory for Photofunctional Organic Chemistry

Graduate School of Materials Science

Nara Institute of Science and Technology

Table of Contents

Abbreviations

APCI: Atmospheric pressure chemical ionization

B3LYP: Becke, three-parameter, Lee-Yang-Parr

BF_3•OEt_2: Boron trifluoride diethyl etherate

C_6F_5CHO: Pentafluorobenzaldehyde

CH_2Cl_2: Dichloromethane

COSY: Correlation spectroscopy

CV: Cyclic voltammetry

DDQ: 2,3-Dichloro-5,6-dicyano-1,4-benzoquinone

DFT: Density functional theory

DPV: Differential pulse voltammetry

DMF: *N,N*-Dimethylformamide

EtOAc: Ethyl acetate

EPR: Electron paramagnetic resonance

EDDM: Electron density difference map

HR: High-resolution

HOMA: Harmonic-oscillator model for aromaticity

TEA: Triethylamine

HOMO: Highest occupied molecular orbital

IR: Infrared spectroscopy

LUMO: Lowest unoccupied molecular orbital

MALDI: Matrix assisted laser desorption/ionization

MS: Mass spectroscopy

NaOAc: Sodium acetate

NICS: Nucleus independent chemical shift

NOESY: Nuclear Overhauser effect spectroscopy

NMR: Nuclear magnetic resonance

TLC: Thin−layer chromatography

THF: Tetrahydrofuran

TFA: Trifluoroacetic acid

$TBAPF_6$: Tetrabutylammonium hexafluorophosphate

TD-DFT: Time dependent-density functional theory

UV-Vis: Ultraviolet–visible

Chapter 1

General Introduction

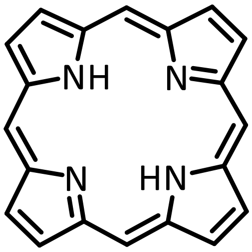

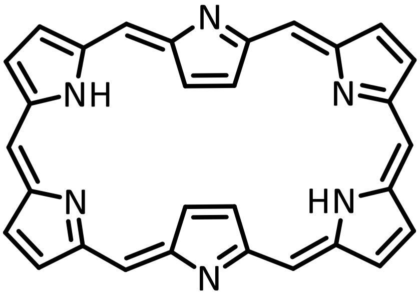

In this Chapter, the general introduction of porphyrins is described.

1-1 Porphyrins

In recent decades, researchers have given their focus toward porphyrin chemistry because of potential applications in various fields, such as photodynamic therapy (PDT), catalytic ability, dye-sensitized solar cell (DSSC), organic photovoltaic (OPV), anion recognition and magnetic resonance imaging (MRI).[1] These meaningful and intriguing applications encourage researchers to synthesize more and more novel porphyrin molecules to study porphyrin chemistry. Therefore, the synthetic chemistry of porphyrins is still an active research filed to produce new molecules for exploring properties and potential functions.

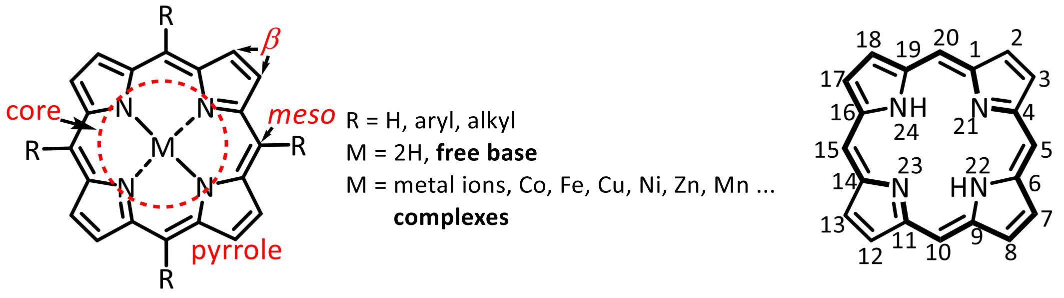

Figure 1.1. Main framework of porphyrins.

In a narrow sense, porphyrin is a planar molecule comprising four pyrrole subunits and four *meso*-carbons (Figure 1.1).[1e] Porphyrins are highly conjugated macrocyclic molecules with 18π-electrons (Figure 1.1). Roughly, the main framework of porphyrin molecules can be divided into four subparts: pyrrole subunit, core, *β*- and *meso*-positions (Figure 1.1). The members of porphyrin family are produced by modification of *β*- and *meso*-positions, core and pyrrole subunits (Figure 1.2).[1d-1k]

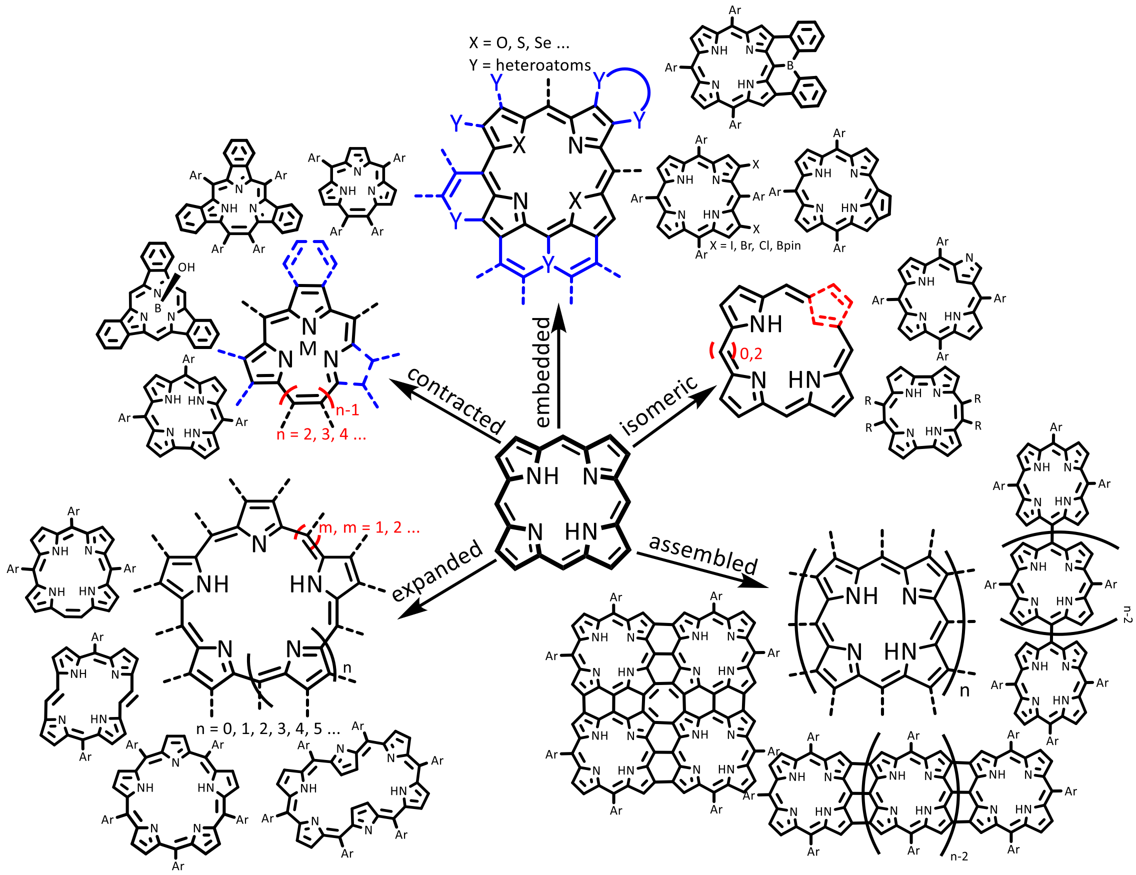

Figure 1.2. Modified modes of porphyrins and representative molecules.

In general, porphyrin is synthesized by pyrrole and benzaldehydes under a condensation reaction, such as Lindsey's and Rothemound's methods. The one-pot synthesis of *meso*-substituted porphyrins by simple acid-catalyzed condensation reaction has been developed well to date.[1f,2] Prof. Osuka and co-workers reported a series of *meso*-substituted porphyrins, including hexaphyrin, heptaphyrin, octaphyrin and further expanded porphyrins by modified Lindsey's condensation conditions. The detailed reaction condition involves acid-catalyzed condensation of pyrrole or *β*-substituted pyrrole and aromatic aldehydes in CH_2Cl_2 solution, and then oxidation with DDQ to afford expanded porphyrins (scheme 1.1).[2]

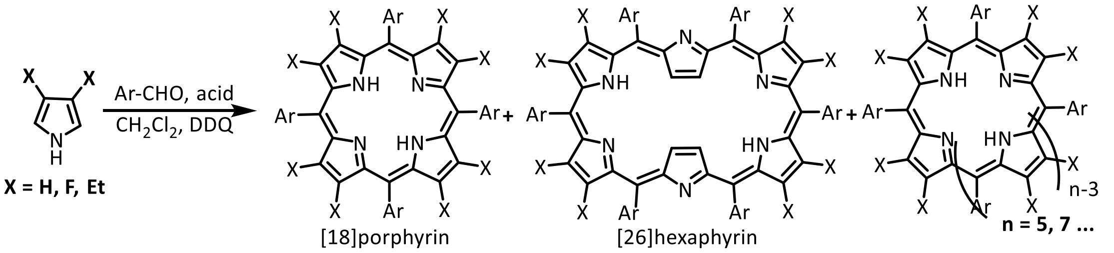

Scheme 1.1. Synthetic scheme of *meso*-substituted porphyrins.

To get better yields of porphyrins, the size-selective synthesis was proposed.[1f,2d,3] The dipyrromethane and tripyrrane can be used for size-selective synthesis reaction (Scheme 1.2). The acid-catalyzed condensation reaction of them with C_6H_5CHO afforded expanded porphyrins in higher yields compared with conventional condensation reaction. Furthermore, this size-selective method made it possible to synthesize *meso*-A_3B_3 type expanded porphyrins by stepwise reactions (Scheme 1.2).[1f,4] These synthesis processes provide the improved yields and simple purification progress relative to one-pot synthesis of porphyrins. As mentioned above, almost all *meso*-substituted porphyrins are generally one carbon atom at *meso*-positions because they are synthesized from pyrroles and aldehydes by above condensation reactions.[1e-1f,2-6]

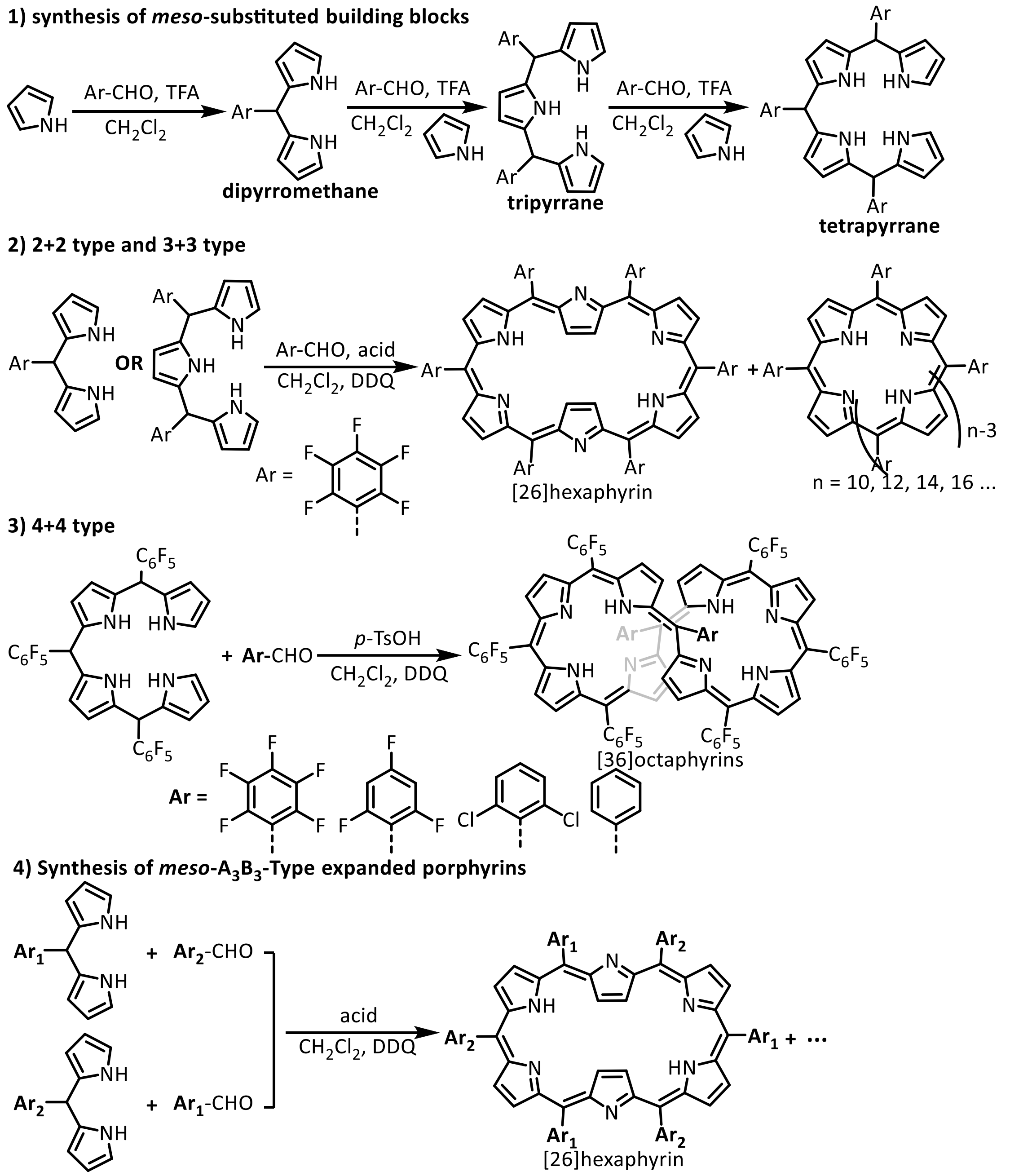

Scheme 1.2. Size-selective synthesis of *meso*-substituted porphyrins.

1-2 Coordination

Porphyrins can work as multi-dipyrrin ligands to capture metal ions to form metal complexes. The coordination of porphyrins have been still a dynamic research field (Figure 1.3).[1f,5,7] For coordination behaviors of porphyrins and expanded porphyrins, it should be noted that the products of reactions are not easy to predict. The large and flexible annulene-like expanded porphyrins consist of various coordination modes which lead to unexpected metal complexes.[7] Therefore, extremely careful screening of reaction conditions and purification processes are needed.

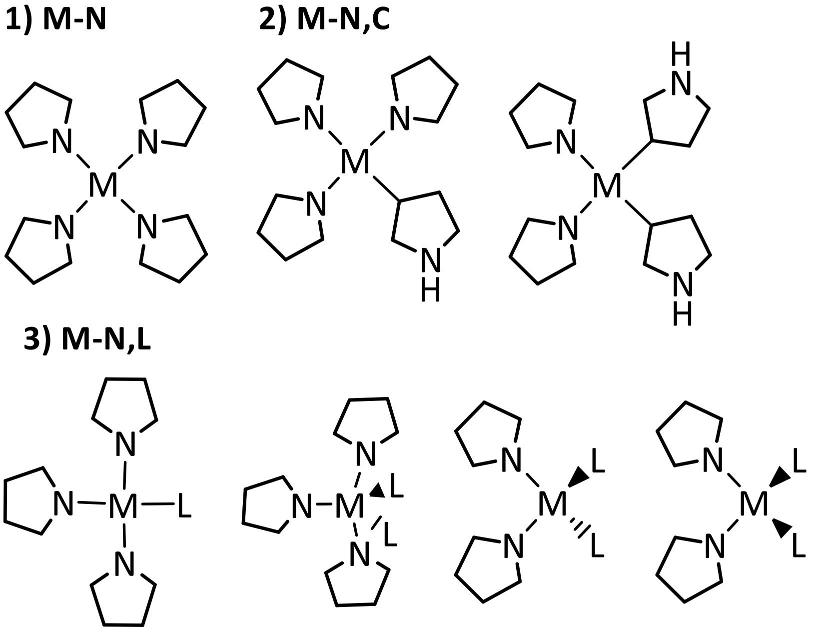

4) coordinated metal ions: B, Si, P, V, Mn, Fe, Co, Ni, Cu, Zn, Y, Rh, Pd, Ag, Cd, In, Ir, Pt, Au, Hg, La, Ce, Nd, Eu, Gd, Dy, Lu, U, Np, Pu

Figure 1.3. Representative coordination modes of porphyrins and reported coordinated metal ions.

The metal complexes of porphyrins employ three general coordination modes with metal ions (Figure 1.3). The first mode is that metal ions bind to only nitrogen atoms of pyrrole subunits, namely “**M-N**”. The second mode is that metal ions bind to *β*-carbon and nitrogen atoms of pyrrole subunits, namely “**M-N, C**”. The last mode is that metal ions bind to nitrogen atoms of pyrrole subunits and ligands, namely “**M-N, L**”. The incorporation of metal ions could be as a trigger to give molecular structures of metal complexes with planar, figure-of-eight, V- and Möbius shaped structures.[1e,1f,7]

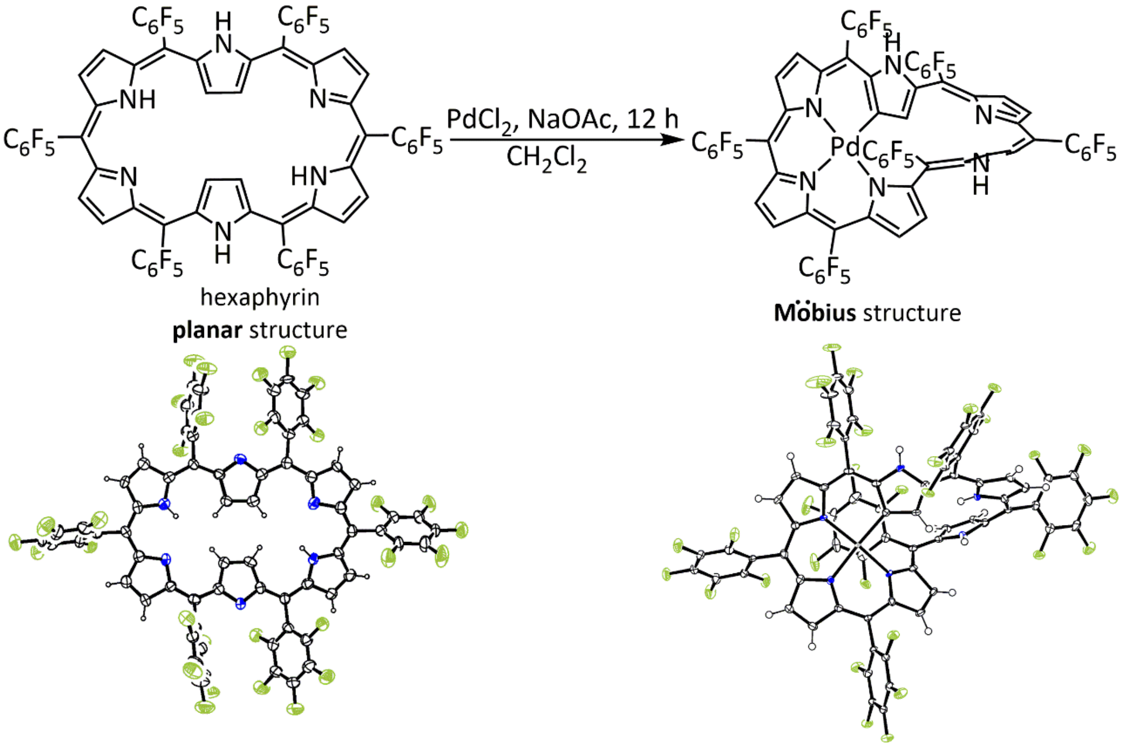

Figure 1.4. Synthesis of singlet twisted Möbius [28]hexaphyrin(1.1.1.1.1.1) complex.

Figure 1.4. shows the example of the metal complex of [28]hexaphyrin(1.1.1.1.1.1)

reported by Osuka group. The planar [28]hexaphyrin(1.1.1.1.1.1) is a Hückel antiaromatic molecule. Treatment of [28]hexaphyrin(1.1.1.1.1.1) with 10 eq. of $PdCl_2$ in CH_2Cl_2 under a reflux condition for 12 hours in the presence of excess NaOAc afforded the mono palladium complex in 50% yield.[7d] The X-ray crystal structure of mono palladium complex shows the singlet twisted Möbius molecular structure. The Möbius aromatic property of mono palladium complex is further investigated by the ^1H NMR spectroscopy.[7d] The coordination of porphyrins, thus, makes it possible to induce the significant structural transformation from free-base to metal complexes.[1,7] Therefore, special porphyrins with large and flexible macrocyclic ring walk on the path to evaluate Hückel/Möbius anti-/aromaticity.

1-3 Aromaticity

Aromaticity is a classical and still indispensable concept in porphyrin chemistry.[1c-1f,8-11] In 1934, Hückel proposed the Hückel rules for the aromaticity of cyclic compounds.[8] The Hückel rule is as follows: a monocyclic aromatic compound should have a delocalized conjugated system and (4n + 2) π electrons. For Hückel topology, the aromatic compounds generally form planar shaped conformations (Figure 1.5).

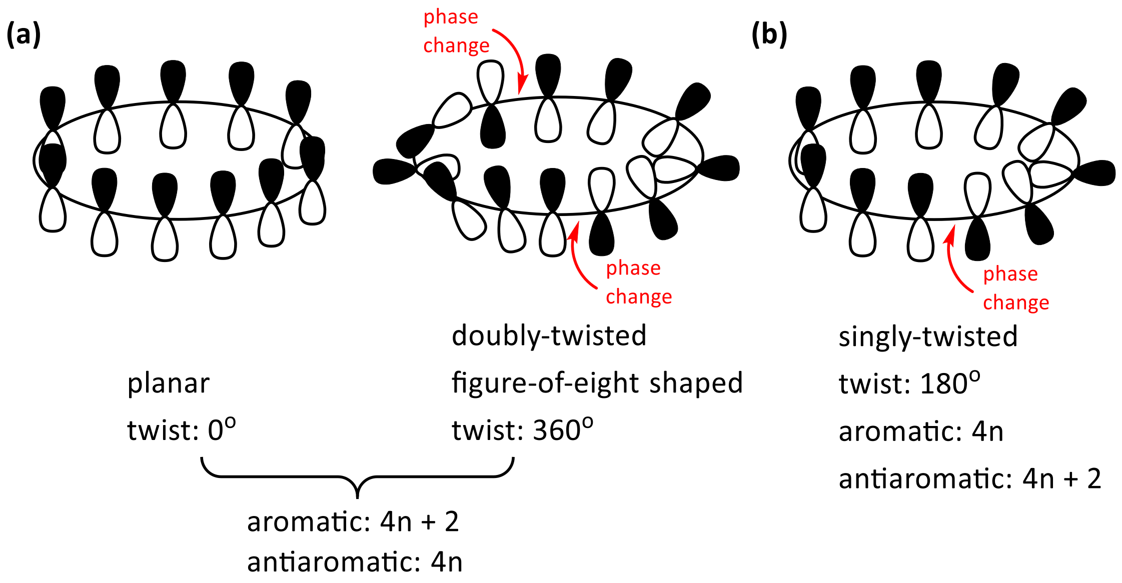

Figure 1.5. Topologies of molecular structures with (a) Hückel and (b) Möbius aromaticity, along with the numbers of π-electrons required for aromatic and antiaromatic properties.

The theoretical Möbius concept was predicted by Heilbronner in 1964.[9a] The Möbius aromaticity concept predicts that singly twisted Möbius topological compounds show an aromatic characteristic with 4n π-electrons.[1c,1d,9]

However, the Möbius aromatic systems were little-studied until appearance of porphyrin type Möbius aromatic compounds.[1c-1f,9-11] The conformational flexibilities of porphyrins are useful for evaluating aromatic and antiaromatic properties in various conformations.[1c-1f,10,11]

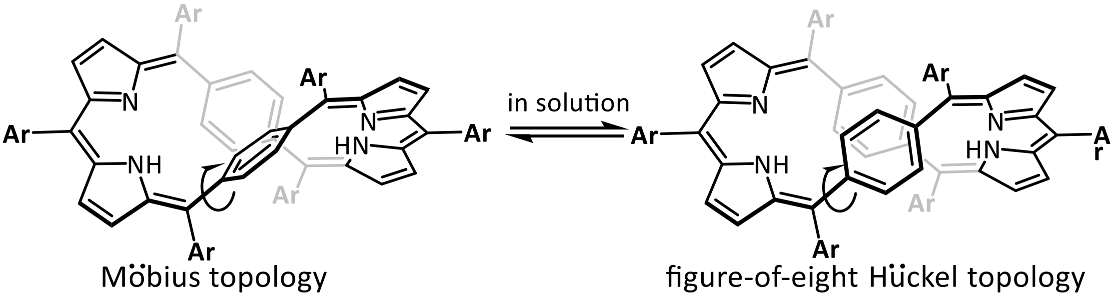

Figure 1.6. Conformation transformation of di-*p*-benzi[28]hexaphyrin(1.1.1.1.1.1).

The first Möbius aromatic porphyrin was reported by Prof. Latos-Grażyński and co-workers.[10] Di-*p*-benzi[28]hexaphyrin(1.1.1.1.1.1) showed transformations between Hückel and Möbius conformations by controlling solvents and temperatures (Figure 1.6).[10] Prof. Osuka and Prof. Kim groups subsequently reported that expanded porphyrins are ideal platforms to explore stable Möbius anti-/aromatic systems.[1c,1d,11]

Hexaphyrins(1.1.1.1.1.1), which is one of the most famous expanded porphyrins, form five conformations to date (Figure 1.7).[11] Among five conformations, conformations of figure-of-eight, dumbbell, rectangular and triangular shapes are categorized to the Hückel topology. The singlet twisted conformation is categorized to the Möbius topology. Those published works make us realize that porphyrins are important players in the game of the

Hückel and Möbius anti-/aromaticity due to their remarkably conformational flexibilities.[11] Therefore, development of novel porphyrins with large and flexible conformations is a necessary and pressing work for exploring new Hückel and Möbius anti-/aromaticity systems.

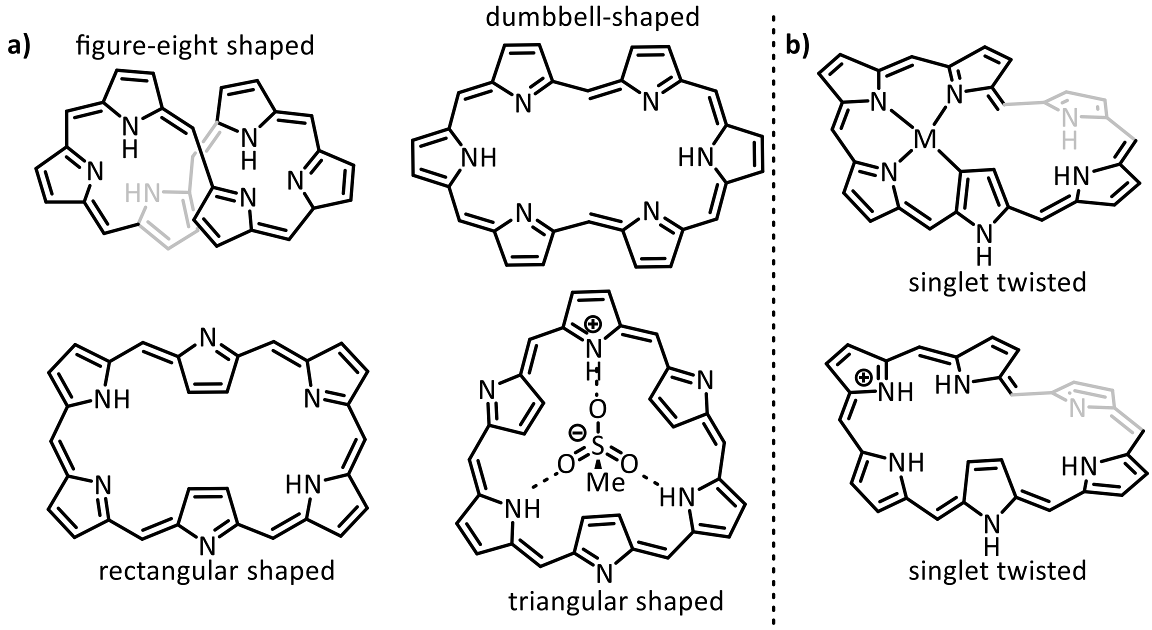

Figure 1.7. Molecular conformations of hexaphyrin(1.1.1.1.1.1), (a) Hückel topologies and (b) Möbius topologies. Aryl groups are omitted for clarity.

1-4 Diversity

Production of a diversity of porphyrin family have been developed by various synthetic methods (Figure 1.2).[1,12-16] Besides, molecular structures have a strong effect on their electronic structures, such as optical and aromatic properties.[1b,1c] Among modification methods, the number and conformation of *meso*-positions are important factors to determine their molecular structures and electronic properties.

For example, hexaphyrin(1.1.1.1.1.1) with CF_3 groups at meso-positions shows a twisted figure-of-eight shaped molecular structure, whereas hexaphyrin(1.1.1.1.1.1) with phenyl rings at *meso*-positions shows a planar molecule (Figure 1.8).[1n-1p] Corroles(1.1.1.0) is a contracted porphyrin, which have only three *meso*-carbon.[1] The planar and anti-aromatic [20]porphyrin(2.1.2.1) has two trans-vinylene-bridges at two meso-positions.[1n] The [20]homoporphyrin(2.1.1.1) with one diphenyl vinylene-bridge exhibits the smallest Möbious molecular structure with 20π-electron aromatic property.[1p] The stable porphyrin radical cations with near-IR absorption were synthesized by modifications of the *β*- and meso-positions of porphyrins platforms.

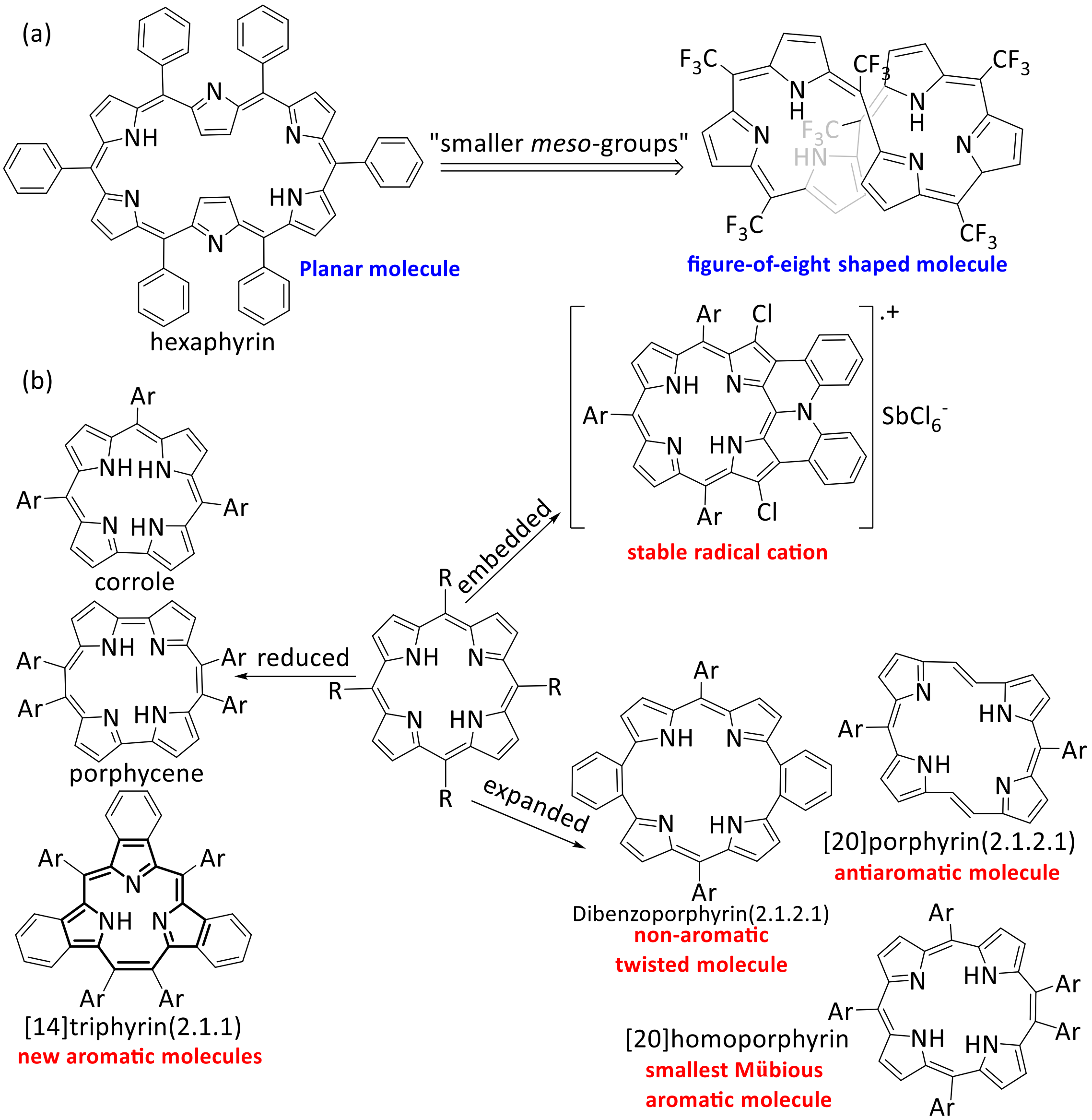

Figure 1.8. Modification method of the structure of porphyrins by manipulation of the structure of *meso*-positions.

Therefore, development of the derivatization methods of the porphyrins at *meso*-positions are important to investigate the relationship between molecular structure and property.[1] Our group has already developed the contracted [14]triphyrin(2.1.1) and expanded dibenzoporphyrin(2.1.2.1). [14]Triphyrins(2.1.1) generally have a 14π-electron system and have a one-valence tridentate coordination structures. The expanded dibenzoporphyrin(2.1.2.1) exhibits a deeply saddle-shaped structure with non-aromatic property.[1o] However, porphyrins with vinylene-bridges at *meso*-positions have been rarely reported to date.[1n,1o, 1p] Accordingly, we have been interested in developing new porphyrins with vinylene-bridges at *meso*-positions to explore molecular property.

1-5 Cyclic Oligomers

As a fragment of single-walled carbon nanotube (SWNT), the belt-shaped compounds comprising fused benzene rings have attracted great attentions because of unique molecular structures, optical and electronic properties.[17,18]

The first carbon nanobelt has been reported in 2017 by Prof. Itami and co-workers (Figure 1.9).[19] Researchers believe that the carbon nanobelt has a great potential to be a seed molecule for growing the carbon nanotube.[19] These belted compounds could be seen as bent aromatic molecule structures which employ the novel electronic properties relative to common planar aromatic molecules.[20]

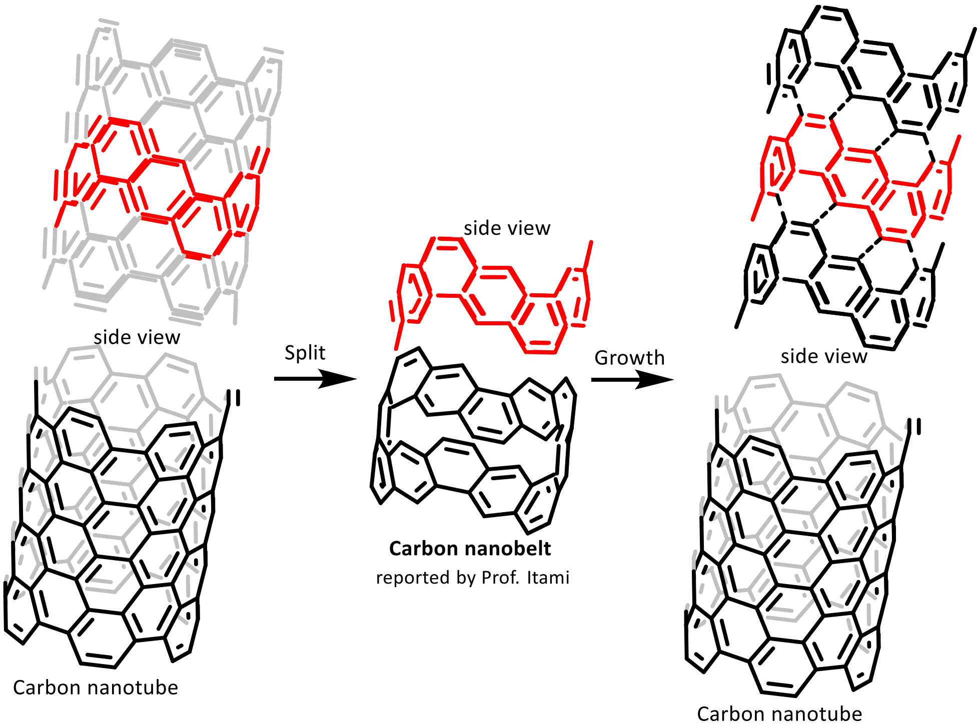

Figure 1.9. Carbon nanobelt as possible seed to growing carbon nanotube.

Photosynthesis system is composed of assembled cyclic porphyrinoid structures to efficiently collect the photo-energy and transfer the energy to reaction center.[21] Therefore, cyclic porphyrins oligomers are important synthetic targets for fundamentally understanding photochemical properties.

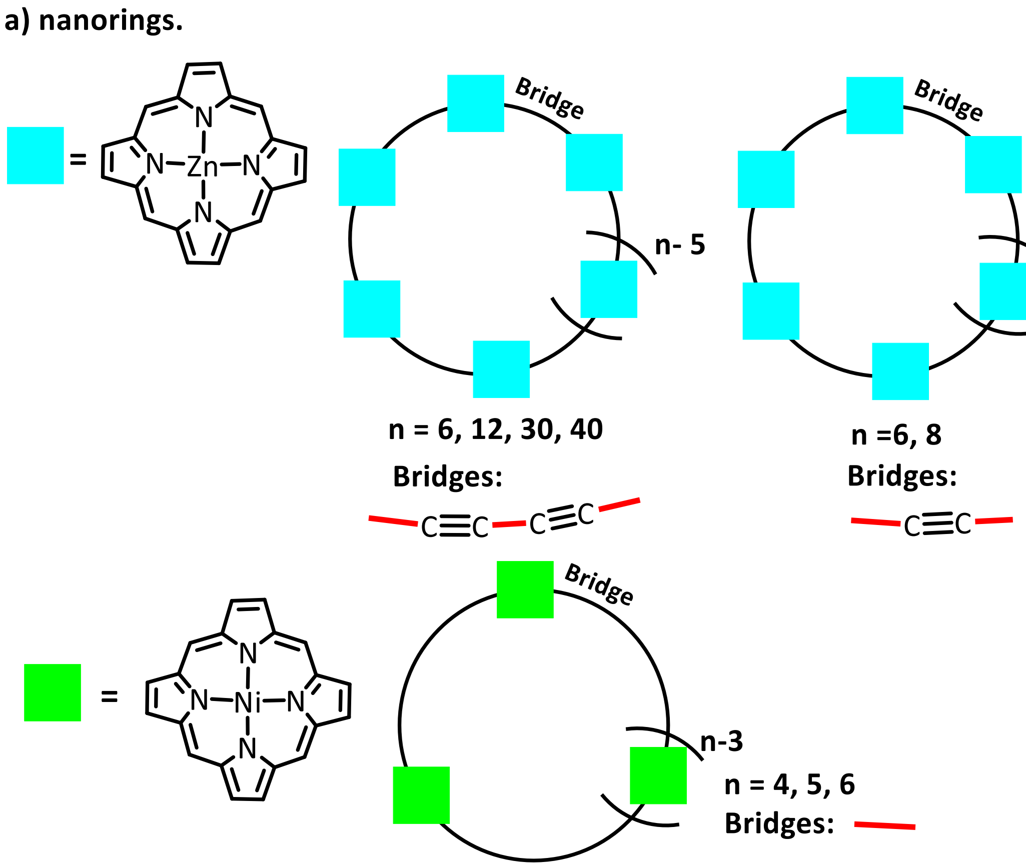

Figure 1.10. Selected porphyrin nanorings.

The syntheses of cyclic porphyrins oligomers have been developed by metal-catalyzed cyclization reactions and template methods.[22] Porphyrin can be used for construction of cyclic oligomers: nanoring, nanotube, nanobarrel, Ruassian Doll and nanoball (Figure 1.10).[22] However, porphyrin-based nanobelt has not been reported yet. In addition, large

π-surface of porphyrin is advantageous to making super-molecular assemblies with the host-guest interaction.[22]

Porphyrin-based nanobelts may form sufficient 3D π-surface, giving the possibilities to create functional supramolecular assemblies. Consequently, we have been interested in developing the synthetic method of porphyrin-based nanobelt to explore bent molecule structures and its supramolecular assembly.

1-6 Research Purposes

The author realized that porphyrin with various vinylene-bridges is little-studied field in porphyrin chemistry. The vinylene bridges give two more electrons and more distances between dipyrrins than regular porphyrins with one carbon at *meso*-position. The structural characteristics could be employed to show strong influences on molecular structures and electronic properties. Therefore, addition of various vinylene-bridges into porphyrin skeleton induce specific molecular conformations that give us a chance to investigate the unique aromaticity, optical and electronic properties. They also can work as ligands to produce various metal complexes with novel molecular structures and electronic properties. In this dissertation, the author aims to develop novel porphyrins molecules and porphyrin-based nanobelts including various vinylene-bridges to explore molecular structures, optical and electronic properties, aromaticity, coordination behaviour and supramolecular assembly.

This research work is started with the synthesis of porphyrins with diphenyl vinylene-bridges and their metal complexes in Chapter 2. The condensation reaction of dipyrrolyldiphenylethene and C_6F_5CHO will be discussed. The redox and optical properties, coordination behaviours and aromaticity of obtained porphyrins with diphenyl vinylene-bridges and their metal complexes will be described. In Chapter 3, the 1,2-

di(pyrrol-2-yl)ethene as the simplest vinylene-bridge was chosen to produce the porphyrins with vinylene-bridges. The porphyrins with vinylene-bridge are expected to form planar molecules with aromatic properties and as multi-dipyrrins ligand to produce multi-nuclear metal complexes. In Chapter 4, porphyrins with dimethyl vinylene-bridges were designed to produce BODIPY macrocycles because the insertion of dimethyl vinylene-bridges can produce good solubility and weak steric hindrance. The author hopes the development of a synthetic method of BODIPY macrocycles. In Chapter 5, the effective synthetic method of porphyrin(2.1.2.1)-based nanobelts from arch-shaped porphyrin(2.1.2.1) will be presented. The binding ability with fullerene of porphyrin(2.1.2.1)-based nanobelt will be investigated by UV and NMR titration because porphyrin(2.1.2.1)-based nanobelt may have large exposed 3D π-surface and suitable cavity size for C_{60}. The redox properties of porphyrin(2.1.2.1)-based nanobelts also will be discussed. Finally, general conclusion of this dissertation and reasonable prospects of porphyrin-based nanobelt were described in Chapter 6.

1-7 References

[1] (a) H. Shinokubo, A. Osuka, *Chem. Commun.,* **2009**, *9,* 1011; (b) Z. Yoon, A. Osuka, D. Kim, *Nat. Chem.,* **2009***, 1,* 113; (c) A. Osuka, S. Saito. *Chem. Commun.,* **2011***, 47,* 4330; (d) S. Saito, A. Osuka. *Angew. Chem. Int. Ed.,* **2011***, 50,* 4342; (e) T. Tanaka, A. Osuka. *Chem. Rev.,* **2017***, 117,* 2584; (f) B. Szyszko, M. Bialek, E. Pacholska-Dudziak, L. Latos-Grażyńshi. *Chem. Rev.,* **2017***, 117,* 2839; (g) T. Sarma, P. Panda. *Chem. Rev.,* **2017***, 117,* 2785; (h) S. Shimizu. *Chem. Rev.,* **2017***, 117,* 2730; (i) R. Orłowski, D. Gryko, D. Gryko. *Chem. Rev.,* **2017***, 117,* 3102; (j) N. Fukui, K. Fujimoto, H. Yorimitsu, A. Osuka. *Dalton Trans.,* **2017***, 46,* 13322; (k) M. Panda, K. Ladomenou, A. Goutsolelos. *Coord. Chem. Rev.,* **2012***, 256,* 2601; (l) V. Roznyatovskiy, C. Lee, J. Sessler. *Chem. Soc. Rev.* **2013***, 42,* 1921; (m) M. Umetani, T. Yoneda, T. Kim, D. Kim, A. Osuka, *Angew. Chem. Int. Ed.,* **2016**, *55*, 8095; (n) D. Kuzuhara, W. Furukawa, A. Kitashiro, N. Aratani, H. Yamada, *Chem. Eur. J.,* **2016***, 22,* 10671; (o) K. S. Anju, M. Das, B. Adinarayana, C. H. Suresh, A. Srinivasan, *Angew. Chem. Int. Ed.,* **2017***, 56,* 15667.

[2] (a) S. Shimizu, N. Aratani, A. Osuka. *Chem. Eur. J.,* **2006,** *12*, 4909; (b) A. Osuka. *Chem. Rec.,* **2015***, 15,* 143.

[3] R. Taniguchi, S. Shimizu, M. Suzuki, J. Shin, H. Furuta, A. Osuka. *Tetrahedron Lett.,* **2003***, 44,* 2505.

[4] (a) M. Suzuki, A. Osuka. *Org. Lett.,* **2003***, 5,* 3943; (b) M. Suzuki, A. Osuka. *Chem. Commun.,* **2005***,* 3685.

[5] (a) S. Saito, A. Osuka. *Chem. Eur. J.,* **2006***, 12,* 9095; (b) S. Mori, J. Shin, S. Shimizu, F. Ishikawa, H. Furuta, A. Osuka. *Chem. Eur. J.,* **2005***, 11,* 2417; (c) T. Yoneda, H. Mori, B. Sun, M. Yoon, D. Kim, A. Osuka. *Chem. Commun.,* **2012***, 48,* 6785

[6] (a) E. Vogel, H. Schmickler, *Angew. Chem. Int. Ed.,* **1990***, 29,* 1387; (b) M. Umetani, T. Yoneda, T. Kim, D. Kim, A. Osuka, *Angew. Chem. Int. Ed.,* **2016***, 55,* 8095; (c) T. Yoneda, T. Hoshino, S. Neya, *J. Org. Chem.,* **2017***, 82,* 10737; (d) D. Kuzuhara, W. Furukawa, A. Kitashiro, N. Aratani, H. Yamada, *Chem. Eur. J.,* **2016***, 22,* 10671; (e) K. S. Anju, M. Das, B. Adinarayana, C. H. Suresh, A. Srinivasan, *Angew. Chem. Int. Ed.,* **2017***, 56,* 15667.

[7] (a) JL. Sessler, E. Tomat. *Acc. Chem. Res.,* **2007***, 40,* 371; (b) Y. Tanaka, S. Saito, S. Mori, N. Aratani, H. Shinokubo, N. Shibata, Y. Higuchi, Z. Yoon, K. Kim, S. Noh. *Angew. Chem., Int. Ed.,* **2008***, 47,* 681; (c) Y. Sung, M. Yoon, J. Lim, H. Rath, K. Naoda, A. Osuka, D. Kim. *Nat. Chem.,* **2015***, 7,* 418; (d) S. Saito, K. Furukawa, A. Osuka. *Angew. Chem., Int. Ed.,* **2009***, 48,* 8086.

[8] E. Hückel. *Physik.,* **1931***, 70,* 20.

[9] (a) E. Heilbronner, *Tetrahedron Lett.,* **1964***, 5,* 1923; (b) H. S. Rzepa, *Chem. Rev.,*

2005*, 105,* 3697; (c) R. Herges, *Chem. Rev.,* **2006***, 106,* 4820; (d) M. Mauksch, V. Gogonea, H. Jiao, P. Schleyer. *Angew. Chem., Int. Ed.,* **1998***, 37,* 2395; (e) C. Castro, C. M. Isborn, W. L. Karney, M. Mauksch, P. Schleyer. *Org. Lett.,* **2002***, 4,* 3431; (f) J. Aihara, H. Horibe. *Org. Biomol. Chem.,* **2009***, 7,* 1939.

[10] M. Stępień, L. Latos-Grażyński, N. Sprutta, P. Chwalisz, L. Szterenberg. *Angew. Chem., Int. Ed.,* **2007**, *46*, 7869.

[11] (a) T. Higashino, B. Lee, J. Lim, D. Kim, A. Osuka. *Angew. Chem. Int. Ed.,* **2012***, 51,* 13105; (b) W. Cha, T. Soya, T. Tanaka, H. Mori, Y. Hong, S. Lee, K. Park, A. Osuka, D. Kim. *Chem. Commun.,* **2016,** *52,* 6076; (c) S. Ishida, T. Higashino, S. Mori, H. Mori, N. Aratani, T. Tanaka, J. Lim, D. Kim, A. Osuka. *Angew. Chem. Int. Ed.,* **2014***, 53,* 3427.

[12] JL. Sessler, D. Seidel. *Angew. Chem., Int. Ed.,* **2003***, 42,* 5134.

[13] (a) B. Franck, A. Nonn. *Angew. Chem., Int. Ed. Engl.,* **1995***, 34,* 1795; (b) A. Jasat, D. Dolphin. *Chem. Rev.,* **1997***, 97,* 2267.

[14] (a) K. S. Kim, S. B. Noh, T. Katsuda, S. Ito, A. Osuka, D. Kim, *Chem. Commun.,* **2007***,* 2479; (c) Z. S. Yoon, D.-G. Cho, K. S. Kim, JL. Sessler, D. Kim, *J. Am. Chem. Soc.,* **2008***, 130,* 6930; (d) H. Mori, Y. Sung, B. Lee, D. Kim, A. Osuka. *Angew. Chem., Int. Ed.,* **2012***, 51,* 12459.

[15] S. Shimizu, A. Osuka. *Eur. J. Inorg. Chem.,* **2006,** *7,* 1319.

[16] (a) S. Tokuji, J. Shin, K. Kim, J. Lim, K. Youfu, S. Saito, D. Kim, A. Osuka. *J. Am. Chem. Soc.,* **2009**, *131,* 7240; (b) J. Oh, Y. Sung, H. Mori, S. Park, K. Jorner, H. Ottosson, M. Lim, A. Osuka, D. Kim. *Chem,* **2017**, *3,* 870; (c) M. Izawa, T. Kim, S. Ishida, T. Tanaka, T. Mori, D. Kim, A. Osuka. *Angew. Chem. Int. Ed.,* **2017**, *56,* 3982.

[17] H. Kroto, J. Heath, S. O'Brien, R. Curl, R. Smalley. *Nature,* **1985**, *318*, 162.

[18] (a) K. Tahara, Y. Tobe. *Chem. Rev.,* **2006**, *106,* 5274; (b) D. Eisenberg, R. Shenhar, M. Rabinovitz. *Chem. Soc. Rev.,* **2010**, *39*, 2879.

[19] (a) G. Povie, Y. Segawa, T. Nishihara, Y. Miyauchi, K. Itami. *Science.* **2017**, *356,* 172; (b) H. Wegner. *Angew. Chem. Int. Ed.,* **2017**, *56,* 10995.

[20] (a) H. Omachi, T. Nakayama, E. Takahashi, Y. Segawa, K. Itami. *Nat. Chem.,* **2013**, *5,* 572; (b) D. Kondratuk, L. Perdigão, A. Esmail, J. O'Shen, P. Beton, H. Anderson. *Nat. Chem.,* **2015**, *7,* 317; (c) S. Richert, J. Cremers, I. Kuprov, M. Peeks, H. Anderson. C. Timmel. *Nat. Commum.,* **2017**, *8*, 14842.

[21] (a) M. Wasielewski. *Chem. Rev.,* **1992**, *92,* 435; (b) A. Harriman, J. Sauvage. *Chem. Soc. Rev.,* **1996**, *25,* 41; (c) D. Guldi. *Chem. Soc. Rev.,* **2002**, *31,* 22; (d) H. Imahori. *Org. Biomol. Chem.,* **2004**, *2*, 1425; (e) M. El-Khouly, O. Ito, P. Smith, F. D'Souza. *J. Photochem. Photobiol. C: Photochem. Rev.,* **2004**, *5,* 79; (f) M. Wasielewski. *Acc. Chem. Res.,* **2009**, *42,* 1910; (g) G. Bottari, O. Trukhina, M. Ince, T. Torres. *Coord. Chem. Rev.,*

2012*, 256,* 2453.

[22] (a) J. Song, N. Ararani, H. Shinokubo, A. Osuka. *J. Am. Chem. Soc.,* **2010***, 132,* 16356; (b) M. O`Sullivan, J. Sprafke, D. Kondratuk, C. Rinfray, T. Claridge, A. Saywell, M. Blunt, J. O`Shea, P. Beton, M. Malfois, H. Anderson. *Nature,* **2011***, 469,* 72; (c) M. Rickhaus, A. Jentzsch, L. Tejerina, I. Grübner, M. Jirasek, T. Claridge, H. Anderson. *J. Am. Chem. Soc.,* **2017***, 139,* 16502; (d) J. Cremers, R. Haver, M. Rickhaus, J. Gong, L. Favereau, M. Peeks, T. Claridge, L. Herz, H. Anderson. *J. Am. Chem. Soc.,* **2018***, 140,* 5352.

Chapter 2

Porphyrins with Diphenyl Vinylene-Bridges

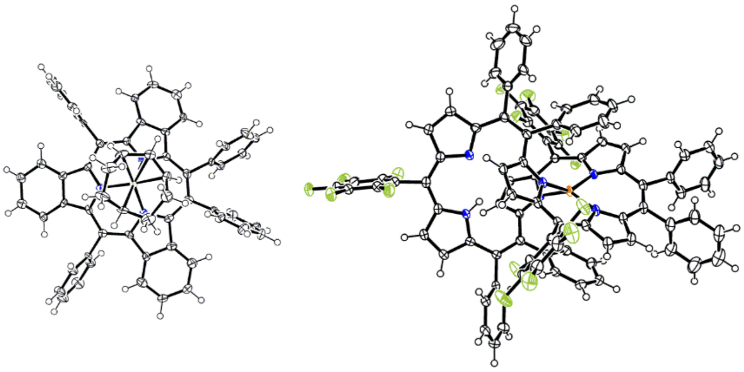

In this Chapter, the synthesis, characterization and complexation of a series of porphyrins and their metal complexes with diphenyl vinylene-bridges are described.

2-1 Triphyrin(2.1.1)

2-1-1 Introduction

Contracted porphyrins, relatively new members of the porphyrin family, have attracted the attention of researchers for the potential applications in a variety of fields because of the coordination abilities and catalysis activities in the last decade.[1] Triphyrins consist of three pyrrole or related subunits, which show unique optical and electric properties compared with the parent porphyrins. Our group has developed the synthesis and metalations of [14]triphyrins(2.1.1) and related compounds.[1,2] The [14]triphyrins(2.1.1) generally show a 14π-electron system and have one valence tridentate coordination structures. The [14]triphyrins(2.1.1) can act as triangle shaped ligand to produce various metal complexes with B^{III}, Mn^{I}, Re^{I}, Ru^{II}, Fe^{II}, Pd^{II}, Pt^{II} and Pt^{IV} ions.[1b, 2] The iridium complex of triphyrin was chosen as the next target complex because iridium complexes show rich applications such as catalysis ability and organic light-emitting diode.[3] In the first part of Chapter 2, the metalation of [14]triphyrins(2.1.1) **2-1** with $[IrCl(cod)]_2$ is described. This is the first example of iridium [14]triphyrins(2.1.1) complex containing an η^1,η^3-C_8H_{12} ring as a π-allyl ligand. The molecular structure, optical and redox properties are investigated by HR-MALDI-MS spectroscopy, NMR spectroscopy, X-ray crystallography, UV-Vis-NIR spectroscopy, electrochemistry and DFT calculation.

2-1-2 Synthesis

The detailed synthesis scheme of TriP-Ir^{III} (**2-2**) is shown in Scheme 2.1. The triphyrin free base **2-1** was synthesized via an established method.[1a] The treatment of **2-1** with 5 eq. of $[IrCl(cod)]_2$ in dry-DMF under a reflux condition for 1 hour afforded the iridium complex **2-2** in 46% yield (Scheme 2.1). The HR-MALDI-MS revealed the molecular ion peak at *m/z* 999.3159 (calcd. for $C_{60}H_{45}IrN_3$: 999.3164 $[M]^+$).

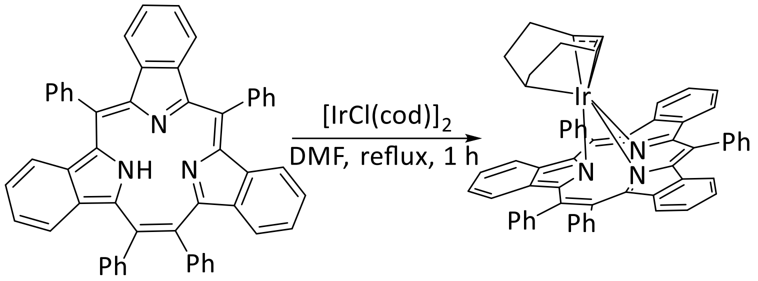

2-1

2-2, 46%

Scheme 2.1. Synthesis of complex **2-2.**

The molecular structure of complex **2-2** was confirmed by X-ray crystallography (Figure 2.1). The crystal structure of **2-2** shows a *fac*-coordination fashion of Ir^{III} and a sandwiched molecular structure with one cod ring and one triphyrin macrocycle.[2c] The Ir^{III} ion coordinates to three nitrogen atoms upon triphyrin unit and one sp^3–carbon (C57) and three π–allylic carbon (C60, C53 and C54) atoms upon C_8H_{12} ring (Figure 2.1). The bond lengths of η^1,η^3-C_8H_{12} ring are 1.418 Å (C53-C60), 1.452 Å (C53-C54), 1.523 Å (C54-C55), 1.494 Å (C55-C56), 1.523 Å (C56-C57), 1.504 Å (C57-C58), 1.511 Å (C58-

C59) and 1.493 Å (C59-C60), which imply the π-allyl structure of C53-C54-C56 part and other C-C single bonds. Therefore, the cod ring is transformed from 1,5-cod to η^1,η^3-C_8H_{12} ring. Besides, the valence of iridium ion is changed from Ir^{I} to Ir^{III}. The bond lengths between the Ir^{III} ion and each carbon atoms of η^1,η^3-C_8H_{12} ring are 2.186 Å (C60-Ir), 2.090 Å (C53-Ir), 2.193 Å (C54-Ir) and 2.116 Å (C57-Ir), that are similar with published π-allyl cod ring iridium complexes.[4]

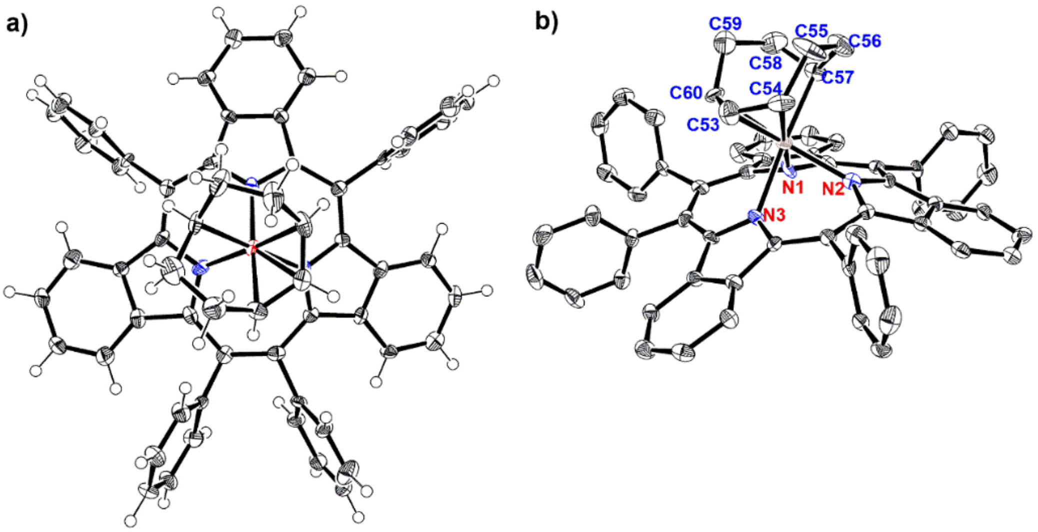

Figure 2.1. Crystal structure of **2-2**. (a) top view , (b) side view with selected label atoms. The hydrogen atoms are omitted for clarity. The thermal ellipsoids represent for 50% probability.

The ^1H NMR spectra of **2-1** and **2-2** are shown in Figure 2.2. The ^1H NMR spectrum of **2-2** exhibits broadened signals at room temperature. Therefore, VT-NMR spectra of complex **2-2** were carried out from 293 K to 193 K. With decreasing the measurement temperature, complex **2-2** becomes sharpened and assignable peaks. The ^{1}H-^{1}H COSY spectrum of complex **2-2** was measured at 193 K. The twelve protons of the cod ring of **2-2** are observed in the range of 0.0 ppm to 4.0 ppm because of the diamagnetic ring current effect of triphyrin unit (Figure 2.2).

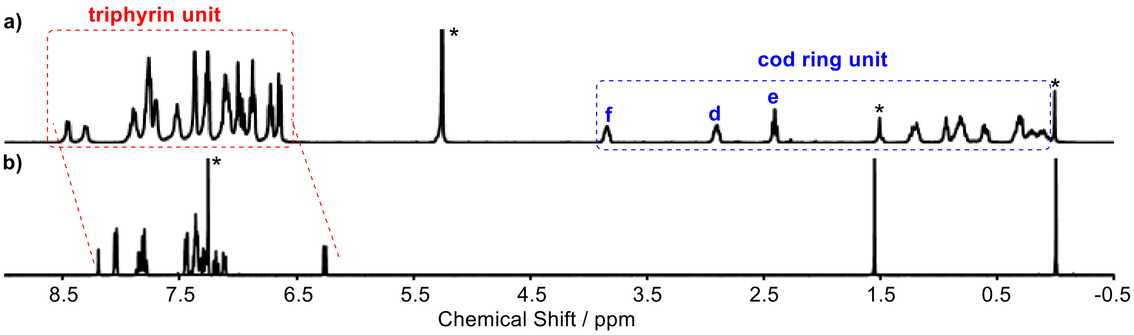

Figure 2.2. The ^{1}H NMR spectra of (a) **2-2** in CD_2Cl_2 at 193 K and (b) **2-1** in $CDCl_3$ at 293 K. * indicates residual solvent peaks.

For the result of ^{1}H-^{1}H COSY spectroscopy, the protons of the π-ally part of the cod ring are observed at 3.84 (f), 2.89 (d) and 2.41 (e) ppm (Figure 2.2). The protons of triphyrin part are observed in the range of 6.5 ppm to 8.5 ppm as multiplet signals because of low molecular symmetry relative to free-base **2-1**. The molecular dynamic of complex **2-2** was investigated by VT-NMR at 323, 348 and 373 K. They show almost similar signals to those observed signals at room temperature. Thus the triphyrin and cod units are fixed by Ir^{III} ion even in high temperature.

2-1-3 Optical and Redox Properties

The absorption spectra of **2-1** and **2-2** in CH_2Cl_2 are shown in Figure 2.3. The complex **2-2** shows the Soret-band at 346 and 390 nm, which exhibits a blue-shift and broadening compared with that of free base **2-1**. The complex **2-2** shows very broad absorption at 526 and 658 nm and absorption edge reached around 800 nm at the Q-bands region.

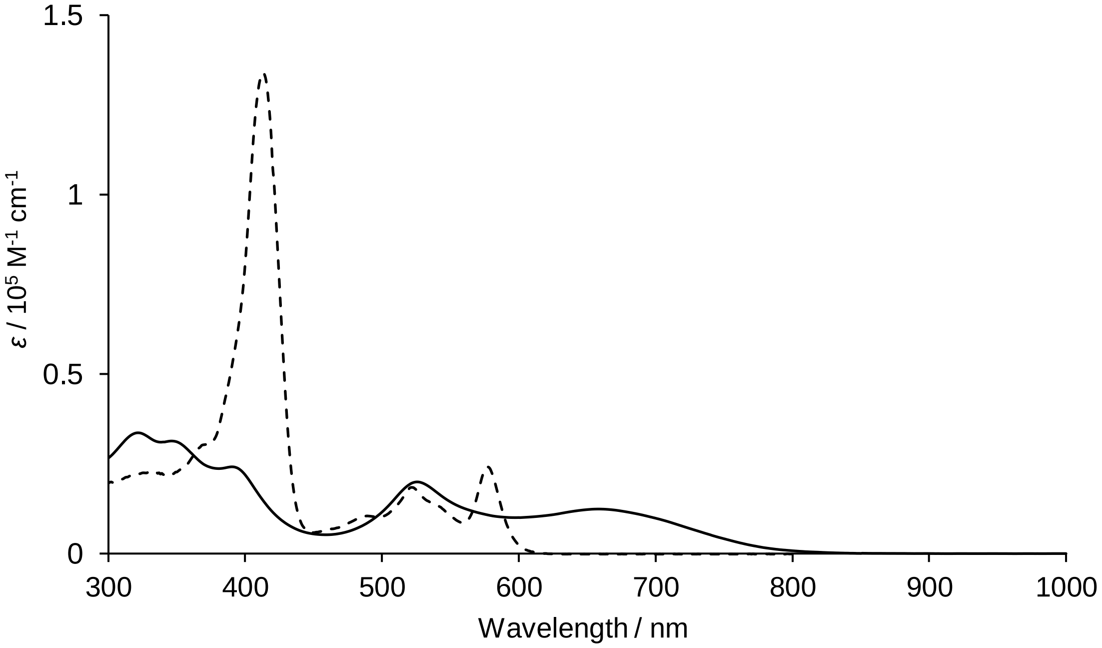

Figure 2.3. The UV-Vis absorption spectra of **2-1** (dash line) and **2-2** (solid line) in CH_2Cl_2.

The TD-DFT calculation of complex **2-2** was performed at the B3LYP/6-31G*/SDD level with Gaussian 09[5] to investigate the optical property. The TD-DFT calculation of **2-2** reveals that the mixture of metal-to-ligand charge transfer (MLCT) band and Q-bands is obtained at broadened peaks between 450 and 800 nm. The S_0–S_1 transition of complex

2-2 at 609 nm is predicted by TD-DFT calculation (Figure 2.4 and Table 2.1). The main composition of this transition is HOMO-1 to LUMO (0.60572). The HOMO–1 of **2-2** is mainly contributed by the iridium metal ion, whereas LUMO is mainly contributed by triphyrin core, suggesting the presence of the MLCT from the Ir^{III} metal center to the triphyrin part (Figure 2.5)

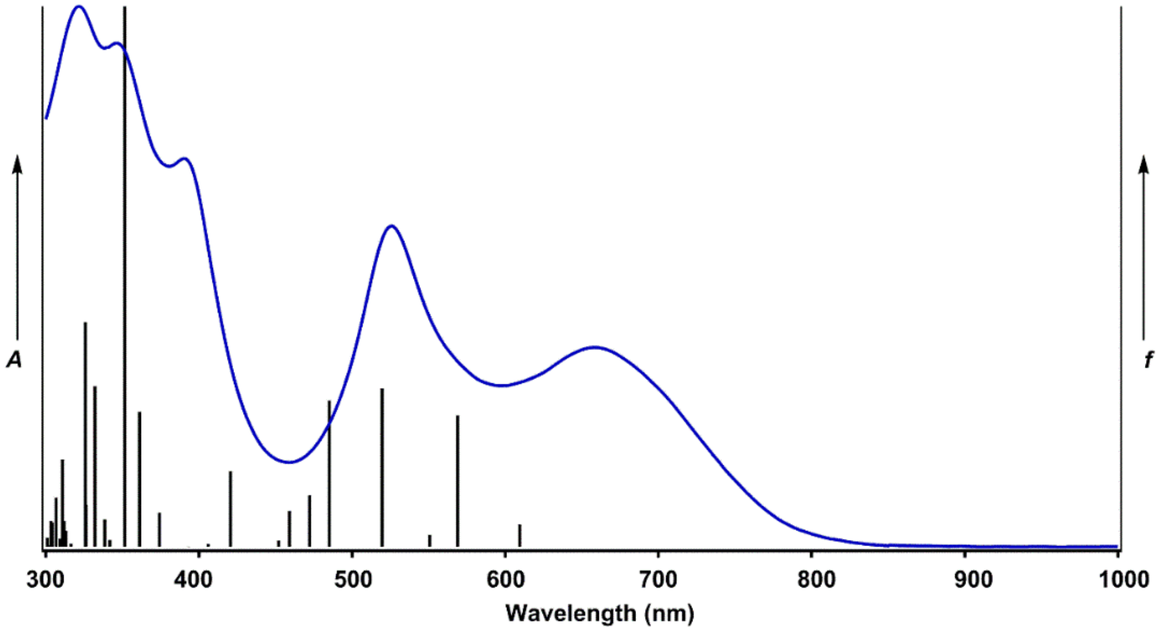

Figure 2.4. The UV-Vis absorption spectrum (blue line, left axis) and oscillator strengths (black bar, right axis), which is calculated at the B3LYP/6-31G*/SDD level of theory of **2-2.**

Table 2.1. Composition, Vertical Excitation Energies (*E,* eV/nm) and Oscillator Strengths (*f*) for the Lowest Optically Allowed Excited States of **2-2**, calculated at the B3LYP/6-31G*/SDD level of theory.

State	Composition	Exci.(eV/nm)	*f*
1	H-2 -> L (-0.24126), H-1 -> L (0.60572) H-1 -> L+1 (-0.12056), H -> L (-0.16108) H -> L+1 (-0.16483)	2.03/609	0.0188
2	H-1 -> L+1 (0.41297), H -> L (0.52003)	2.18/569	0.1103
3	H-2 -> L (0.65394), H-1 -> L (0.24229)	2.15/551	0.0100
4	H-1 -> L+1 (0.53172), H -> L (-0.41059)	2.39/520	0.1329

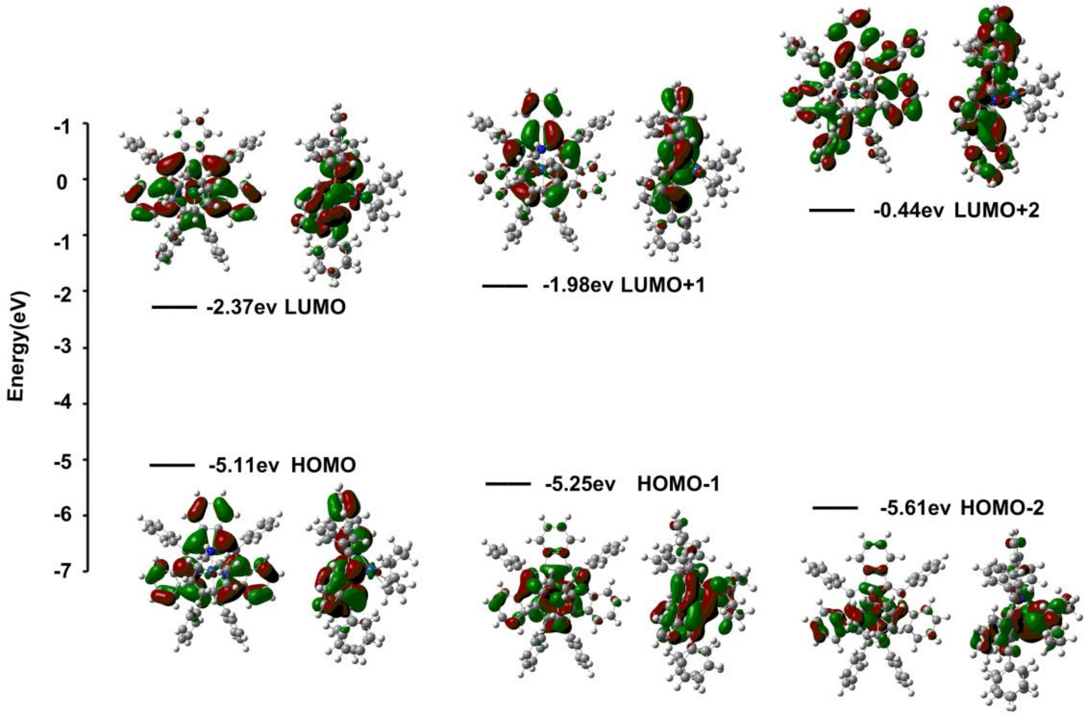

Figure 2.5. Frontier molecular orbital and energy diagram for the optimized structure of **2-2** calculated at the B3LYP/6-31G*/SDD level of theory.

The electrochemical properties of **2-1** and **2-2** were investigated by CV in CH_2Cl_2 at room temperature, containing 0.1 M ^{n}Bu$_4$NPF$_6$ as an electrolyte (Figure 2.6). The free base **2-1** shows two irreversible reduction peaks at –1.86 and –2.05 V (vs. Fc/Fc$^+$) and two oxidation waves at 0.54 and 1.04 V (vs. Fc/Fc$^+$). Complex **2-2** shows two reversible reduction peaks at –1.62 and –1.97 V (vs. Fc/Fc$^+$), respectively. The first reversible oxidation wave is observed at 0.16 V, and the second irreversible oxidation wave is observed at 0.84 V. The two reductions and two oxidation of complex **2-2** are located at the triphyrin unit.[2,4a] The absolute potential differences between the first oxidation and first reduction (HOMO-LUMO) gap of **2-1** and **2-2** are 2.40 eV and 1.78 eV, respectively.

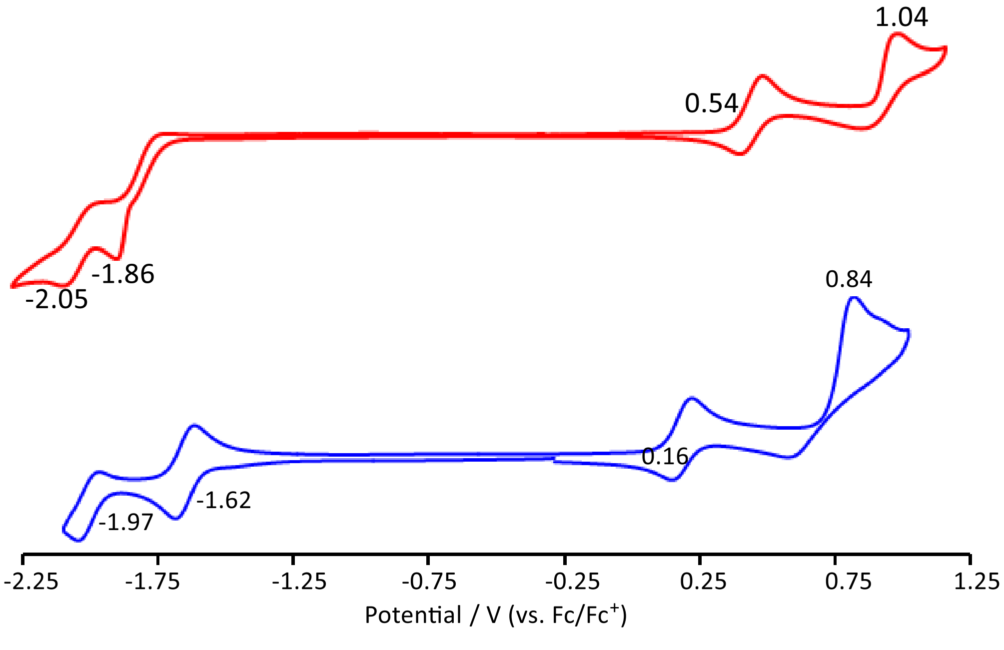

Figure 2.6. CV of **2-1** (red line) and **2-2** (blue line) in CH_2Cl_2 containing 0.1 M $^n Bu_4NPF_6$. Scan rate is 0.1 V s^{-1}

In conclusion, a sandwich complex of **2-2** has been synthesized from free-base **2-1** and $[IrCl(cod)]_2$. X-ray diffraction analysis reveals that the cod ring is transformed from 1,5-

cod to η^1,η^3-C_8H_{12} fashion as a π-allyl ligand associated with the valence change of iridium from Ir^I to Ir^{III}. Compound **2-2** also shows very broad absorption in the near-IR region, which can be assigned to a mixture of Q- and MLCT bands. Thus [14]triphyrin(2.1.1) with one diphenyl vinylene-bridge can produce mono-nuclear metal complexes.[1,2] This result encouraged us to prepare other porphyrins with diphenyl vinylene-bridges to investigate functional properties of free base and possible various multi-nuclear metal complexes.

2-2 Hexaphyrin(2.1.2.1.2.1)

2-2-1 Introduction

Expanded porphyrins consisted of more than four pyrroles into macrocyclic structures show flexible structures and properties such as multi-nuclear metal complexes, non-linear optics, unique Hückel/Möbious aromaticity/anti-aromaticity.[6,7] Porphyrin generally forms a planar molecular structure with 18π-electron aromaticity. With increasing ring size of porphyrins, they are difficult to keep planar structures (Figure 2.7). Molecular structures strongly have an effect to their electronic structures.[6,7] Therefore, the larger and flexible porphyrins are important platforms to investigate structure-property relationship.[8]

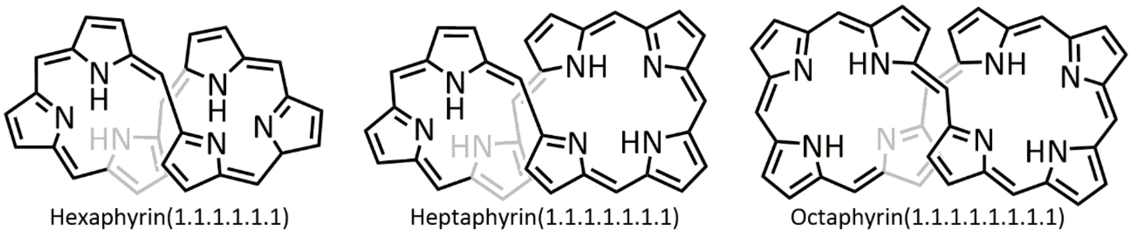

Figure 2.7. Selected molecular structures of expanded porphyrins.

The one-pot synthesis of *meso*-aryl substituted expanded porphyrins by condensation reaction was developed from dipyrrin or tripyrrane (Scheme 2.2).[6d] Depending on our previous research work of dibenzoporphyrin(2.1.2.1) (in Chapter 1), we assumed that dipyrrolylethene **(DPE)** and its derivatives can be used as new building units for constructing porphyrins with vinylene linkages (Scheme 2.2). The synthesis of **DPE** derivatives has been already established well via McMurry coupling reactions. In the second part of Chapter 2, diphenyldipyrrolylethenes (**DPhDPEs**)[9] were chosen to produce porphyrins with diphenyl vinylene-bridges. **DPhDPEs** are included with *Z*- and *E*- two isomeric structures. However, we found that two isomers gave same porphyrin molecular structures by condensation reactions. Three porphyrins with diphenyl vinylene-bridges, namely porphyrin(2.1.2.1) **2-3,** hexaphyrin(2.1.2.1.2.1) **2-4** and octaphyrin(2.1.2.1.2.1.2.1) **2-5**, were obtained under acidic condensation conditions. The synthesis procedure, molecular structures, optical and electronic properties, aromaticity properties and coordination abilities will be discussed.

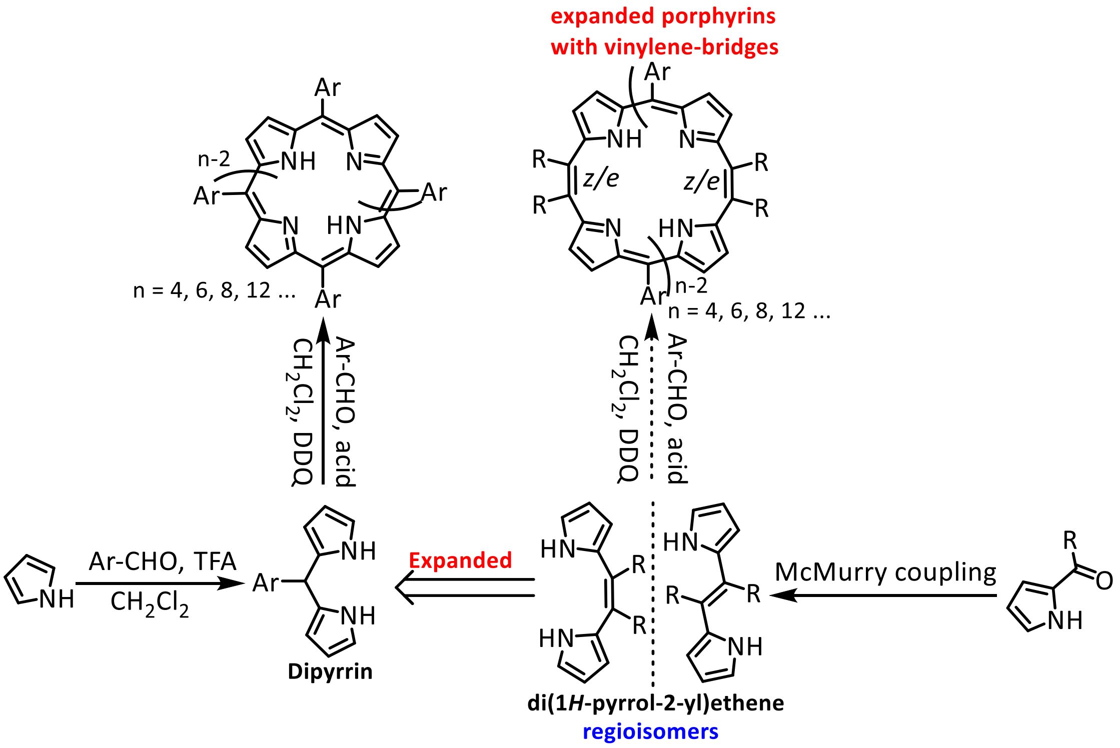

Scheme 2.2. Synthetic strategy of novel expanded porphyrins with vinylene linkages.

2-2-2 Synthesis

The detailed synthetic scheme of expanded porphyrins is shown in Scheme 2.3. The key intermediate ***E/Z*-DPhDPEs** were prepared via the established method.[9a] Isomeric pure ***E*-** and ***Z*-DPhDPEs** were obtained by purification with silica gel chromatography and recrystallizations. The structure of ***E/Z*-DPhDPEs** was confirmed by ^{1}H NMR spectroscopy.

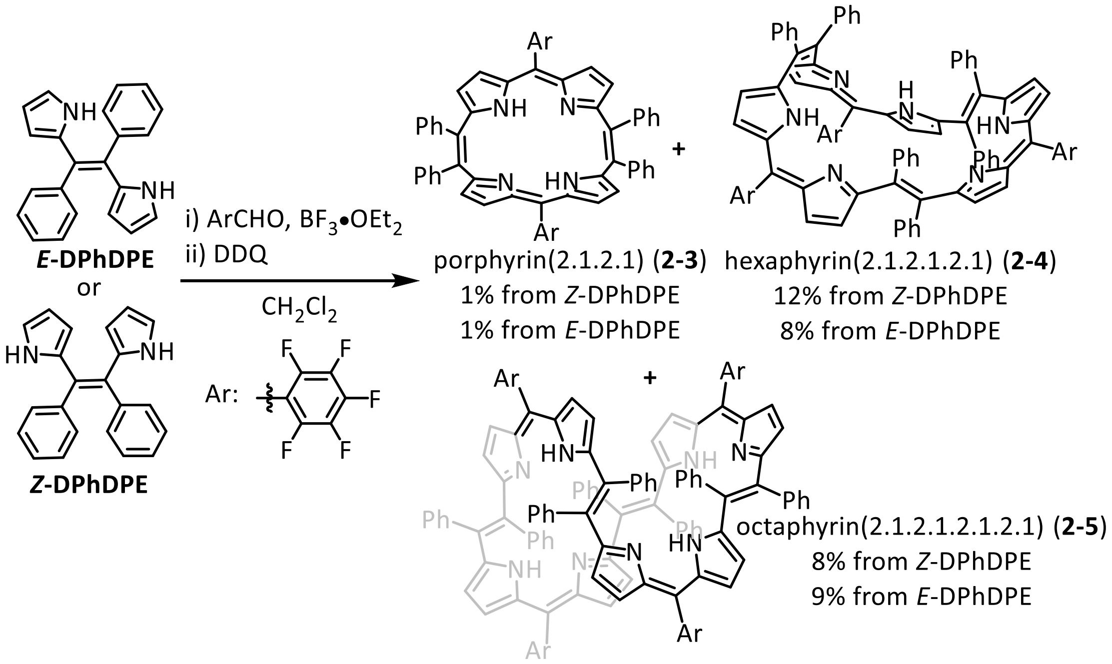

Scheme 2.3. Synthetic scheme of **2-3**, **2-4** and **2-5** from ***E/Z*-DPhDPE**s.

Treatment of ***Z*-DPhDPE** with C_6F_5CHO in the presence of BF_3•OEt_2 as an acid catalyst in dry CH_2Cl_2, followed by oxidation with DDQ gave three porphyrins **2-3**, **2-4** and **2-5** in 1, 12 and 8% yields, respectively. Interestingly, although ***E*-DPhDPE** has the different conformation at diphenyl vinylene linkages relative to ***Z*-DPhDPE**, the ***E*-**

DPhDPE gave the same compounds **2-3, 2-4** and **2-5** in 1, 8 and 9% yields by the same reaction condition, supported by ^{1}H NMR spectra. The reason might be that acid induced isomerization of **DPhDPEs** proceed during cyclization reaction. The presumable reaction mechanism of expanded porphyrins from **DPhDPEs** is shown in supporting information.[1e] The HR-MALDI-MS detected corresponding molecular ion peaks of **2-3** at *m/z* = 972.2399 (calcd. for $C_{58}H_{30}F_{10}N_4$ = 972.2311 $[M]^+$), **2-4** at *m/z* = 1458.3833 (calcd. for $C_{87}H_{45}F_{15}N_6$ = 1458.3466 $[M]^+$) and **2-5** at *m/z* = 1944.4616 (calcd. for $C_{116}H_{60}F_{20}N_8$ = 1944.2622$[M]^+$.

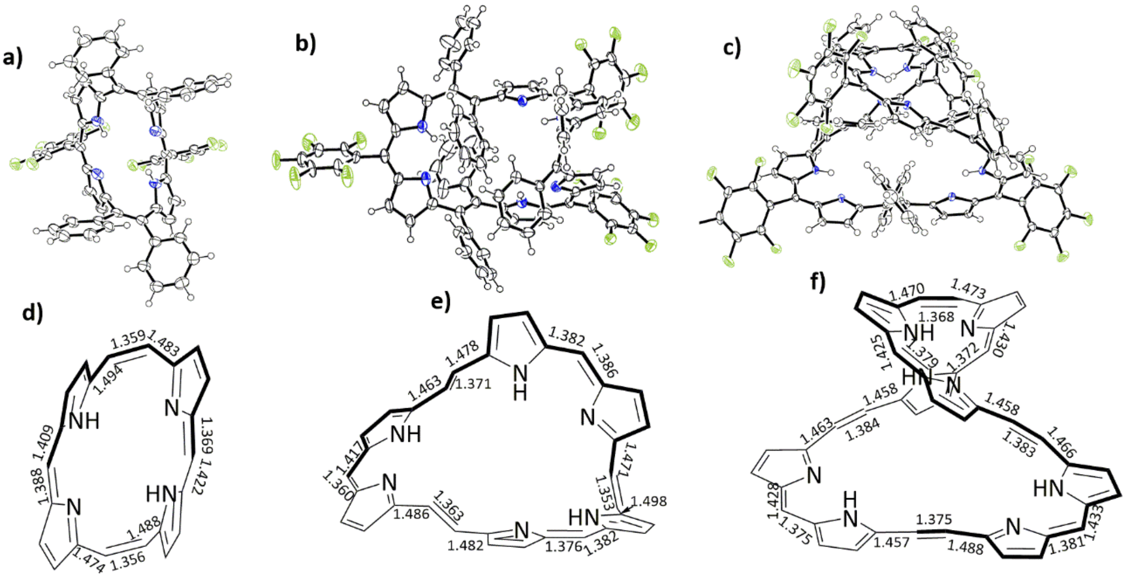

Figure 2.8. Crystal structures of a) **2-3**, b) **2-4** and c) **2-5**. Thermal ellipsoids represent for 50% probability. Selected bond lengths (Å) are given in d) **2-3**, e) **2-4** and f) **2-5**.

The solid-state structures of porphyrins were unambiguously determined by single crystal X-ray diffraction analysis (Figure 2.8). Compound **2-3** shows a V-shaped structure consisting with *cis*-conformations on diphenyl vinylene bridges because steric hindrances of diphenyl rings make difficult to form *trans*-conformations. Compound **2-5** shows a twisted molecular structure consisting with all *trans*-conformations. The reason is that expansion of ring size allows more space to form more stable *trans*-conformations. Compound **2-4** consists of one *cis*- and two *trans*-conformations at the diphenyl vinylene-bridges, resulted in the formation of highly twisted macrocyclic structures. The bond lengths of diphenyl vinylene bonds are 1.359 and 1.356 Å for **2-3**, 1.371, 1.363 and 1.353 Å for **2-4,** and 1.368, 1.375, 1.383 and 1.384 for **2-5**. These bond lengths are slightly longer than typical double bond length (1.34 Å). The bond lengths of the methene carbon and the adjacent pyrrole *β*-carbon clearly show bond alternations. These features of bond lengths indicate lack of contributions of the macrocyclic aromatic properties due to highly twisted molecular structures of obtained porphyrins.

The ^{1}H NMR spectrum of **2-3** is shown in Figure 2.9. The NH proton is observed as a broad peak at 12.60 ppm. Pyrrolic *β*-position protons are observed at 6.33 and 6.12 ppm as doublet peaks (Figures 2.9). The aromaticity of porphyrins can be evaluated by the chemical shifts of inner and outer protons along with π-conjugated ring.[6] Compound **2-3** shows no specific up/down fields shifts, indicating a non-aromatic property.[8b]

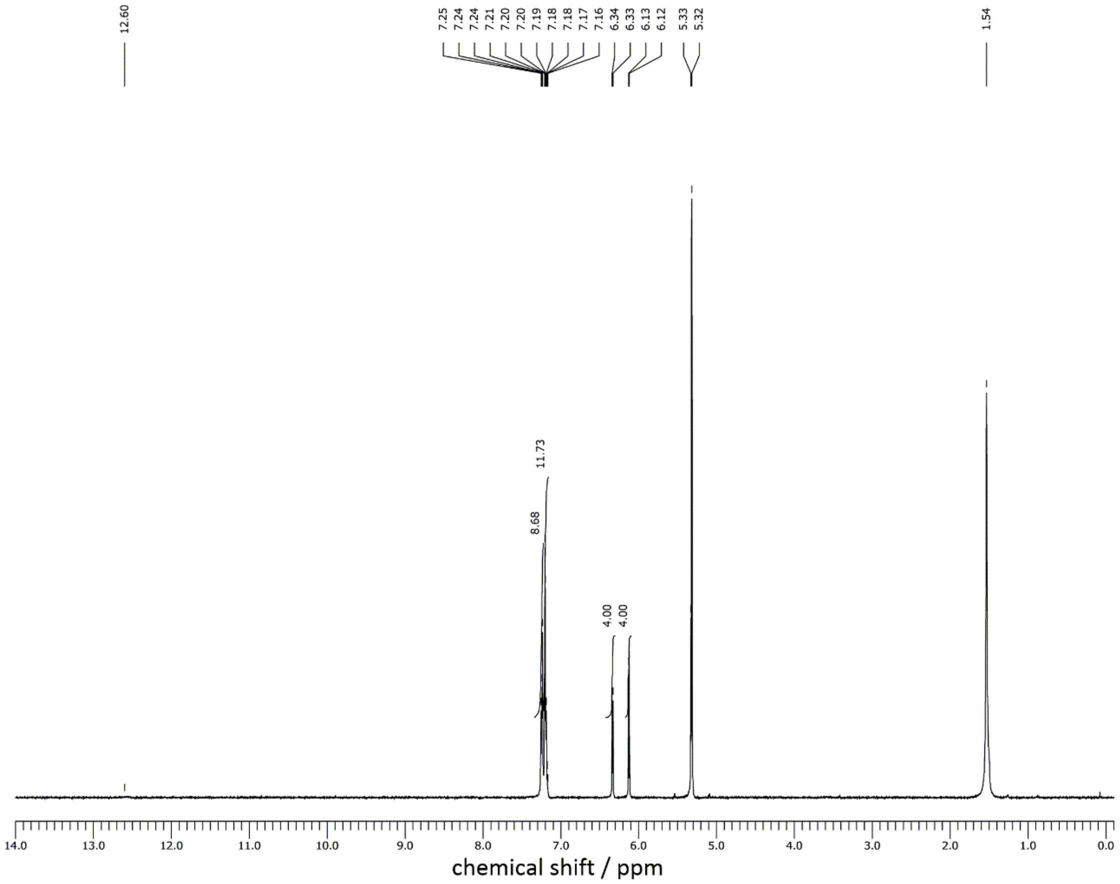

Figure 2.9. ^1H NMR spectrum of **2-3** in CD_2Cl_2 at 298 K.

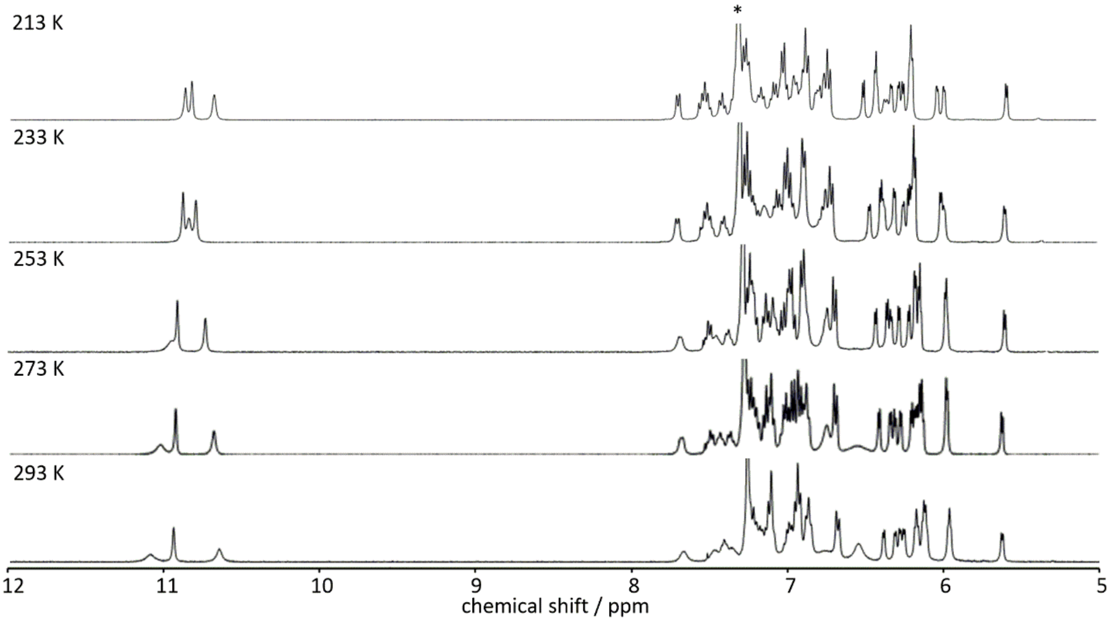

Figure 2.10. Temperature dependent ^1H NMR spectra of **2-4** in $CDCl_3$.

The ^{1}H NMR spectra of **2-4** and **2-5** show similar broad signals at room temperature because of flexible and highly twisted molecular structures. Therefore, temperature dependent NMR for compounds **2-4** and **2-5** were carried out from 293 K to 213 K. With decreasing the measurement temperatures, the signals of compound **2-4** were sharpened and became assignable peaks (Figure 2.10). Additionally, the COSY and NOESY spectroscopies of **2-4** were performed at 213 K. The NH signals are observed as three broad singlet peaks at 10.87, 10.83 and 10.69 ppm, which were confirmed by the deuterium exchange reaction with the addition of D_2O (Figure 2.11). At 213K, the compound **2-4** exhibits sets of doublet signals from 6.51 to 5.57 ppm, corresponding to twelve pyrrolic β-protons. By the results of NOESY, the cross peaks are observed at peaks of β-protons, which assign to pyrrolic β-positions H^1 and H^2 protons of the *cis*-vinylene bridge. These results suggest that **2-4** involves the *cis*-vinylene conformation either solid and solution states.

With decreasing the measurement temperature from 293 K to 213 K, the signals of **2-5** are also sharpened and became assignable peaks. However, at 193 k, two group signals of protons are observed. Probably, compound **2-5** has two molecular conformations in solution.

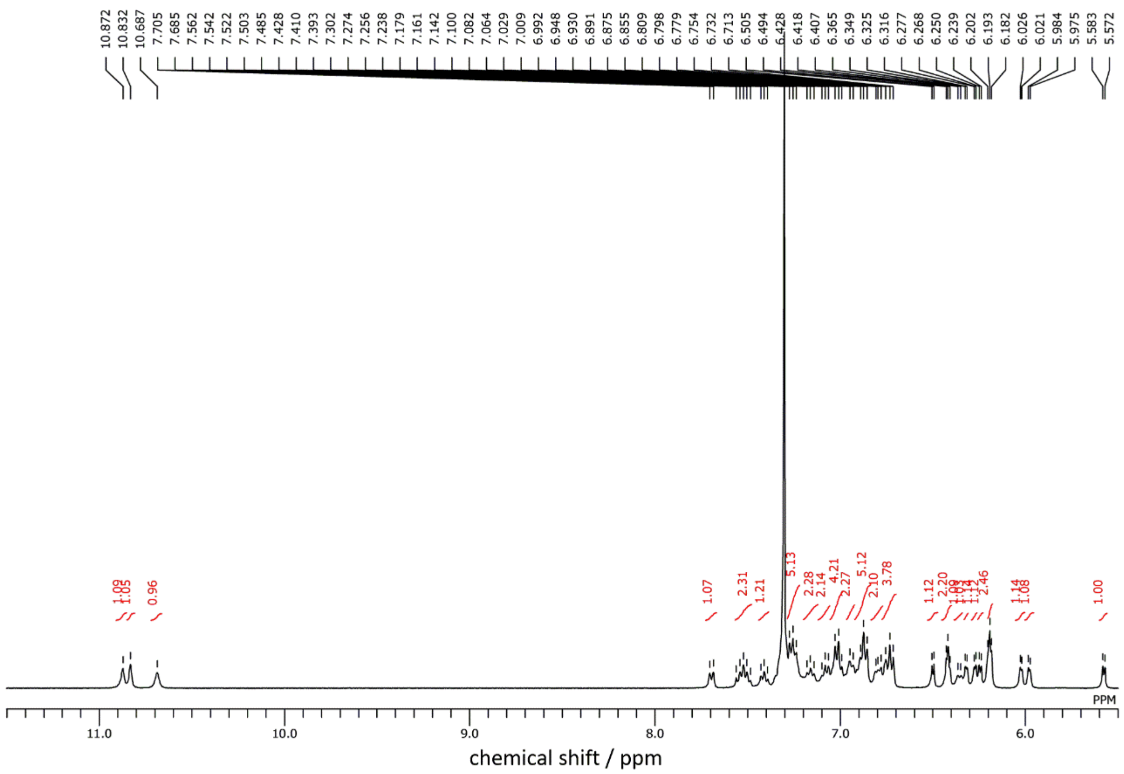

Figure 2.11. ^{1}H NMR spectrum of **2-4** in $CDCl_3$ at 213 K.

The optical properties of expanded porphyrins were investigated by UV-Vis-NIR absorption spectra in CH_2Cl_2 (Figure 2.12). Compounds **2-3**, **2-4** and **2-5** show broad absorption bands. The compound **2-3** shows strong absorption at 456 nm and broad absorption band around 520 to 800 nm. Compound **2-4** shows strong absorption band at 544 nm and broad absorption band around 750 to 900 nm, and compound **2-5** shows strong absorption band at 612 nm and broad absorption band around 850 to 1000 nm. With increasing in the macrocyclic ring size from **2-3** to **2-5**, the maximum absorption bands are red-shifted from 456 to 612 nm. All compounds have no fluorescence due to non-aromatic properties.[6]

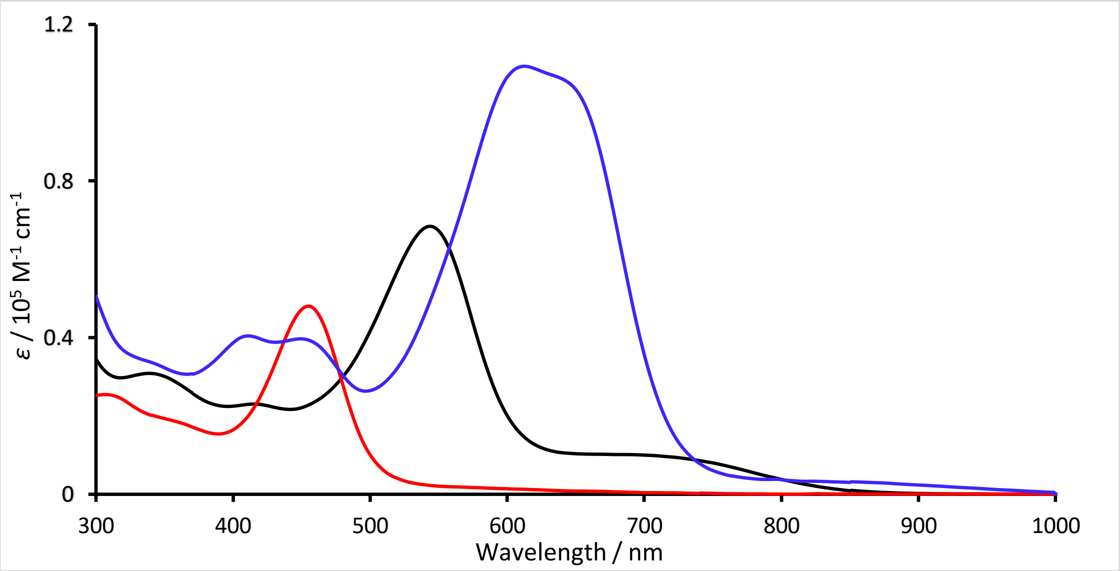

Figure 2.12. The UV-Vis-NIR absorption spectra of **2-3** (red), **2-4** (black) and **2-5** (blue) in CH_2Cl_2.

The redox properties of expanded porphyrins were examined by CV in CH_2Cl_2 with 0.1 M $TBAPF_6$ as an electrolyte (Figure 2.13). Compound **2-3** exhibits one irreversible oxidation potential at 0.32 V and two reversible reduction potentials at –1.52 and –1.69 V (vs. Fc/Fc^+). Compound **2-4** also shows one reversible oxidation potential at 0.11 and two reduction potentials at –1.45 and –1.64 V (vs. Fc/Fc^+). Interestingly, **2-5** shows three oxidation potentials at -0.03, 0.14 and 0.59 V and three reduction potentials at –1.31, –1.46 and –1.66 V (vs. Fc/Fc^+). The oxidation potentials of three porphyrins are negative-shifted with increasing of macrocyclic ring size. With increasing in the macrocyclic ring size from **2-3** to **2-5**, the absolute potential differences between the first oxidation and first reduction (HOMO-LUMO) gaps decrease from 1.85 to 1.33 eV.

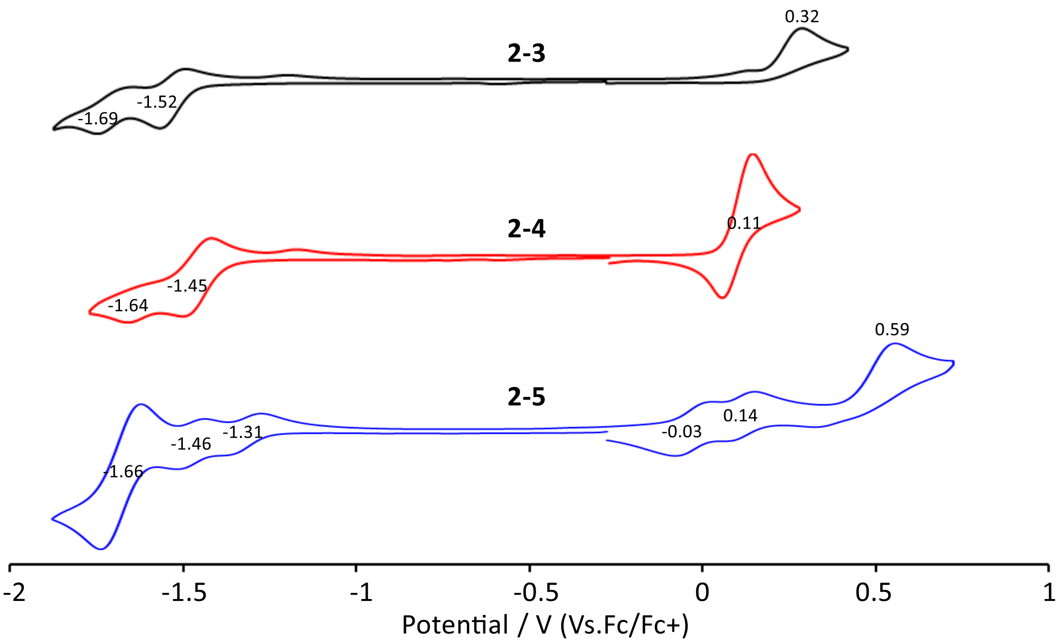

Figure 2.13. CV of **2-3**, **2-4** and **2-5** in CH_2Cl_2 with 0.1 M $TBAPF_6$. Scan rate = 0.1 V s^{-1}.

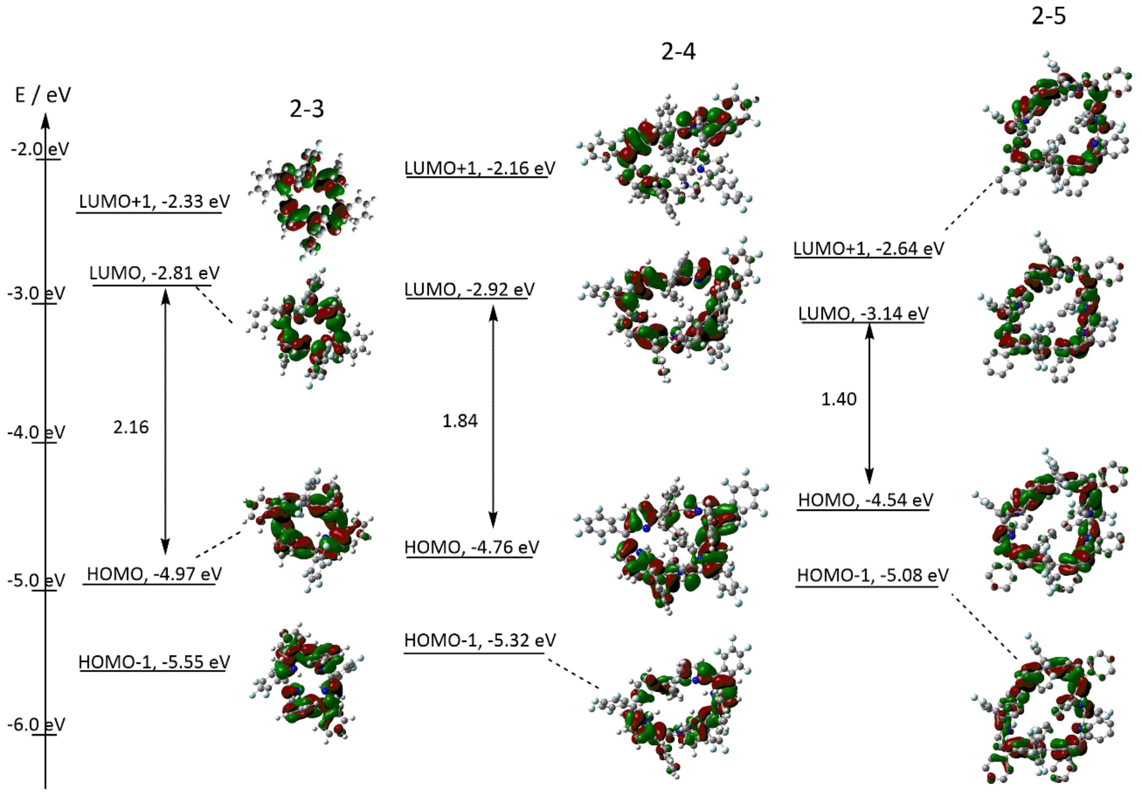

Figure 2.14. Frontier molecular orbitals and energy diagrams for the optimized structures of **2-3**, **2-4** and **2-5**, calculated at the B3LYP/6-31G* level.

To investigate the electronic properties of obtained porphyrins, DFT calculations were carried out at B3LYP/6-31G* level.[5] Frontier molecular orbitals and energy diagrams of **2-3**, **2-4** and **2-5** are shown in Figure 2.14. All obtained expanded porphyrins exhibit non-degenerated HOMO and LUMO pairs consisted with non-aromatic properties.

2-2-3 Coordination

Porphyrins show the rich coordination abilities that benefit from multiple coordination sites and flexible molecular frameworks. Therefore, the coordination abilities of **2-4** and **2-5** were investigated. After screening of the metalation conditions with various metal ions, zinc and copper complexes of compound **2-4** were obtained. In contrast, any metal complexes of compound **2-5** were not isolated.

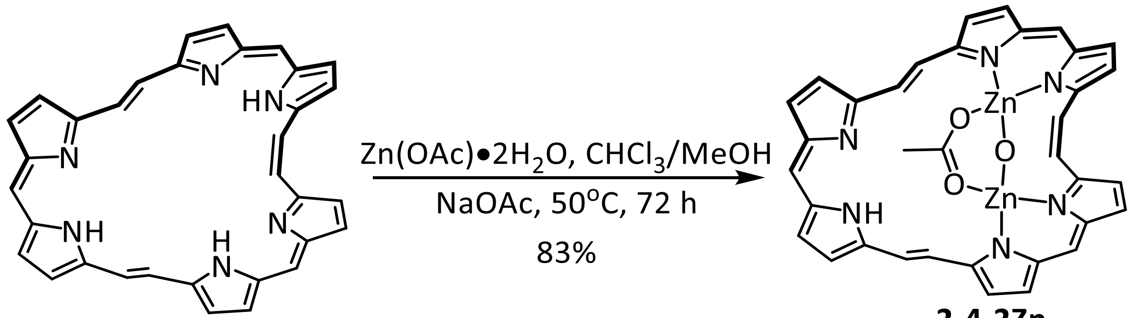

2-4

2-4-2Zn

Scheme 2.4. Synthetic scheme of **2-4-2Zn**. *meso*-C_6F_5 and Ph groups are omitted for clarity.

Metalation of zinc atom to **2-4** was attempted with 10 eq. of $Zn(OAc)_2$•$2H_2O$ and 10 eq. of sodium acetate in methanol and chloroform at 50°C under nitrogen (Scheme 2.4). After careful purification by alumina column chromatography eluted with *n*-hexane and ethyl acetate, zinc complex (**2-4-2Zn**) was isolated in 83% yield. HR-MALDI-MS revealed that the molecular ion peak is observed at m/z = 1663.1049, indicating that zinc complex involves two zinc atoms.

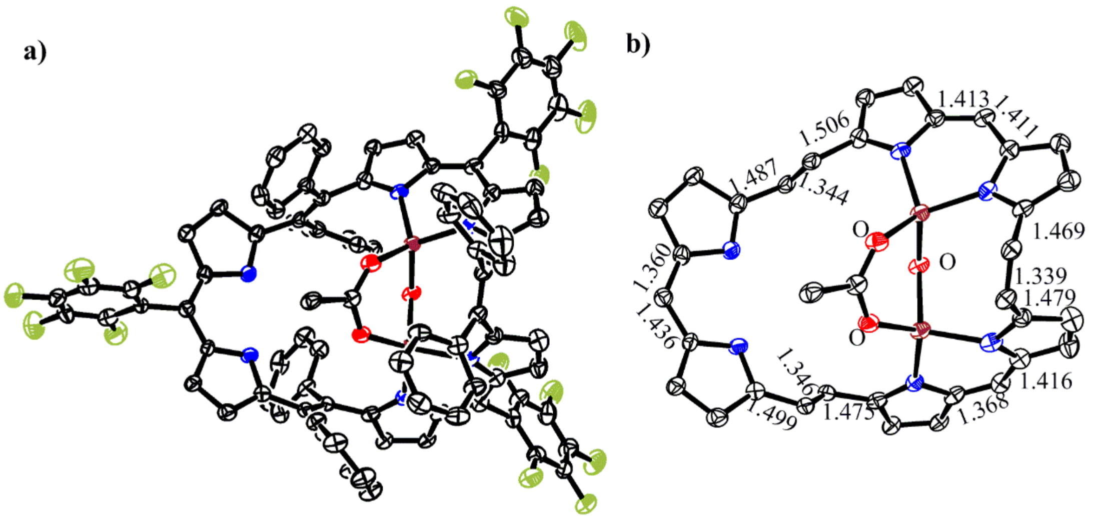

Figure 2.15. Crystal structure of **2-4-2Zn** (a) with selected bond lengths (Å) (b). The thermal ellipsoids represent for 40% probability. Hydrogen atoms are omitted for clarity

The crystal structure of **2-4-2Zn** was determined by X-ray crystallography (Figure 2.15). The single crystal of **2-4-2Zn** was obtained from slow diffusion of *n*-hexane into dichloromethane solution. Two zinc atoms coordinate to two dipyrrin units connected through *cis*-vinylene linkage, and each zinc atom coordinate with one acetyl group and one oxygen atom, giving the tetrahedral geometry. The remaining dipyrrin unit maintains the free base form. The bond lengths of vinylene bridges of **2-4-2Zn** are 1.344, 1.339 and 1.346 Å, respectively. The feature of the bond lengths is consistent with free−base **2-4**. The free base **2-4** and zinc complex show highly twisted molecular structures with non-aromatic properties.

The ^{1}H NMR spectrum of **2-4-2Zn** shows sharp peaks at room temperature because molecular dynamic motion is fixed by insertion of two zinc atoms (Figure 2.16). The NH signal is observed at 11.90 ppm as a broad peak. The acetyl group was observed at 1.82 ppm as a singlet peak. The protons of pyrrolic *β*-position exhibit doublet signals in a range from 6.40 to 5.92 ppm. The ^{19}F NMR spectrum of **2-4-2Zn** exhibit three group signals assigned to *o*-F, *m*-F and *p*-F of C_6F_5 groups.

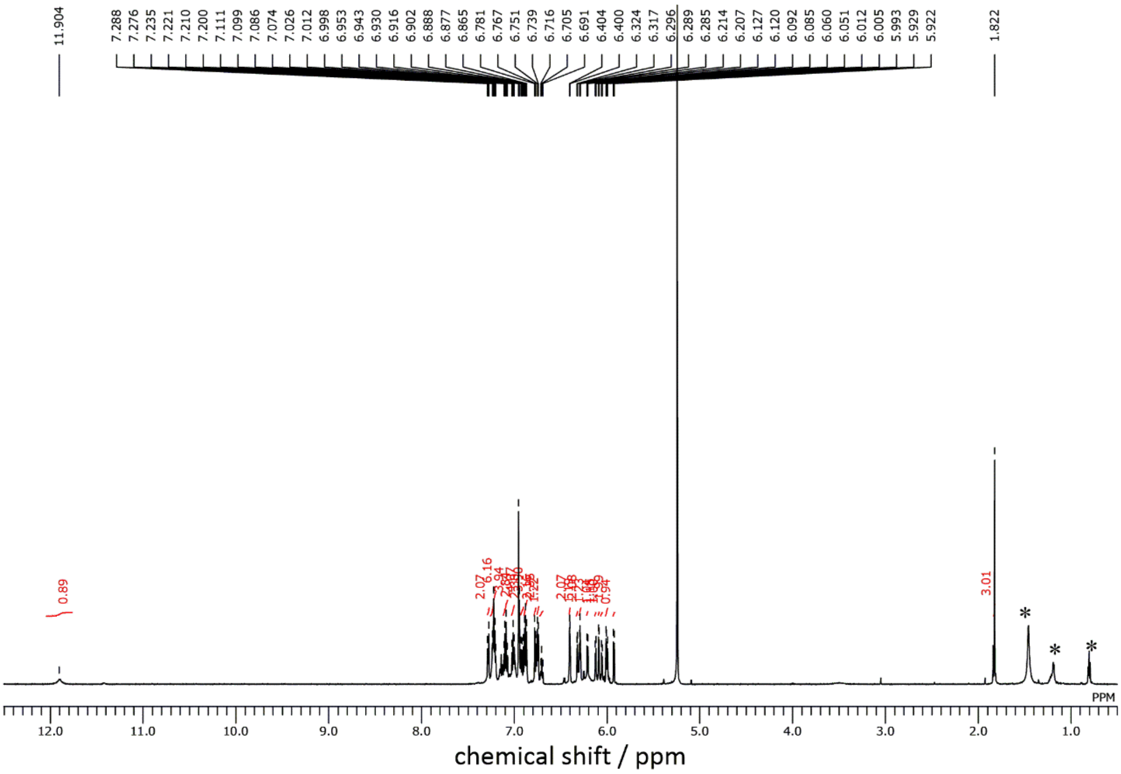

Figure 2.16. ^{1}H NMR spectrum of **2-4-2Zn** in CD_2Cl_2. * indicates residual solvent.

Compound **2-4** reacted with excess $Cu(OAc)_2$•H_2O in a mixture of chloroform and methanol solution under reflux conditions (Scheme 2.5). By monitoring reactions using APCI-MS, two molecular ion peaks of mono-copper and bis-copper complexes are detected (**2-4-Cu** and **2-4-2Cu**). However, after purification by silica gel column chromatography, **2-4-2Cu** disappeared and **2-4-Cu** was only isolated in 50% yield. By careful screening of the reaction conditions, reaction solvents and purification processes were turned out to be key factors to synthesize **2-4-2Cu**. The reaction was performed with 10 eq. $Cu(OAc)_2•H_2O$ and compound **2-4** in methanol under a reflux condition for 4 hours. After removal of methanol, the crude **2-4-2Cu** was washed with small amount of *n*-hexane twice. The residual solid was dissolved again in small amount of dry CH_2Cl_2, and then the crude mixture including undissolved solid was filtrated through filter paper. After removal of solvent, the collected solid was dried in a vacuum chamber to give **2-4-2Cu** in 30% yield. It should be noted that **2-4-2Cu** is sensitive under silica gel and acidic conditions caused by releasing one copper atom from **2-4-2Cu** to form **2-4-Cu**. In addition, **2-4-2Cu** can be transformed from **2-4-Cu** under the same reaction condition for preparation of **2-4-2Cu** from free-base **2-4**. HR-MALDI-MS revealed that the molecular ion peaks of **2-4-Cu** and **2-4-2Cu** were observed at m/z = 1519.2893 (calcd. for $C_{87}H_{43}F_{15}N_6Cu$ = 1519.2606 $[M]^+$) and 1581.1819 (calcd. for $C_{87}H_{42}F_{15}N_6Cu_2$ = 1581.1823 $[M]^+$), respectively.

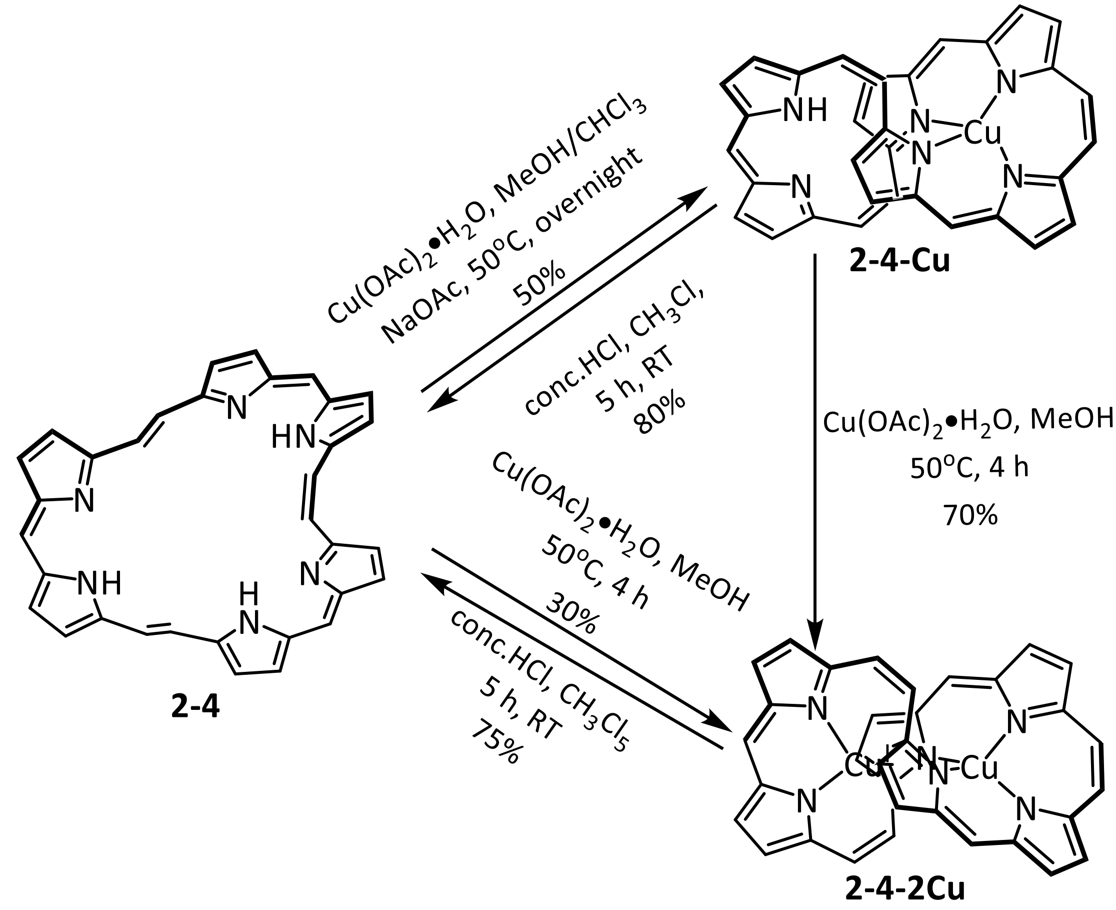

Scheme 2.5. Synthetic schemes of **2-4-Cu** and **2-4-2Cu**. *meso*-C_6F_5 and -Ph groups are omitted for clarity.

Single crystals of **2-4-Cu** and **2-4-2Cu** for X-ray crystallography were obtained from slow diffusion of *n*-hexane into dichloromethane solution (Figure 2.17). Unexpectedly, copper complexes of **2-4-Cu** and **2-4-2Cu** are composed of figure-of-eight shaped molecular structures transformed from the twisted structure of the free base **2-4**. In addition, all diphenyl vinylene bridges changed to *cis*-conformations, indicating that *cis-/trans-* isomerization occurs by the metalation progress. The copper atom of **2-4-Cu** is inserted to the four nitrogen atoms of the two dipyrrin units as a distorted square planar geometry. The remained dipyrrin unit is kept as a free base form. Interestingly, the second copper atom of **2-4-2Cu** bonds the remaining two nitrogen atoms on the dipyrrin unit and pyrrolic *sp*^{2} carbons as a η^2-coordination manner. The distances of Cu^{I}-C$_{30}$ and Cu^{I}-C$_{31}$ are 2.040 Å and 2.309 Å, which are shorter than the sum of the van der Waals radii (3.40 Å) (Figure 2.17). Those distances are longer than the covalent bond distance of Cu^{II}-C(*sp*^{2}) (1.94 Å).[10] We concluded that additional copper is +1 valence and consists of Cu^{I}–arene interaction.

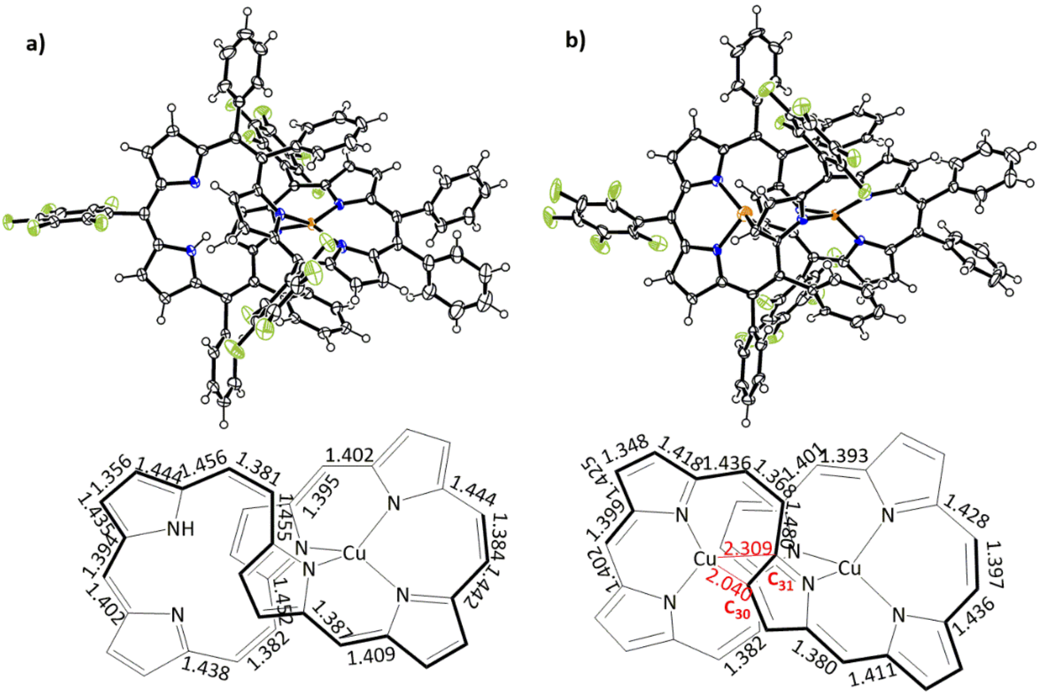

Figure 2.17. Crystal structures and selected bond lengths (Å) of a) **2-4-Cu** and b) **2-4-2Cu**. The thermal ellipsoids represent for 50% probability.

Furthermore in order to evaluate the Cu^{I}–arene interaction, DFT calculation was carried out at the UB3LYP/6-31G* level. The optimized structure of **2-4-2Cu** is predicted

Cu^{I}–arene interaction with Cu^{I}-C$_{30}$ (1.954 Å) and Cu^{I}-C$_{31}$ (2.422 Å) (Figure 2.18). Insight into selected molecular orbital shows orbital overlap between Cu^{I}(d) and C$_{30}$-C$_{31}$(π) orbitals, supporting the existent of Cu^{I}-arene interaction.[10]

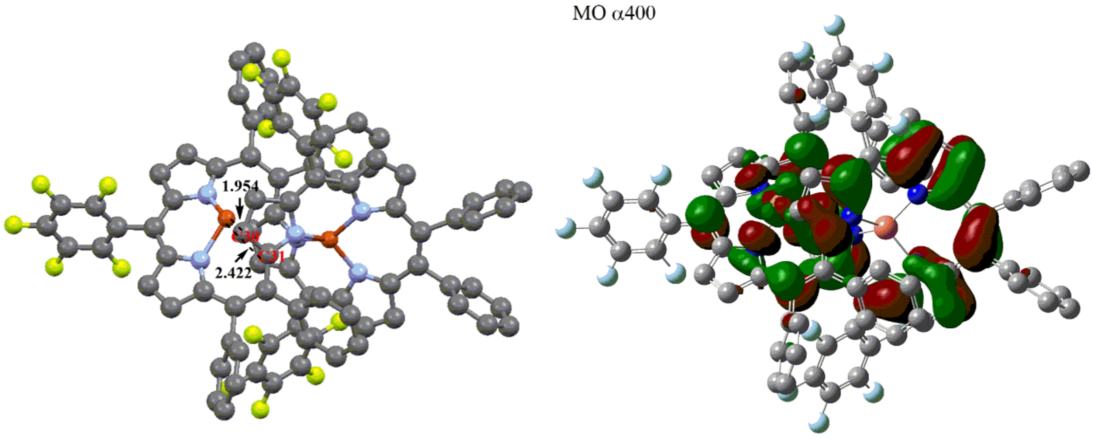

Figure 2.18. Optimized structure of **2-4-2Cu** calculated at the UB3LYP/6-31G* level of theory. a) Optimized structure and selected bond lengths b) molecular orbital at MO α400.

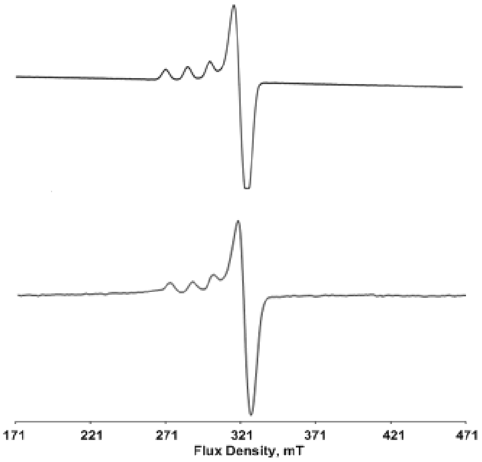

Figure 2.19. ESR spectra of **2-4-Cu** (up) and **2-4-2Cu** (bottom) in CH_2Cl_2 at 110 K.

To investigate magnetic property of copper complexes, the EPR spectroscopy measurement of **2-4-Cu** and **2-4-2Cu** was performed in frozen dichloromethane at 110 K

(Figure 2.19). EPR spectrum of **2-4-Cu** shows that copper(II) ion has a $3d_{(x2\text{-}y2)}$ ground state. The EPR spectrum of **2-4-2Cu** shows similar spectrum with **2-4-Cu** consistent with Cu^{I}-Cu^{II} mixture valence.

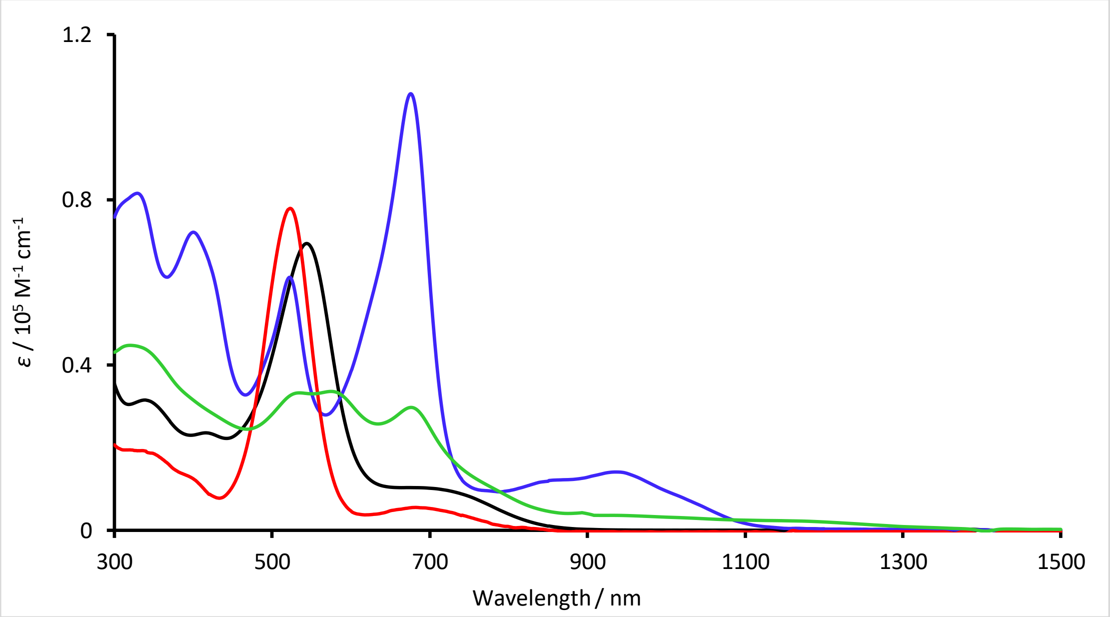

Figure 2.20. The UV-Vis absorption spectra of **2-4** (black), **2-4-Cu** (blue), **2-4-2Cu** (green) and **2-4-2Zn** (red) in CH_2Cl_2.

The absorption spectra of the copper and zinc complexes were measured in CH_2Cl_2 at room temperature (Figure 2.20). The compound **2-4** shows absorption band at 544 nm associated with broad absorption band around 750 nm and absorption edge reached around 900 nm. **2-4-2Zn** shows a similar absorption feature with that of free-base **2-4**. The maximum absorption peak is observed at 523 nm. Interestingly, two copper complexes exhibit remarkably different absorptions properties because they showed aromatic properties. The Soret-like band of **2-4-Cu** shows at 680 nm and clear Q-bands shows in near-IR region at 850 and 944 nm with absorption edge reached around 1150 nm. **2-4-2Cu** shows multi-absorption bands from 500 to 700 nm and weak near-IR absorption associated with broad absorption band around 1200 to 1450 nm.

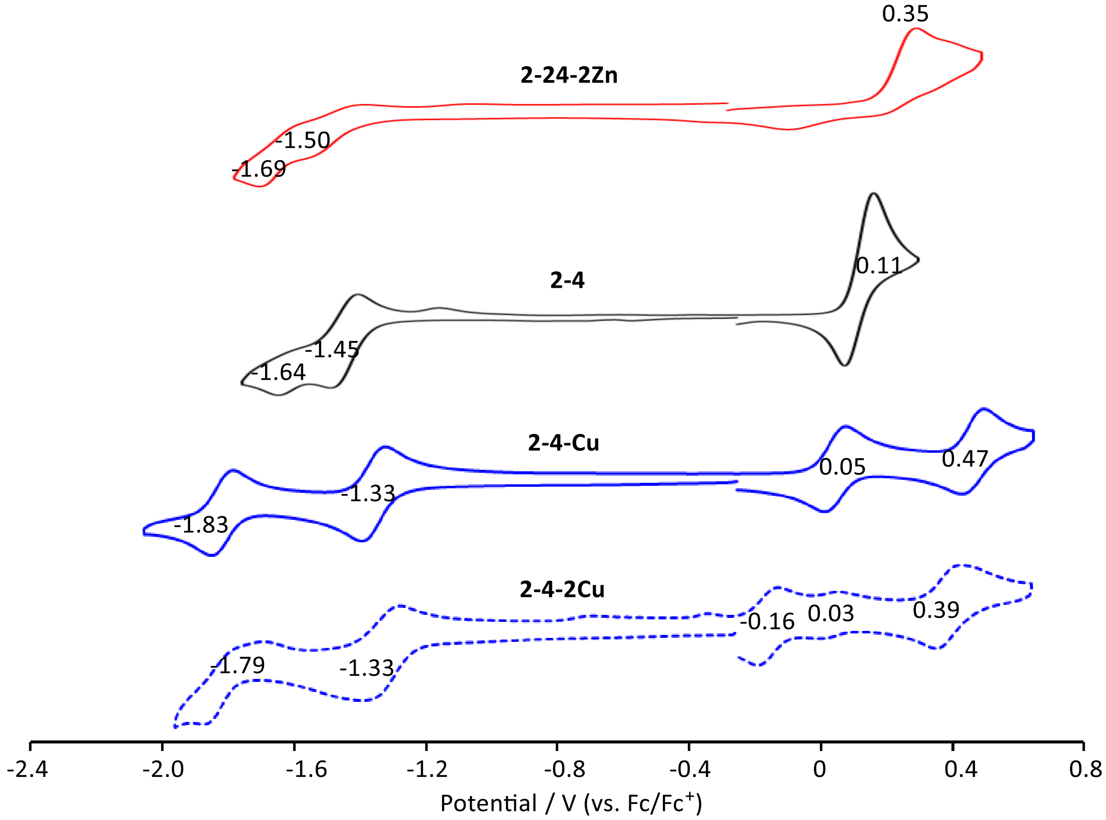

Figure 2.21. CV of **2-4-2Zn**, **2-4**, **2-4-Cu** and **2-4-2Cu** in CH_2Cl_2, containing 0.1 M $TBAPF_6$. Scan rate is 0.1 V s^{-1}.

The redox properties of the free base **2-4** and metal complexes were measured by CV in CH_2Cl_2 with 0.1 M $TBAPF_6$ as an electrolyte (Figure 2.21). The free base **2-4** shows oxidation and reduction potential at 0.11 V and –1.45 and –1.64 V (vs. Fc/Fc^+). The zinc complex **2-4-2Zn** shows two reduction potentials and one oxidation potential at –1.50, –

1.69 and 0.35 V (vs. Fc/Fc$^+$). The reductions and oxidation of **2-4** and **2-4-2Zn** are located at the non-aromatic hexaphyrin(2.1.2.1.2.1) unit.[6] Copper complexes, **2-4-Cu** and **2-4-2Cu**, show two reversible reduction potentials at –1.33 and –1.83 V (vs. Fc/Fc$^+$) and –1.33 and –1.79 V (vs. Fc/Fc$^+$), respectively. Oxidation potentials of **2-4-Cu** are observed at 0.05 and 0.47 V (vs. Fc/Fc$^+$). **2-4-2Cu** shows three reversible oxidation potentials at –0.16, 0.03 and 0.39 V (vs. Fc/Fc$^+$), including the redox of Cu^{I}/Cu^{II} (0.03 V). The copper complexes **2-4-Cu** and **2-4-2Cu** give a narrower HOMO–LUMO gap than that of **2-4** and **2-4-2Zn** due to aromatic properties.

The mechanism of *trans-/cis-* isomerization during metalation reaction is still not settled, but a possible mechanism was proposed in supporting information.

2-2-4 Aromaticity

The bond lengths of the copper complexes **2-4-Cu** and **2-4-2Cu** are changed from **2-4** and **2-4-2Zn** accomplished with the change of the conformations of vinylene bonds (Figure 2.22).

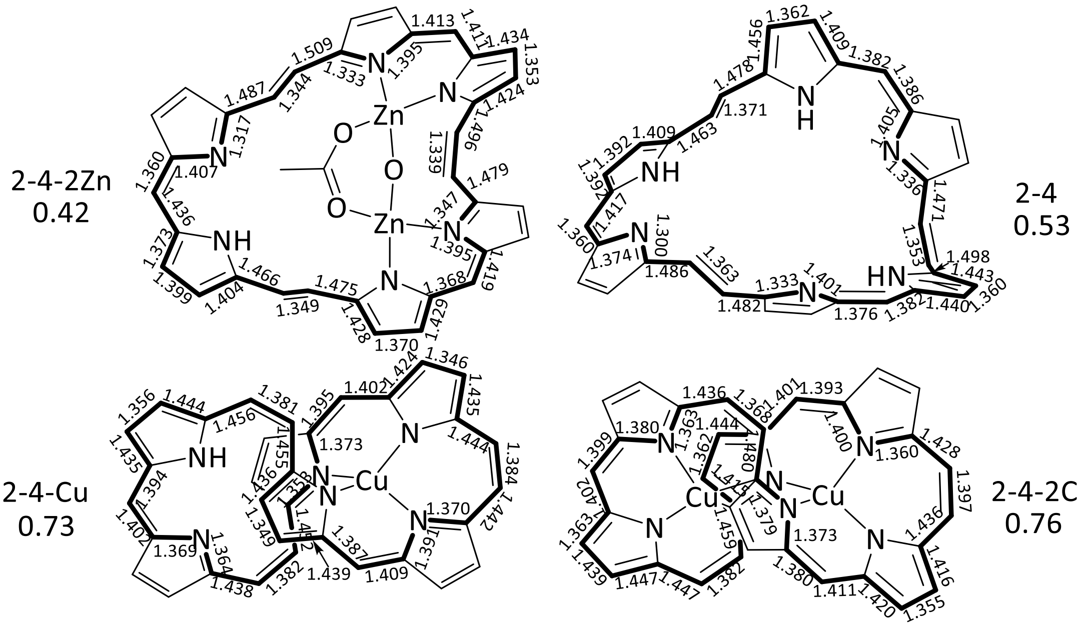

Figure 2.22. Selected bond lengths (Å) and calculated HOMA values of **2-4**, **2-4-2Zn**, **2-4-Cu** and **2-4-2Cu**. The bonds used for HOMA calculations are indicated in bold lines. *meso*-C_6F_5 and -Ph groups are omitted for clarity.

The bond lengths of diphenyl vinylene bridges are 1.381, 1.382 and 1.384 Å for **2-4-Cu**, and 1.368, 1.382 and 1.397 Å for **2-4-2Cu**, which are slightly longer than those of **2-4** and **2-4-2Zn**. The bond lengths of the methene carbon and the adjacent pyrrole *β*-carbon of two copper complexes clearly show no bond. These results suggested that figure-of-eight shaped structures of copper complexes might have macrocyclic aromaticity as well as figure-of-eight hexaphyrin(1.1.1.1.1.1). The HOMA values provide an important information about the extent of effective electronic delocalization.[12] In order to interpret the aromaticity, we calculated the HOMA values based on the conjugated pathway from crystal structures (Figure 2.22). The HOMA values of **2-4-Cu** and **2-4-2Cu** are 0.73 and 0.76, respectively, which could be categorized into aromatic compounds, while **2-4** and **2-4-2Zn** are 0.53 and 0.42, respectively, with non-aromatic characteristics. These results indicate that conformational changes to figure-of–eight shaped structures turn on the aromaticity from non-aromatic distorted structures triggered by insertion copper atoms into **2-4**.

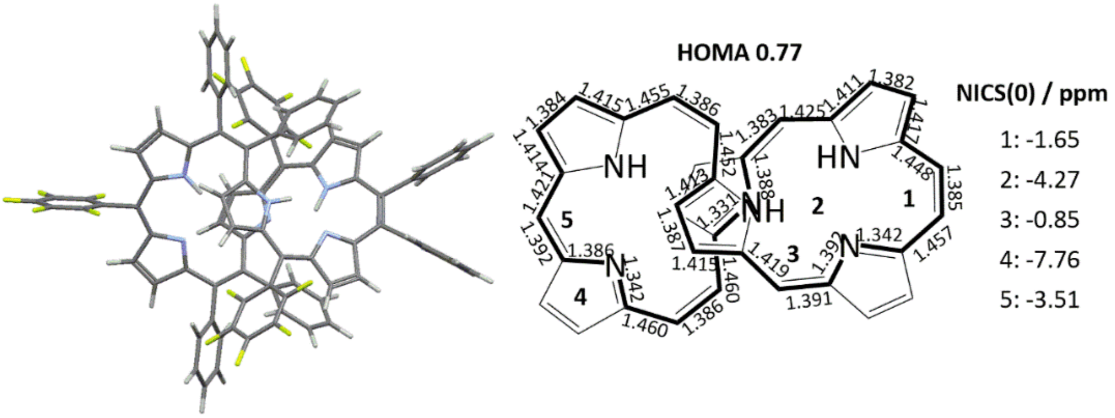

Figure 2.23. Optimized structure, selected bond lengths (Å), HOMA value and NICS(0) values of **2-4-*cis***. Optimized structure was calculated at the B3LYP/6-31G* level of theory. The bonds used for HOMA calculations are indicated in bold lines.

Bond distances and NICS [13] values of **2-4-*cis*** were obtained by DFT calculation to evaluate the aromatic property of figure-of-eight shaped expanded hexaphyrin(2.1.2.1.2.1) (Figure 2.23). **2-4-*cis*** is one of the isomer of **2-4** and optimized structure was calculated based on the crystal structure of **2-4-Cu** after removing its copper atom. The optimized structure of **2-4-*cis*** shows similar bond-length characteristics with the crystal structure of **2-4-Cu**. The HOMA value of **2-4-*cis*** is 0.77. The negative NICS values of various positions are obtained. These calculation results indicate that **2-4-*cis*** may exhibit the aromatic property

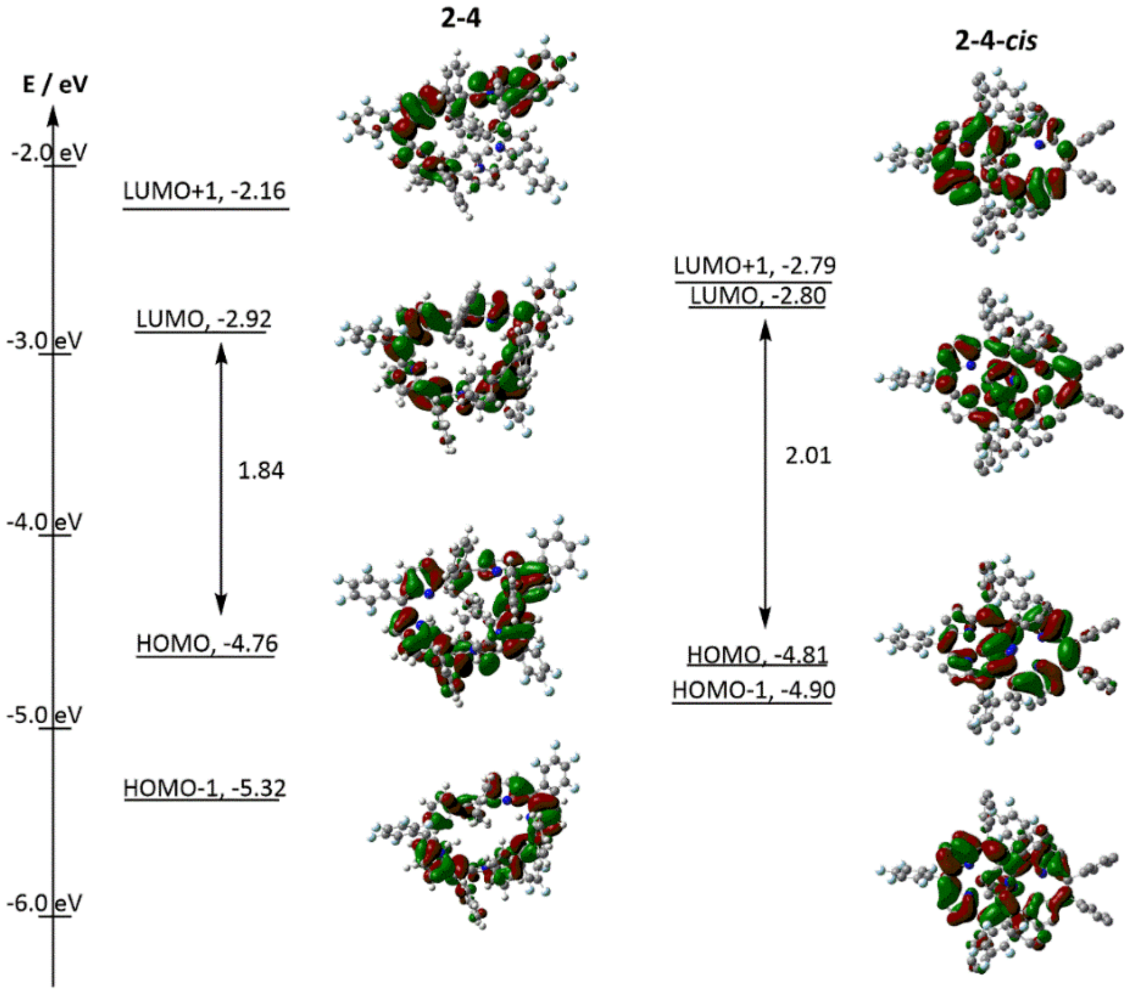

Figure 2.24. Frontier molecular orbitals and energy diagrams of **2-4** and **2-4-*cis***, calculated at the B3LYP/6-31G* level of theory.

Compound **2-4** exhibits no degeneracy HOMO and LUMO pairs which calculated at the B3LYP/6-31G* level of theory (Figure 2.24). This is attributed to their macrocyclic non-aromaticity. In contrast, **2-4-*cis*** exhibits degeneracy HOMO and LUMO pairs. These calculation results suggested that aromaticity of **2-4** relies on its macrocyclic structure.[6]

2-3 Conclusion

Diphenyl vinylene-bridges incorporated porphyrins and their metal complexes were synthetized. The contracted porphyrin triphyrin(2.1.1) **2-1** produces the sandwich iridium complex **2-2**. The cod ring is transformed from 1,5-cod to η^1,η^3-C_8H_{12} unit as a π-allyl ligand associated with the valence change of iridium from Ir^{I} to Ir^{III}.

Next part, three distorted twisted porphyrins with diphenyl vinylene-bridges, porphyrin(2.1.2.1) **2-3**, hexaphyrin(2.1.2.1.2.1) **2-4** and octaphyrin(2.1.2.1.2.1.2.1) **2-5**, were obtained from ***E-/Z*-DPhDPEs**. The X-ray diffraction analysis revealed that conformations on diphenyl vinylene-bridges of obtained porphyrins depend on the sizes of molecular macrocyclic rings. Expanded porphyrins **2-3**, **2-4** and **2-5** are non-aromatic compounds because of highly twisted molecular structures. Compound **2-4** can be converted to zinc and copper complexes. The zinc complex has a twisted molecular structure with non-aromatic property, while copper complexes have figure-of-eight shaped molecular structures with aromatic property. This result suggests that aromaticity of obtained hexaphyrin relies on their molecular structures.

The findings in Chapter are that ***E/Z*-DPhDPE** isomers can produce three porphyrins with the same molecular structures. The regioisomeric structure of ***E/Z*-DPhDPE** do not reflect their molecular structures to obtained porphyrins.

2-4 References

[1] (a) L. Xue, Z. Shen, J. Mack, D. Kuzuhara, H. Yamada, T. Okujima, N. Ono, X. You, N. Kobayashi, *J. Am. Chem. Soc.,* **2008***, 130,* 16478; (b) D. Kuzuhara, H. Yamada, L. Xue, T. Okujima, S. Mori, Z. Shen, H. Uno, *Chem. Commun.,* **2011,** *47,* 722; (c) S. Anju, S. Ramakrishnan. A. Srinivasan, *Org. Lett.,* **2011***, 13,* 2498; (d) D. Kuzuhara, Y. Sakakibara, S. Mori, T. Okujima, H. Uno, H. Yamada, *Angew. Chem., Int. Ed.,* **2013***, 125,* 3444; (e) K. S. Anju.; S. Ramakrishnan.; A. Srinivasan. *Org. Lett.,* **2011**, *13*, 2498.

[2] (a) L. Xue, J. Mack, H. Lu, L. Zhang, X. You, D. Kuzuhara, M. Stillman, H. Yamada, S. Yamauchi, N. Kobayashi, Z. Shen, *Chem. Eur. J.,* **2011***, 17,* 4396; (b) L. Xue, D. Kuzuhara, S. Ikeda, T. Okujima, S. Mori, H. Uno, H. Yamada, *Inorg. Chem.,* **2013***, 52,* 1688; (c) L. Xue, D. Kuzuhara, S. Ikeda, Y. Sakakibara, K. Ohkubo, N. Aratani, T. Okujima, H. Uno, S. Fukuzumi, H. Yamada, *Angew. Chem., Int. Ed.,* **2013***, 52,* 7306; (d) L. Xue, Y. Wang, J. Mack, W. Zhu, Z. Ou, *Chem. Eur. J.,* **2015***, 21,* 2045; (e) L. Xue, Y. Wang, J. Mack, Y. Fang, Z. Ou, W. Zhu, K. Kadish, *Inorg. Chem.,* **2015***, 54,* 11852.

[3] (a) G. Modugno, A. Monney, M. Bonchio, M. Albrecht, M. Carraro, *Eur. J. Inorg. Chem.,* **2014***, 2014,* 2356; (b) Y. Ebe, T. Nishimura, *J. Am. Chem. Soc.,* **2015***, 137,* 5899; (c) A. Tsuboyamo, H. Iwawaki, M. Furugori, T. Mukaide, J. Kamatani, S. Igawa, T.

Moriyama, S. Miura, T. Takiguchi, S. Okada, M. Hoshino, K. Ueno, *J. Am. Chem. Soc.,* **2003***, 125,* 12971.

[4] (a) K. Yoshida, T. Nakashima, S. Yamaguchi, A. Osuka, H. Shinokubo, *Daltan. Trans.,* **2011***, 40,* 8773; (b) S. Madrahimov, D. Markovic, J. Hartwig, *J. Am. Chem. Soc.,* **2009***, 131,* 7228.

[5] Gaussian 09, Revision B.01, M. J. Frisch, G. W. Trucks, H. B. Schlegel, G. E. Scuseria, M. A. Robb, J. R. Cheeseman, G. Scalmani, V. Barone, B. Mennucci, G. A. Petersson, H. Nakatsuji, M. Caricato, X. Li, H. P. Hratchian, A. F. Izmaylov, J. Bloino, G. Zheng, J. L. Sonnenberg, M. Hada, M. Ehara, K. Toyota, R. Fukuda, J. Hasegawa, M. Ishida, T. Nakajima, Y. Honda, O. Kitao, H. Nakai, T. Vreven, J. A. Montgomery, Jr., J. E. Peralta, F. Ogliaro, M. Bearpark, J. J. Heyd, E. Brothers, K. N. Kudin, V. N. Staroverov, T. Keith, R. Kobayashi, J. Normand, K. Raghavachari, A. Rendell, J. C. Burant, S. S. Iyengar, J. Tomasi, M. Cossi, N. Rega, J. M. Millam, M. Klene, J. E. Knox, J. B. Cross, V. Bakken, C. Adamo, J. Jaramillo, R. Gomperts, R. E. Stratmann, O. Yazyev, A. J. Austin, R. Cammi, C. Pomelli, J. W. Ochterski, R. L. Martin, K. Morokuma, V. G. Zakrzewski, G. A. Voth, P. Salvador, J. J. Dannenberg, S. Dapprich, A. D. Daniels, O. Farkas, J. B. Foresman, J. V. Ortiz, J. Cioslowski, D. J. Fox, Gaussian, Inc., Wallingford CT, 2010.

[6] (a) S. Saito, A. Osuka, *Angew. Chem. Int. Ed.*, **2011**, *50,* 4342; b) JL. Sessler, D. Seidel, *Angew. Chem. Int. Ed.*, **2003**, *42,* 5134; c) A. Osuka, S. Saito, *Chem. Commun.*, **2011**, *47,* 4330; d) T. Tanaka, A. Osuka, *Chem. Rev.*, **2017**, *117,* 2584; e) J-Y. Shin, K. S. Kim, M-C. Yoon, J. M. Lim, Z. S. Yoon, A. Osuka , D. Kim, *Chem. Soc. Rev.*, **2010**, *39,* 2751; f) R. Herges, *Chem. Rev.*, **2006**, *106,* 4820; g) Z. S. Yoon, A. Osuka, D. Kim, *Nat. Chem.*, **2009**, *1,* 113; h) S. Hiroto, Y. Miyake, H. Shinokubo, *Chem, Rev.*, **2017**, *117,* 2910; i) T. D. Lash, *Chem, Rev.*, **2017**, *117,* 2313; j) W. Zhang, W. Lai, R. Cao, *Chem, Rev.*, **2017**, *117,* 3717; k) Y. M. Sung, J. Oh, W. Y. Cha, W. Kim, J. M. Lim, M. C. Yoon, D. Kim, *Chem, Rev.*, **2017,** *117,* 2257; l) T. Chatterjee, V S. Shetti, R. Sharma, M. Ravikanth, *Chem, Rev.*, **2017,** *117,* 3254.

[7] (a) C. Bruckner, E. D. Sternberg, R. W. Boyle, D. Dolphin, *Chem. Commun.*, **1997,** *17,* 1689; b) M. G. P. M. S. Neves, R. M. Martins, A. C. Tomé, A. J. D. Silvestre, A. M. S. Silva, V. Félix, M. G. B. Drew, J. A. S. Cavaleiro, *Chem. Commun.*, **1999**, *4,* 385; c) J. Shin, H. Furuta, K. Yoza, S. Igarashi, A. Osuka, *J. Am. Chem. Soc.*, **2001**, *123,* 7190; d) S. Shimizu, J. Shin, H. Furuta, R. Ismael, A. Osuka, *Angew. Chem., Int. Ed.*, **2003**, *42,* 78; (e) M. Suzuki, A. Osuka, *Org. Lett.*, **2003**, *5,* 3943.

[8] (a) E. Vogel, H. Schmickler, *Angew. Chem., Int. Ed.*, **1990**, *29,* 1387; (b) M. Umetani, T. Tanaka, T. Kim, D. Kim, A. Osuka, *Angew. Chem., Int. Ed.*, 2016, 55, 8095; (c) T.

Yoneda, T. Hoshino, S. Neya, *J. Org. Chem.*, **2017**, *82,* 10737; (d) D. Kuzuhara, W. Furukawa, A. Kitashiro, N. Aratani, H. Yamada, *Chem. Eur. J.*, **2016**, *22,* 10671; (e) K. S. Anju, M. Das, B. Adinarayana, C. H. Suresh, A. Srinivasan, *Angew. Chem., Int. Ed.*, **2017**, *56*, 15667.

[9] (a) K. Garg, E. Ganapathi, P. Rajakannu, M. Ravikanth, *Phys. Chem. Chem. Phys.*, **2015**, *17*, 19465; (b) L. Bras, C. Adamo, A. Perrier, *J. Phys. Chem. C*, **2017**, *121*, 25603; (c) K.Keshav, A. Dvivedi, M. Ravikanth, *Chem. Select.*, **2017**, *2*, 2014.

[10] (a) S. Saito, K. Furukawa, A. Osuka, *Angew. Chem., Int. Ed.,* **2009***, 48,* 8086; b) T. Osako, Y. Tachi, M. Doe, M. Shiro, K. Ohkubo, S. Fukuzumi, S. Itoh, *Chem. Eur. J.,* **2004***, 10,* 237.

[11] C. Dugave, L. Demange, *Chem. Rev.,* **2003***, 103,* 2475.

[12] T. M. Krygowski, *J. Chem. Inf. Comput. Sci.,* **1993***, 33,* 70.

[13] P. v. R. Schleyer, C. Maerker, A. Dransfeld, H. Jiao, N. R. v. E. Hommes, *J. Am. Chem. Soc.,* **1996***, 118,* 6317.

2-5 Supporting Information

Spectroscopy ^{1}H NMR and ^{19}F NMR spectra were recorded on a JNM–ECX 300/400 and JNM–ECA 600 spectrometers (operating as 300 MHz, 400 MHz and 600 MHz for ^{1}H, 100 MHz for ^{13}C and 376 MHz for ^{19}F) using the residual solvent as the internal reference for ^{1}H (δ = 7.26 ppm in $CDCl_3$, δ = 5.32 ppm in CD_2Cl_2, δ = 2.50 ppm in DMSO-d_6) and CF_3COOH as the external reference for ^{19}F (δ = – 76.5 ppm). HR–MALDI–TOF mass spectra were recorded on a Bruker Daltonics autoflex MALDI–TOF MS spectrometer. The APCI–MS were measured by a BRUKER microTOFII–KR spectrometer using positive ion modes. UV–vis–NIR absorption spectra were measured with a JASCO UV/VIS/NIR Spectrophotometer V–670. CV and DPV measurements were conducted in a solution of 0.1 M $TBAPF_6$ in dry-dichloromethane with a scan rate of 0.1 V s^{-1} in an argon-filled cell. A glassy carbon electrode and a platinum wire were used as a working and a counter electrode, respectively. An $Ag/AgNO_3$ electrode was used as reference electrodes, which were normalized with the half-wave potential of ferrocene/ferrocenium (Fc/Fc^+) redox couple. Electron spin resonance (ESR) measurements were performed on a JEOL, JES–FA100N spectrometer at 110K under an argon atmosphere.

Materials All solvents and chemicals were reagent grade quality, obtained commercially and used without further purification except as noted. For spectral measurements, spectral grade dichloromethane was purchased from Nakalai Tesque Co. Thin−layer chromatography (TLC), flush column chromatography, and gravity column chromatography were performed on Art. 5554 (Merck KGaA), Silica Gel 60 (Merck KGaA), and Silica Gel 60N (Kanto Chemical Co.), respectively.

X−ray Analysis X−ray crystallographic data for **2-2, 2-3, 2-4, 2-5** and **2-4-Cu** were recorded at 103 K. All measurements were made on a Rigaku R-AXIS RAPID diffractometer using multi-layer mirror monochromated Mo-Kα radiation (detailed crystallographic information in SI). X−ray crystallographic data for **2-4-2Cu** and **2-4-2Zn** were recorded at 100 K on a Rigaku CCD detector (Saturn 724) mounted on a Rigaku rotating anode X−ray generator (MicroMax-007HF) using Mo-Kα radiation from the corresponding set of confocal optics. The structures were solved by direct methods and refined on F^2 by full−matrix least−squares using the CrystalClear, SHELXS−97 and SHELXT−2014/5 programs.[S1] CCDC: 1473974, 1473975, 1505987, 1511828, 1473977, 1473978 and 1501616 contain the supplementary crystallographic data for **2-2, 2-3**, **2-4**, **2-5**, **2-3-Cu**, **2-4-2Cu** and **2-4-2Zn**, respectively. These data can be obtained free of charge from the Cambridge Crystallographic Data Centre via www.ccdc.cam.ac.uk/data_request/cif.

Theoretical calculations All density functional theory calculations were achieved with the Gaussian 09 program package. The geometry of expanded porphyrins and their metal complexes were fully optimized at the Beckes three-parameter hybrid functional combined with the Lee-Yang-Parr correlation functional abbreviated as the B3LYP and UB3LYP level of density functional theory with 6-31G (d) basis set. The geometry of **2-2** was fully optimized at the Beckes three-parameter hybrid functional combined with the Lee-Yang-Parr correlation functional abbreviated as the B3LYP level of density functional theory with 6-31G*/SDD basis set. [S3]

Synthesis 2-2.

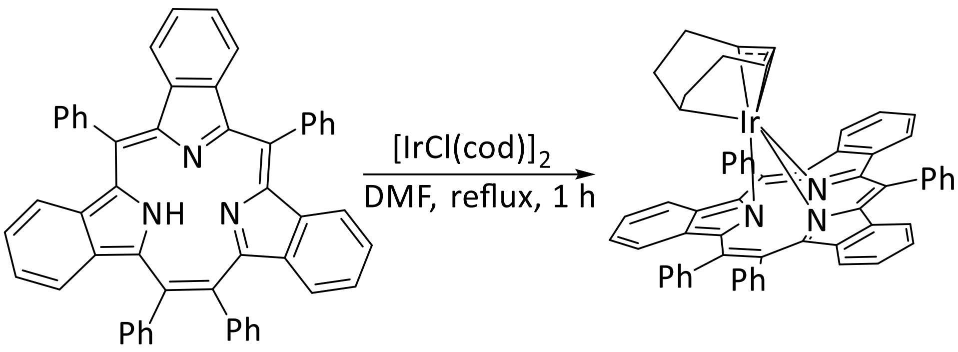

2-1

2-2, 46%

A solution of **2-1** (20 mg, 0.026 mmol) and $[IrCl(cod)]_2$ (87 mg, 0.13 mmol) in DMF (15 ml) was bubbled with argon for 5 minutes, and then the mixture was refluxed for 1 hour under an argon atmosphere. After cooling to room temperature, the crude mixture was diluted with CH_2Cl_2. The organic layer was washed with water, aqueous $NaHCO_3$ and brine, and then dried over anhydrous Na_2SO_4. After solvent was evaporated, the residue was purified by silica gel column chromatography using chloroform as an eluent. The first eluted deep-purple fraction was collected and evaporated to give **2-2** in 46% (12 mg, 0.012 mmol).

2-2 ^{1}H NMR (400 MHz, CD_2Cl_2, 193 K) $\delta = 8.46$ (d, $J = 4$ Hz, 1H, benzo), 8.30 (d, $J = 4$ Hz, 1H, benzo), 7.93 (m, 3H, benzo, phenyl ring), 7.80 (m, 3H, phenyl ring), 7.53 (m, 3H, phenyl ring), 7.41 (m, 2H, phenyl ring), 7.30 (m, 4H, phenyl ring), 7.14 (m, 3H, benzo, phenyl ring), 7.02 (m, 5H, benzo, phenyl ring), 6.85 (m, 4H, benzo, phenyl ring), 6.65 (m, 1H, benzo), 6.63 (d, $J = 4$ Hz, 2H, benzo), 3.89 (m, 1H, cod), 2.93 (m, 1H, cod), 2.56 (m, 1H, cod), 1.24 (m, 1H, cod), 0.92 (s, 1H, cod), 0.81 (m, 2H, cod), 0.67 (m, H, cod), 0.34 (d, $J = 4$ Hz, 2H, cod), 0.14 (s, 2H, cod) ppm. ^{13}C NMR (100 MHz, CD_2Cl_2, 298K) δ = 155.3, 150.1, 149.1, 148.1, 144.9, 142.9, 141.5, 139.0, 138.5, 138.3, 138.1, 137.2, 136.7, 136.6, 136.4, 136.1, 134.1, 133.1, 131.5. 129.6, 129.5, 129.4, 128.1, 127.6, 127.2, 126.9, 126.1, 126.0, 125.9, 125.9, 125.8, 123.6, 123.3, 123.1, 122.7, 122.5, 55.2, 54.6, 54.3, 54.0, 48.5, 46.2, 27.3, 27.1, 27.2 ppm. HR-MALDI-TOF-MS: calcd. for $C_{60}H_{44}IrN_3$: 999.3164 $[M]^+$, Found: 999.3159. UV-Vis (in CH_2Cl_2) λ [nm] (ε [$M^{-1}cm^{-1}$]): 322 (33600), 345 (31300), 390 (24200), 526 (19900) and 658 (12400).

Synthesis of *E/Z*-DPhDPEs

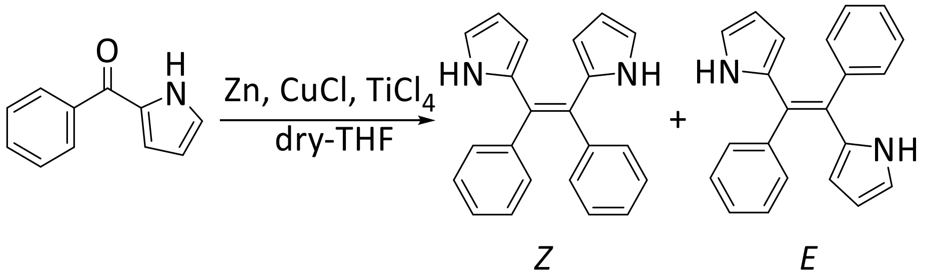

Zinc powder (16.64 g, 256 mmol) and copper(I) chloride (840 mg, 8.47 mmol) in dry-THF (300 mL) were placed in a three-neck round bottomed flask under nitrogen. After cooling to 0°C, $TiCl_4$ (13.4 ml, 128 mmol) was slowly added to reaction mixture at which the temperature maintained at 0°C in an ice bath. The mixture was allowed to warm to room temperature for 30 min, and then the reaction mixture was refluxed for 2 hours. The mixture was cooled again until 0°C, and then a solution of 2-benzoylpyrrole (7.30 g, 42.7

mmol) in THF (100 mL) was slowly added. The reaction mixture was refluxed for 2 hours until the starting material was completely consumed monitored by TLC analysis. The reaction mixture was quenched by the addition of a 10% aqueous K_2CO_3 solution. The resulting mixture was extracted with CH_2Cl_2. The combined organic layer was dried over anhydrous Na_2SO_4 and concentrated. The crude compound was purified by repeated chromatography on a silica gel column (CH_2Cl_2/*n*-hexane = 1/5) to give *E*- isomer and *Z*-isomer in 20% (1.30 g, 4.19 mmol) and 11% (0.75 g, 2.42 mmol), respectively.

***Z*-DPhDPE**, ^1H NMR (400 MHz, $CDCl_3$, 298 K): δ = 8.07 (s, 2H, NH), 7.09 (s, 10H, phenyl ring), 6.71 (m, 2H, pyrrole), 6.18 (m, 2H, pyrrole), 5.96 (m, 2H, pyrrole) ppm.

***E*-DPhDPE**, ^1H NMR (400 MHz, $CDCl_3$, 298 K): δ = 7.49 (s, 10H, phenyl ring), 7.22 (s, 2H, NH), 6.44 (m, 2H, pyrrole), 5.95 (m, 2H, pyrrole), 5.38 (m, 2H, pyrrole) ppm.

Synthesis of 2-3, 2-3 and 2-5

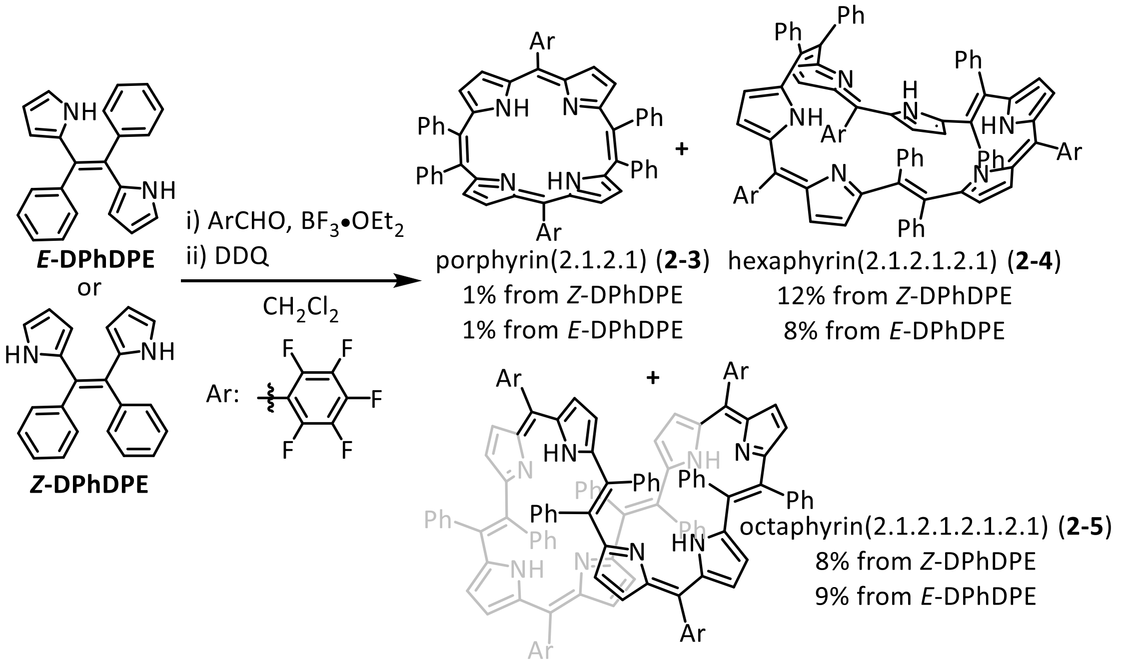

From ***E*-DPhDPE**: Pentafluorobenzaldehyde (196 mg, 1 mmol) and ***E*-DPhDPE** (310 mg, 1.0 mmol) were dissolved in 150 mL dry-CH_2Cl_2 under an argon atmosphere. The mixture was stirred for 5 min and then BF_3•OEt_2 (4.30 mg, 0.03 mmol) was added. After stirring for 2 hours at room temperature, DDQ (227 mg, 1 mmol) was added to the mixture, which was stirred for 1 h. After concentration of the solvent, the residue was purified by chromatography on silica gel (CH_2Cl_2) and alumina (*n*-hexane/CH_2Cl_2 = 5/1), respectively. The first eluted yellow fraction was collected to afford **2-3** in 1 % (5 mg, 0.005 mmol), the second purple-red fraction was collected to afford **2-4** in 8 % (38 mg, 0.026 mmol) and the third deep green fraction was collected to afford **2-5** in 9 % (40 mg, 0.021 mmol).

From ***Z*-DPhDPE**: Pentafluorobenzaldehyde (196 mg, 1 mmol) and ***Z*-DPhDPE** (310 mg, 1 mmol) were dissolved in 150 mL dry-CH_2Cl_2 under an argon atmosphere. The mixture was stirred for 5 min, and then BF_3•Et_2O (4.3 mg, 0.03 mmol) was added to reaction mixture. After stirring for 2 hours at room temperature, DDQ (227 mg, 1 mmol) added and the mixture stirred for 1 hour. The reaction mixture removed solvent under a reduced pressure. After doing the same purifications, **2-3**, **2-4** and **2-5** were isolated in 1 % (5 mg, 0.005 mmol), 12 % (58 mg, 0.04 mmol) and 8 % (38 mg, 0.02 mmol), respectively.

2-3: Deep purple solid. ^{1}H NMR (400 MHz, CD_2Cl_2, 298 K): δ = 12.60 (brs, 2H, NH), 7.20 (m, 20H, phenyl), 6.34 (d, J = 4 Hz, 4H, pyrrole), 6.14 (d, J = 4 Hz, 4H, prrrole) ppm. ^{19}F NMR (376 MHz, $CDCl_3$, 298 K): δ = –114.99 (m, 4F), –129.12 (m, 2F), –137.88 (m, 4F) ppm. HR-MALDI-MS: calcd. for $C_{58}H_{30}F_{10}N_4$: 972.2311 $[M]^+$, Found: 972.2399. UV-Vis-NIR (in CH_2Cl_2) λ [nm] (ε [M^{-1} cm^{-1}]): 456 (72000), 650 (837).

2-4: Dark red solid. ^{1}H NMR (400 MHz, $CDCl_3$, 213 K): δ = 10.87 (brs, 1H, NH), 10.83 (brs, 1H, NH), 10.69 (brs, 1H, NH), 7.70 (d, J = 8 Hz, 1H, phenyl ring), 7.53 (m, 2H, phenyl ring), 7.41 (m, 1H, phenyl ring), 7.25 (m, 5H, phenyl ring), 7.16 (m, 2H, phenyl ring), 7.08 (m, 2H, phenyl ring), 7.02 (m, 4H, phenyl ring), 6.94 (d, J = 8Hz, 2H, phenyl ring), 6.88 (m, 5H, phenyl ring), 6.80 (m, 2H, phenyl ring), 6.73 (m, 4H, phenyl ring), 6.50 (d, J = 4 Hz, 1H, pyrrole), 6.42 (m, 2H, pyrrole), 6.35 (d, J = 4 Hz, 1H, pyrrole), 6.32 (d, J = 4 Hz, 1H, pyrrole), 6.27 (d, J = 4 Hz, 1H, pyrrole), 6.25 (d, J = 4 Hz, 1H, pyrrole), 6.29 (m, 2H, pyrrole), 6.02 (d, J = 4 Hz, 1H, pyrrole), 5.98 (d, J = 4 Hz, 1H, pyrrole), 5.58 (d, J = 4 Hz, 1H, pyrrole) ppm. ^{19}F NMR (376 MHz, $CDCl_3$, 298 K): $\delta = -114.58$ (m, 6F), -129.54 (m, 3F), -138.13 (m, 6F) ppm. HR-MALDI-MS: calcd. for $C_{87}H_{45}F_{15}N_6$: 1458.3466 $[M]^+$, Found: 1458.3833. UV-Vis-NIR (in CH_2Cl_2) λ [nm] (ε [M^{-1} cm^{-1}]): 349 (30000), 417 (23000), 544 (68000), 723 (9400).

2-5: Deep purple solid. ^{1}H NMR (400 MHz, CD_2Cl_2, 293 K): δ = 12.46 (brs, 1H, NH), 11.52 (brs, 3H, NH), 7.3 (br, 40H, phenyl ring), 6.06 (br, 8H, pyrrole), 5.67 (br, 8H, pyrrole) ppm. ^{19}F NMR (376 MHz, $CDCl_3$, 298 K): $\delta = -112.738$ (s, 1F), -114.08 (m, 6F), -115.388 (s, 1F), -129.498 (s, 4F), -137.654 (s, 8F) ppm. HR-MALDI-MS: calcd. for $C_{116}H_{60}F_{20}N_8$: 1944.4622 $[M]^+$, Found: 1944.4616. UV-Vis-NIR (in CH_2Cl_2) λ [nm] (ε [M^{-1} cm^{-1}]): 417 (40000), 458 (39000), 612 (109300), 850 (3095).

Synthesis of 2-4-2Zn

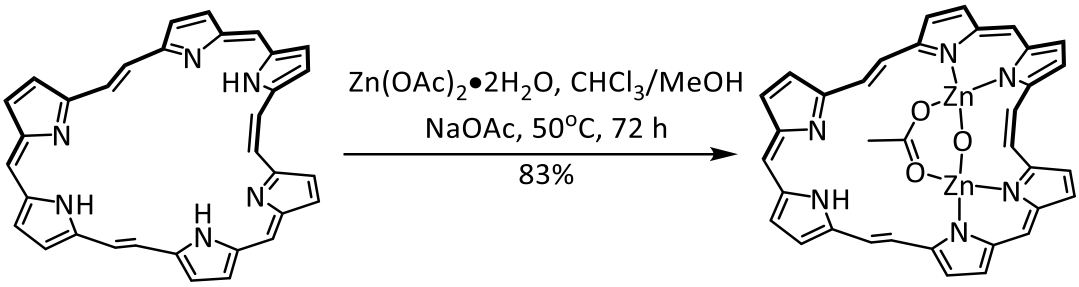

2-4

2-4-2Zn

Aryl groups are omitted for clarity.

$Zn(OAc)_2{\bullet}2H_2O$ (15 mg, 0.07 mmol) and sodium acetate (6 mg, 0.07 mmol) were added to a mixture of **2-4** (10 mg, 0.007 mmol) in methanol (2 ml) and chloroform (8 ml). The mixture was heated at 50°C for 72 hours. After removal of the solvent, the residue was purified by alumina column chromatography (*n*-hexane/ethyl acetate = 10/1) to give **2-4-2Zn** in 83% (9 mg, 0.0057 mmol).

2-4-2Zn: Purple-red solid. ^{1}H NMR (600 MHz, CD_2Cl_2, 293 K) δ = 11.90 (brs, 1H, NH), 7.29 (d, *J* = 6 Hz, 2H, phenyl ring), 7.22 (m, 6H, phenyl ring), 7.09 (m, 4H, phenyl ring), 7.01 (m, 3H, phenyl ring), 6.95 (d, *J* = 6 Hz, 4H, phenyl ring), 6.92 (m, 2H, phenyl ring), 6.88 (m, 4H, phenyl ring), 6.77 (d, *J* = 6 Hz, 2H, phenyl ring), 6.75 (m, 2H, phenyl ring), 6.71 (m 1H, phenyl ring), 6.41 (d, *J* = 6 Hz, 2H, pyrrole), 6.33 (d, *J* = 6 Hz, 1H, pyrrole), 6.29 (m, 2H, pyrrole), 6.22 (d, *J* =6 Hz, 1H, pyrrole), 6.12 (d, *J* = 6 Hz, 1H, pyrrole), 6.08 (d, *J* = 6 Hz, 1H, pyrrole), 6.06 (d, *J* = 6 Hz, 1H, pyrrole), 6.01 (m, 2H, pyrrole), 5.93 (d, *J* = 6 Hz, 1H, pyrrole), 1.82 (s, 3H, methyl) ppm. ^{19}F NMR (376 MHz, $CDCl_3$): δ = –114.74 (m, 5F), –115.091 (s, 1F), –129.30 (m, 3F), –137.76 (m, 6F) ppm. HR-MALDI-MS: calcd. for $C_{87}H_{47}F_{15}N_6O_3Zn_2$: 1660.2053 $[M]^+$, Found: 1660.2048. UV-Vis-NIR (in CH_2Cl_2) λ [nm] (ε [M^{-1} cm^{-1}]): 523 (89400), 687 (6340).

Synthesis of 2-4-Cu and 2-4-2Cu

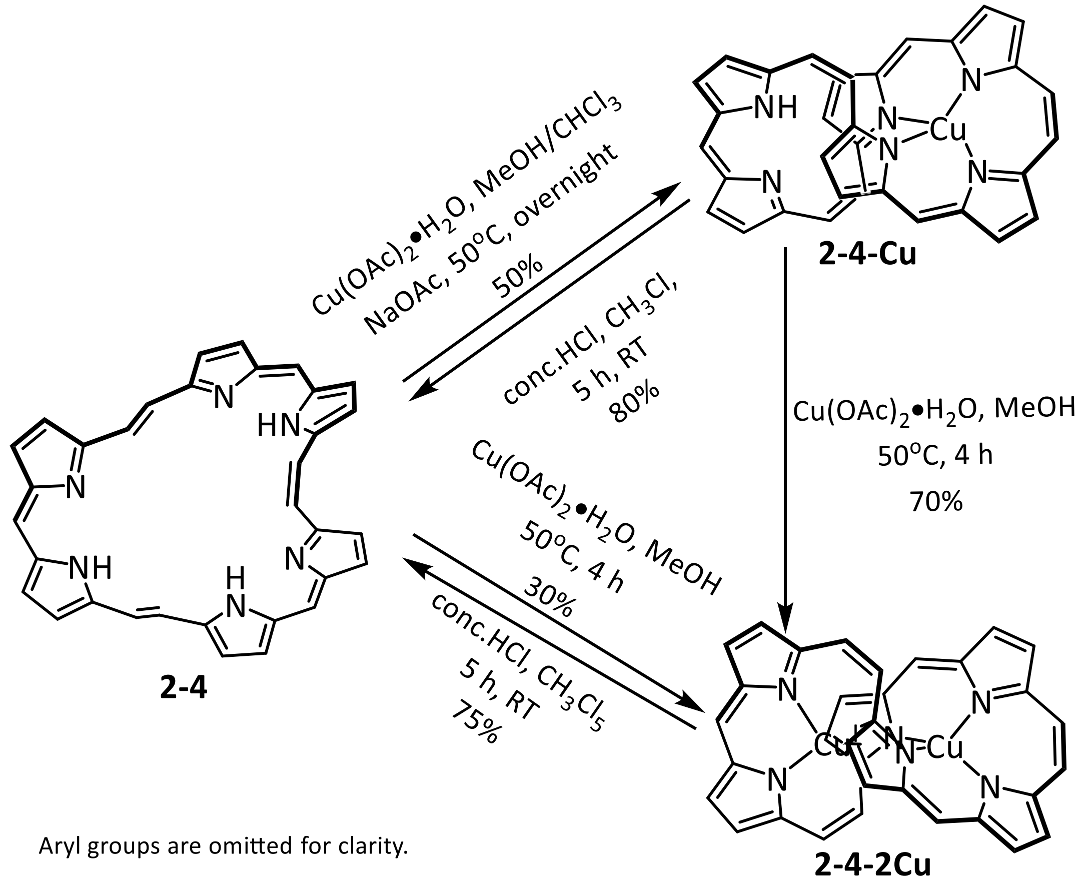

Aryl groups are omitted for clarity.

Synthesis of **2-4-Cu from 2-4**: $Cu(OAc)_2$•H_2O (28 mg, 0.14 mmol) was added to a solution of **2-4** (20 mg. 0.014 mmol) and NaOAc (11.5 mg, 0.14 mmol) in methanol (4 ml) and chloroform (16 ml). The mixture was stirred at 50°C for 12 hours. After removal of the solvent, the residue was purified by silica gel column chromatography (*n*-hexane/CH_2Cl_2 = 2/1) to give **2-4-Cu** in 50% (10 mg, 0.0033 mmol).

2-4-Cu: Black solid. HR-MALDI-MS: calcd. for $C_{87}H_{43}CuF_{15}N_6$: 1519.2606 $[M]^+$, Found: 1519.2606. UV-Vis-NIR (in CH_2Cl_2) λ [nm] (ε [M^{-1} cm^{-1}]): 334 (77600), 402 (69000), 521 (57900), 680 (100000), 850 (11860), 947 (14000).

Synthesis of 2-4-2Cu from 2-4: **2-4** (10 mg, 0.007 mmol), $Cu(OAc)_2•H_2O$ (14 mg, 0.07 mmol) and NaOAc (11.5 mg, 0.07 mmol) were dissolved in 10 mL dry-methanol under an argon atmosphere. The mixture was stirred at 50°C for 4 h. After removal of solvent, the residue was washed with *n*-hexane and then the remaining solid dissolved in small amount of CH_2Cl_2 through filtrate paper. The resulted CH_2Cl_2 solution was concentrated to give **2-4-2Cu** in 30% (7.7 mg, 0.0049 mmol).

2-4-2Cu: Deep violet solid. HR-MALDI-MS: calcd. for $C_{87}H_{42}Cu_2F_{15}N_6$: 1581.1818 $[M]^+$, Found: 1581.1819. UV-Vis-NIR (in CH_2Cl_2) λ [nm] (ε [$M^{-1}cm^{-1}$]): 320 (21260), 535 (30700), 585 (31000), 676 (27400).

Synthesis of 2-4-2Cu from 2-4-Cu: 2-4-Cu (5 mg, 0.0033 mmol), $Cu(OAc)_2•H_2O$ (7 mg, 0.035 mmol) and NaOAc (6 mg, 0.035 mmol) were dissolved in 10 mL dry- methanol under an argon atmosphere. The mixture was stirred for at 50°C for 4 hours. After removal of solvent, the residue was washed with *n*-hexane and then the remaining solid dissolved in small amount of CH_2Cl_2 through filtrate paper. The obtained CH_2Cl_2 solution was concentrated to give **2-4-2Cu** in 70% (3.6 mg, 0.0023 mmol).

Supporting Figures

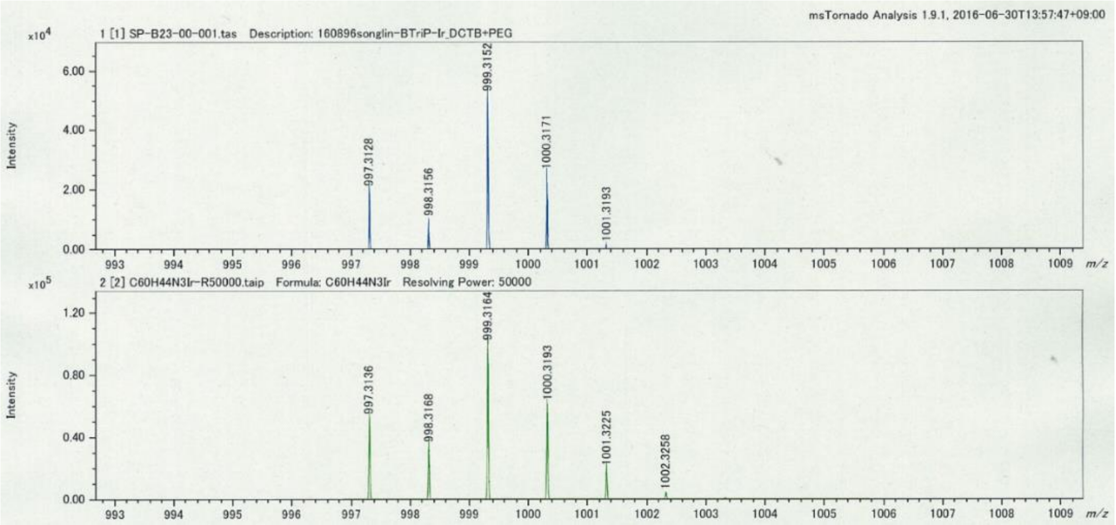

Figure S2.1. HR-MALDI-TOF-MS spectrum of **2-2**.

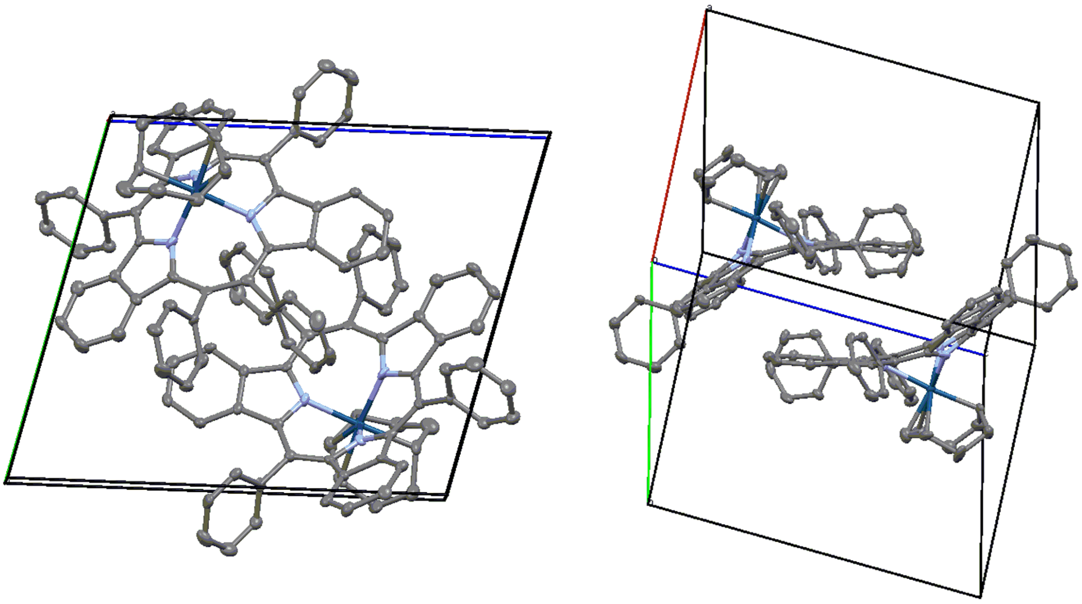

Figure S2.2. Packing diagram of **2-2,** left (top view) and right (side view). Hydrogen atoms are omitted for clarity. Thermal ellipsoids are set at 50% probability.

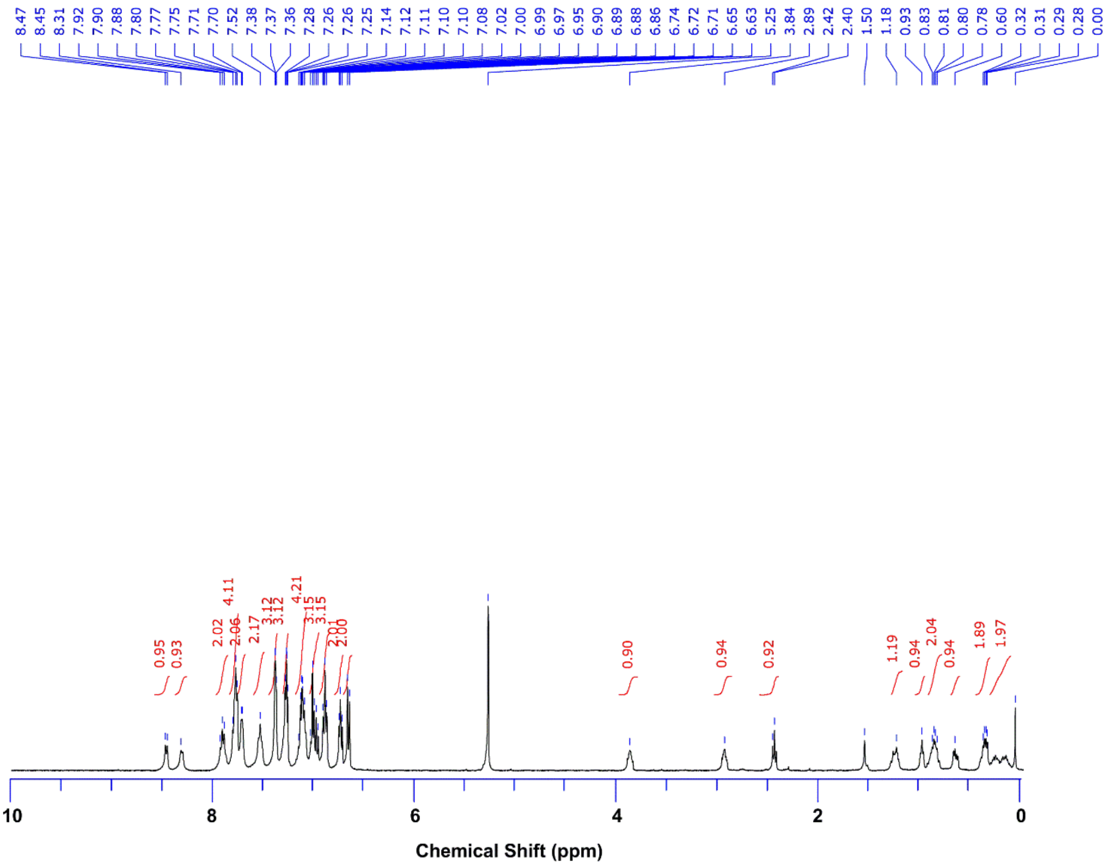

Figure S2.3. ^{1}H NMR spectrum of **2-2** in CD_2Cl_2 at 273 K.

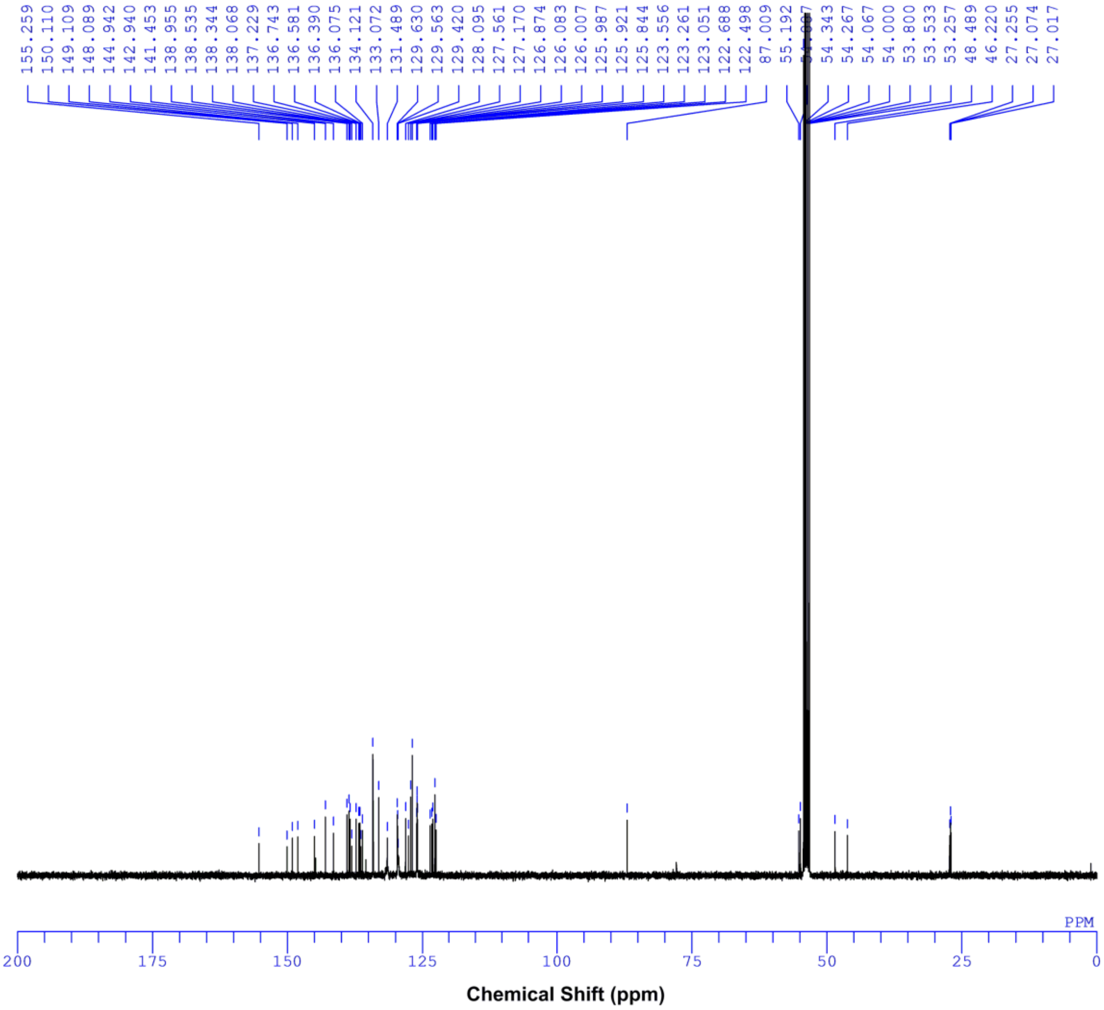

Figure S2.4. ^{13}C NMR spectrum of **2-2** in CD_2Cl_2 at 298 K.

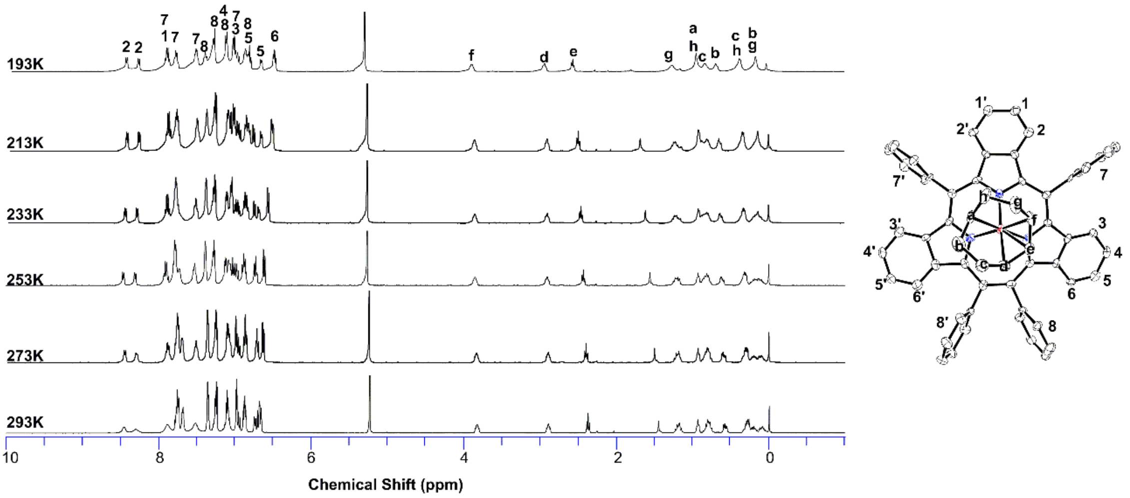

Figure S2.5. Variable temperature ^{1}H NMR spectra of **2-2** in CD_2Cl_2. The picture at right part is label of hydrogens on carbon atoms. Hydrogen atoms are omitted for clarity

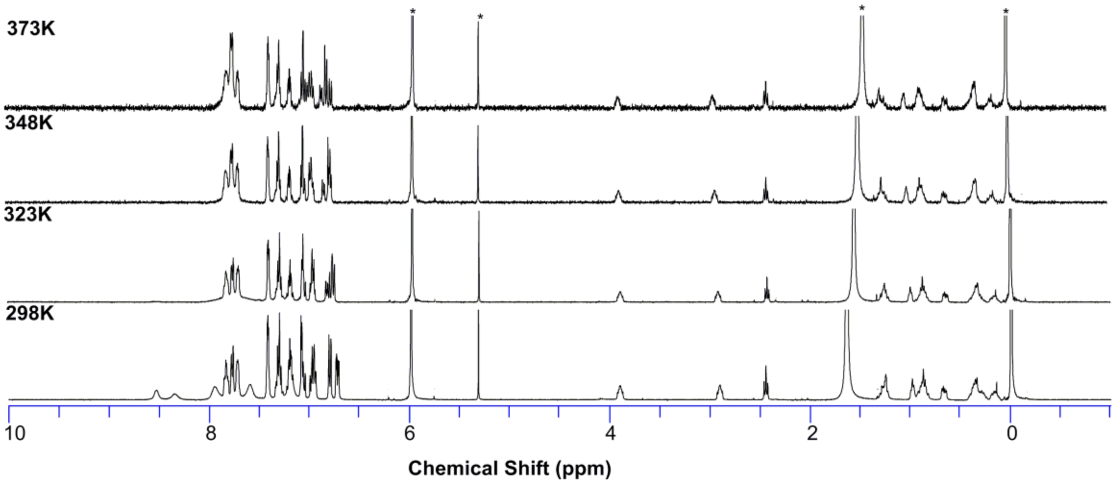

Figure S2.6. Variable temperature ^{1}H NMR spectra of **2-2** in $C_2D_2Cl_4$-d_2. * indicates residual solvents and TMS peak.

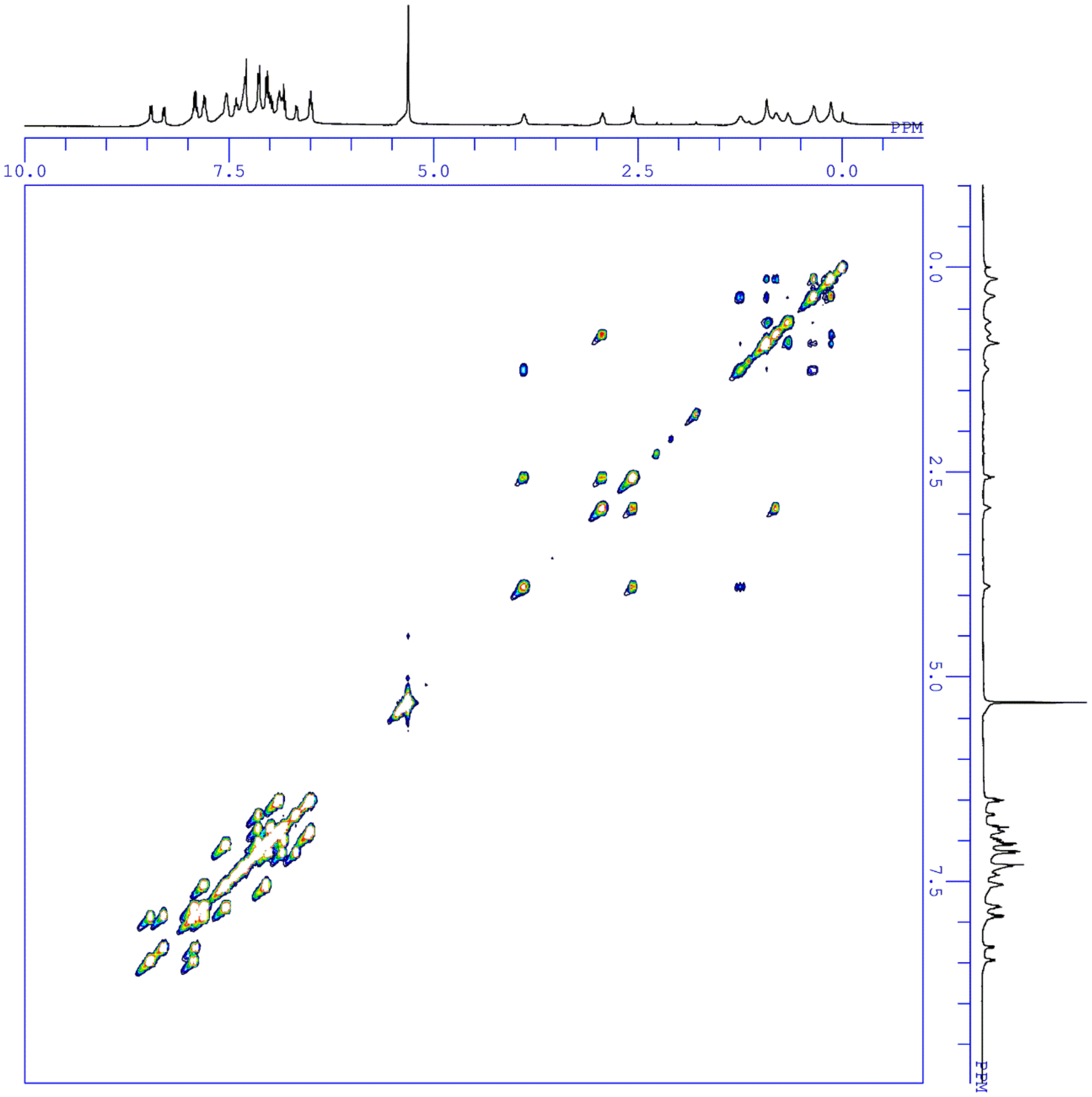

Figure S2.7. ^{1}H-^{1}H COSY NMR spectrum of **2-2** in CD_2Cl_2, at 193 K.

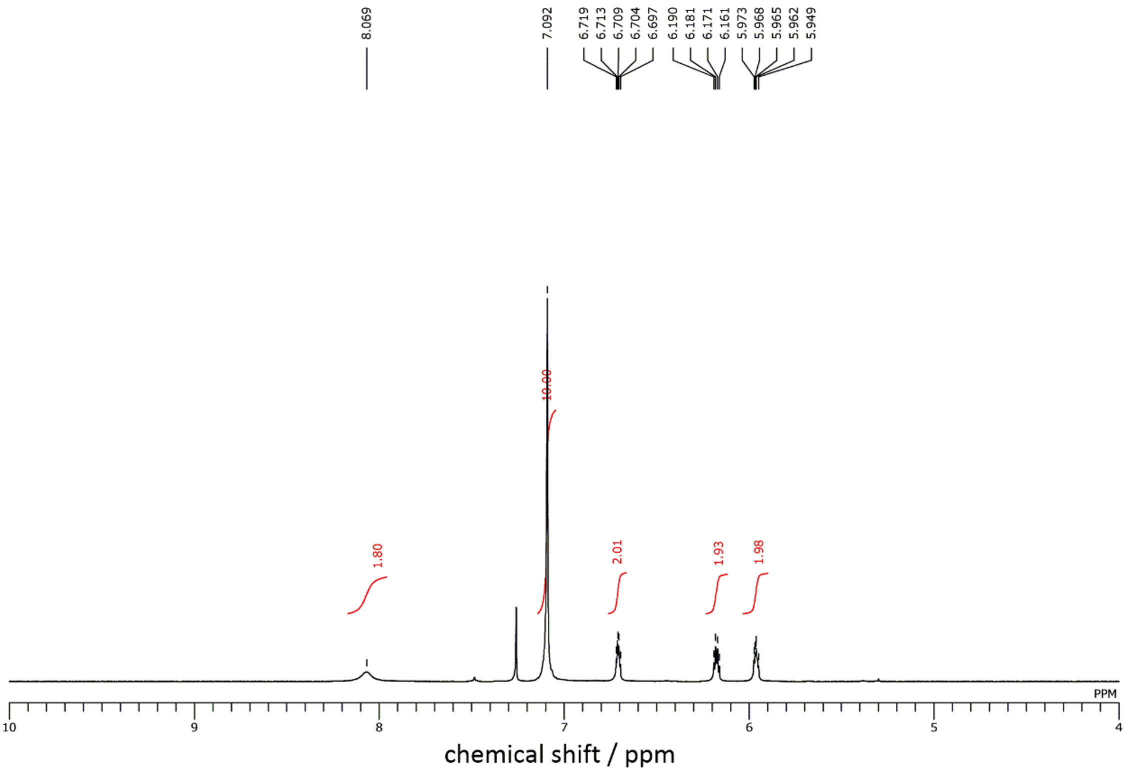

Figure S2.8. ^{1}H NMR spectrum of ***Z*-DPhDPE** in $CDCl_3$.

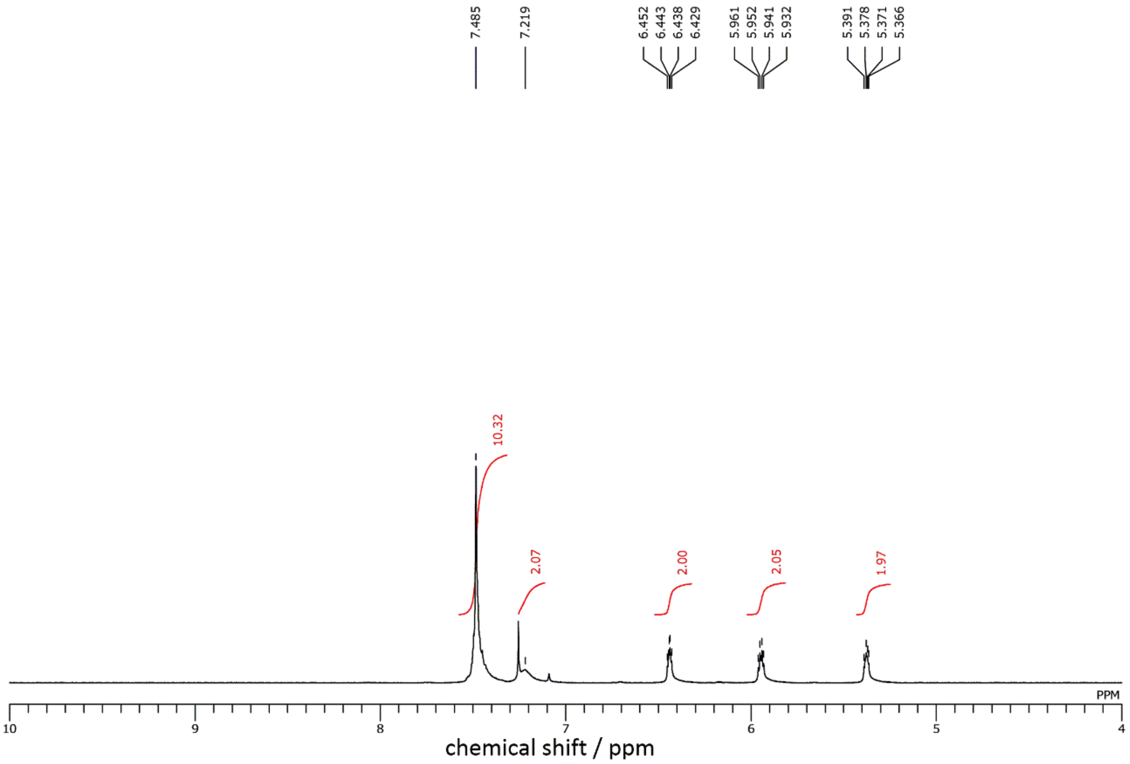

Figure S2.9. ^{1}H NMR spectrum of ***E*-DPhDPE** in $CDCl_3$.

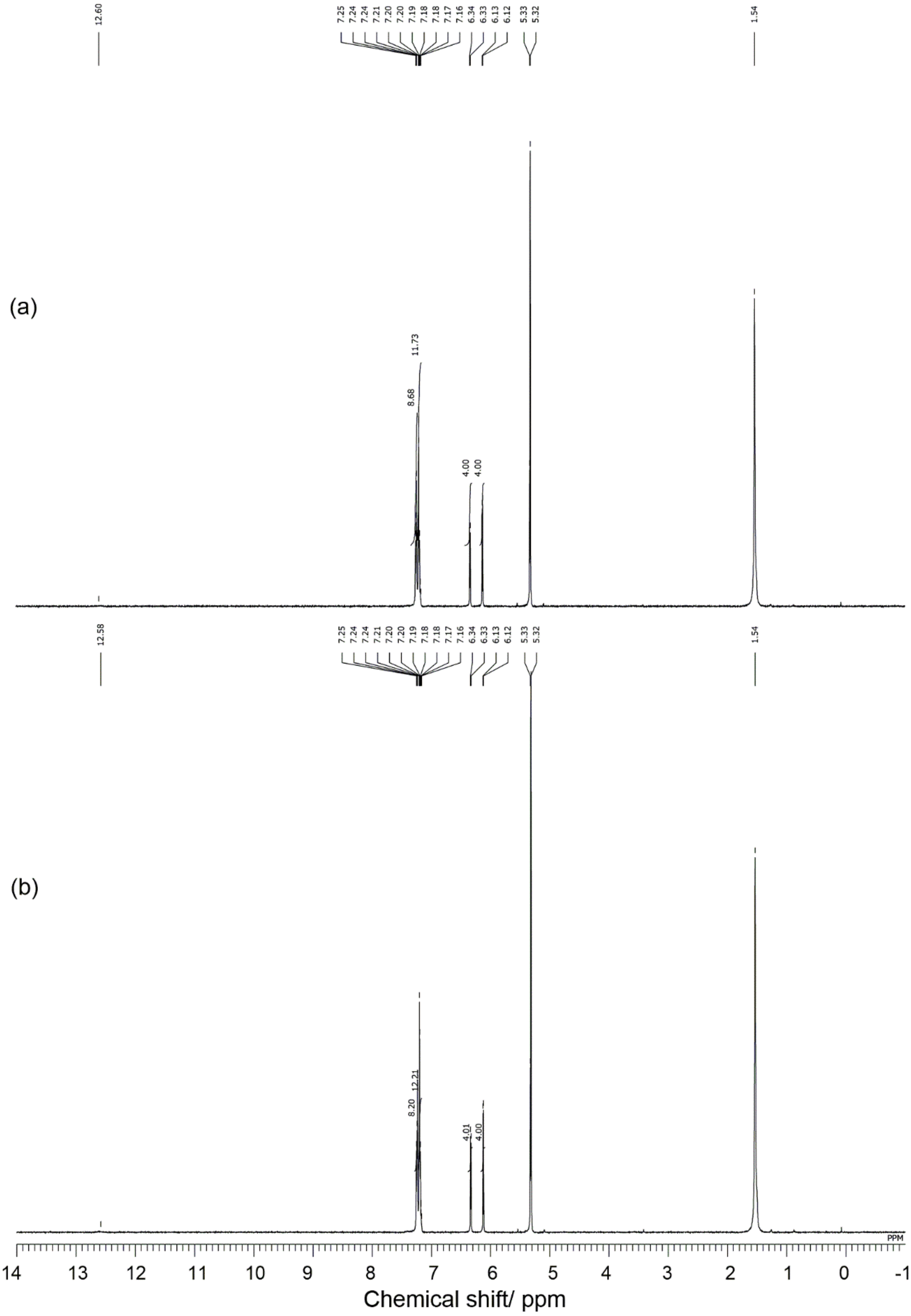

Figure S2.10. ^{1}H NMR spectra of **2-3** in CD_2Cl_2. **2-3** was synthesized from a) ***Z*-DPhDPE** and b) ***E*-DPhDPE**.

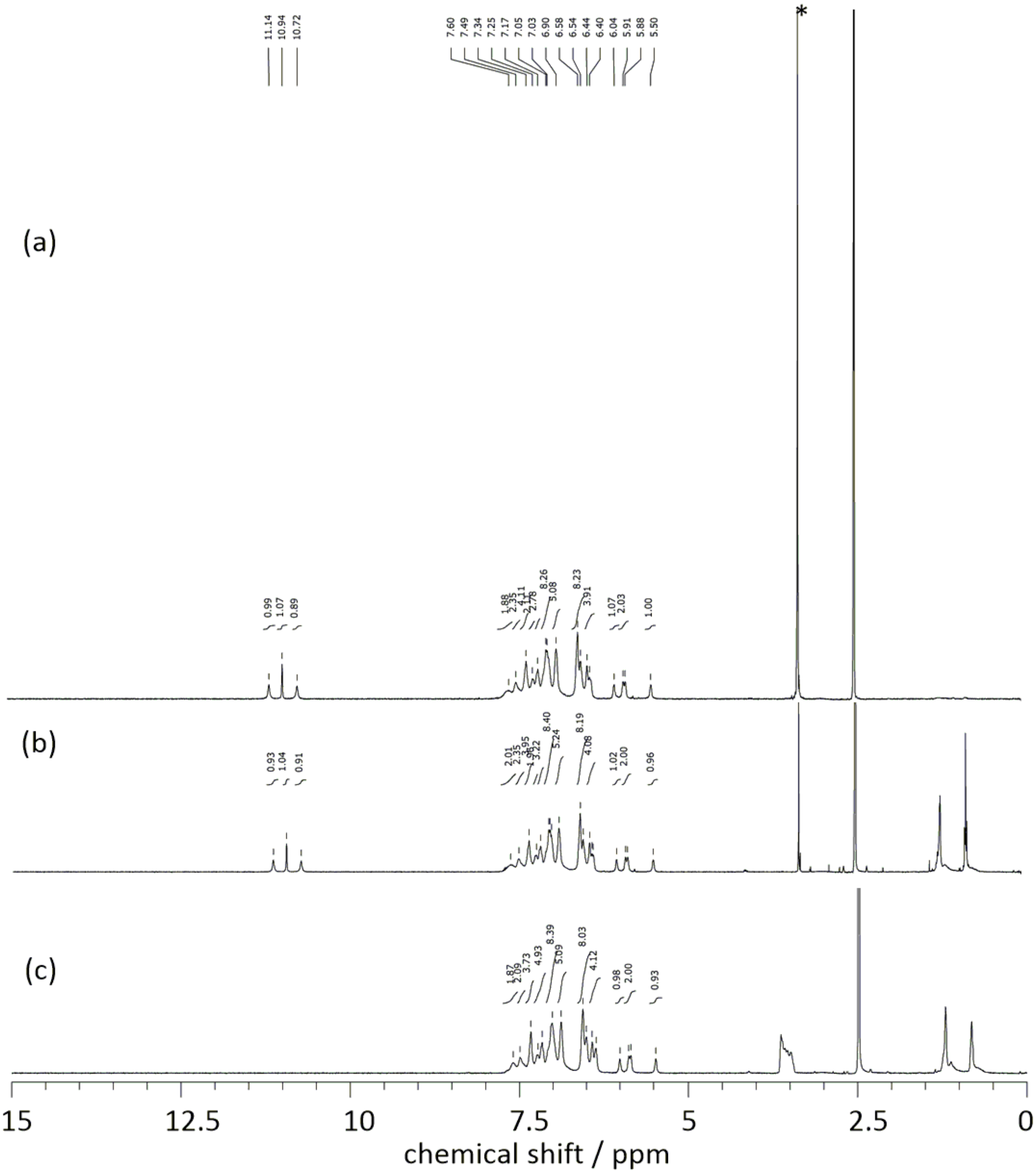

Figure S2.11. ^{1}H NMR spectra of **2-4** in DMSO-d_6. **2-4** was synthesized from a) ***Z*-DPhDPE**, b) ***E*-DPhDPE** and c) **2-4** with D_2O.

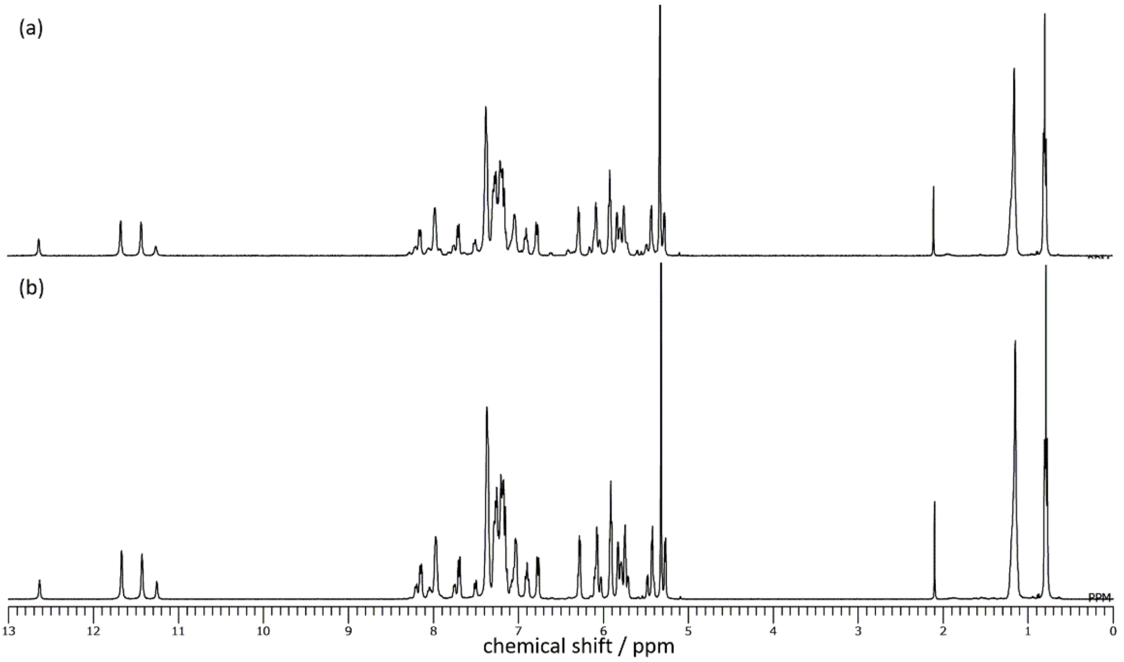

Figure S2.12. ^{1}H NMR spectra of **2-5** in CD_2Cl_2 at 193 K. **2-5** was synthesized from a) ***Z*-DPhDPE**, b) ***E*-DPhDPE**.

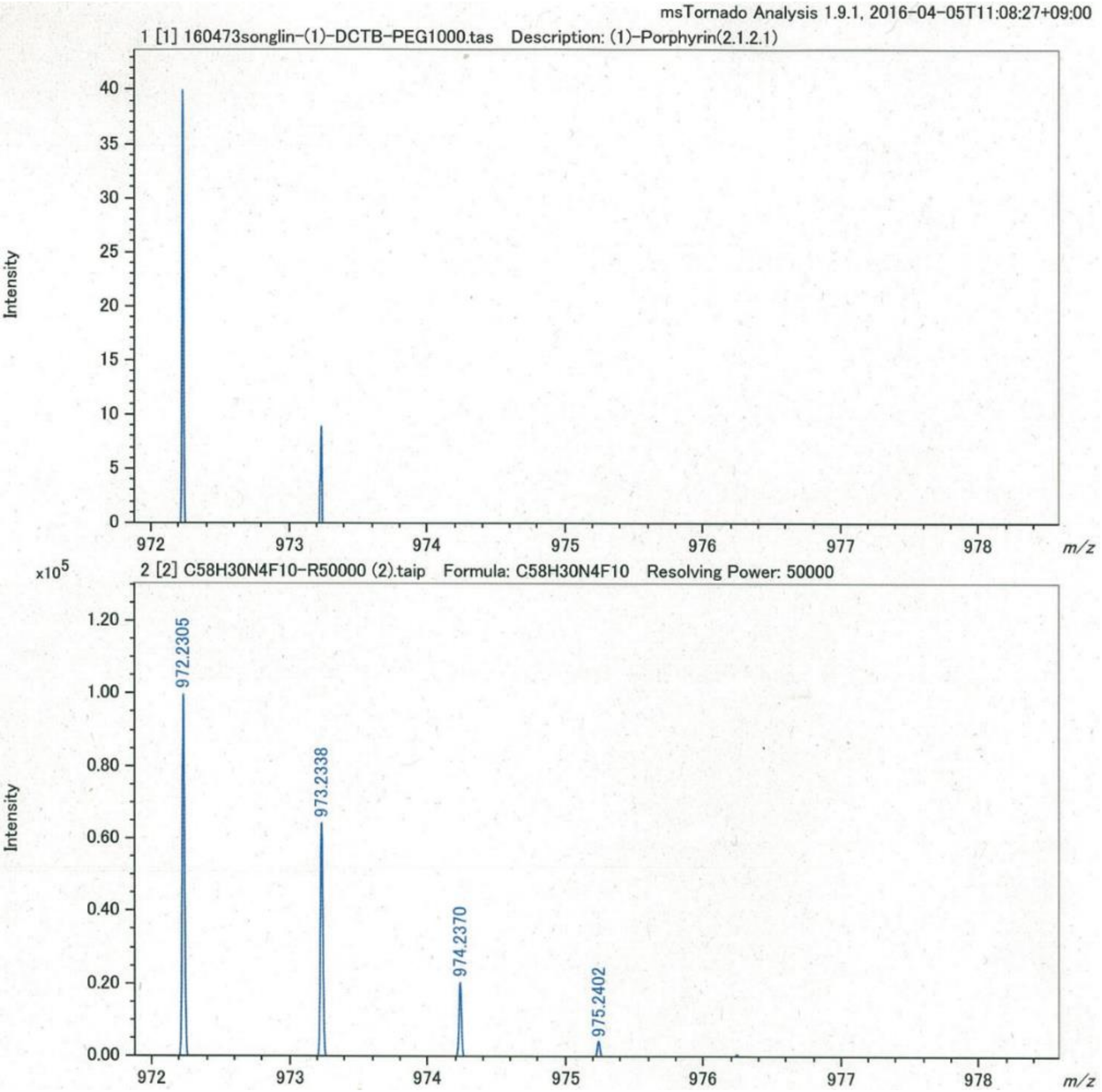

Figure S2.13. HR-MALDI-MS spectrum of **2-3**.

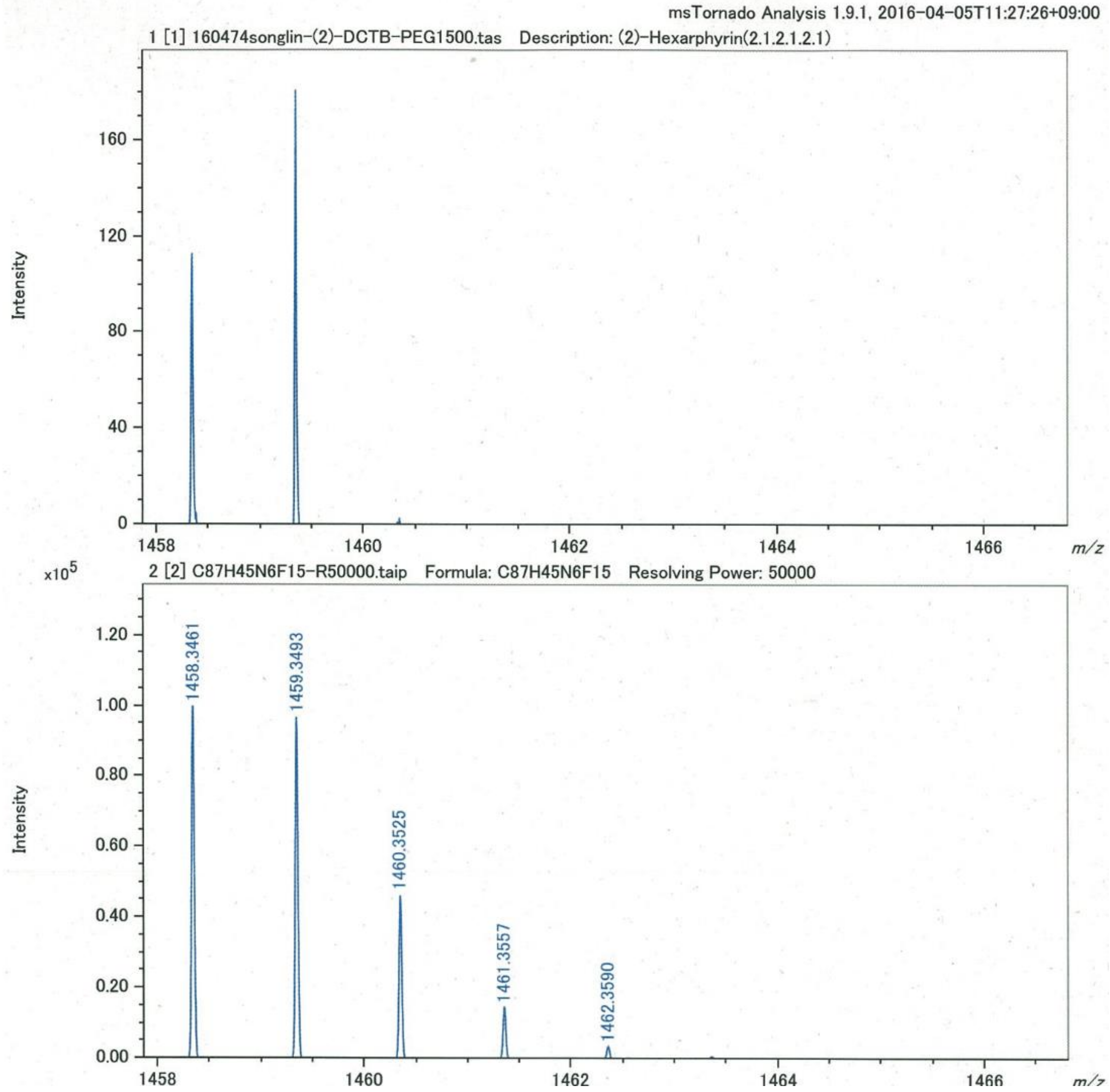

Figure S2.14. HR-MALDI-MS spectrum of **2-4**.

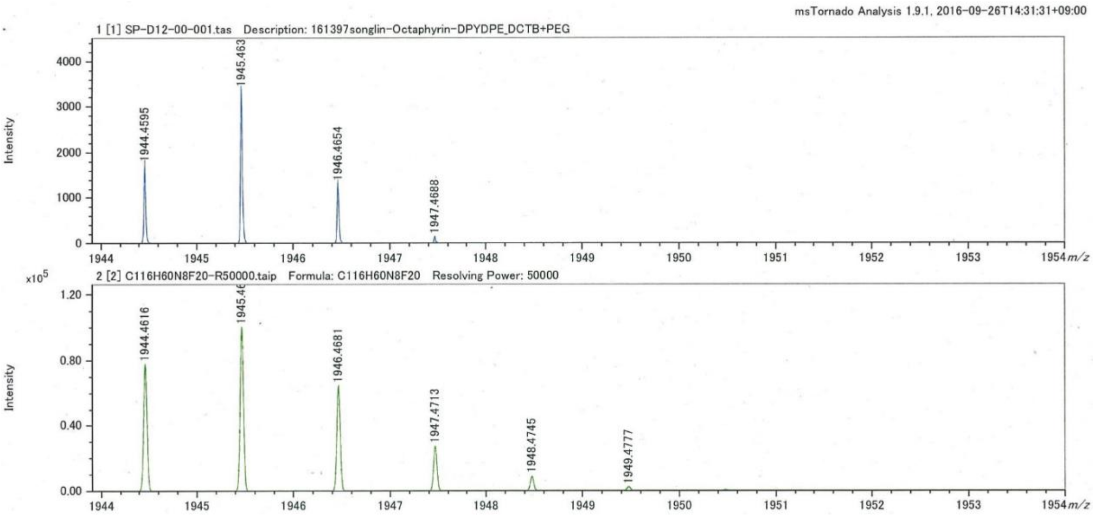

Figure S2.15. HR-MALDI-MS spectrum of **2-5**.

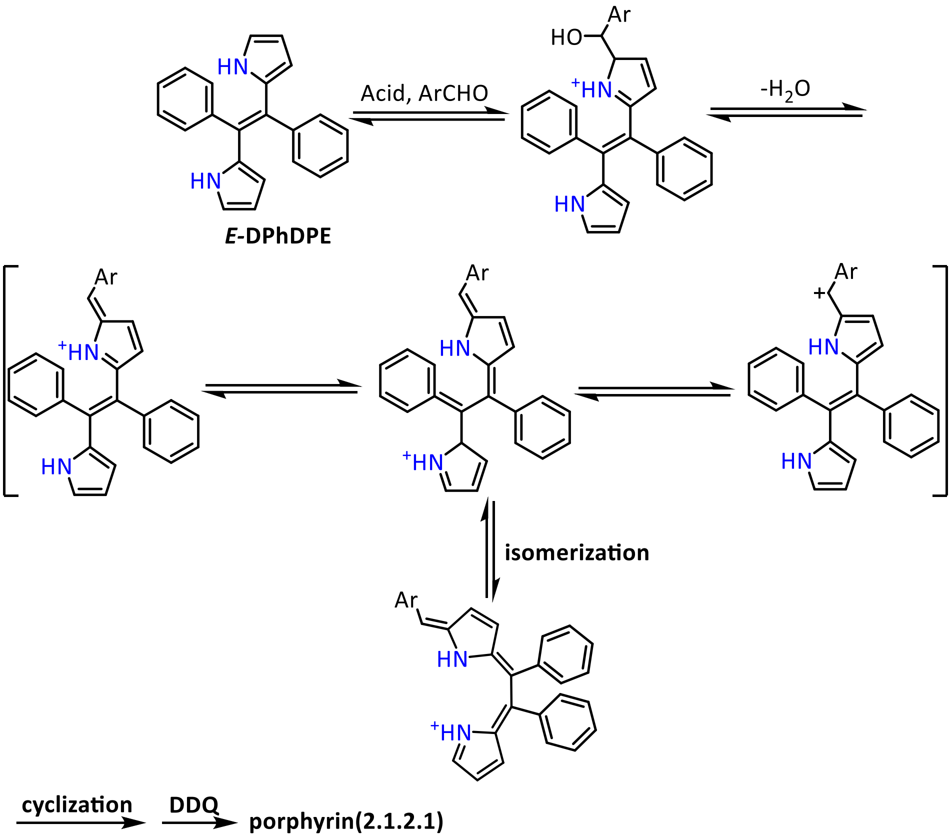

Scheme S2.1. Presumable reaction mechanism of expanded porphyrins from **DPhDPEs**

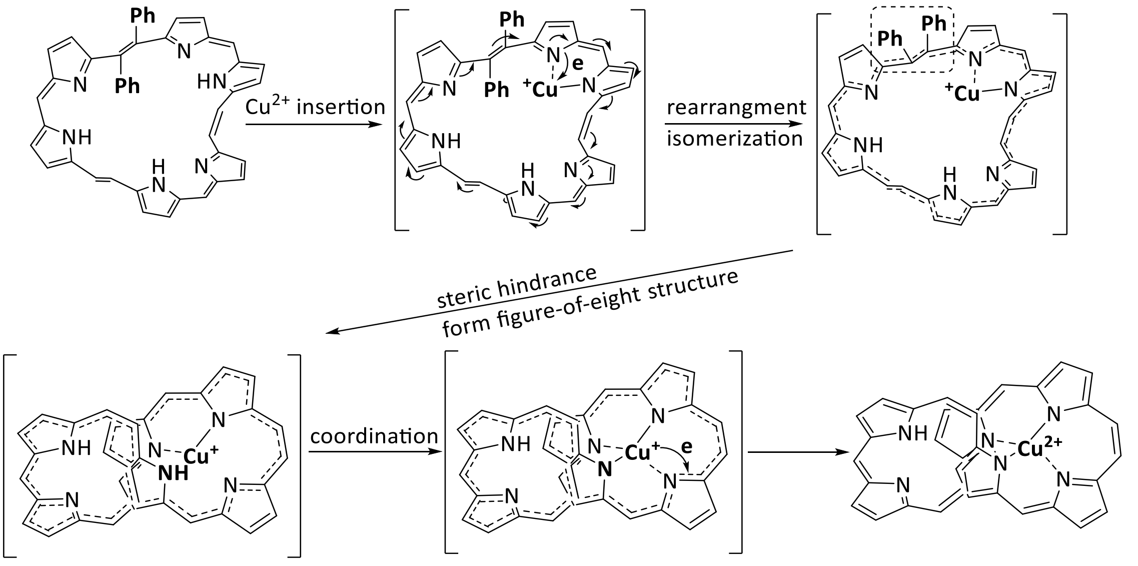

Scheme S2.2. Presumable reaction mechanism of *trans-/cis-* isomerization. All aryl groups omitted for clarity.

COSY spectrum

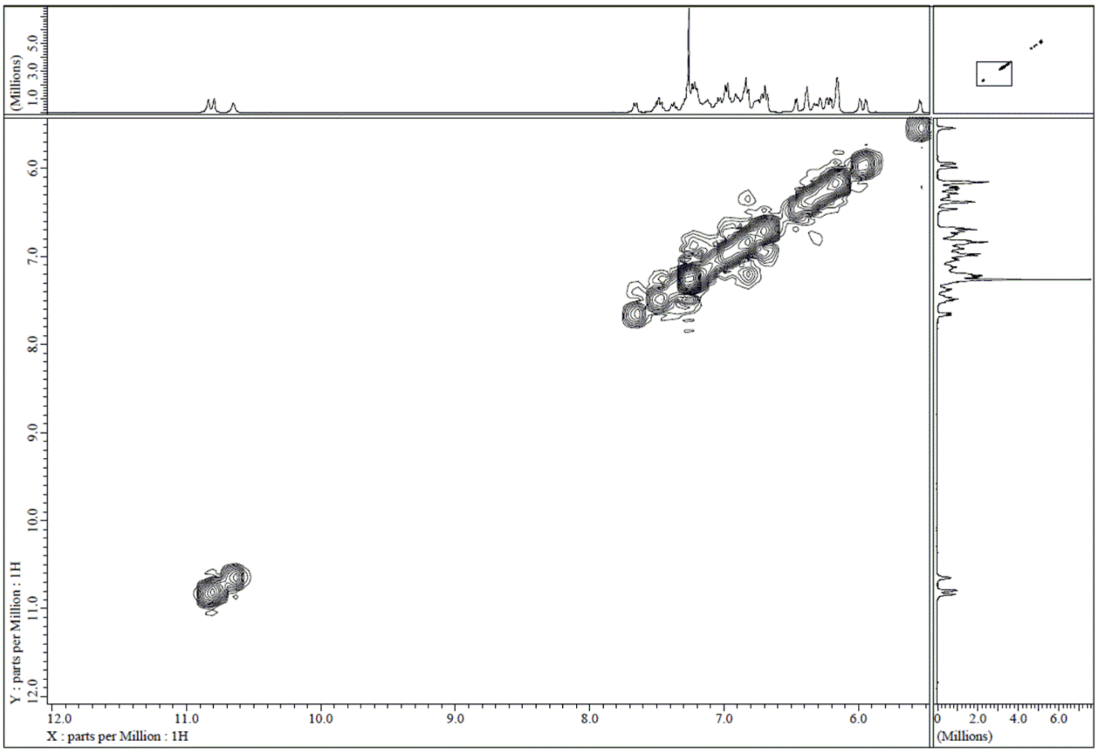

NOESY spectrum

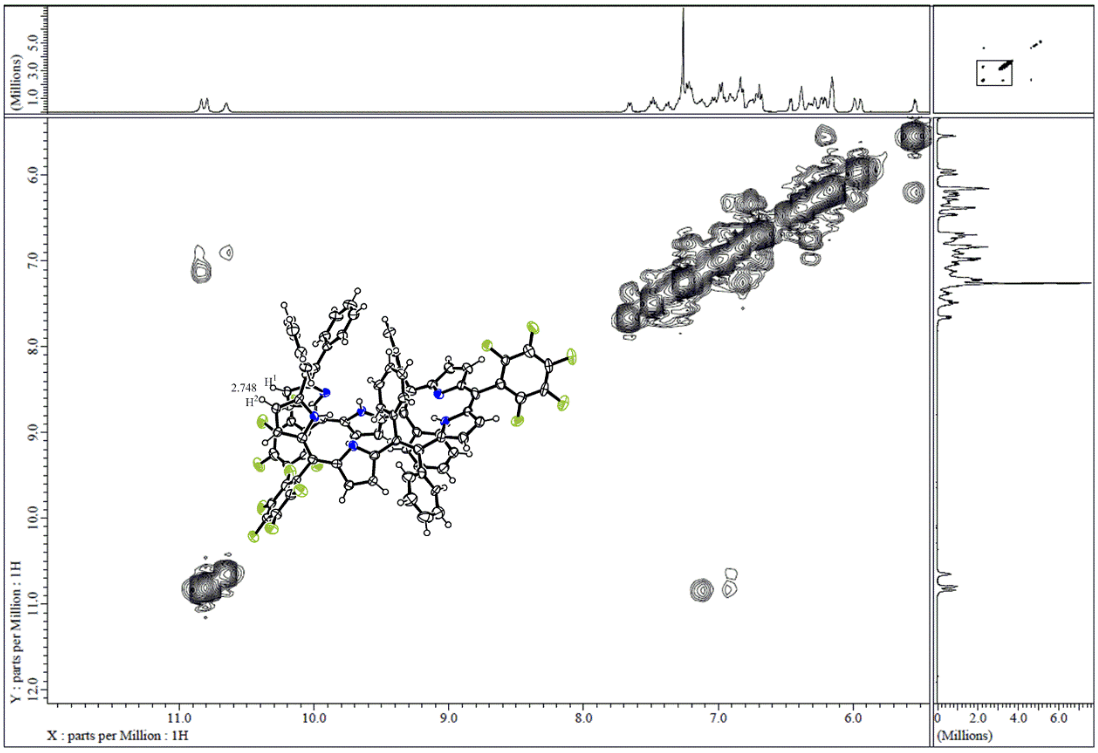

Figure S2.16. ^{1}H-^{1}H COSY and NOESY spectra of **2-4** in CDCl$_3$ at 213 K.

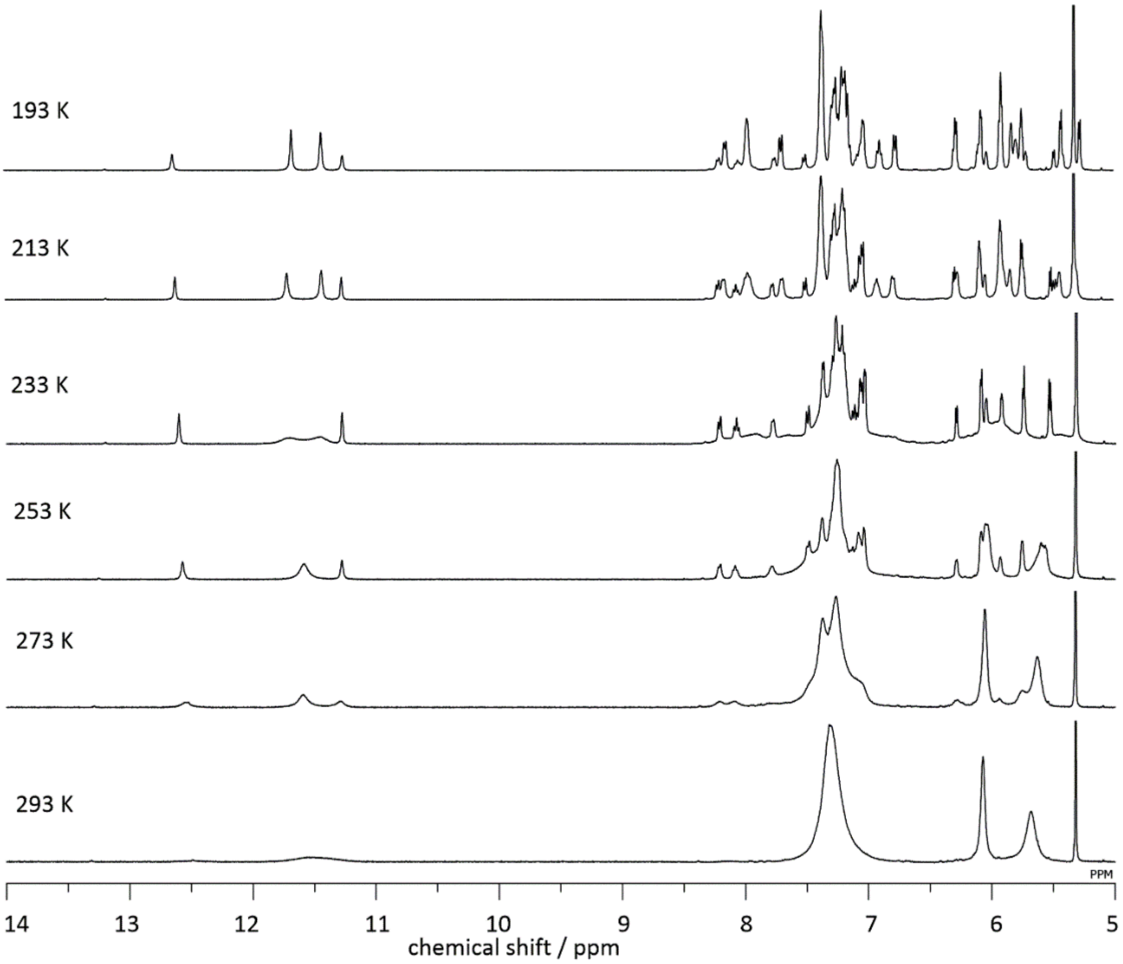

Figure S2.17. Temperature dependent ^{1}H NMR spectra of **2-5** in CD_2Cl_2.

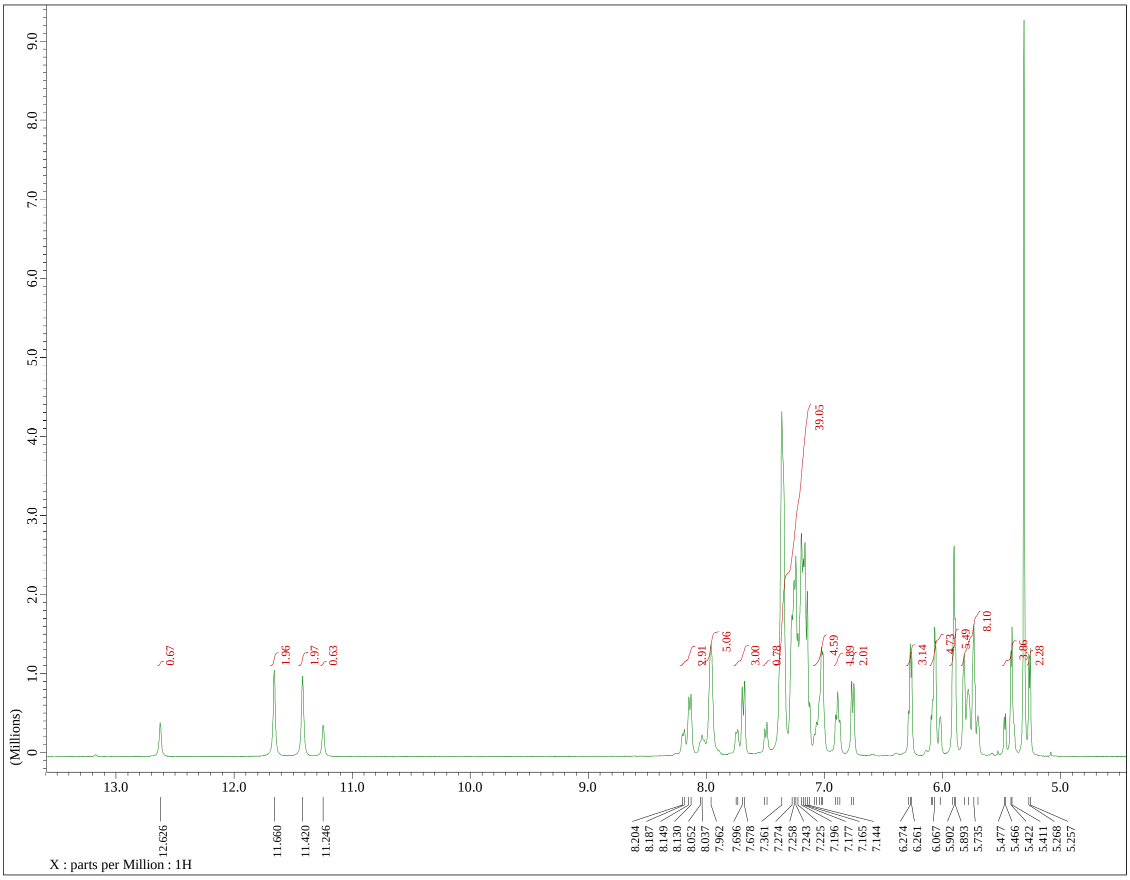

Figure S2.18. ^{1}H NMR spectrum of **2-5** in CD_2Cl_2 at 193 K.

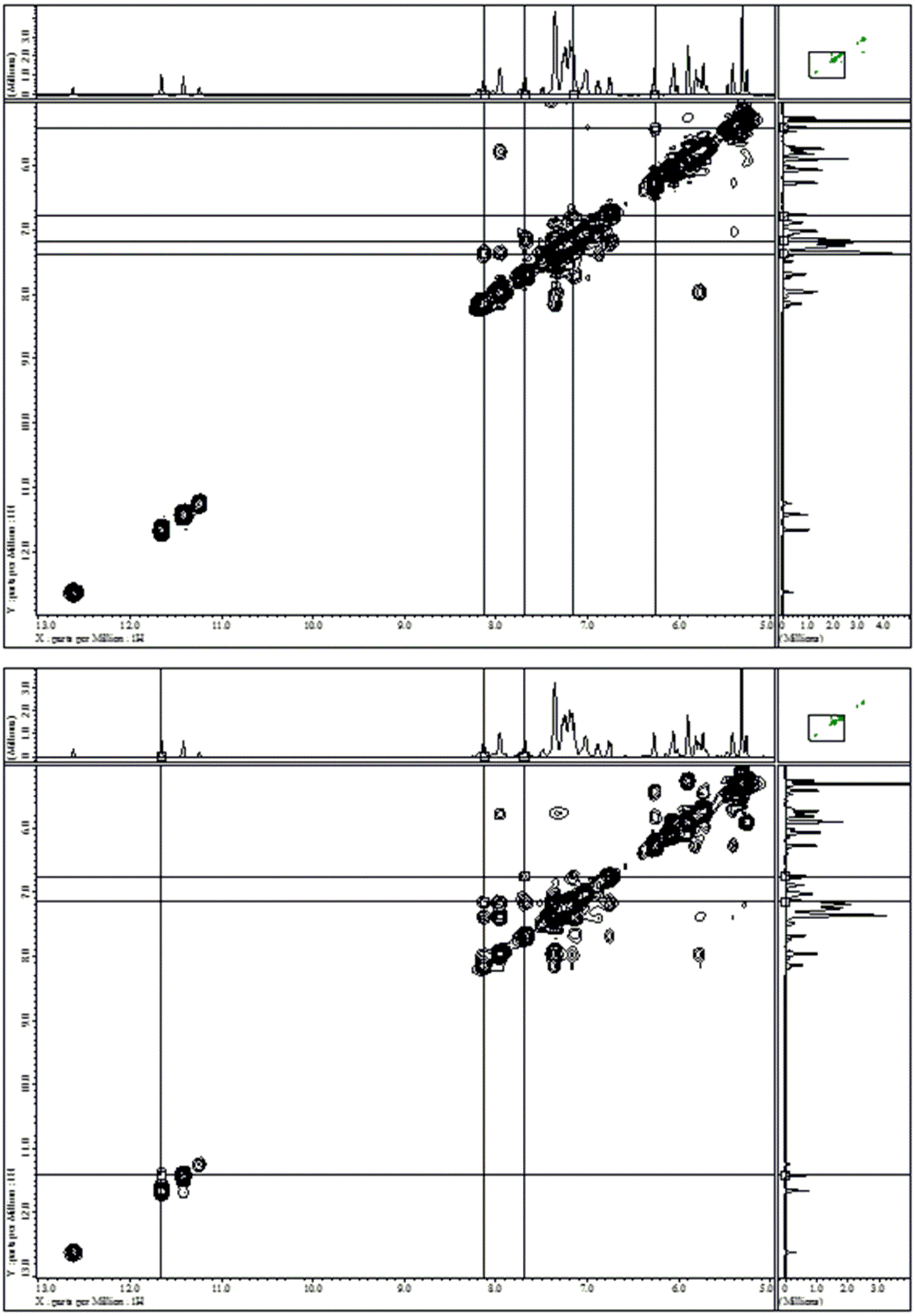

Figure S2.19. ^{1}H-^{1}H COSY and NOESY spectra of **2-5** in CD_2Cl_2 at 193 K.

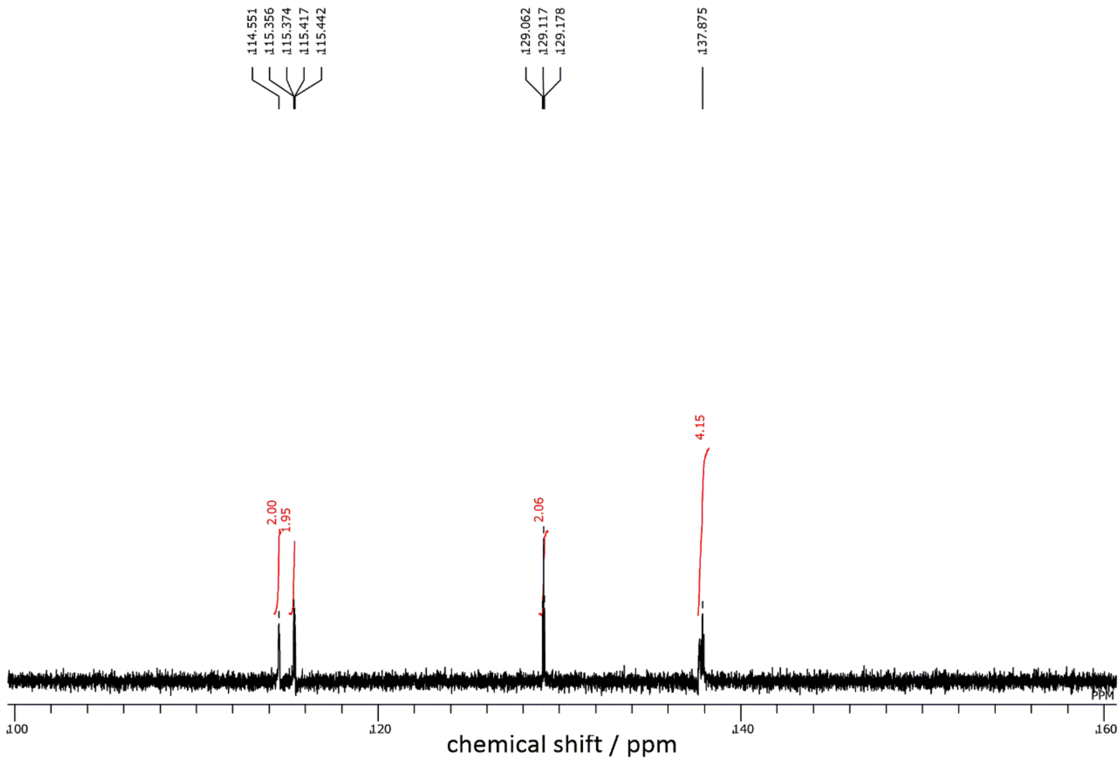

Figure S2.20 ^{19}F NMR spectrum of **2-3** in $CDCl_3$.

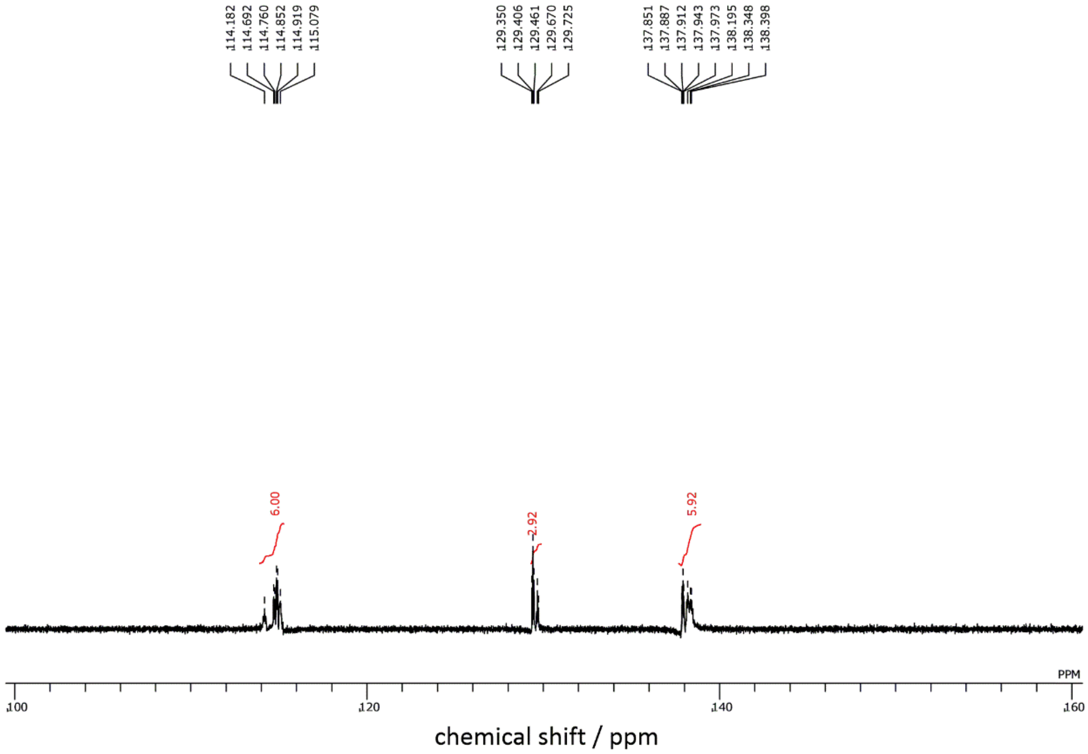

Figure S2.21. ^{19}F NMR spectrum of **2-4** in $CDCl_3$.

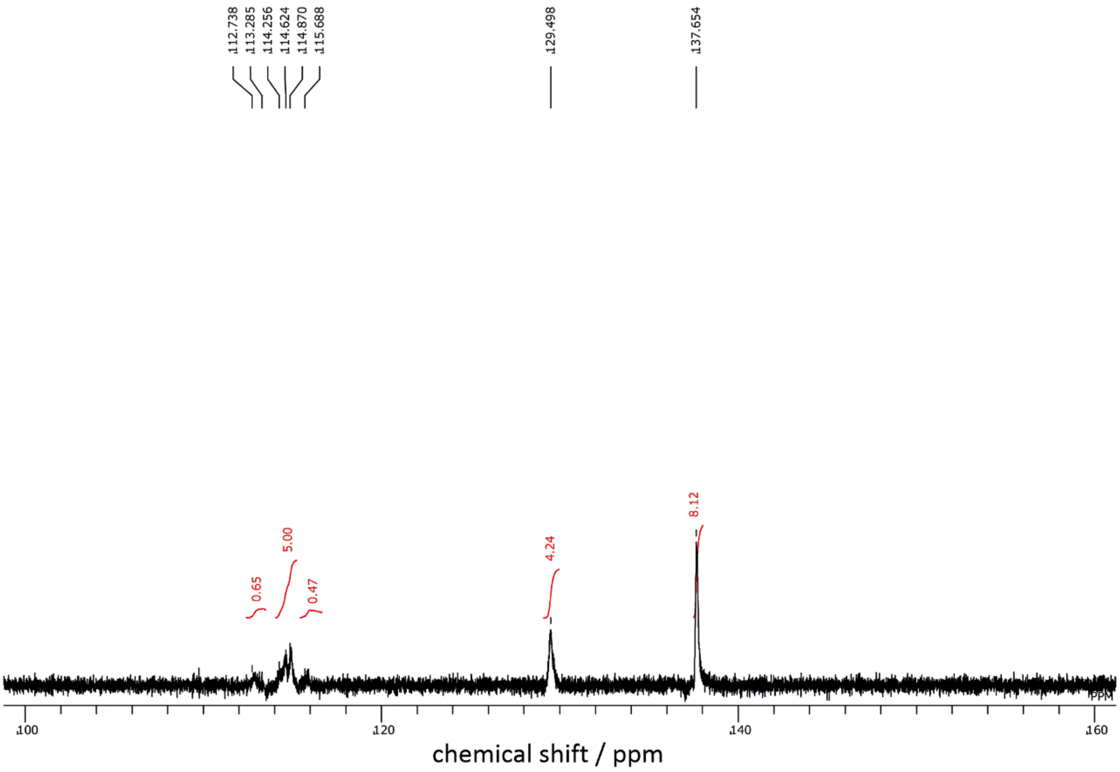

Figure S2.22. ^{19}F NMR spectrum of **2-5** in $CDCl_3$.

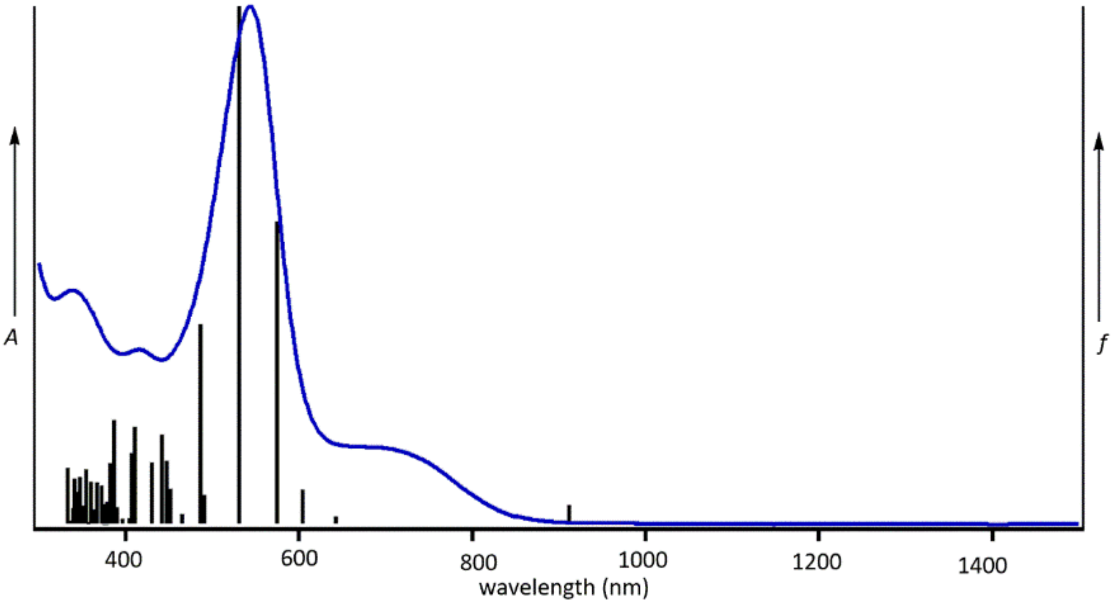

Figure S2.23. The UV-Vis-NIR absorption spectra (blue line, left axis) and oscillator strengths (black bar, right axis), which is calculated at the B3LYP/6-31G* level of theory of **2-3.**

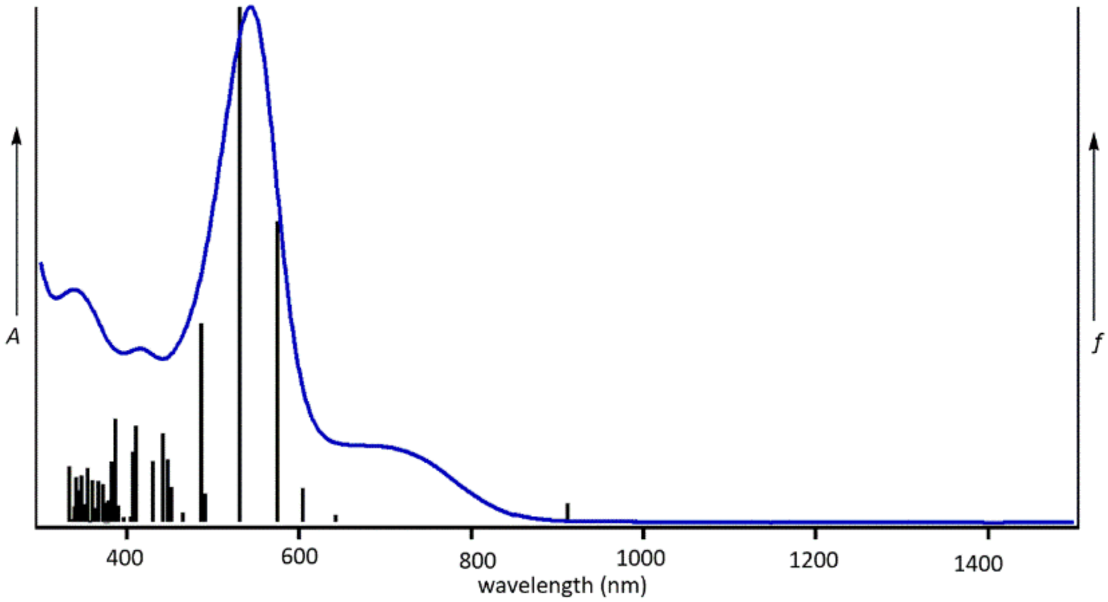

Figure S2.24. The UV-Vis-NIR absorption spectra (blue line, left axis) and oscillator strengths (black bar, right axis), which is calculated at the B3LYP/6-31G* level of theory of **2-4.**

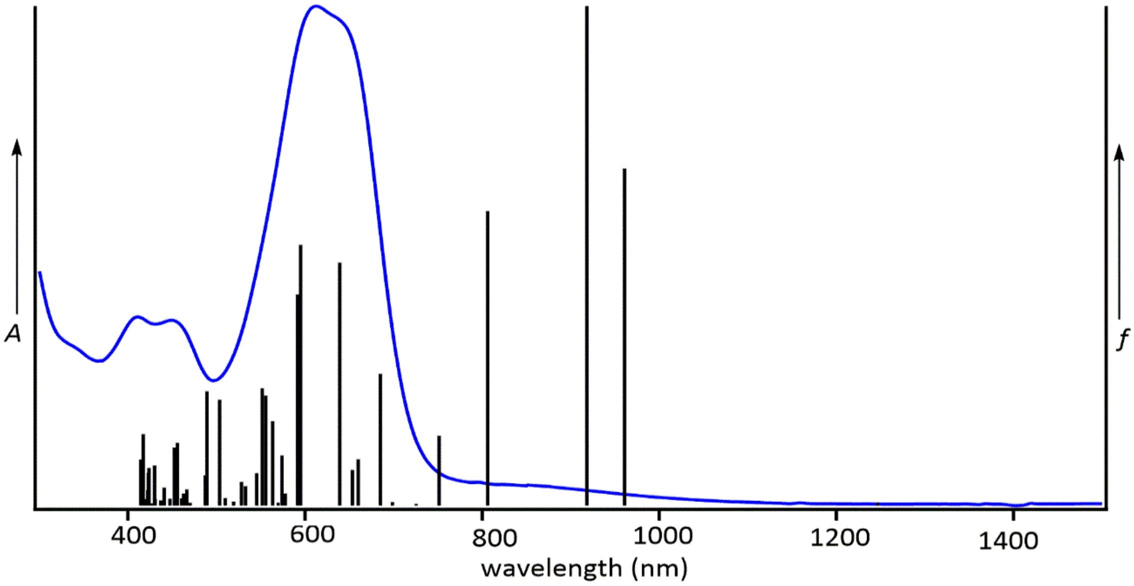

Figure S2.25. The UV-Vis-NIR absorption spectra (blue line, left axis) and oscillator strengths (black bar, right axis), which is calculated at the B3LYP/6-31G* level of theory of **2-5**.

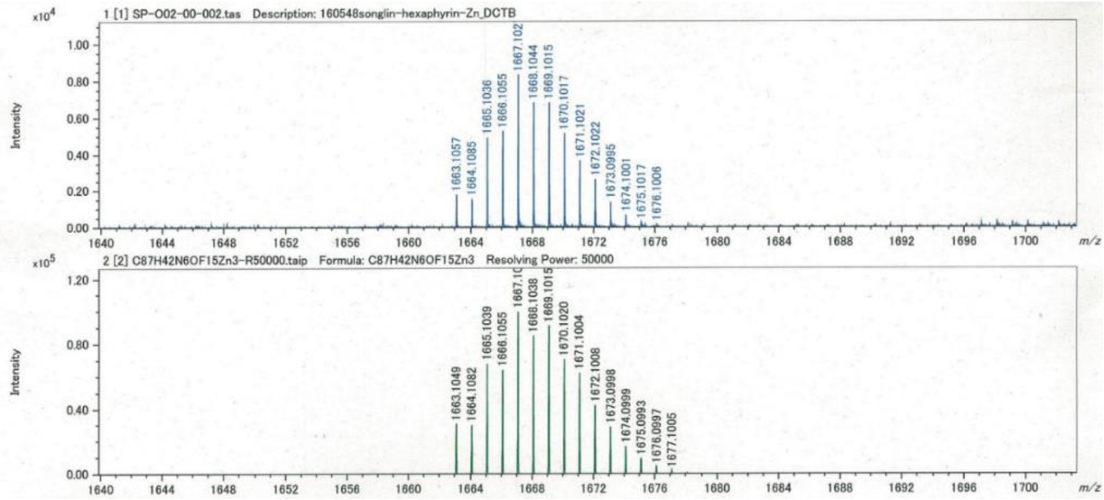

Figure S2.26. HR-MALDI-MS spectrum of **2-4-2Zn**.

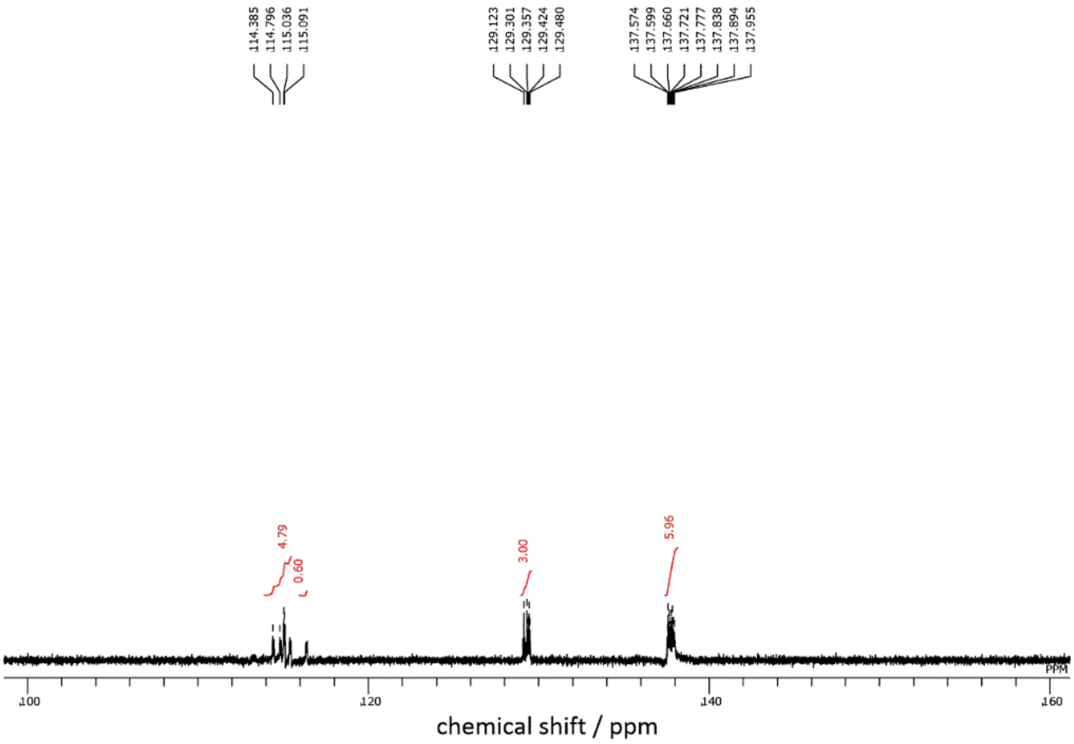

Figure S2.27. ^{19}F NMR spectrum of **2-4-2Zn** in $CDCl_3$

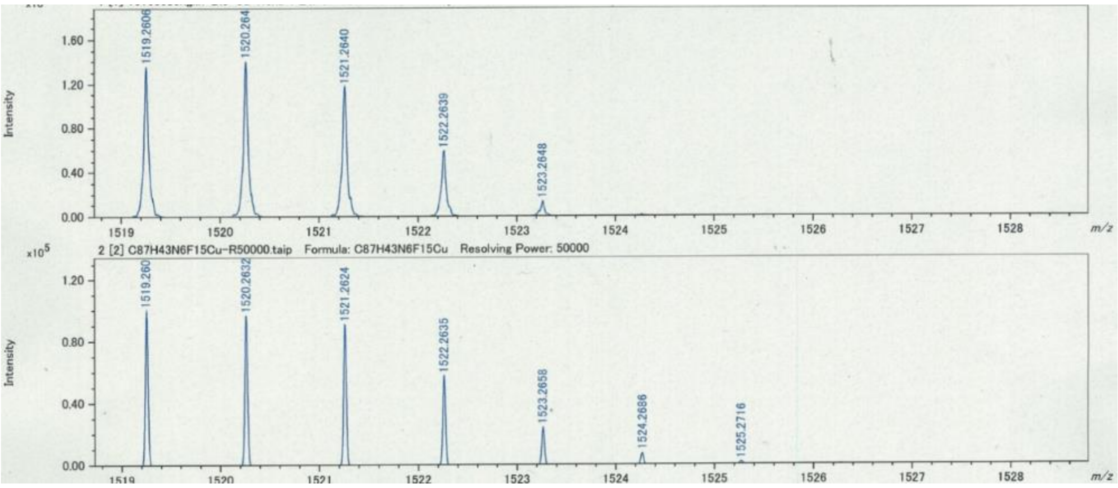

Figure S2.28. HR-MALDI-MS spectrum of **2-4-Cu**.

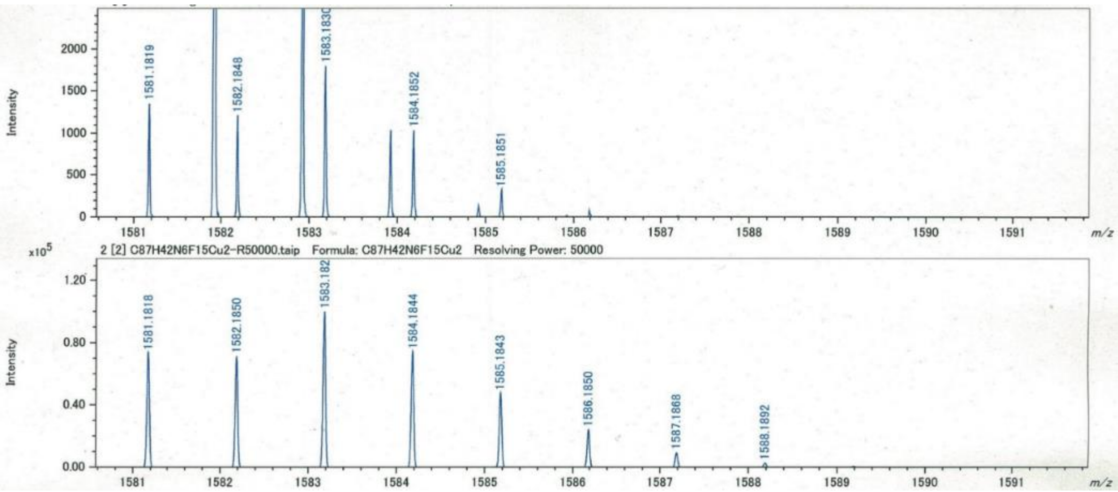

Figure S2.29. HR-MALDI-MS spectrum of **2-4-2Cu**.

Table S 2.1. X-ray Structure Report for 2-2.

Identification code	60227SX_0m_a	
Empirical formula	$C_{60}H_{44}IrN_3$	
Formula weight	999.18	
Temperature	90 K	
Wavelength	0.71073 Å	
Crystal system	Triclinic	
Space group	*P*-1	
Unit cell dimensions	*a* = 11.906(4) Å	α = 98.325(5)°.
	b = 13.081(4) Å	β = 106.248(5)°.
	c = 15.435(4) Å	γ = 106.072(5)°.
Volume	2152.4(11) Å^3	
Z	2	
Density (calculated)	1.542 g/cm^3	
Absorption coefficient	3.148 mm^{-1}	
F(000)	1004	
Crystal size	0.100 x 0.050 x 0.030 mm^3	
Theta range for data collection	1.669 to 25.998°.	
Index ranges	–13 <= *h* < = 14, –15<= *k* <=16, –18 <= *l* <= 19	
Reflections collected	12439	
Independent reflections	8392 [*R*(int) = 0.0554]	
Completeness to theta = 25.242°	99.2 %	
Absorption correction	Semi-empirical from equivalents	

Max. and min. transmission	0.911 and 0.748
Refinement method	Full-matrix least-squares on F^2
Data / restraints / parameters	8392 / 0 / 577
Goodness-of-fit on F^2	1.024
Final *R* indices [*I*>2sigma(*I*)]	R_1 = 0.0529, wR_2 = 0.0940
R indices (all data)	R_1 = 0.0845, wR_2 = 0.1044
Extinction coefficient	n/a
Largest diff. peak and hole	1.998 and –1.730 e.Å^{-3}

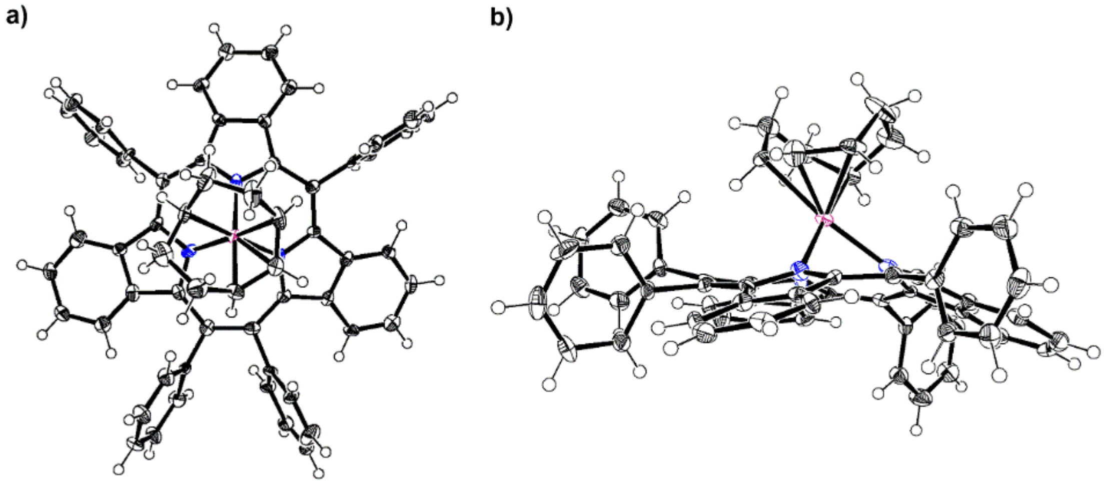

Figure S2.30. Crystal structure of **2-2**. The thermal ellipsoids represent for 50% probability.

Table S 2.2. X-ray Structure Report for 2-3.

Empirical Formula	$C_{58}H_{30}F_{10}N_4$
Formula Weight	972.89
Crystal Color, Habit	green, platelet
Crystal Dimensions	0.090 x 0.050 x 0.010 mm
Crystal System	triclinic
Lattice Type	Primitive
Lattice Parameters	a = 10.9778(8) Å
	b = 12.2355(8) Å
	c = 18.2096(13) Å
	α = 71.543(5) ^{o}
	β = 83.587(6) ^{o}
	γ = 81.973(6) ^{o}
	V = 2291.4(3) Å^3
Space Group	P-1 (#2)
Z value	2
Dcalc	1.410 g/cm^3
F000	992.00
μ(MoKα)	1.115 cm^{-1}
Diffractometer	R-AXIS RAPID
Radiation	MoKα (λ = 0.71075 Å)
	multi-layer mirror monochromated
Voltage, Current	50 kV, 24 mA
Temperature	-170.0^{o}C

Detector Aperture	460.0 x 256.0 mm
Data Images	192 exposures
ω oscillation Range ($\chi = 45.0$, $\phi = 0.0$)	130.0 - 190.0°
Exposure Rate	140.0 sec./°
ω oscillation Range ($\chi = 45.0$, $\phi = 180.0$)	0.0 - 162.0°
Exposure Rate	140.0 sec./°
ω oscillation Range ($\chi = 45.0$, $\phi = 90.0$)	0.0 - 162.0°
Exposure Rate	140.0 sec./°
Detector Position	127.40 mm
Pixel Size	0.100 mm
$2\theta_{\max}$	0.0°
No. of Reflections Measured	Total: 0 Unique: 0 ($R_{\text{int}} = 0.1039$)
Corrections	Lorentz-polarization Absorption (trans. factors: 0.404 - 0.999)
Structure Solution	Direct Methods (SHELXT Version 2014/5)
Refinement	Full-matrix least-squares on F^2
Function Minimized	$\Sigma\, w\, (Fo^2 - Fc^2)^2$
Least Squares Weights	$w = 1/ [\, \sigma^2(Fo^2) + (0.0842 \cdot P)^2$ $+ 0.8243 \cdot P\,]$ where $P = (\mathrm{Max}(Fo^2,0) + 2Fc^2)/3$

$2\theta_{max}$ cutoff	50.7°
Anomalous Dispersion	All non-hydrogen atoms
No. Observations (All reflections)	8368
No. Variables	649
Reflection/Parameter Ratio	12.89
Residuals: R_1 ($I > 2.00\sigma(I)$)	0.0761
Residuals: R (All reflections)	0.1301
Residuals: wR_2 (All reflections)	0.1994
Goodness of Fit Indicator	1.054
Max Shift/Error in Final Cycle	0.000
Maximum peak in Final Diff. Map	0.28 $e^{-}/\text{Å}^{3}$
Minimum peak in Final Diff. Map	-0.31 $e^{-}/\text{Å}^{3}$

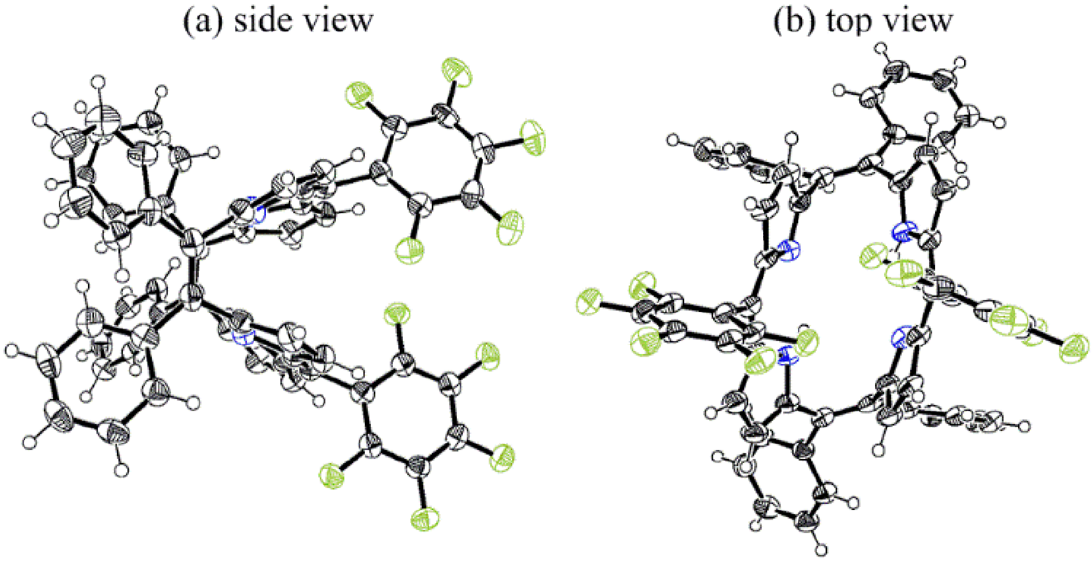
(a) side view

(b) top view

Figure S2.31. Crystal structure of **2-3**. The thermal ellipsoids represent for 50% probability.

Table S 2.3. X-ray Structure Report for 2-4

Empirical Formula	$C_{268}H_{151}F_{45}N_{18}$
Formula Weight	4478.19
Crystal Color, Habit	purple, prism
Crystal Dimensions	0.090 x 0.070 x 0.030 mm
Crystal System	monoclinic
Lattice Type	Primitive
Lattice Parameters	a = 21.6454(5) Å
	b = 10.2823(2) Å
	c = 52.2217(12) Å
	β = 100.813(7) $^{\circ}$
	V = 11416.3(5) Å^3
Space Group	*P*n (#7)
Z value	2
*D*calc	1.303 g/cm^3
*F*000	4580.00
μ(MoKα)	1.023 cm^{-1}
Diffractometer	R-AXIS RAPID
Radiation	MoKα (λ = 0.71075 Å)
	multi-layer mirror monochromated
Voltage, Current	50 kV, 24 mA
Temperature	-170.0 $^{\circ}$C
Detector Aperture	460.0 x 256.0 mm
Data Images	192 exposures

ω oscillation Range (χ = 45.0, ϕ = 0.0)	130.0 - 190.0°
Exposure Rate	140.0 sec./$^{\circ}$
ω oscillation Range (χ = 45.0, ϕ = 180.0)	0.0 - 162.0°
Exposure Rate	140.0 sec./$^{\circ}$
ω oscillation Range (χ = 45.0, ϕ= 90.0)	0.0 - 162.0°
Exposure Rate	140.0 sec./$^{\circ}$
Detector Position	127.40 mm
Pixel Size	0.100 mm
$2\theta_{max}$	50.7°
No. of Reflections Measured	Total: 44568 Unique: 27761 (R_{int} = 0.0554)
Parsons quotients (Flack x parameter): 4760	
Corrections	Lorentz-polarization Absorption (trans. factors: 0.590 - 0.997)
Structure Solution	Direct Methods (SHELXT Version 2014/5)
Refinement	Full-matrix least-squares on F^2
Function Minimized	Σ w $(Fo^2 - Fc^2)^2$
Least Squares Weights	w = 1/ [$\sigma^2(Fo^2) + (0.0674 \cdot P)^2$ $+ 0.0000 \cdot P$] where P = $(Max(Fo^2,0) + 2Fc^2)/3$
$2\theta_{max}$ cutoff	50.7°

Anomalous Dispersion	All non-hydrogen atoms
No. Observations (All reflections)	27761
No. Variables	2947
Reflection/Parameter Ratio	9.42
Residuals: R_1 ($I>2.00\sigma(I)$)	0.0565
Residuals: R (All reflections)	0.0883
Residuals: wR_2 (All reflections)	0.1324
Goodness of Fit Indicator	0.997
Flack parameter (Parsons' quotients = 4760)	0.5(4)
Max Shift/Error in Final Cycle	0.001
Maximum peak in Final Diff. Map	0.39 $e^-/Å^3$
Minimum peak in Final Diff. Map	-0.24 $e^-/Å^3$

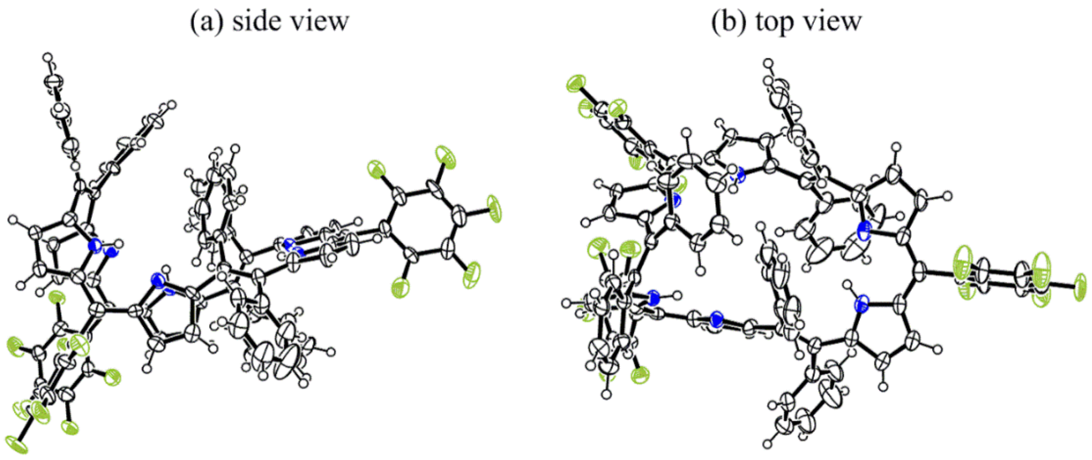
(a) side view

(b) top view

Figure S2.32. Crystal structure of **2-4**. The thermal ellipsoids represent for 50% probability.

Table S 2.4. X-ray Structure Report for 2-5.

Empirical Formula	$C_{130}H_{92}F_{20}N_8$
Formula Weight	2146.18
Crystal Color, Habit	green, prism
Crystal Dimensions	0.190 x 0.190 x 0.080 mm
Crystal System	orthorhombic
Lattice Type	Primitive
Lattice Parameters	a = 25.6357(5) Å
	b = 20.9621(4) Å
	c = 19.6620(4) Å
	V = 10565.9(3) Å^3
Space Group	Pna2$_1$ (#33)
Z value	4
D_{calc}	1.349 g/cm^3
F_{000}	4432.00
μ(MoKα)	1.036 cm^{-1}
Diffractometer	R-AXIS RAPID
Radiation	MoKα (λ = 0.71075 Å)
	multi-layer mirror monochromated
Voltage, Current	50 kV, 24 mA
Temperature	-170.0^{o}C
Detector Aperture	460.0 x 256.0 mm
Data Images	192 exposures
ω oscillation Range (χ = 45.0, ϕ = 0.0)	130.0 - 190.0^{o}

Exposure Rate	90.0 sec./$^{\circ}$
ω oscillation Range (χ = 45.0, ϕ = 180.0)	0.0 - 162.0°
Exposure Rate	90.0 sec./$^{\circ}$
ω oscillation Range (χ = 45.0, ϕ = 90.0)	0.0 - 162.0°
Exposure Rate	90.0 sec./$^{\circ}$
Detector Position	127.40 mm
Pixel Size	0.100 mm
$2\theta_{max}$	50.7°
No. of Reflections Measured	Total: 145667 Unique: 18746 (R_{int} = 0.0273)
Parsons quotients (Flack x parameter): 7747	
Corrections	Lorentz-polarization Absorption (trans. factors: 0.827 - 0.992)
Structure Solution	Direct Methods (SIR2011)
Refinement	Full-matrix least-squares on F^2
Function Minimized	Σ w $(Fo^2 - Fc^2)^2$
Least Squares Weights	w = 1/ [$\sigma^2(Fo^2) + (0.0345 \cdot P)^2$ $+ 1.7791 \cdot P$] where P = $(Max(Fo^2,0) + 2Fc^2)/3$
$2\theta_{max}$ cutoff	50.7°
Anomalous Dispersion	All non-hydrogen atoms
No. Observations (All reflections)	18746

No. Variables	1427
Reflection/Parameter Ratio	13.14
Residuals: R_1 (I>2.00σ(I))	0.0260
Residuals: R (All reflections)	0.0286
Residuals: wR_2 (All reflections)	0.0619
Goodness of Fit Indicator	1.028
Flack parameter (Parsons' quotients = 7747)	0.17(5)
Max Shift/Error in Final Cycle	0.000
Maximum peak in Final Diff. Map	0.24 $e^-/Å^3$
Minimum peak in Final Diff. Map	-0.20 $e^-/Å^3$

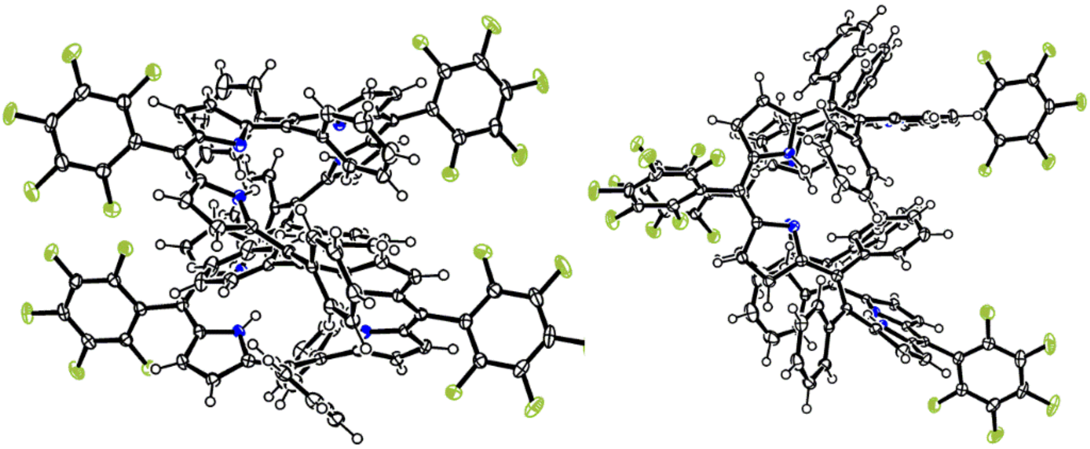
(a) side view

(b) top view

Figure S2.33. Crystal structure of **2-5**. The thermal ellipsoids represent for 50% probability.

Table S 2.5. Crystal data and structure refinement of 2-4-2Zn.

Empirical formula	$C_{97}H_{60}Cl_{11.48}F_{15}N_6O_{3.51}Zn_2$
Formula weight	1833.77
Temperature	90 K
Wavelength	0.71073Å
Crystal system	Monoclinic
Space group	$P2_1/c$
Unit cell dimensions	a = 24.767(4) Å
	b = 14.691(2) Å β = 105.685(3)°.
	c = 24.861(4) Å
Volume	8709(2) Å^3
Z	4
Density (calculated)	1.399 Mg/m^3
Absorption coefficient	0.683 mm^{-1}
F(000)	3729
Crystal size	0.200 x 0.100 x 0.010 mm^3
Theta range for data collection	1.628 to 24.000°.
Index ranges	$-28 \leq h \leq 28$, $-16 \leq k \leq 16$, $-28 \leq l \leq 28$
Reflections collected	42231
Independent reflections	13655 [R(int) = 0.1750]
Completeness to theta = 24.000°	99.9 %
Max. and min. transmission	0.993 and 0.824
Refinement method	Full-matrix least-squares on F^2
Data / restraints / parameters	13655 / 115 / 1152

Goodness-of-fit on F^2	1.011
Final R indices [$I > 2.00\sigma(I)$]	$R_1 = 0.0754$
R indices (all data)	$wR_2 = 0.2205$
Largest diff. peak and hole	0.742 and -0.708 e.Å^{-3}

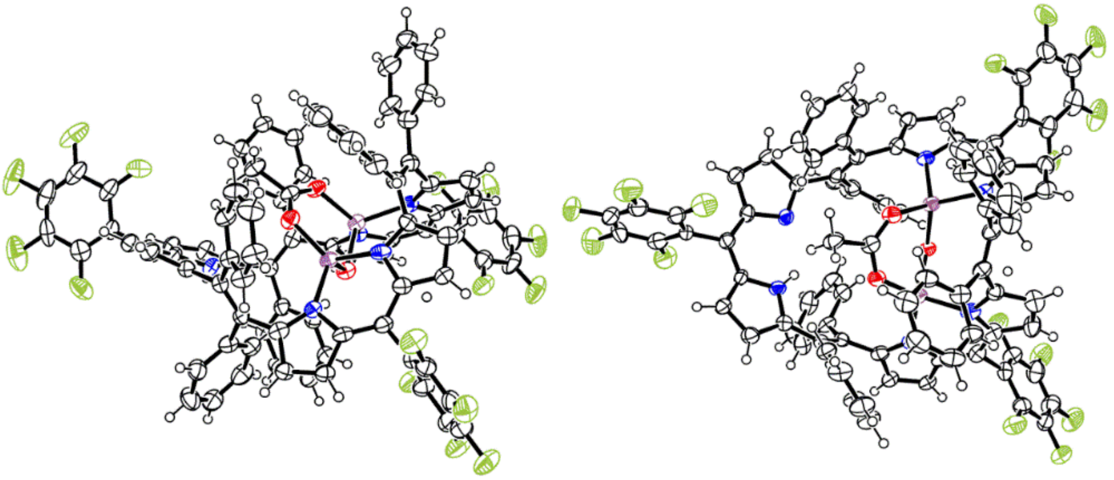
(a) side view

(b) top view

Figure S2.34. Crystal structure of **2-4-2Zn**. The thermal ellipsoids represent for 50% probability.

Table S 2.6. X-ray Structure Report for 2-4-Cu

Empirical Formula	$C_{87}H_{43}CuF_{15}N_6$
Formula Weight	1520.86
Crystal Color, Habit	purple, prism
Crystal Dimensions	0.150 x 0.070 x 0.030 mm
Crystal System	monoclinic
Lattice Type	Primitive
Lattice Parameters	a = 14.6148(3) Å
	b = 18.4705(3) Å
	c = 26.6194(5) Å β = 100.364(7) $^{\mathrm{o}}$
	V = 7068.5(3) $Å^3$
Space Group	$P2_1$/n (#14)
Z value	4
D_{calc}	1.429 g/cm^3
F_{000}	3084.00
μ(MoKα)	4.016 cm^{-1}
Diffractometer	R-AXIS RAPID
Radiation	MoKα (λ = 0.71075 Å)
	multi-layer mirror monochromated
Voltage, Current	50 kV, 24 mA
Temperature	-170.0 $^{\mathrm{o}}$C
Detector Aperture	460.0 x 256.0 mm
Data Images	192 exposures
ω oscillation Range (χ = 45.0, ϕ = 0.0)	130.0 - 190.0$^{\mathrm{o}}$

Exposure Rate	80.0 sec./$^{\circ}$
ω oscillation Range ($\chi = 45.0$, $\phi = 180.0$)	0.0 - 162.0°
Exposure Rate	80.0 sec./$^{\circ}$
ω oscillation Range ($\chi = 45.0$, $\phi = 90.0$)	0.0 - 162.0°
Exposure Rate	80.0 sec./$^{\circ}$
Detector Position	127.40 mm
Pixel Size	0.100 mm
$2\theta_{max}$	50.7°
No. of Reflections Measured	Total: 97701 Unique: 12925 ($R_{int} = 0.0569$)
Corrections	Lorentz-polarization Absorption (trans. factors: 0.727 - 0.988)
Structure Solution	Direct Methods (SHELXT Version 2014/5)
Refinement	Full-matrix least-squares on F^2
Function Minimized	Σ w $(Fo^2 - Fc^2)^2$
Least Squares Weights	$w = 1/ [\sigma^2(Fo^2) + (0.0435 \cdot P)^2 + 6.4031 \cdot P]$ where $P = (Max(Fo^2,0) + 2Fc^2)/3$
$2\theta_{max}$ cutoff	50.7°
Anomalous Dispersion	All non-hydrogen atoms
No. Observations (All reflections)	12925

No. Variables	982
Reflection/Parameter Ratio	13.16
Residuals: R_1 (I>2.00σ(I))	0.0434
Residuals: R (All reflections)	0.0592
Residuals: wR_2 (All reflections)	0.1016
Goodness of Fit Indicator	1.031
Max Shift/Error in Final Cycle	0.002
Maximum peak in Final Diff. Map	0.42 $e^-/Å^3$
Minimum peak in Final Diff. Map	-0.45 $e^-/Å^3$

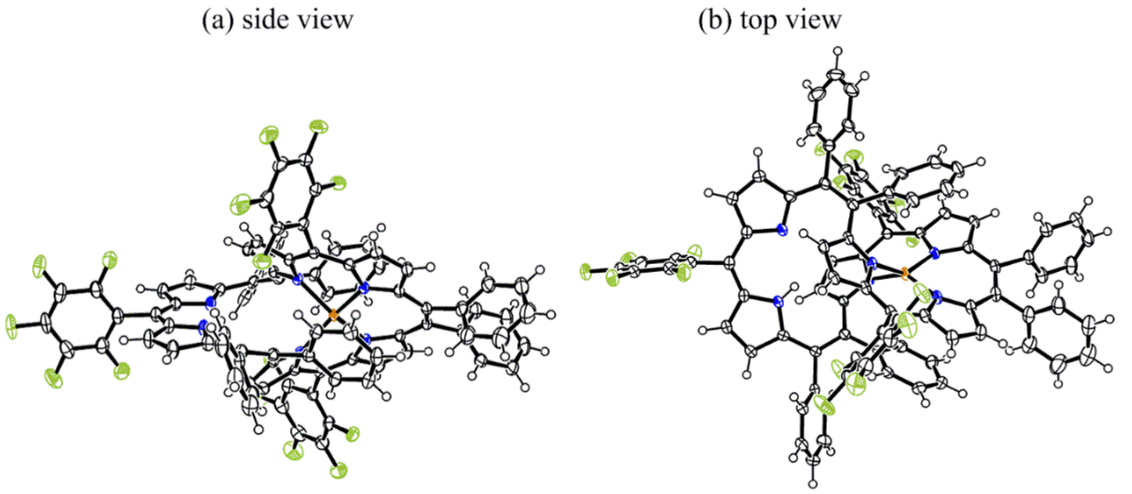
(a) side view

(b) top view

Figure S2.35. Crystal structure of **2-4-Cu**. The thermal ellipsoids represent for 50% probability.

Table S 2.7. Crystal data and structure refinement of 2-4-2Cu.

Empirical formula	$C_{94}H_{43}Cl_3Cu_2F_{15}N_6$	
Formula weight	1774.77	
Temperature	90 K	
Wavelength	0.71073Å	
Crystal system	Monoclinic	
Space group	$P2_1/c$	
Unit cell dimensions	a = 17.756(2) Å	
	b = 30.268(3) Å	β = 96.367(2)°.
	c = 14.9944(16) Å	
Volume	8008.8(15) Å^3	
Z	4	
Density (calculated)	1.472 Mg/m^3	
Absorption coefficient	0.719 mm^{-1}	
F(000)	3572	
Crystal size	0.200 x 0.200 x 0.050 mm^3	
Theta range for data collection	1.773 to 26.999°.	
Index ranges	$-20 \leq h \leq 22$, $-22 \leq k \leq 38$, $-18 \leq l \leq 19$	
Reflections collected	50778	
Independent reflections	17458 [R(int) = 0.1058]	
Completeness to theta = 24.000°	99.8%	
Max. and min. transmission	0.965 and 0.902	
Refinement method	Full-matrix least-squares on F^2	
Data / restraints / parameters	17458 / 33 / 1157	

Goodness-of-fit on F^2	1.034
Final R indices [$I > 2.00\sigma(I)$]	$R_1 = 0.0888$
R indices (all data)	$wR_2 = 0.2961$
Largest diff. peak and hole	0.978 and -2.364 e.Å^{-3}

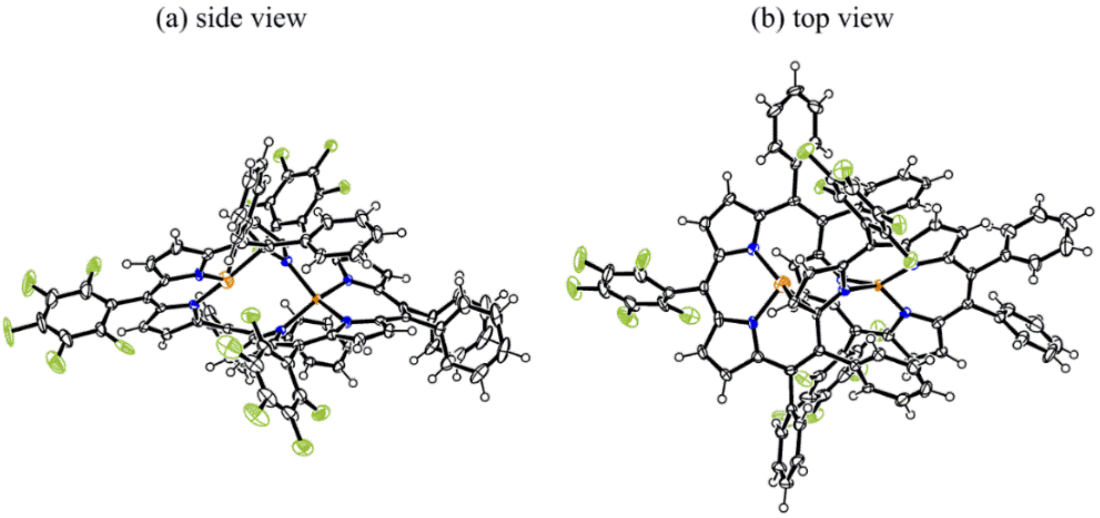
(a) side view

(b) top view

Figure S2.36. Crystal structure of **2-4-2Cu**. The thermal ellipsoids represent for 50% probability.

Chapter 3

Porphyrins with Vinylene-Bridges

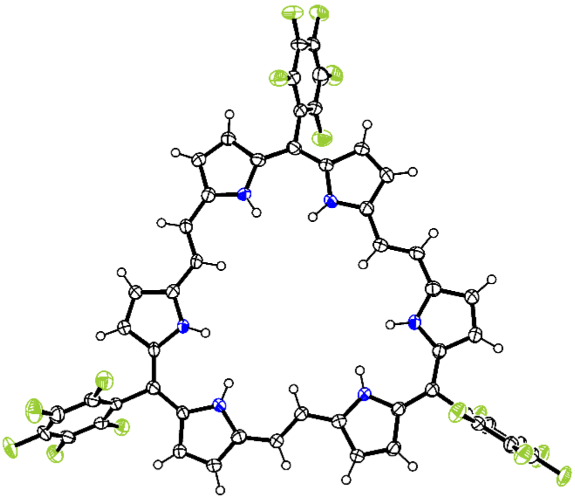

In this Chapter, the synthesis, characterization and complexation of aromatic planar [30]hexaphyrin(2.1.2.1.2.1) with vinylene-bridges are described.

3-1 Introduction

Expanded porphyrins with vinylene bridges at *meso*-positions have been rarely reported to date (Figure 3.1).[1-3] The [22]porphyrin(2.2.2.2) is the first expanded porphyrin with vinylene bridges between pyrroles. It is obtained by hydrogenation of acetylene-cumulene porphyrin or cyclization of 2,5-diformylpyrrole by McMurry coupling (Figure 3.1).[1a]

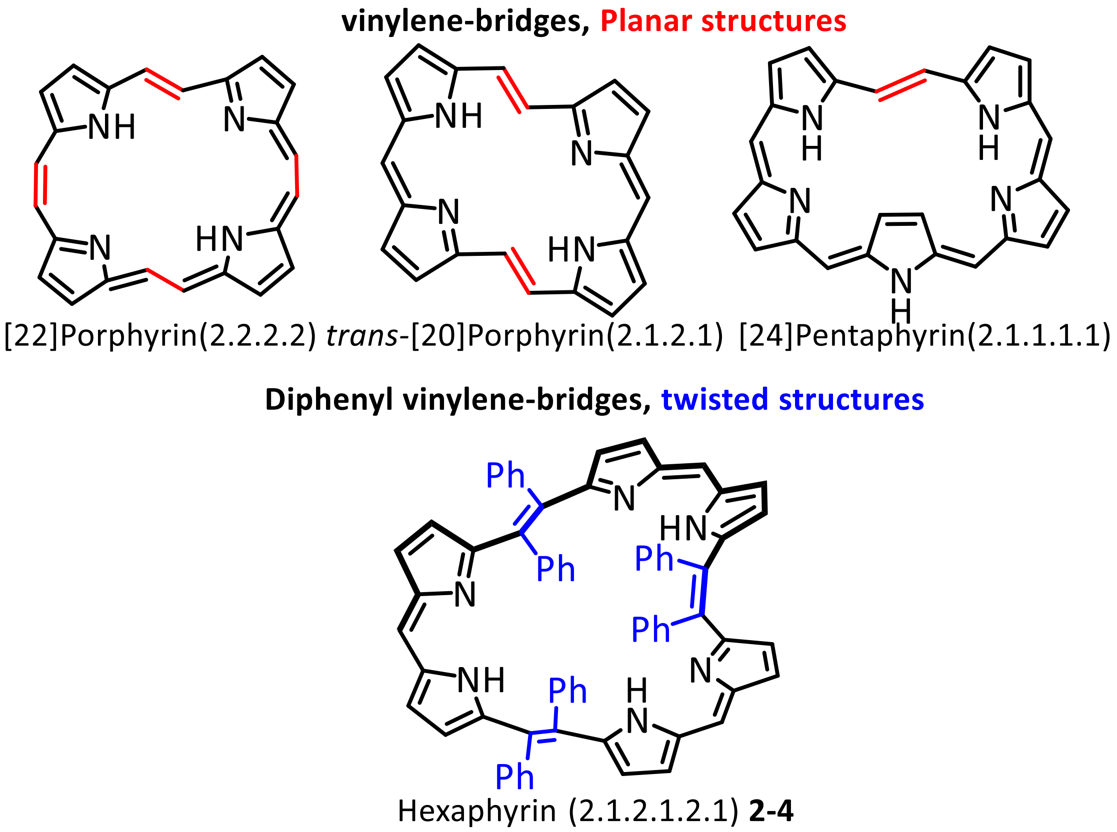

Figure 3.1. Selected porphyrins with vinylene-bridges.

In 2016, Osuka's group reported the preparation of a planar and anti-aromatic *trans*-[20]porphyrin(2.1.2.1) with *trans*-vinylene bridges, which is obtained by hydrogenation of tetradehydro[20]porphyrin(2.1.2.1).[1b] Neya and co-workers reported the synthesis of an anti-aromatic and planar [24]pentaphyrin(2.1.2.1.1) with *trans*-vinylene bridges by [3+2] type condensation reaction.[1c] These three reported expanded porphyrins show planar molecular structures with anti-/aromatic properties. The highly twisted hexaphyrin(2.1.2.1.2.1) **2-4** with diphenyl vinylene bridges showed non-aromatic property (in Chapter 2). However larger planar and aromatic hexaphyrins with multi vinylene bridges have not been developed yet.

In this context, the 1,2-di(pyrrol-2-yl)ethene (**DPE**) was selected as the simplest vinylene-bridges unit for construction of expanded porphyrins by condensation reactions. The treatment of **DPE** and C_6H_5CHO in the presence of acid selectively gave *trans*-[30]hexaphyrin(2.1.2.1.2.1) **3-1** in 4%. The compound **3-1** has a planar molecular structure and 30π-electron aromatic property. The coordination ability of free-base **3-1** was screened with various metal ions because free-base **3-1** consists of multi-dipyrrin-like coordination sites. A tri-nuclear rhodium(I) complex **3-2** was obtained in good yield. The molecular structures, aromaticity, optical and redox properties were investigated by mass spectroscopy, NMR spectroscopy, X-ray crystallography, UV-Vis-NIR spectroscopy, electrochemistry and DFT calculation.

3-2 Synthesis

The detailed synthetic scheme is shown in scheme 3.1. The key starting material **DPE** was synthesized via an established method.[4] The **DPE** was characterized by ^{1}H NMR spectroscopy. Condensation reaction of **DPE** with C_6F_5CHO in the BF_3•OEt_2 in dry CH_2Cl_2 and followed by oxidation with DDQ afforded *trans*-[30]hexaphyrin(2.1.2.1.2.1) **3-1** in 4% yield. The HR-MALDI-MS detected corresponding molecular ion peak of **3-1** at *m/z* = 1002.1590 (calcd. for $C_{51}H_{21}F_{15}N_6$ = 1002.1588 $[M]^+$). However, the porphyrin(2.1.2.1) and other larger expanded porphyrins are not isolated under this reaction condition because poor solubility of products in organic solvents or instability in ambient atmosphere.

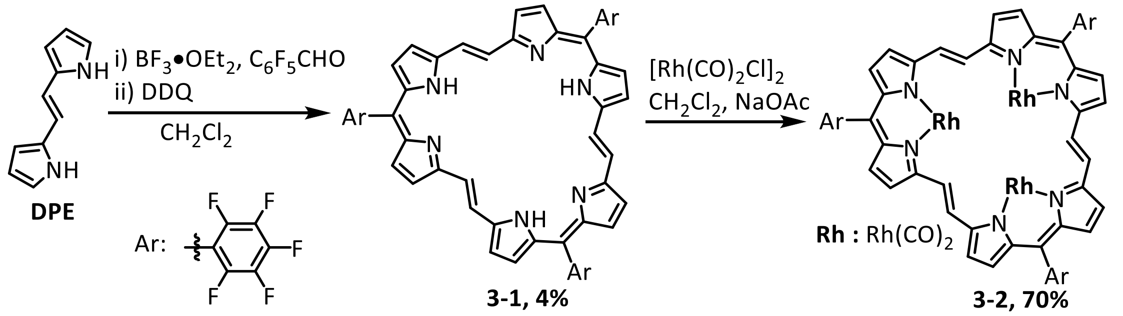

Scheme 3.1. Synthetic scheme of **3-1** and **3-2**.

The metalation reactions of **3-1** were investigated. The treatment of **3-1** with 10 eq. of $[Rh(CO)_2Cl]_2$ and 20 eq. of NaOAc in dry CH_2Cl_2 under a reflux condition for 12 hours afforded a rhodium complex **3-2** in 70% yield (Scheme 3.1). HR-MALDI-MS revealed the molecular ion peak at *m/z* = 1475.8239 (calcd. for $C_{57}H_{18}F_{15}N_6O_6Rh_3$ = 1475.8213 $[M]^+$), indicating the formation of a tri-nuclear rhodium complex. This result indicates that **3-1** can act as a porphyrin-like ligand with a sufficient cavity size to produce the tri-nuclear metal complex.

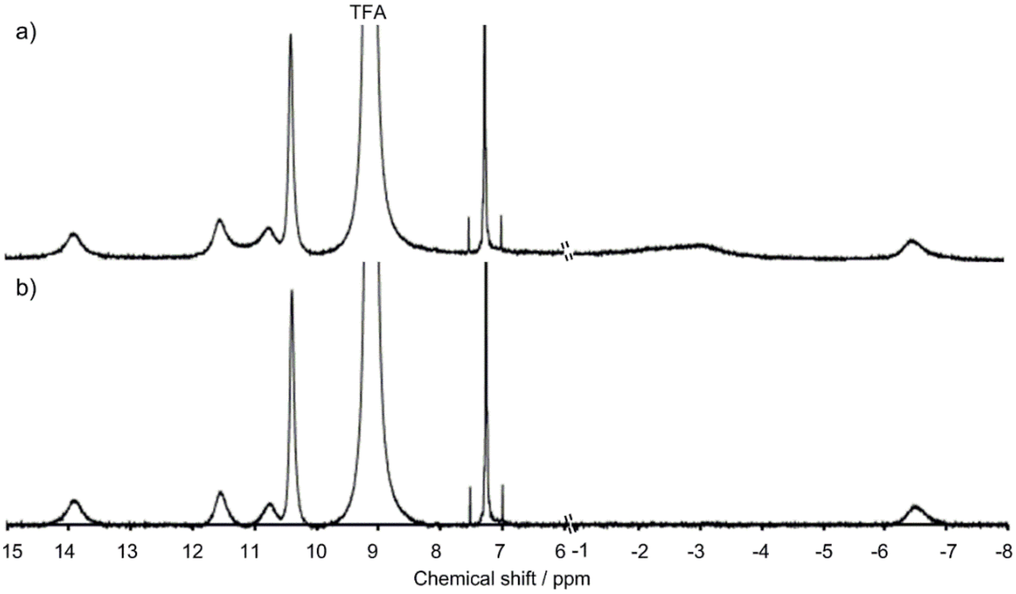

Figure 3.3. ^{1}H NMR spectra of **$(3\text{-}1)H_3^{3+}$** a) without D_2O and b) with D_2O in $CDCl_3$ at room temperature.

The ^{1}H NMR spectrum of **3-1** shows only very weak signals because of poor solubility in common organic solvents even at high temperature. Therefore, the ^{1}H NMR spectrum of protonated **3-1** (**$(3\text{-}1)H_3^{3+}$**) was measured in $CDCl_3$ with 200 eq. TFA. Broad peak in a range of –1 to –4 ppm is observed corresponding to NH signals, which is confirmed by deuterium-exchange experiments with D_2O (Figure 3.3). The signals of inner and outer protons of ethene linkages are observed at –6.5 ppm and 13.8 ppm, respectively. The pyrrolic β-protons are observed at downfield. The chemical shifts of pyrrolic β-protons are at 11.5 (3H), 10.7 (3H) and 10.4 (6H) ppm. Therefore, protonated compound **(3-1)H$_3$$^{3+}$** exhibits aromatic property.[5] The ^{19}F NMR spectrum of **(3-1)H$_3$$^{3+}$** shows three group signals assigned to *o*-F (6F), *m*-F (6F) and *p*-F (3F) of C_6F_5 groups (Figure 3.4).

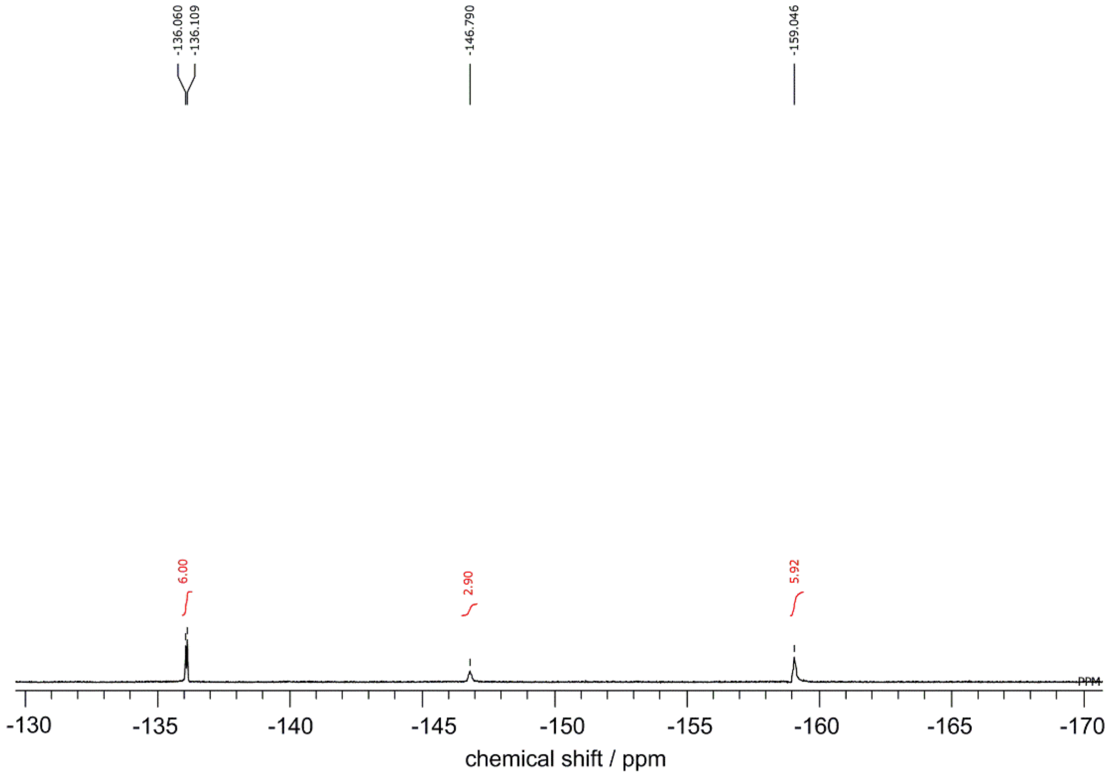

Figure 3.4. ^{19}F NMR spectrum of **(3-1)H$_3$$^{3+}$** in $CDCl_3$ with excess TFA.

The ^{1}H NMR spectrum of **3-2** displays clear signals in CD_2Cl_2 at room temperature because of improvement of the solubility in organic solvents (Figure 3.5). The temperature-dependent NMR spectra were measured from 293 K to 193 K in CD_2Cl_2 (Figure 3.5). With decreasing measurement temperature, the sharpened signals are observed. The signals of six inner and outer protons of ethene linkages display upfield and downfield shifts around –5 ppm and 13 ppm, respectively. Pyrrolic *β*-protons show twelve doublet peaks in the range of 11.02 to 8.96 ppm (Figure 3.6).

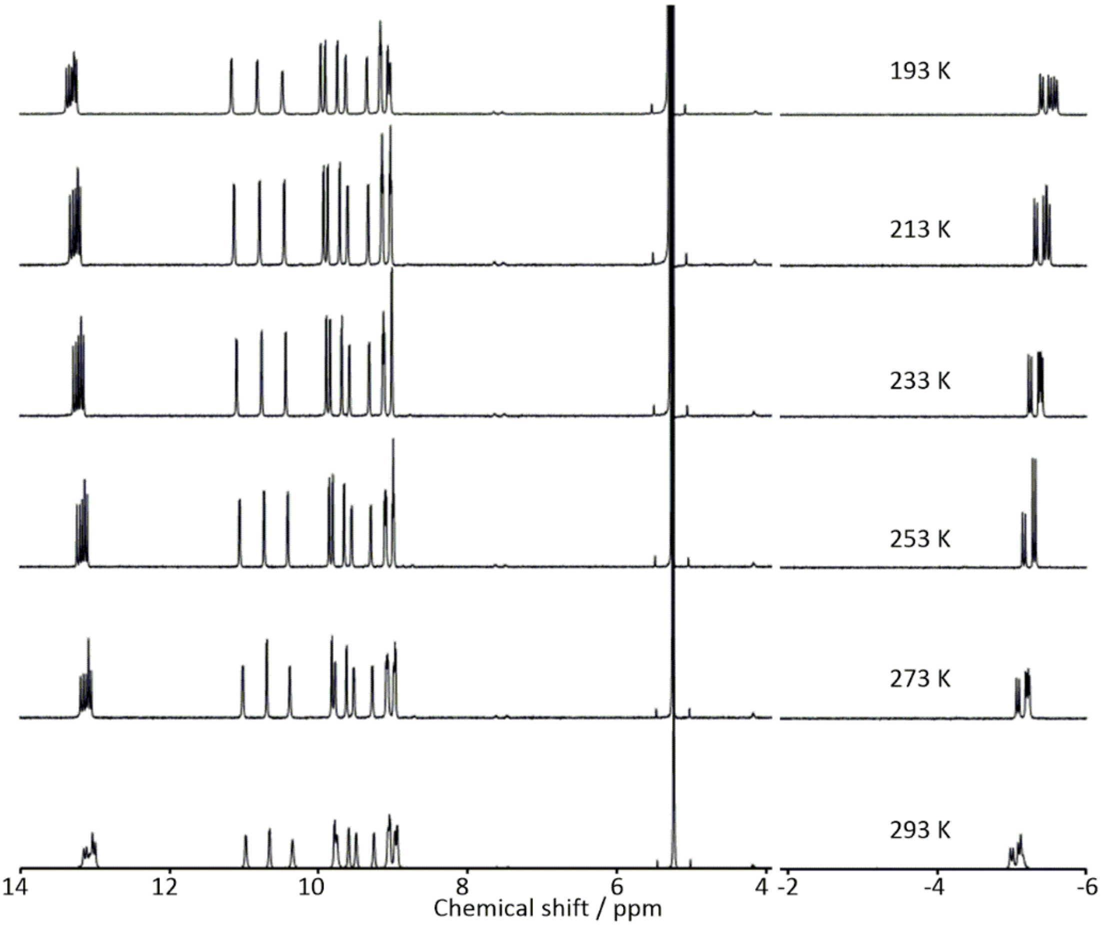

Figure 3.5. Temperature dependent NMR spectra of **3-2** in CD_2Cl_2.

To investigate the molecular structure of complex **3-2**, the COSY spectrum is measured (Figure 3.7). Signals of protons at pyrrolic *β*-position and ethene linkages are independently observed as doublet peaks. The result reveals that complex **3-2** has an asymmetric structure. Therefore, the temperature-dependent NMR spectra are measured from 293 K to 373 K in $C_2D_2Cl_4$ to check molecular dynamics (Figure 3.8). With increasing the measurement temperature, split signals gradually coalesced together, indicating that isomerization barrier between asymmetric structure and symmetric structure is broken on the molecular structures of complex **3-2**. The ^{19}F NMR spectrum of **3-2** exhibits three group signals assigned to the C_6F_5 groups of three *meso* positions (Figure 3.9).

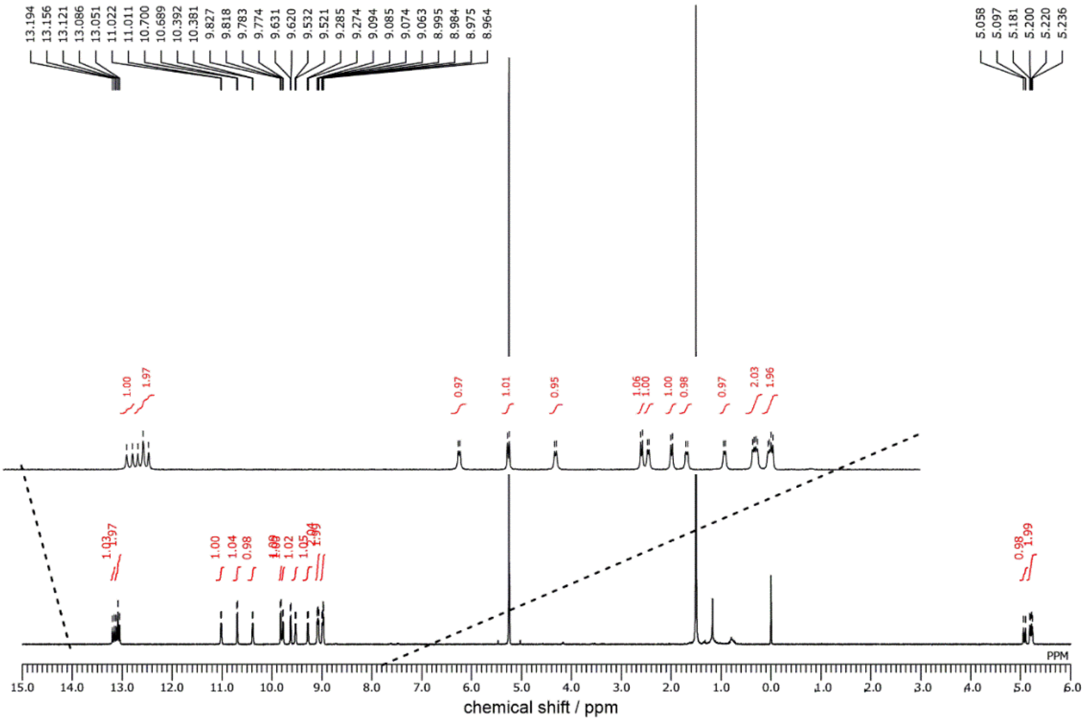

Figure 3.6. ^1H NMR spectrum of **3-2** in CD_2Cl_2 at 273K.

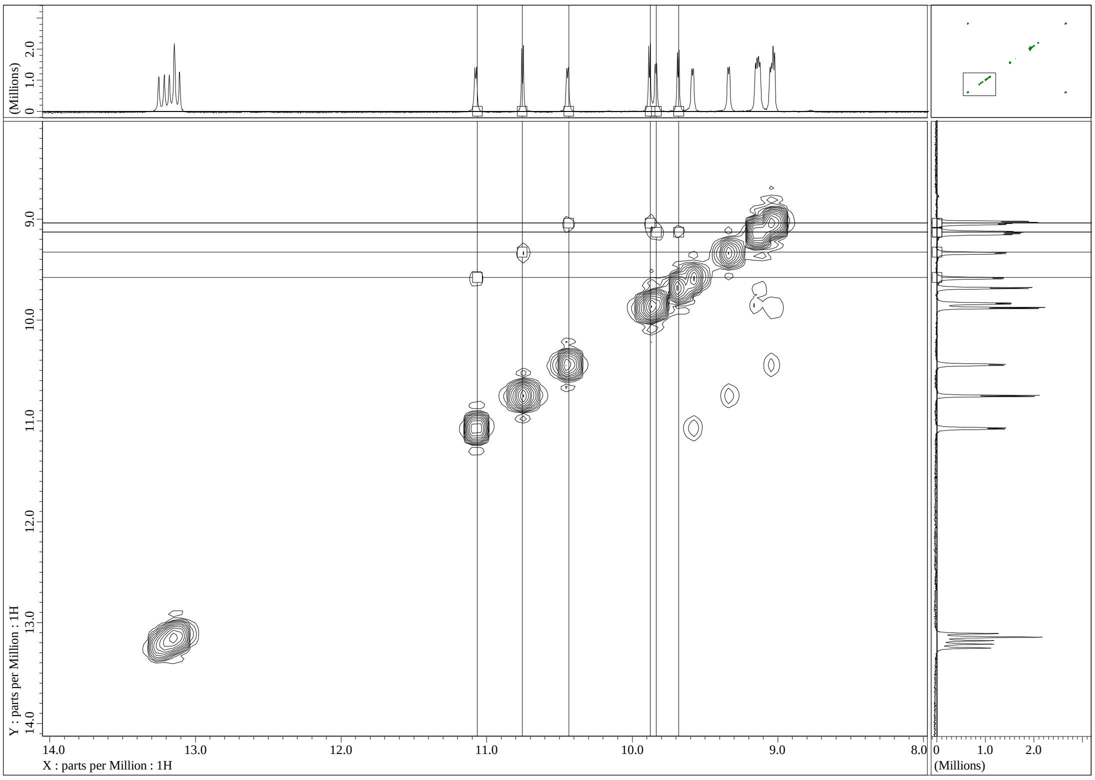

Figure 3.7. ^{1}H-^{1}H COSY spectrum of **3-2** in CD_2Cl_2 at 273K.

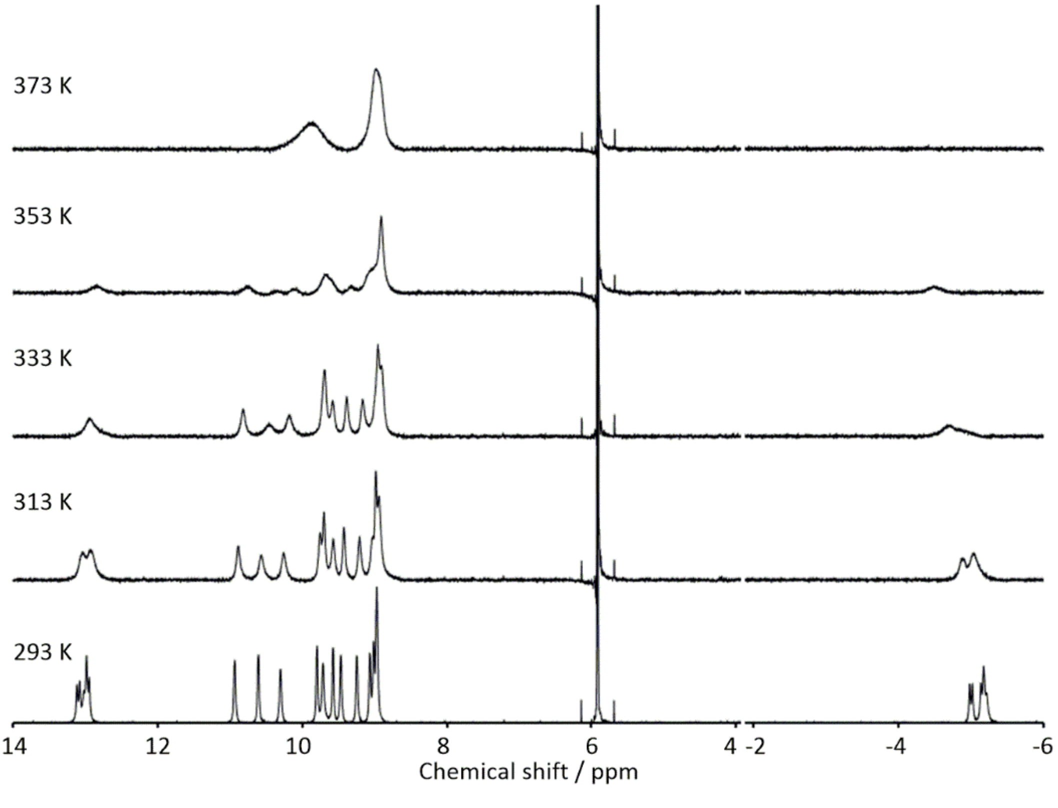

Figure 3.8. Temperature-dependent NMR spectra of **3-2** in $C_2D_2Cl_4$.

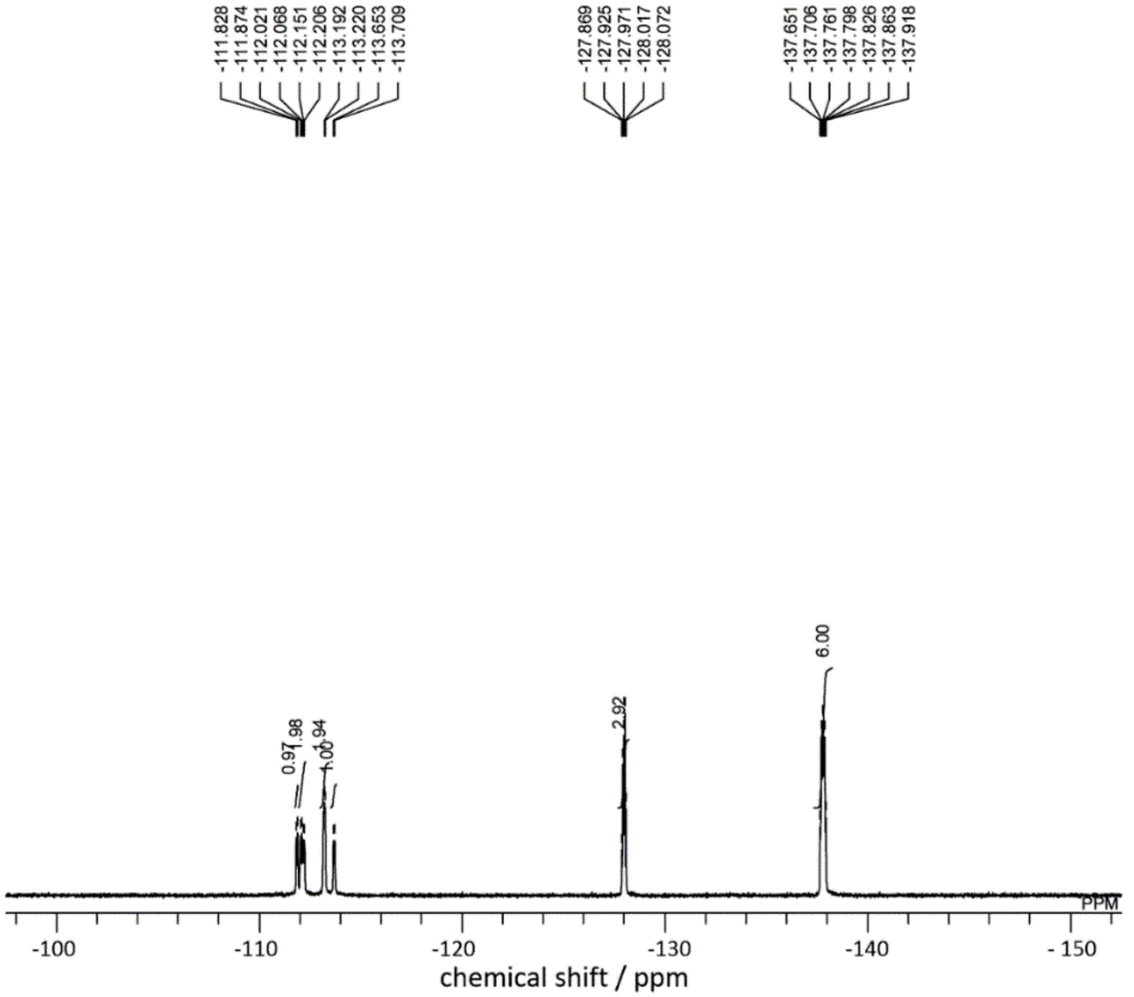

Figure 3.9. ^{19}F NMR spectrum of **3-2** in $CDCl_3$.

The IR spectrum of **3-2** was measured to confirm CO ligands on three rhodium atoms. The IR spectrum of **3-2** shows CO stretching vibrations signals at 2074.32 and 2010.43 cm^{-1} (Figure 3.10).[6]

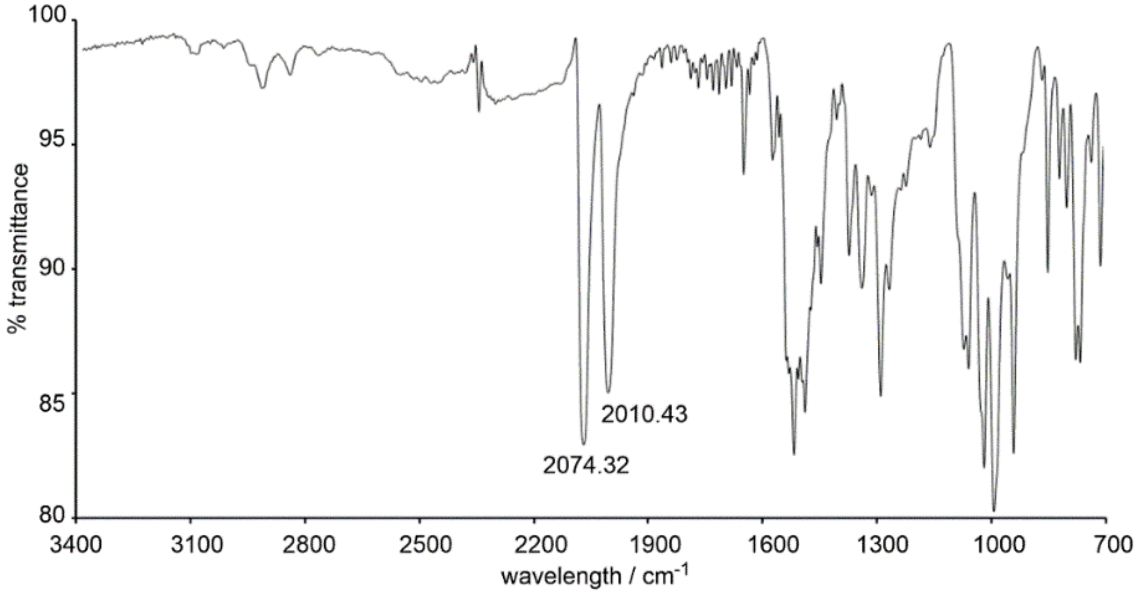

Figure 3.10. IR spectrum of **3-2**.

The solid-state structure of **(3-1)H$_3$$^{3+}$** has been unambiguously revealed by X-ray diffraction analysis (Figure 3.11). The single crystal of **(3-1)H$_3$$^{3+}$** is obtained by slow diffusion of *n*-hexane into the chloroform/TFA mixture solution of **3-1**. The crystal structure of **(3-1)H$_3$$^{3+}$** shows a pseudo rotaxane structure with TFA–H_2O–TFA chain through the **(3-1)H$_3$$^{3+}$** cavity (Figure 3.11). The macrocyclic ring of **(3-1)H$_3$$^{3+}$** displays a highly planar structure with *trans*-conformations at all ethene bridges. A mean-plane deviation defined by the core 39 atoms of the **(3-1)H$_3$$^{3+}$** skeleton is 0.12 Å. The bond lengths of ethene bridges are 1.346(6), 1.359(7) and 1.360(7) Å. These bond lengths are longer than typical double bond length (1.34 Å). Additionally, the bond lengths of the methene carbon and the adjacent pyrrole α-carbon employs no bond alternations supporting the aromatic property of **(3-1)H$_3$$^{3+}$**.

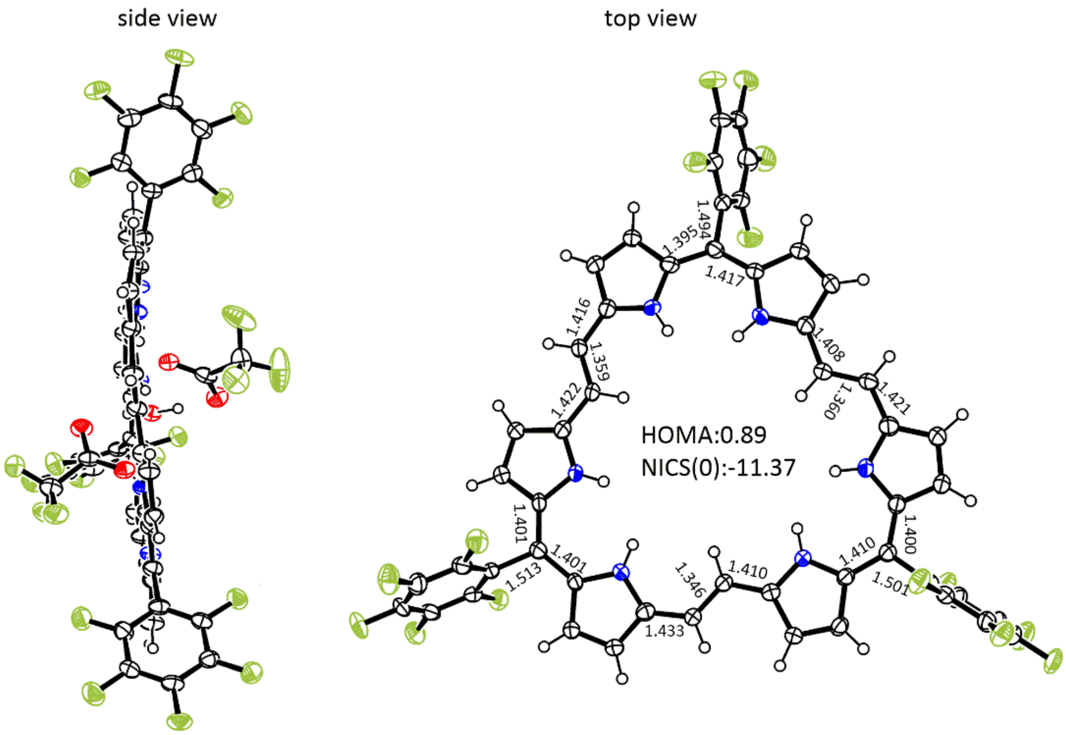

Figure 3.11. X-ray crystal structure and selected bond distances of **(3-1)H$_3$$^{3+}$**. For top view, solvents are omitted for clarity and inserts are HOMA and NICS values. Thermal ellipsoids represent for 50% probability.

In order to evaluate the molecular structure of **3-2**, the DFT calculation was carried out. Two possible molecular conformations of complex **3-2** (two up and one down) and **3-2’** (three up) were optimized at the B3LYP/6-31G*/SDD level with Gaussian 09.[7] The total energy of the asymmetric **3-2** is lower total energy than that of **3-2’** (Figure 3.12). Therefore, rhodium complex form the asymmetric structure consistent with the results of NMR spectroscopy.

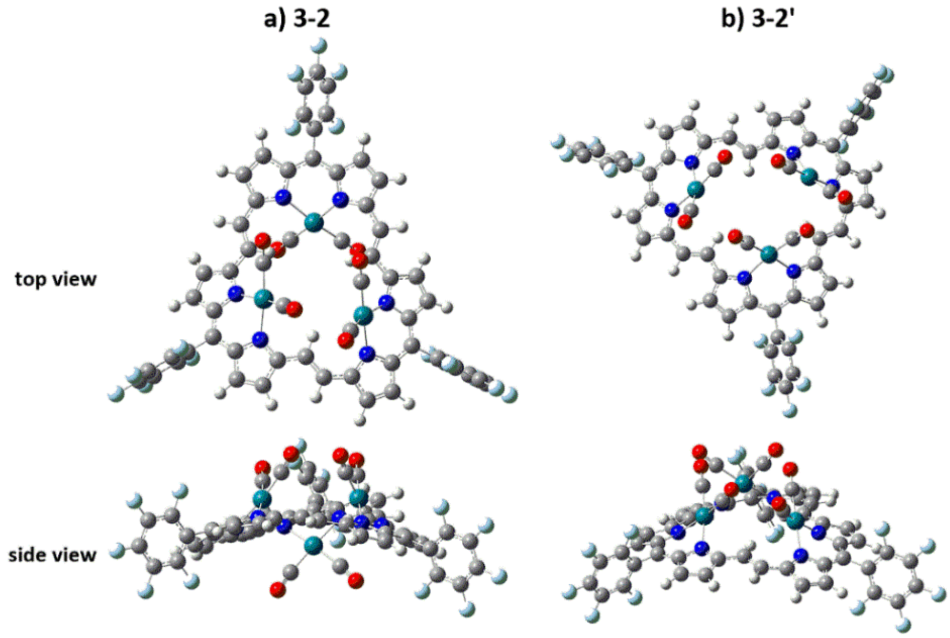

Total energy (hartree)	-4787.31972539	-4787.30889865
Relative energy (kcal/mol)	0	+28.43

Figure 3.12. Optimized structures of **3-2** and **3-2’**. Total energy estimation including zero-point energy correction for **3-2** and **3-2’**, calculated at the B3LYP/6-31G*/SDD level of theory.

3-3 Aromaticity

To interpret aromaticity of **3-1** and **(3-1)H$_3$$^{3+}$** , NICS[8] and HOMA[9] values are calculated. NICS(0) values at various points of **3-1** and **(3-1)H$_3$$^{3+}$** are calculated using the GIAO procedure at the B3LYP/6-31G* level with Gaussian 09 (Figure 3.13). NICS(0) values of center of six nitrogen atoms of **3-1** and **(3-1)H$_3$$^{3+}$** are –7.69 and –11.37 ppm. These negative NICS(0) values indicate strong aromatic properties (Figure 3.13).

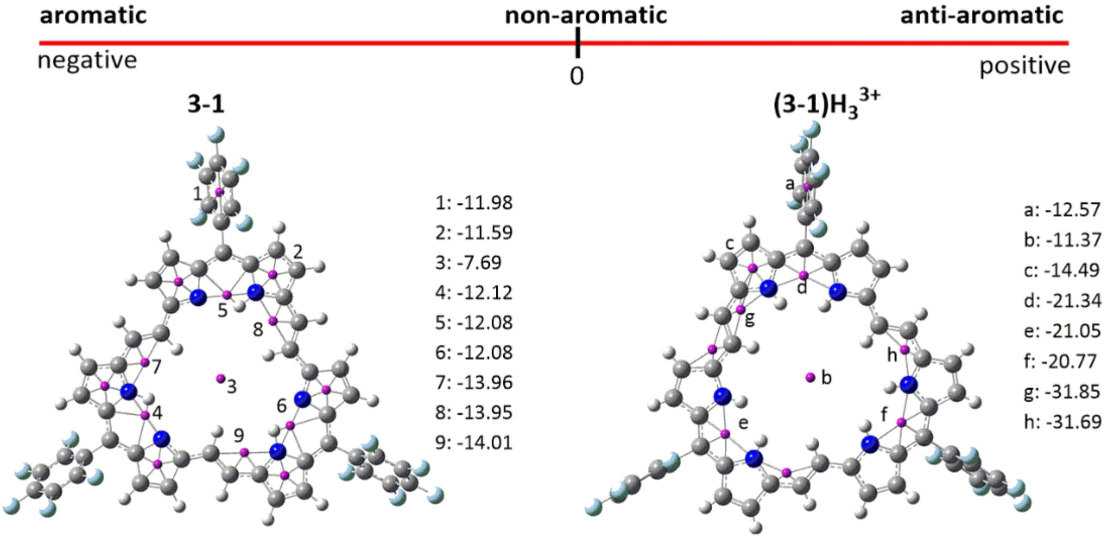

Figure 3.13 NICS(0) values (ppm) of various positions of **3-1** and **(3-1)H$_3$$^{3+}$**, which are calculated at the B3LYP/6-31G* level.

The calculated HOMA values are shown in Figure 3.14 and Figure S3.4. The HOMA values of **(3-1)H$_3$$^{3+}$** are estimated from the conjugated pathway in single crystal and optimized structure (Figure 3.14). The HOMA value of **(3-1)H$_3$$^{3+}$** is 0.89 (Figure 3.14). The HOMA value of **3-1** is 0.74 obtains from optimized structure. These calculated values strongly indicates that **3-1** and **(3-1)H$_3$$^{3+}$** are Hückel aromatic compounds with 30π-electrons.

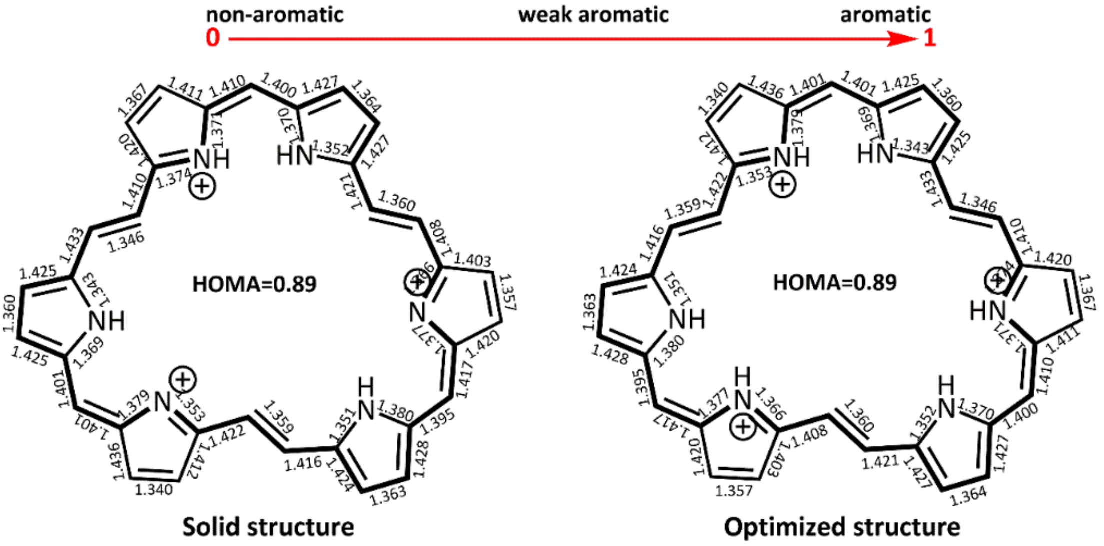

Figure 3.14. Selected bond lengths (Å) and HOMA values of **(3-1)H$_3^{3+}$** in its solid and optimized structures. The optimized structure was calculated at B3LYP/6-31G* level. Bond distances used for HOMA calculations are indicated in bold lines. All aryl groups are omitted for clarity.

The frontier orbitals are obtained by DFT calculations to investigate electronic structures of **3-1**, **(3-1)H$_3^{3+}$** and **3-2**. The frontier orbitals of **3-1**, **(3-1)H$_3^{3+}$** and **3-2** are composed of degenerated HOMO and LUMO levels (Figure 3.15). Additionally, their molecular orbitals are distributed along their macrocyclic rings. These features of electronic properties can be assigned to aromatic properties of **3-1**, **(3-1)H$_3^{3+}$** and **3-2**.[5]

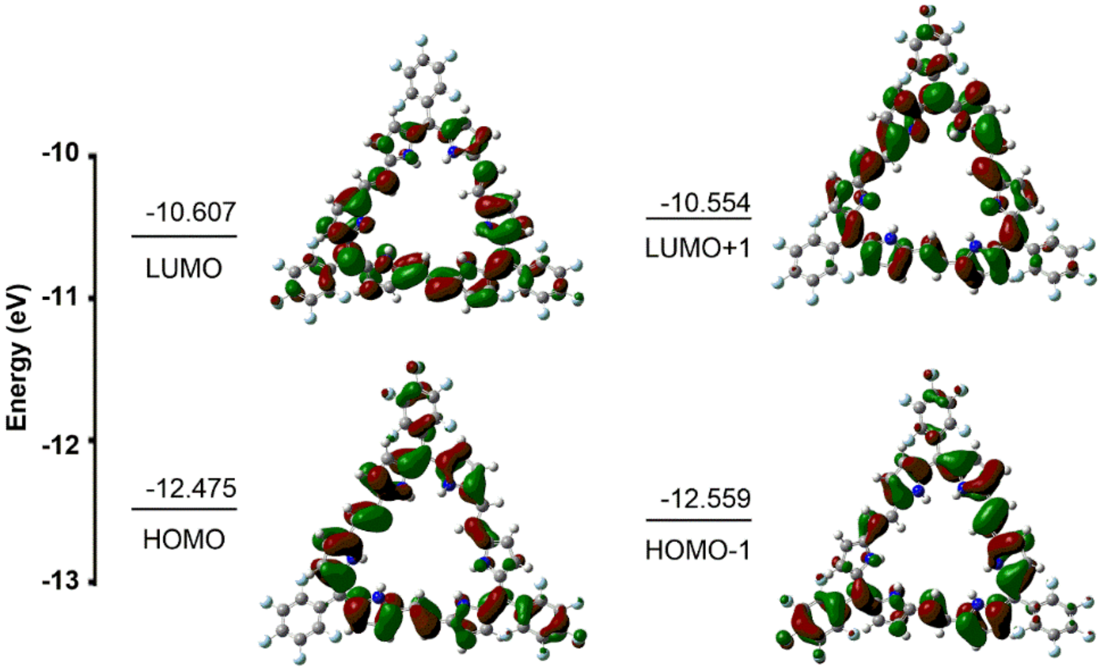

Figure 3.15. Frontier molecular orbital and energy levels of **(3-1)H$_3$$^{3+}$** calculated at the B3LYP/6-31G* level.

3-4 Optical Properties

The absorption spectra of **3-1**, **(3-1)H$_3^{3+}$** and **3-2** in CH_2Cl_2 are shown in Figure 3.16. These three compounds display sharp and intense Soret-like bands and weak Q-like bands in the near-IR region, contributing to aromatic characteristics.[5] The absorption of **3-1** shows an intense band at 541 nm and weak Q-like bands at 685, 798 and 991 nm. The protonated compound **(3-1)H$_3^{3+}$** exhibits red-shifted and sharp absorption bands at 579, 780, 800, 838 and 956 nm. The complex **3-2** also shows an intense and sharp band at 611 nm and weak Q-like bands at 803, 857 and 959 nm.

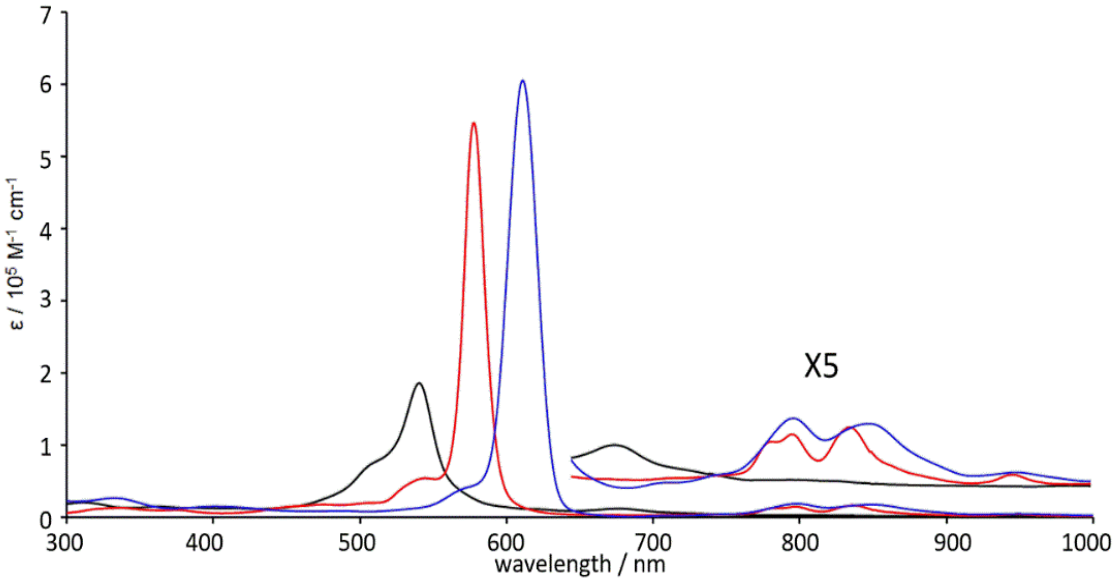

Figure 3.16. The UV-Vis-NIR absorption spectra of **3-1** (black line), **(3-1)H$_3^{3+}$** (red line), and **3-2** (blue line) in CH_2Cl_2.

3-5 Redox Properties

The redox properties of **3-1** and **3-2** are measured by CV in CH_2Cl_2 with 0.1 M $^{n}Bu_4NPF_6$ as an electrolyte (Figure 3.17). Compound **3-1** exhibits a reversible oxidation potential at 0.20 V, and three reduction potentials at –1.22, –1.43 and –1.90 V (vs Fc/Fc^+). Complex **3-2** shows three oxidation potentials at 0.28, 0.51 and 0.69 V, and three reversible reduction potentials at –1.10, –1.42 and –1.82 V (vs Fc/Fc^+). The redox potentials of **3-2** are positively-shifted compared with free base **3-1** because of the electron-withdrawing properties of $Rh(CO)_2$ ligands coordinated on dipyrrin units. These results indicate that the frameworks of hexaphyrin including the rhodium complex can stabilize multi-negative and positive charges.[6,10]

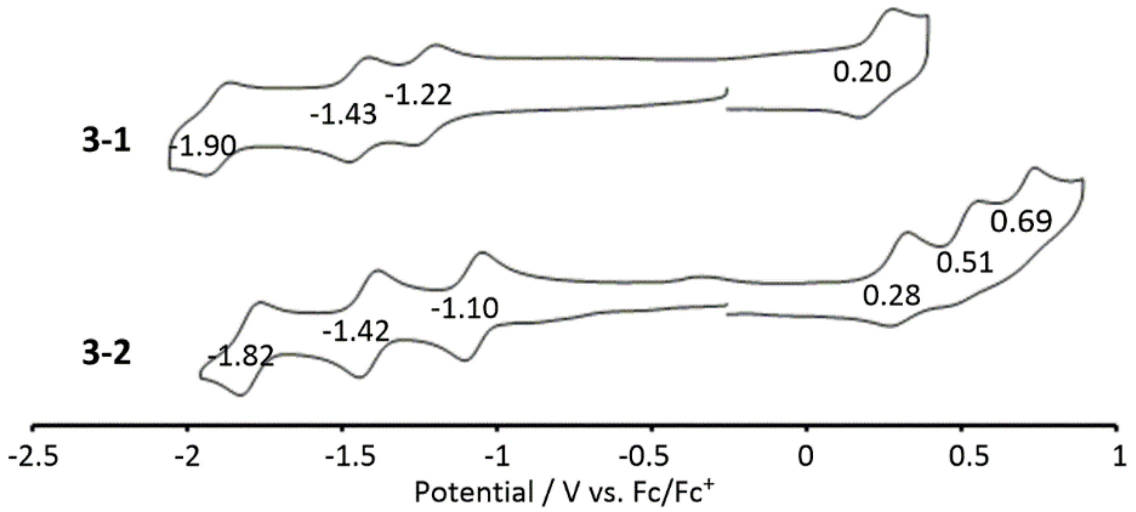

Figure 3.17. CV of **3-1** and **3-2** in CH_2Cl_2 with 0.1 M $^{n}Bu_4NPF_6$. Scan rate = 0.1 V s^{-1}.

3-6 Conclusion

The planar and aromatic *trans*-[30]hexaphyrin(2.1.2.1.2.1) **3-1** is prepared by simple condensation reaction from **DPE** as the simplest double bond sources. The protonated compound **(3-1)**$\mathbf{H_3}^{3+}$ exhibits a highly planar molecular skeleton, as confirmed by X-ray diffraction analysis.

Compound **3-1** can be converted to the tri-nuclear rhodium(I) complex **3-2** in nice yield. This Chapter reveals that the simplest double bond source **DPE** is an effective building block for constructing planar hexaphyrin with extended distance between dipyrrin units to capture multi-metal ions.

3-7 References

[1] (a) E. Vogel, H. Schmickler, *Angew. Chem., Int. Ed.,* **1990***, 29,* 1387; (b) M. Umetani, T. Yoneda, T. Kim, D. Kim, A. Osuka, *Angew. Chem., Int. Ed.,* **2016**, *55*, 8095; (c) T. Yoneda, T. Hoshino, S. Neya, *J. Org. Chem.,* **2017***, 82,* 10737.

[2] D. Kuzuhara, W. Furukawa, A. Kitashiro, N. Aratani, H. Yamada, *Chem. Eur. J.,* **2016***, 22,* 10671.

[3] K. S. Anju, M. Das, B. Adinarayana, C. H. Suresh, A. Srinivasan, *Angew. Chem., Int. Ed.,* **2017***, 56,* 15667.

[4] G. Pagani, A. Berlin, A. Canavesi, G. Schiavon, S. Zecchin, G. Zotti, *Adv. Mater.,* **1996**, *8*, 819.

[5] T. Tanaka, A. Osuka, *Chem. Rev.,* **2017**, *117*, 2584.

[6] J.-I. Setsune, M. Toda, T. Yoshida, *Chem. Commun*., **2008**, *12*, 1425.

[7] Gaussian 09, Revision B.01, M. J. Frisch, G. W. Trucks, H. B. Schlegel, G. E. Scuseria, M. A. Robb, J. R. Cheeseman, G. Scalmani, V. Barone, B. Mennucci, G. A. Petersson, H. Nakatsuji, M. Caricato, X. Li, H. P. Hratchian, A. F. Izmaylov, J. Bloino, G. Zheng, J. L. Sonnenberg, M. Hada, M. Ehara, K. Toyota, R. Fukuda, J. Hasegawa, M. Ishida, T. Nakajima, Y. Honda, O. Kitao, H. Nakai, T. Vreven, J. A. Montgomery, Jr., J. E. Peralta, F. Ogliaro, M. Bearpark, J. J. Heyd, E. Brothers, K. N. Kudin, V. N. Staroverov, T. Keith, R. Kobayashi, J. Normand, K. Raghavachari, A. Rendell, J. C. Burant, S. S. Iyengar, J.

Tomasi, M. Cossi, N. Rega, J. M. Millam, M. Klene, J. E. Knox, J. B. Cross, V. Bakken, C. Adamo, J. Jaramillo, R. Gomperts, R. E. Stratmann, O. Yazyev, A. J. Austin, R. Cammi, C. Pomelli, J. W. Ochterski, R. L. Martin, K. Morokuma, V. G. Zakrzewski, G. A. Voth, P. Salvador, J. J. Dannenberg, S. Dapprich, A. D. Daniels, O. Farkas, J. B. Foresman, J. V. Ortiz, J. Cioslowski, D. J. Fox, Gaussian, Inc., Wallingford CT, 2010.

[8] P. v. R. Schleyer, C. Maerker, A. Dransfeld, H. Jiao, N. R. v. E. Hommes, *J. Am. Chem. Soc.,* **1996***, 118,* 6317.

[9] T. M. Krygowski, *J. Chem. Inf. Comput. Sci.,* **1993**, *33*, 70.

[10] K. Naoda, H. Mori, N. Aratani, B. S. Lee, D. Kim, A. Osuka, *Angew. Chem., Int. Ed.,* **2012**, *51*, 9856.

3-8 Supporting Information

Spectroscopy Absorption spectra were measured with a JASCO UV/VIS/NIR Spectrophotometer V-670. ^{1}H NMR and ^{19}F NMR spectra were recorded on a JNM-ECX 400 spectrometers (operating as 400 MHz for ^{1}H and 376 MHz for ^{19}F) using the residual solvent as the internal reference for ^{1}H ($\delta = 7.26$ ppm in $CDCl_3$, $\delta = 5.95$ ppm in $C_2D_2Cl_4$) and CF_3COOH as the external reference for ^{19}F ($\delta = -76.5$ ppm). HR−MALDI−TOF mass spectrum was recorded on a Bruker Daltonics autoflex MALDI−TOF MS spectrometer. Infrared spectra were measured on KBr pellets using a JASCO FT/IR−4200 spectrometer. CV and DPV measurements were conducted in a solution of 0.1 M $TBAPF_6$ in dry dichloromethane with a scan rate of 0.1 V s^{-1} in an argon-filled cell. A glassy carbon electrode and a platinum wire were used as a working and a counter electrode, respectively. A $Ag/AgNO_3$ electrode was used as reference electrodes, which were normalized with the half-wave potential of ferrocene/ferrocenium (Fc/Fc^+) redox couple.

X−ray Analysis X−ray crystallographic data for **(3-1)H$_3$$^{3+}$** were recorded at 103 K on a Rigaku R−AXIS RAPID/S using Mo−Kα radiation from the corresponding set of confocal optics. The structures were solved by direct methods and refined on F^2 by full−matrix least−squares using the CrystalClear and SHELXS−2000 program. CCDC: 1501618 contains the supplementary crystallographic data for **(3-**

1)H$_3^{3+}$. These data can be obtained free of charge from the Cambridge Crystallographic Data Centre via www.ccdc.cam.ac.uk/data_request/cif.

Theoretical calculations. All density functional theory calculations were achieved with the Gaussian 09 program package. The geometry of **3-1** and **(3-1)H$_3^{3+}$** were optimized at the Becke's three-parameter hybrid functional combined with the Lee−Yang−Parr correlation functional abbreviated as the B3LYP level of density functional theory with 6-31G(d) basis set. The geometry of **3-2** was optimized at the B3LYP level of density functional theory with 6−31G(d)/SDD basis set.

Materials All solvents and chemicals were reagent grade quality, obtained commercially and used without further purification except as noted. For spectral measurements, spectral grade dichloromethane was purchased from Nakalai Tesque Co. Thin−layer chromatography (TLC) and flush column chromatography were performed on Art. 5554 (Merck KGaA) and Silica Gel 60N (Kanto Chemical Co.).

Synthesis of DPE:

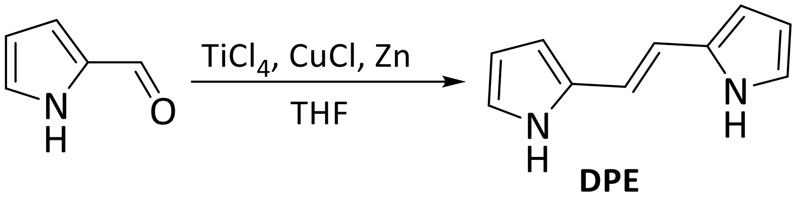

Activated zinc powder (16.4 g, 251 mmol) and CuCl (1.7 g, 17 mmol) in THF (300 mL) were combined in a three-neck round bottomed flask, and the reaction mixture was bubbled with argon for 5 minutes. The reaction mixture was cooled to 0°C, and then $TiCl_4$ (14 ml, 127 mmol) was slowly added at which the temperature maintained at 0°C. The reaction mixture was allows to warm to room temperature for 30 min, and then heated at reflux for 2 hours. After the mixture was once again cooled to 0°C, a solution of the 2-pyrrolecarbaldehyde (5.xx g, 53 mmol) in THF (40 mL) was added dropwise slowly. The reaction mixture was heated at reflux for 1 hour. The reaction mixture was careful quenched by the addition of a 10% aqueous NaOAc solution, and the resulting mixture was extracted with CH_2Cl_2. The combined organic layer was washed with water and brine. The organic phase was dried over anhydrous Na_2SO_4. After removal of the solvent, the crude product was purified by silica gel column chromatography (ethyl acetate/*n*-hexane=1/3) to give the *Z*-isomer in 2% (90 mg, 0.57 mmol) and *E*-isomer (**DPE**) in 19% (800 mg, 5.1 mmol), respectively.

DPE: ^{1}H NMR (400 MHz, $CDCl_3$, 298 K): $\delta = 8.51$ (s, 2H, NH), 6.75 (d, $J = 4$ Hz, 2H, pyrrole), 6.32 (d, $J = 4$ Hz, 2H, pyrrole), 6.22 (m, 2H, pyrrole), 6.19 (s, 2H, ethene) ppm.

Synthesis of 3-1:

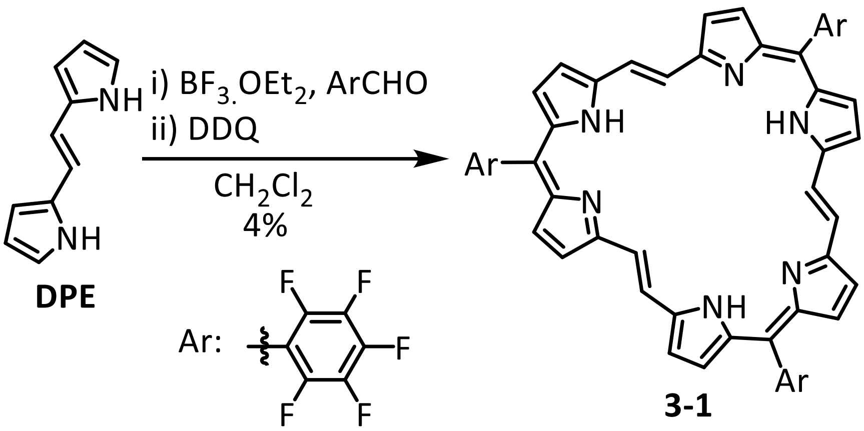

Pentafluorobenzaldehyde (390 mg, 2.0 mmol) and **DPE** (316 mg, 2.0 mmol) were dissolved in dry CH_2Cl_2 (150 mL) under an argon atmosphere. The mixture was stirred for 5 min, and then BF_3•OEt_2 (6 ul, 0.06 mmol) was added to the reaction mixture. After stirring for 2 hours at room temperature in dark, DDQ (454 mg, 2.0 mmol) was added to the reaction mixture for 1 hour. The solvent was removed under a reduced pressure. The residue was purified by silica gel column chromatography (CH_2Cl_2 / ethyl acetate = 10 / 1). The obtained purplish red solid was rinsed with methanol to give **3-1** in 4% (26 mg, 0.026 mmol).

3-1: UV-Vis-NIR (CH_2Cl_2) λ [nm] (ε [M^{-1} cm^{-1}]): 541 (173400), 685 (11500), 798 (2600) and 991 (1500) nm. HR-MALDI-MS: calcd. for $C_{51}H_{21}F_{15}N_6$: 1002.1588 $[M]^+$, Found: 1002.1590. ^{1}H and ^{19}F NMR could not be recorded because of poor solubility in common organic solvents even in high temperatures.

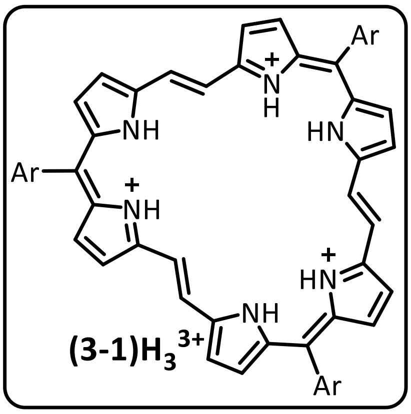

(3-1)H$_3$$^{3+}$: UV-Vis-NIR (CH$_2Cl_2$+TFA) λ [nm] (ε [M^{-1} cm^{-1}]): 579 (546800), 780 (12350), 800 (14100), 838 (15700) and 956 (4500) nm. ^{1}H NMR (400 MHz, CDCl$_3$, 298K): δ = 13.8 (brs, 3H), 11.5 (brs, 3H), 10.7 (brs, 3H), 10.4 (brs, 6H), –2.5 (brs, 6H), –6.5 (brs, 3H) ppm. ^{19}F NMR (376 MHz, CDCl$_3$, 298K): δ = –136.09 (d, 6F), –146.79 (s, 3F), –159.05 (s, 6F) ppm.

Synthesis of 3-2:

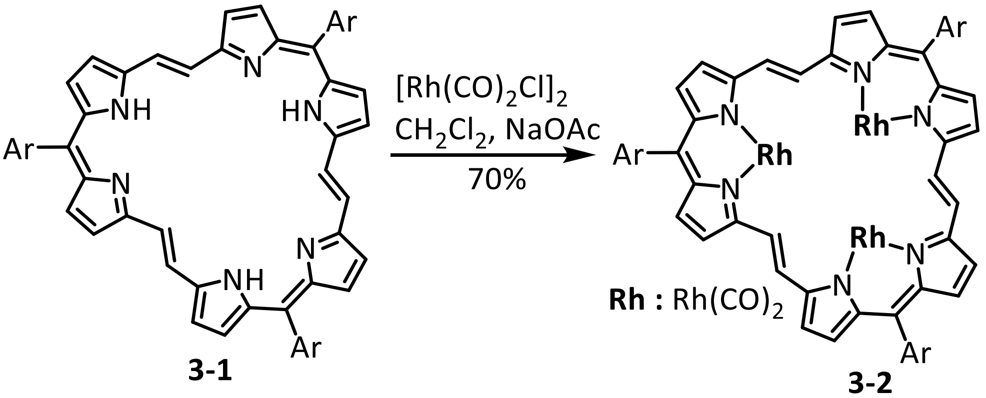

The anhydrous NaOAc (16 mg, 0.20 mmol) and [Rh(CO)$_2$Cl]$_2$ (39 mg, 0.10 mmol) were adde to solution of **3-1** (10 mg, 0.01 mmol) in dry-CH$_2$Cl$_2$ (150 mL). The resulting mixture was refluxed for overnight under an argon atmosphere. The solvent was removed under a reduced pressure and the residue was purified by silica gel column chromatography (CH_2Cl_2 / *n*-hexane = 1 / 2). The deep green fraction was collected to afford complex **3-2** as a deep-red solid in 70% yield (10 mg, 0.07 mmol).

3-2: UV-Vis-NIR (CH_2Cl_2) λ [nm] (ε [M^{-1} cm^{-1}]): 611 (628300), 803 (19130), 857 (17190) and 959 (4500) nm. ^{1}H NMR (400 MHz, CD_2Cl_2, 273 K): δ = 13.17 (d, J = 15.2 Hz, 1H, ethene), 13.09 (m, 2H, ethene), 11.02 (d, J = 4.4 Hz, 1H, pyrrole), 10.69 (d, J = 4.4 Hz, 1H, pyrrole), 10.39 (d, J = 4.4 Hz, 1H, pyrrole), 9.82 (d, J = 3.6 Hz, 1H, pyrrole), 9.78 (d, J = 3.6 Hz, 1H, pyrrole), 9.63 (d, J = 4.4 Hz, 1H, pyrrole), 9.53 (d, J = 4.4 Hz, 1H, pyrrole), 9.28 (d, J = 4.4 Hz, 1H, pyrrole), 9.09 (d, J = 3.6 Hz, 1H, pyrrole), 9.07 (d, J = 4.4 Hz, 1H, pyrrole), 8.99 (d, J = 4.4 Hz, 1H, pyrrole), 8.97 (d, J = 4.4 Hz, 1H, pyrrole), –5.08 (d, J = 15.6 Hz, 1H, ethene), –5.19 (d, J = 7.6 Hz, 1H, ethene), –5.23 (d, J = 6.4 Hz, 1H, ethene) ppm. ^{19}F NMR (376 MHz, $CDCl_3$, 298K): δ = –111.85 (d, 1F), –112.16 (m, 2F), –113.20 (d, 2F), –113.68 (d, 1F), –127.40 (m, 3F), –137.78 (m, 6F) ppm. IR (KBr): $V_{c=o}$ = 2074.32 and 2010.43 cm^{-1}. HR-MALDI-MS: calcd. for $C_{57}H_{18}F_{15}N_6O_6Rh_3$: 1475.8213 $[M]^+$, Found: 1475.8239.

Supporting figures

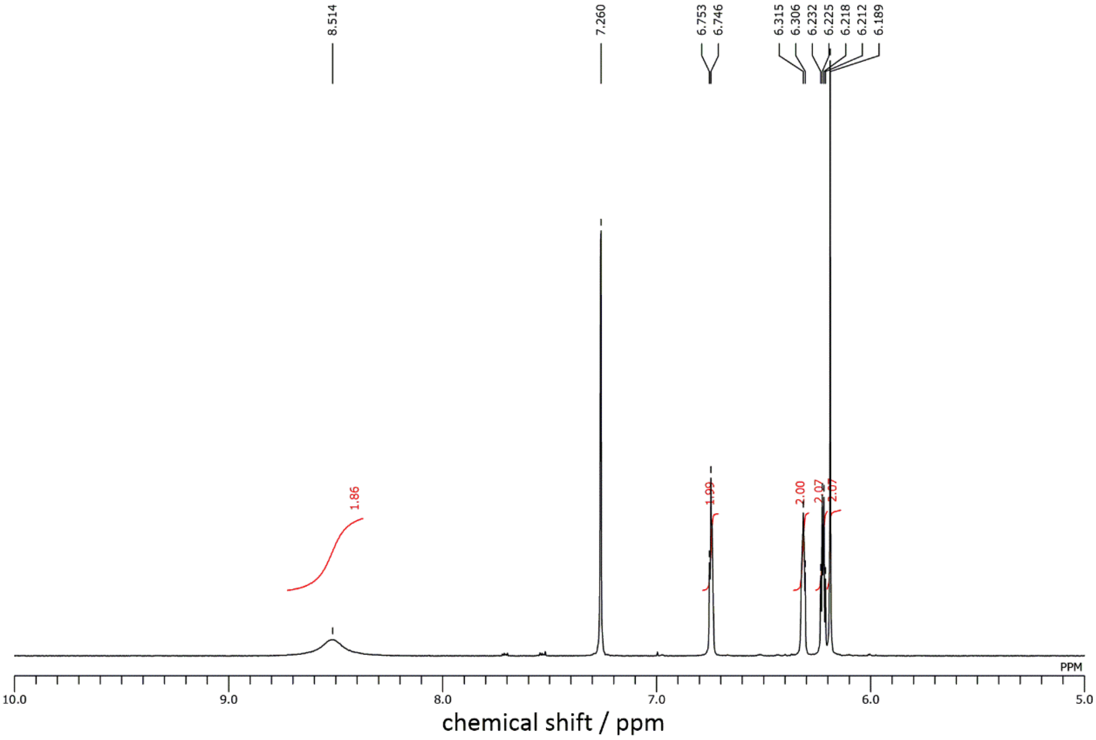

Figure S3.1. ^{1}H NMR spectrum of **DPE** in $CDCl_3$.

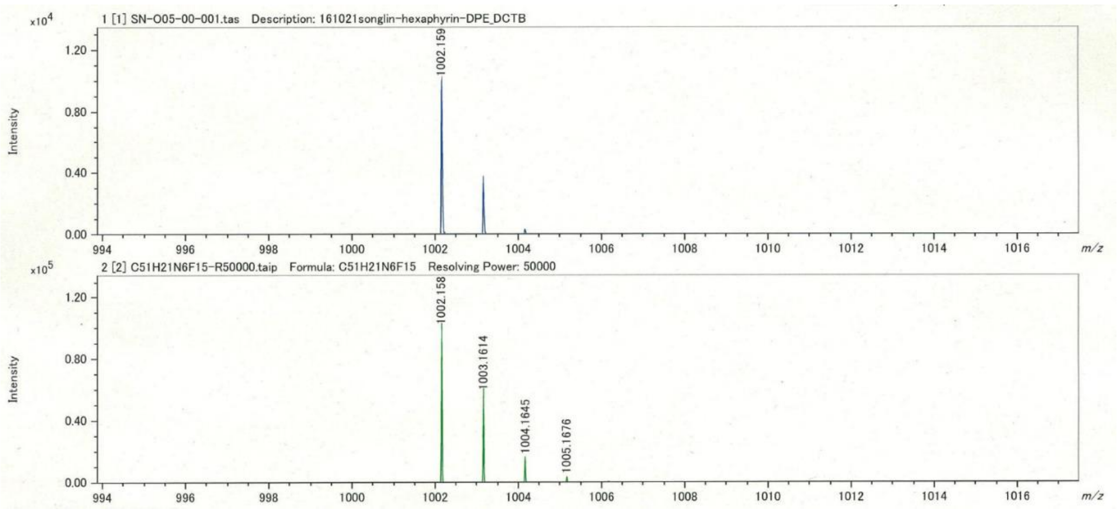

Figure S3.2. HR-MALDI-MS spectrum of **3-1.**

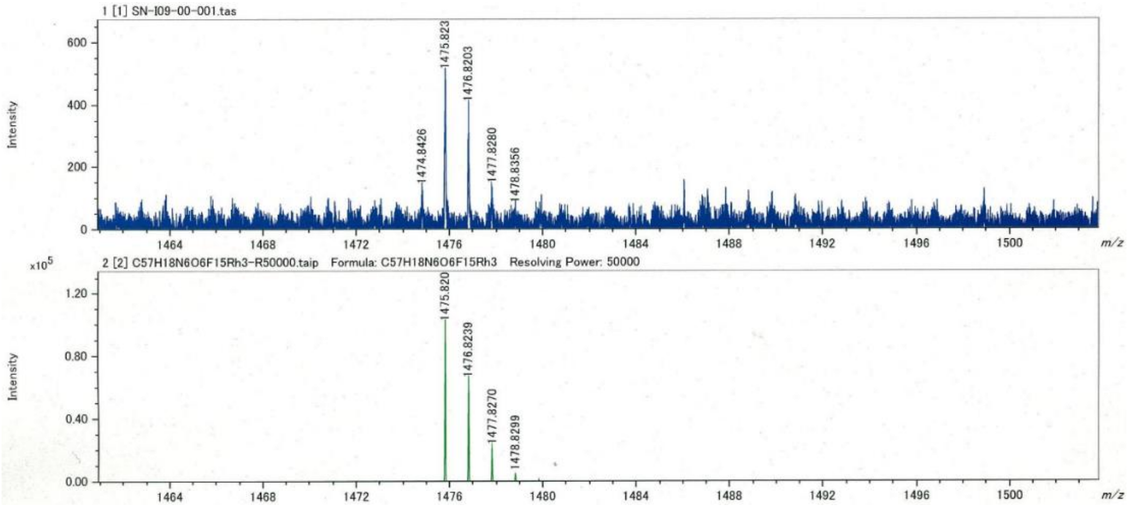

Figure S3.3. HR-MALDI-MS spectrum of **3-2**.

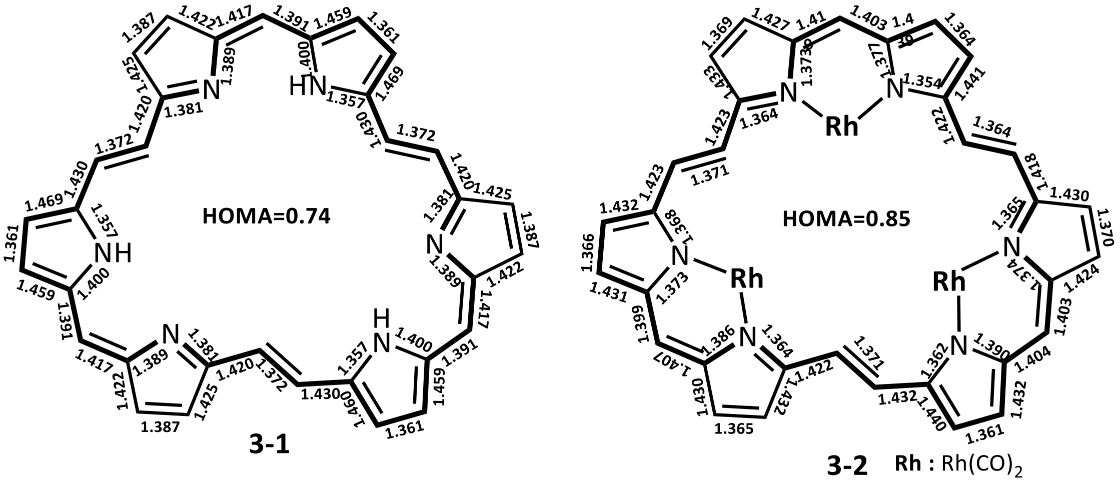

3-1

3-2 **Rh :** Rh(CO)$_2$

Figure S3.4. Selected bond lengths (Å) and HOMA values of **3-1** and **3-2** in their optimized structures which were calculated at B3LYP/6-31G* and B3LYP/6-31G*/SDD levels respectively. The bonds used for HOMA calculations are indicated in bold lines. All aryl groups are omitted for clarity.

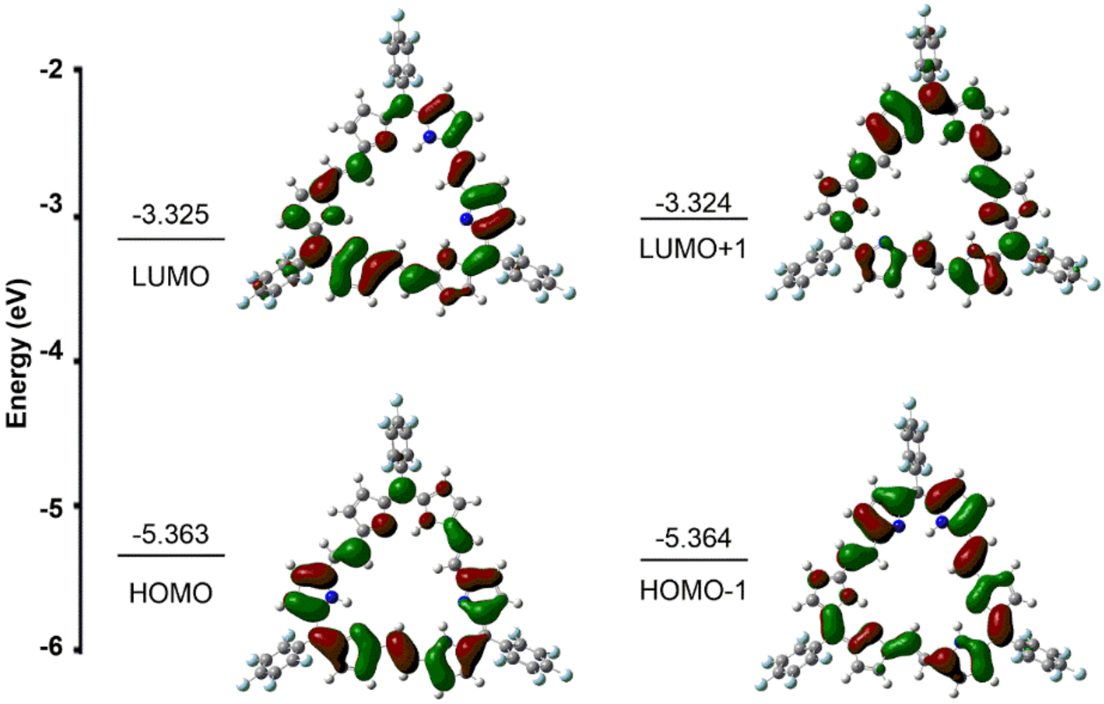

Figure S3.5 Frontier molecular orbital and energy levels of **3-1** calculated at the B3LYP/6-31G* level of theory.

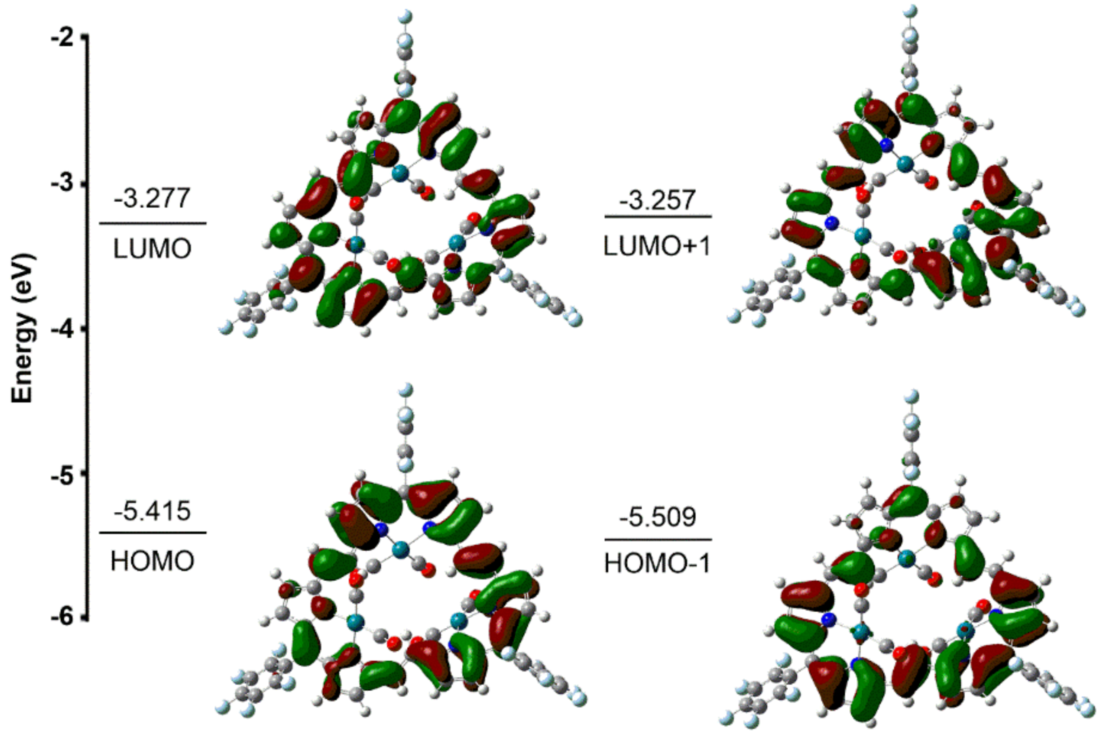

Figure S3.6 Frontier molecular orbital and energy levels of **3-2** calculated at the B3LYP/6-31*/SDD level of theory.

Table S3.1. Crystal data and structure refinement of (3-1)H_3^{3+}.

Empirical formula	$C_{60}H_{27.50}F_{28.50}N_6O_{10}$	
Formula weight	1533.88	
Temperature	103(2) K	
Wavelength	0.71075 Å	
Crystal system	Monoclinic	
Space group	*C*2/*c*	
Unit cell dimensions	a = 34.2288(7) Å	
	b = 19.4470(4) Å	β = 114.932(8)°
	c = 21.3581(5) Å	
Volume	12892.0(9) $Å^3$	
Z	8	
Density (calculated)	1.581 Mg/m^3	
Absorption coefficient	0.162 mm^{-1}	
F(000)	6128	
Crystal size	0.110 x 0.060 x 0.040 mm^3	
Theta range for data collection	3.113 to 25.350°	
Index ranges	$-41 \le h \le 41, -23 \le k \le 23, -25 \le l \le 25$	
Reflections collected	87306	
Independent reflections	11758 [*R*(int) = 0.0968]	
Completeness to theta = 25.242°	99.6%	
Max. and min. transmission	1.000 and 0.5711	
Refinement method	Full-matrix least-squares on F^2	
Data / restraints / parameters	11758 / 17 / 1003	

Goodness-of-fit on F^2	1.066
Final R indices [$I > 2.00\sigma(I)$]	$R_1 = 0.0863$
R indices (all data)	$wR_2 = 0.2450$
Largest diff. peak and hole	1.195 and –0.475 e.Å^{-3}

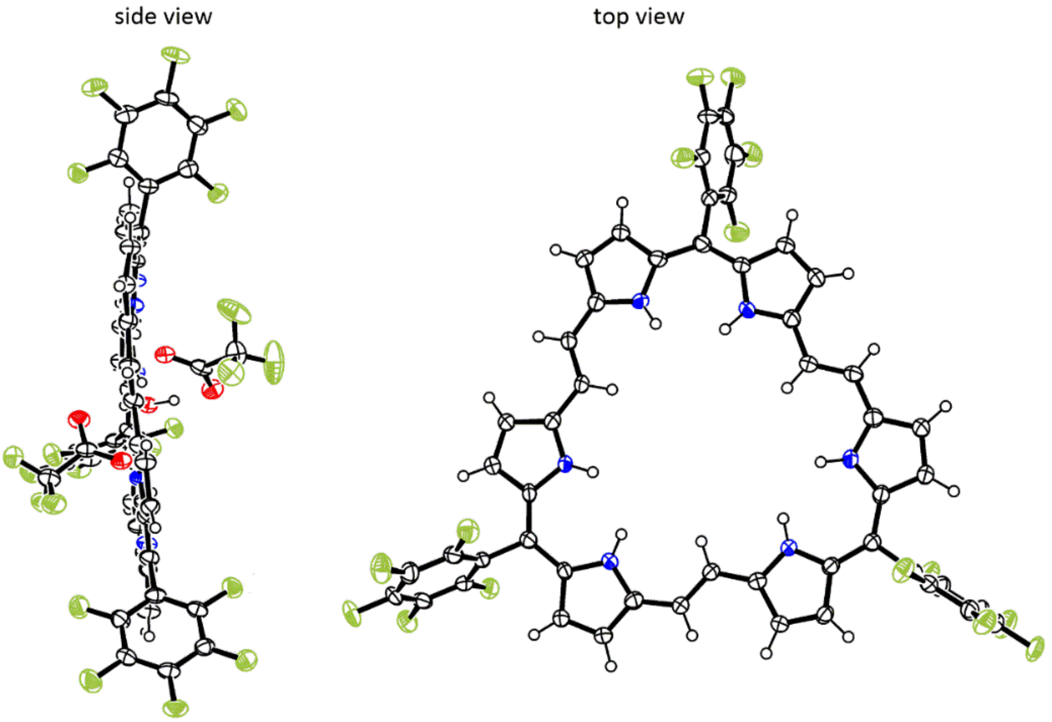
side view

top view

Figure S3.7. X-ray crystal structure of **(3-1)H$_3$$^{3+}$**. Thermal ellipsoids represent for 50% probability. For top view, all solvents are omitted for clarity

Chapter 4

Porphyrins with Dimethyl Vinylene-Bridges

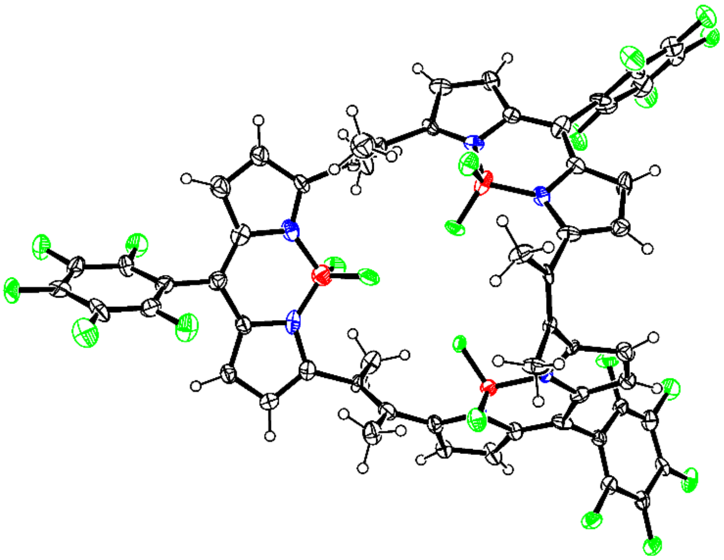

In this Chapter, the synthesis, characterization and optical properties of boron hexaphyrin (2.1.2.1.2.1) complexes with dimethyl vinylene-bridges are described.

4-1 Introduction

Boron-dipyrromethenes (**BODIPY**s), which are well-known as powerful fluorescent dye with intense emission bands, high fluorescence quantum efficiency and efficient photochemical stability in ambient atmosphere, has been attracting great attention in decades (Figure 4.1). [1] Among BODIPY dyes, the cyclic BODIPY macrocycles show special optical properties like unique luminescent and lasing properties, cation recognition and switchable near-IR photoproperties.[1d, 2] However, they have been little-studied because of limitation of efficient synthesis method and screening of suitable ligands.

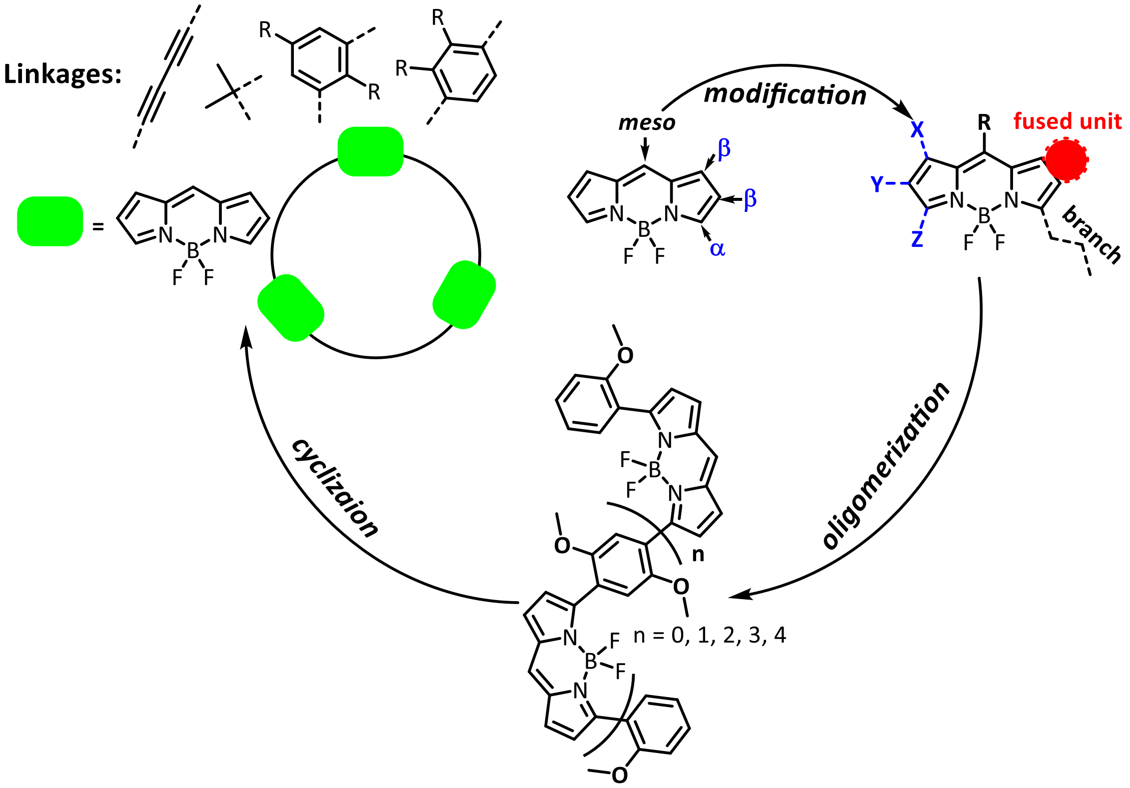

Figure 4.1. Synthetic strategy of functional **BODIPYs.**

In the previous Chapters 2 and 3, two hexaphyrins(2.1.2.1.2.1) **2-4** and **3-1** were synthesized including alternate dipyrrins and vinylene bridges. Generally, BODIPY is prepared from dipyrrin units. Therefore, hexaphyrins(2.1.2.1.2.1) can work as possible platforms to prepare the cyclic BODIPYs and investigate the structure-dependent optical properties. However, boron complexation of **2-4** and **3-1** failed (Scheme 4.1) and only the mono-boron complex of **2-4** was detected. Considering molecular structures, the causes of failure are considered as the strong steric effect of diphenyl rings at vinylene bridges of **2-4** and the poor solubility of highly planar **3-1**. On the other hand, cyclization of dibromo-BODIPY was examined by the Pd-catalyzed Stille coupling. However, this method did not also work because low selectivity of cyclization (Scheme 4.1).

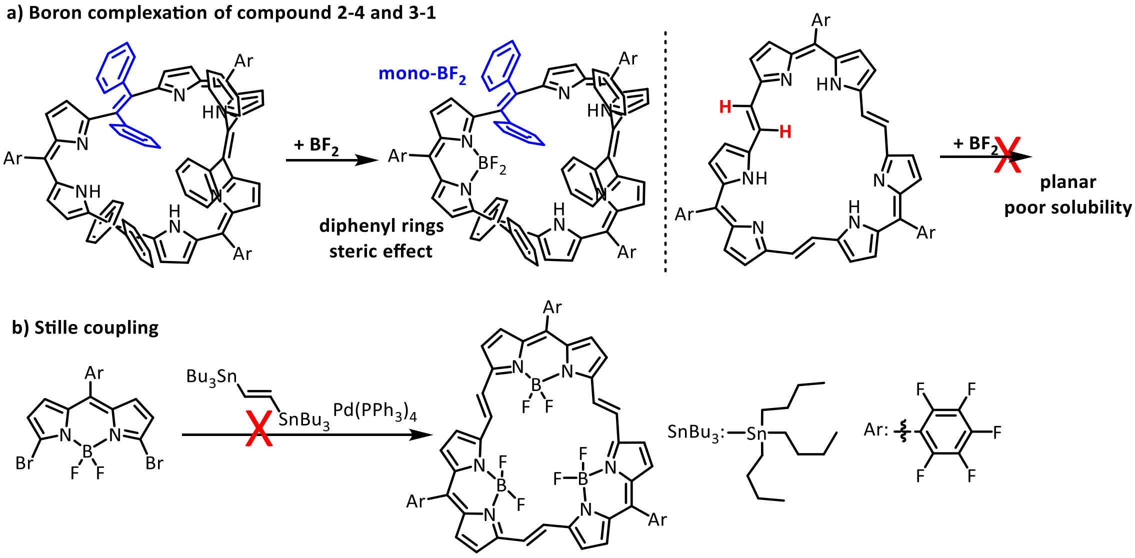

Scheme 4.1. a) Boron complexation of **2**-4 and **3-1**, b) Stille-coupling for cyclic BODIPY macrocycle.

In this context, hexaphyrin(2.1.2.1.2.1) with suitable substituted groups at vinylene-bridges should be developed. The *E-/Z*-dimethyldipyrrolylethene **(DMeDPEs)** is selected because methyl group is smaller than phenyl group, which may reduce the steric effects and induce good solubility (Scheme 4.2). Hexaphyrin(2.1.2.1.2.1) **4-2** was obtained by a condensation reaction from **DMeDPEs** and C_6H_5CHO under acidic conditions. The X-ray crystallography revealed that **4-2** has a twisted molecular structure and three dipyrrin-type coordination sites in its cavity. By boron complexations, five BODIPY macrocycles were successfully obtained, namely **1BF$_2$**, **2BF$_2$-a**, **2BF$_2$-b**, **3BF$_2$-a** and **3BF$_2$-b**. Interestingly, the X-ray crystal structure analysis revealed that **1BF$_2$**, **2BF$_2$-a**, **2BF$_2$-b**, **3BF$_2$-a** show twisted molecular structures the same as free-base **4-2**, while **3BF$_2$-b** shows a co-planar structure. The detailed synthesis, optical properties, electrochemical properties, crystal structures and DFT calculation of BODIPY macrocycles will be presented in this Chapter.

4-2 Synthesis

The detail of the synthetic scheme is shown in Scheme 4.2. The key starting materials **DMeDPE**s are synthesized via an established method.[3] As a result of Chapter **2**, **DPhDPE**s gave the same expanded porphyrins under condensation reactions. Therefore, *Z*- and *E*- isomers of **DMeDPE**s are not separated and are used as the mixture. Condensation reaction of **DMeDPE**s with C_6F_5CHO in the presence of BF_3•OEt_2 in dry-CH_2Cl_2 and the following oxidation with DDQ afforded three expanded porphyrins **4-1, 4-2** and **4-3** in 1%, 6% and 3% yields, respectively. The HR-MALDI-MS detect corresponding molecular ion peaks of **4-1** at *m*/*z* = 724.1683 (calcd. for $C_{38}H_{22}F_{10}N_4$ = 724.1685 [*M*]$^+$), **4-2** at *m*/*z* = 1086.2522 (calcd. for $C_{57}H_{33}F_{15}N_6$ = 1086.2527 [*M*]$^+$) , **4-3** at *m*/*z* = 1448.3364 (calcd. for $C_{76}H_{44}F_{20}N_8$ = 1448.3370 [*M*]$^+$).

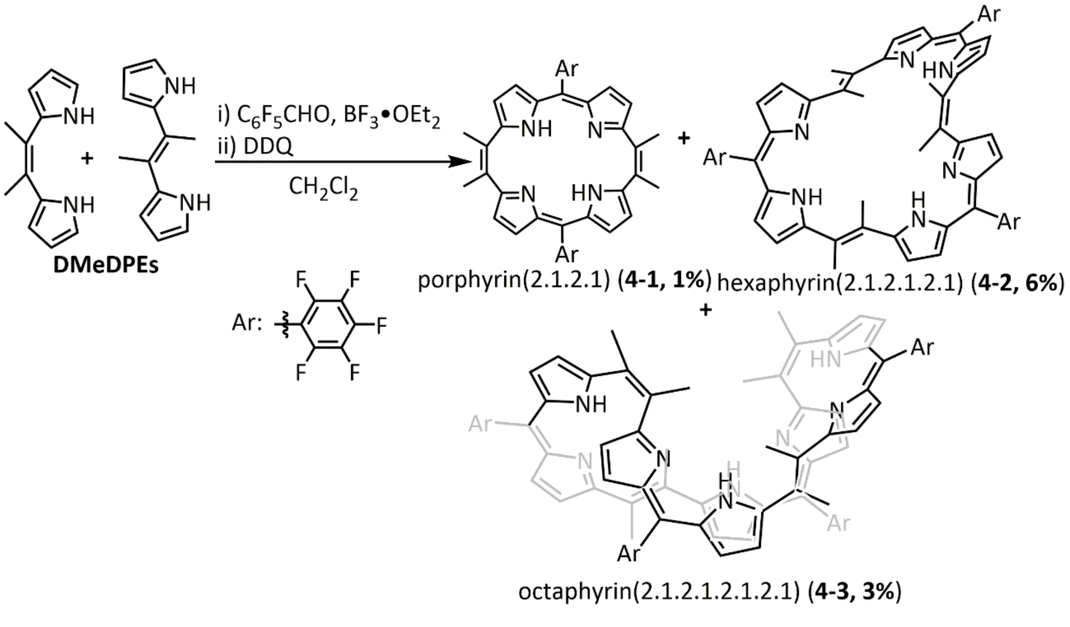

Scheme 4.2. Synthesis of compounds **4-1, 4-2** and **4-3**.

The structures of expanded porphyrins in solution are investigated by ^{1}H NMR and ^{19}F NMR spectroscopy. Compound **4-1** shows a broad and weak peak at 11.9 ppm assigned to the NH protons. Two doublet peaks at 6.23 and 6.21 ppm are assigned to pyrrolic *β*-position protons. The singlet peak at 2.16 ppm is assigned to protons of four methyl groups. For compound **4-3**, the broad peaks at 6.43, 6.34, 6.32 and 6.23 ppm are assigned to pyrrolic *β*-position protons. The two singlet peaks at 2.23 and 2.29 ppm are assigned to protons of six methyl groups. Besides, compound **4-3** shows a broad and weak peak at 12.49 ppm assigned to NH protons.

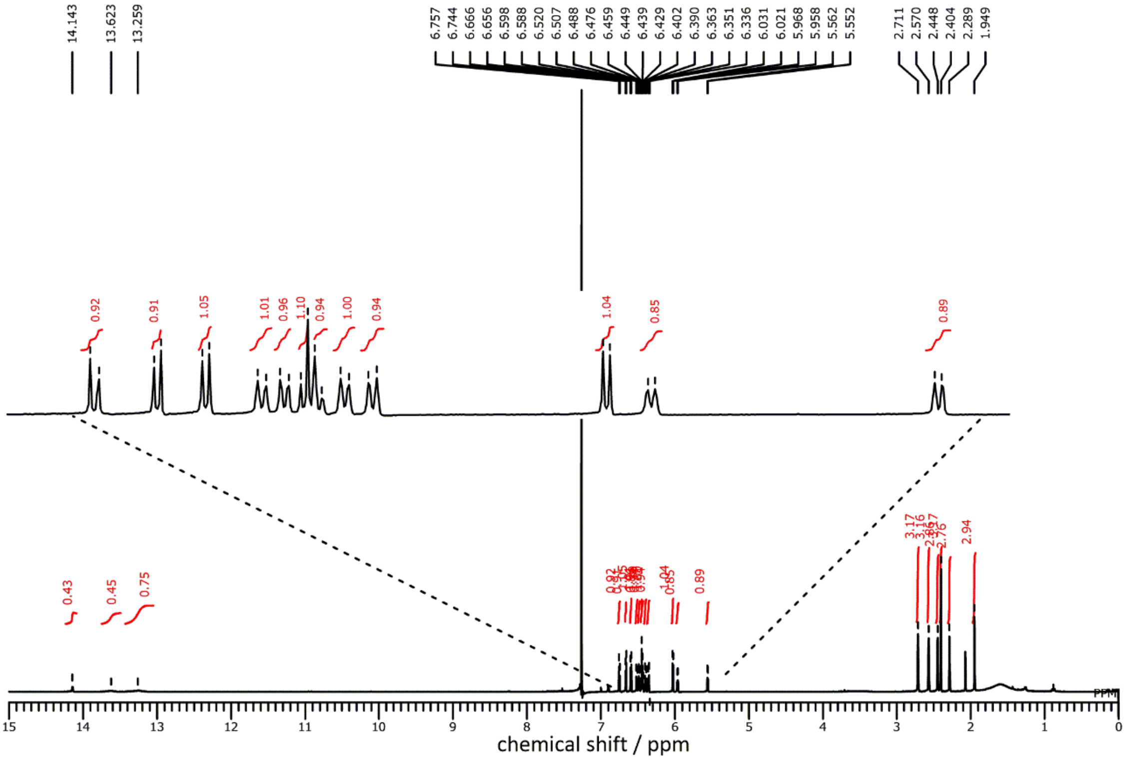

Figure 4.2. ^{1}H NMR spectrum of **4-2** in CDCl$_3$.

^{1}H NMR spectrum of **4-2** shows clear information of the asymmetric molecular structure (Figure 4.2). The ^{1}H NMR spectrum shows twelve doublet peaks assigned to twelve pyrrolic *β*-position protons and six singlet peaks assigned to six methyl groups. Additionally, the chemical shift of protons without remarkably up-/down-field shift suggests non-aromatic properties of all expanded porphyrins.[4]

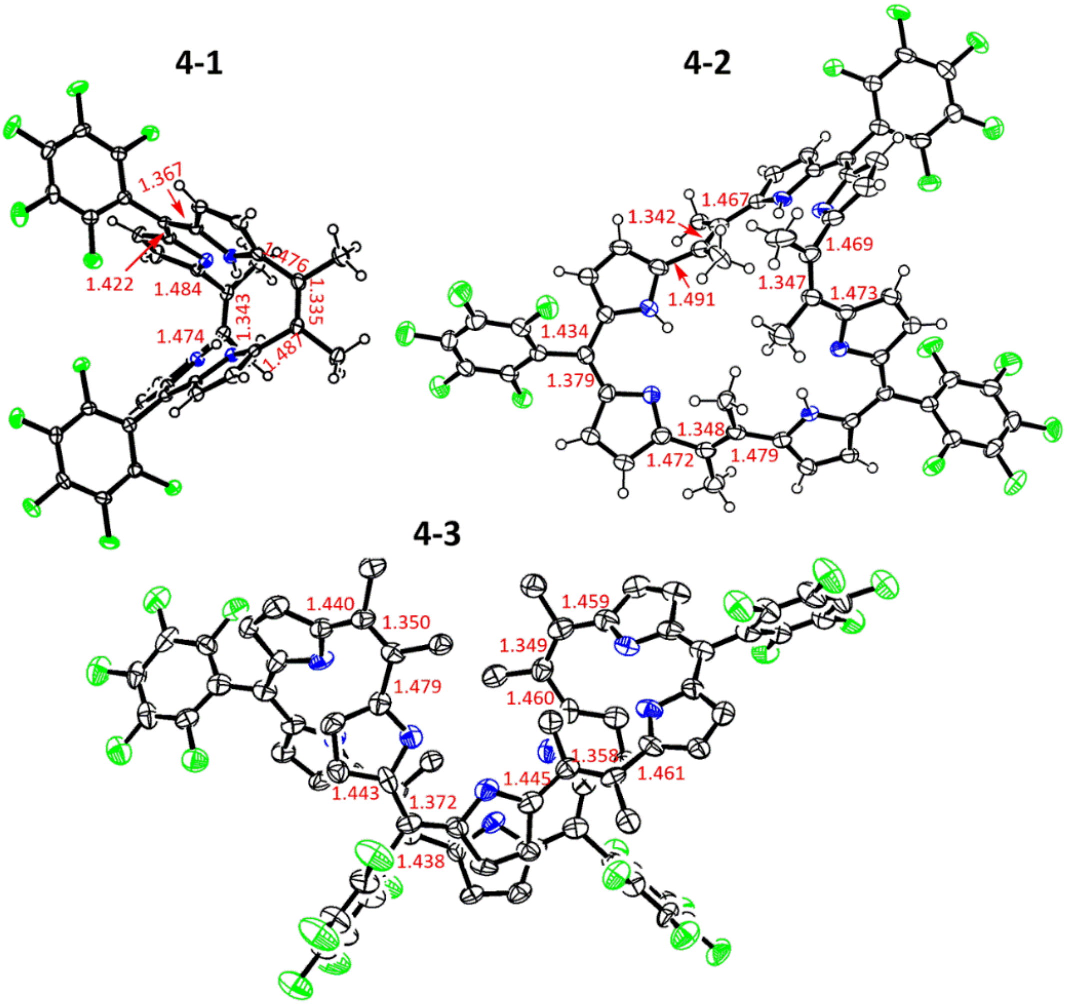

Figure 4.3. X-ray crystal structures and selected distances of **4-1, 4-2** and **4-3**. The thermal ellipsoids represent for 50% probability. Hydrogens atoms of compound **4-3** are omitted for clarity.

The solid-state structures of three porphyrins have unambiguously been determined by X-ray single crystal structure analysis (Figure 4.3). Compound **4-1** shows a saddle-shaped structure consisting with *cis*-conformations of dimethyl vinylene-bridges the same as compound **2-3** (in Chapter 2). Compound **4-2** has one *cis*- and two *trans*-conformations at dimethyl vinylene-bridges, resulting in the formation of twisted macrocyclic structures.

Compound **4-3** has a saddle-shaped twisted molecular structure consisting of two *cis*- and two *trans*- conformations at dimethyl vinylene-bridges. The bond lengths of vinylene-bridges are 1.343 and 1.335 Å for **4-1**, 1.342, 1.347 and 1.348 Å for **4-2,** and 1.350, 1.349, 1.359 and 1.372 for **4-3** (Figure 4.3). The bond lengths of the methene carbon and the adjacent pyrrole *β*-carbon clearly show bond alternations (Figure 4.3). These features of bond lengths indicate the lack of contributions of the macrocyclic aromatic properties because of highly twisted molecular structures of obtained expanded porphyrins.

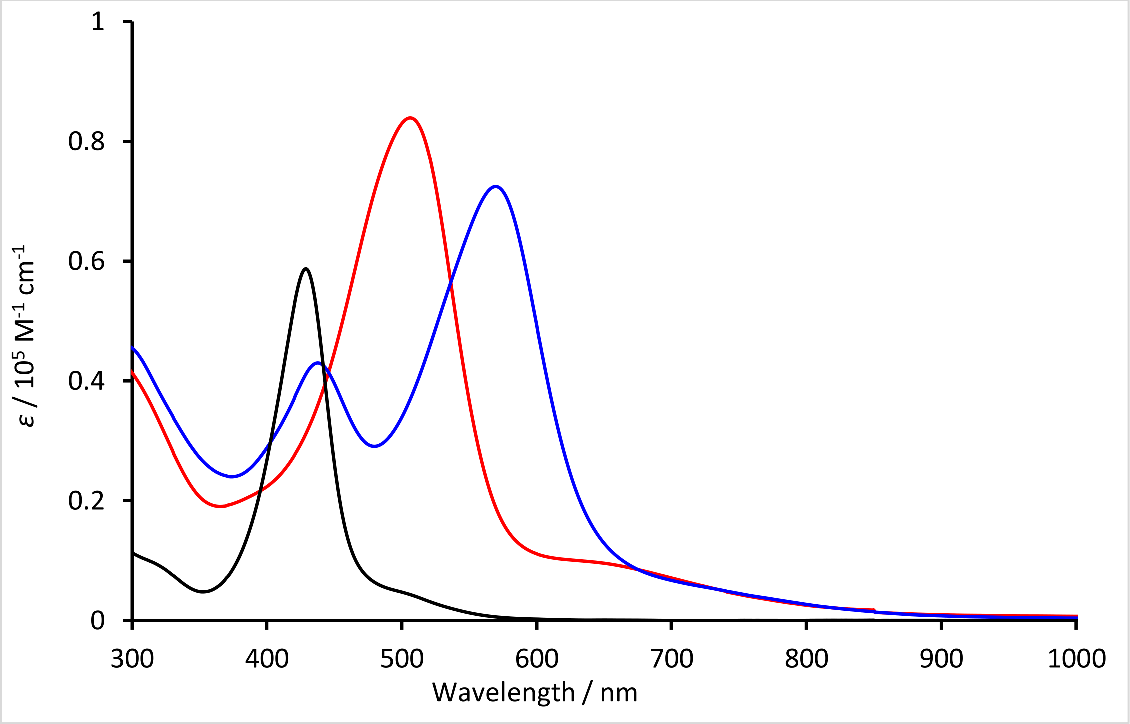

Figure 4.4. The UV-Vis-NIR absorption spectra of **4-1** (black line), **4-2** (red line), and **4-3** (blue line), in CH_2Cl_2.

The optical properties of expanded porphyrins are investigated by UV-Vis-NIR absorption spectra (Figure 4.4). These expanded porphyrins show broad absorption bands, reflecting the non-aromatic properties.[1c] With increasing the size of macrocyclic ring from **4-1** to **4-3**, the maximum absorption bands are red-shifted from 432 nm to 574 nm. The compound **4-1** shows strong absorption at 432 nm and broad absorption band around 500 to 600 nm. Compounds **4-2** and **4-3** both show red-shifted broad band around 650 to 900 nm (Figure 4.5). Any emission spectra have not been detected from all of the obtained expanded porphyrins because of non-aromatic properties.[4c]

4-3 Boron Complexation

Boron complexation of **4-2** is examined with three reaction conditions (Scheme 4.3). The first reaction condition is that treatment of **4-2** with 40 eq. TEA and 80 eq. BF_3•OEt_2 in dry-CH_2Cl_2 at room temperature for 12 hours. After purification, the mono-boron complex **1BF$_2$** is mainly isolated in 60%. When crude product is checked by APCI-MS, the *m*/*z* signals of further boron complexes were detected. Therefore, by the coordination reaction at 40ºC with 120 eq. BF_3•OEt_2, two bis-boron complexes, **2BF$_2$-a** and **2BF$_2$-b**, are isolated in 20 % and 28 %, respectively. By treatment of **4-2** with 40 eq. TEA and 120 eq. BF_3•OEt_2 in dry-toluene at 80ºC for 12 hours, two tri-boron complexes **3BF$_2$-a** and **3BF$_2$-b** are obtained 5 % and 2 %, respectively, accompany with the isolation of **2BF$_2$-a** and **2BF$_2$-b** in 26 % and 29 %, respectively. **3BF$_2$-a** and **3BF$_2$-b** are also obtained from **2BF$_2$-a** and **2BF$_2$-b** under the same reaction condition (Scheme 4.3). All obtained BODIPY macrocycles, **1BF$_2$**, **2BF$_2$-a**, **2BF$_2$-b**, **3BF$_2$-a** and **3BF$_2$-b**, are characterized by HR-MALDI-MS spectra.

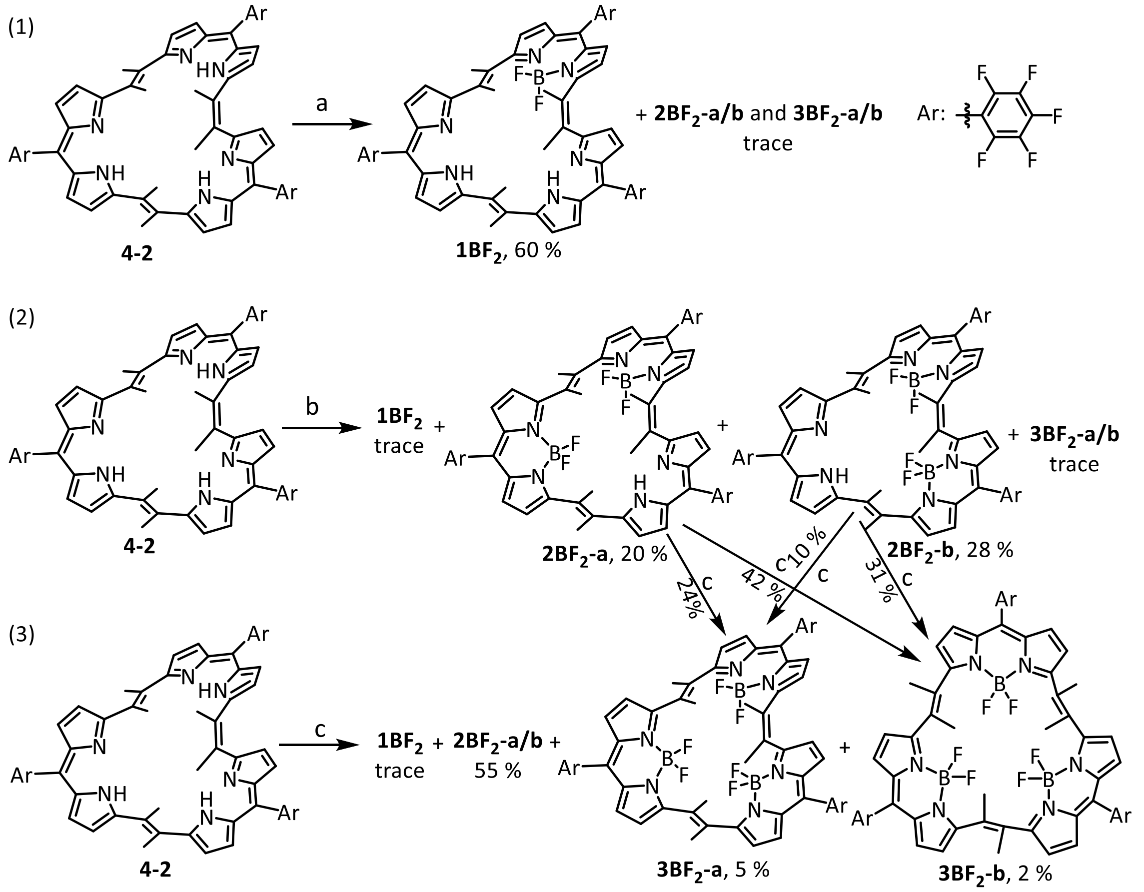

Scheme 4.3. Synthetic schemes of BODIPY macrocycles, **$1BF_2$**, **$2BF_2$-a**, **$2BF_2$-b**, **$3BF_2$-a** and **$3BF_2$-b**. Reaction conditions: (a) 40 eq. TEA, 80 eq. BF_3•OEt_2, CH_2Cl_2, room temperature, 12 hours, (b) 40 eq. TEA, 120 eq. BF_3•OEt_2, CH_2Cl_2, 40℃, 12 hours, (c) 40 eq. TEA, 120 eq. BF_3•OEt_2, toluene, 80℃, 12 hours.

The molecular structures of obtained BODIPY macrocycles were investigated by ^{1}H NMR and ^{19}F NMR spectroscopy at room temperature. ^{1}H NMR spectrum of **$1BF_2$** shows twelve doublet signals of pyrrolic *β*-position protons, which indicate the similar molecular structure to free base **4-2** (Figure 4.5). Two broad and weak peaks at 13.26 and 13.07 ppm are obtained corresponding to the uncoordinated NH protons. The six methyl groups are observed as six singlet peaks corresponding to asymmetric molecular structure.

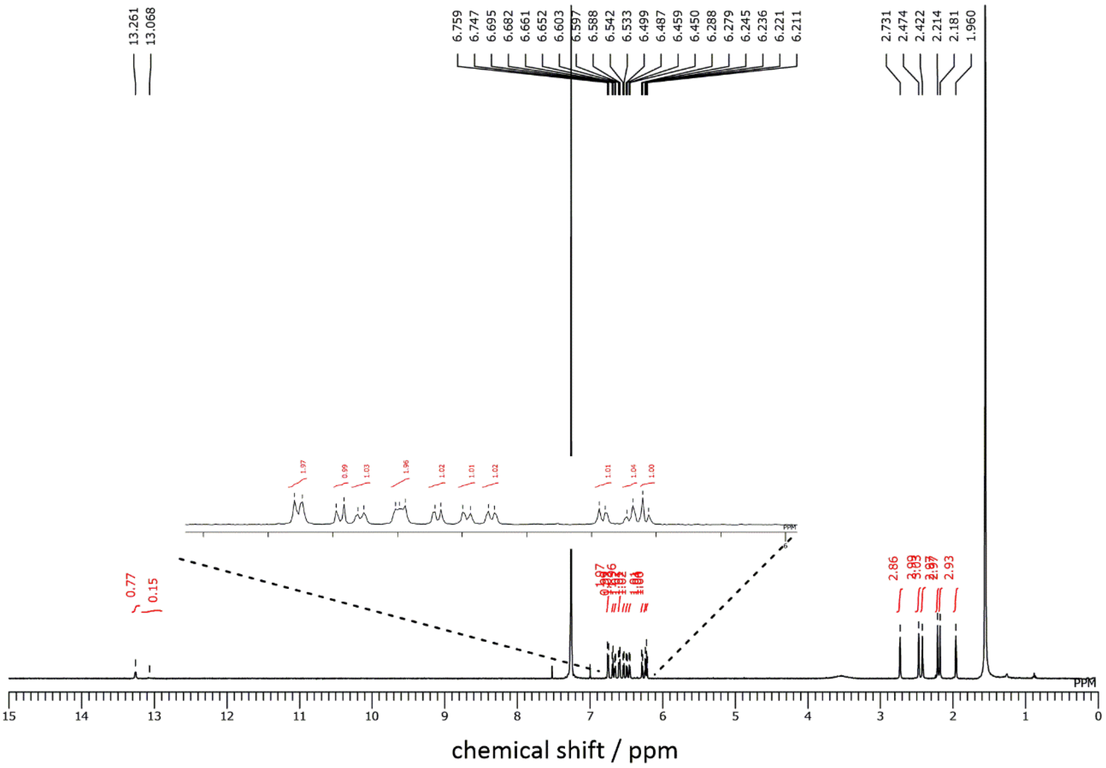

Figure 4.5. ^{1}H NMR spectrum of **$1BF_2$** in $CDCl_3$.

The ^{1}H NMR spectra of **$2BF_2$-a** and **$2BF_2$-b** showed different signal patterns. (Figures 4.6 and 4.7). **$2BF_2$-a** shows six singlet peaks of six methyl groups, indicating an asymmetric molecular structure, similar to free-base **4-2** and mono-boron complex **$1BF_2$**. In contrast, the ^{1}H NMR spectrum of **$2BF_2$-b** shows three singlet peaks and six doublet peaks corresponding to six methyl groups and twelve pyrrolic β-position protons, suggesting that **$2BF_2$-b** forms higher symmetrical structure than **$2BF_2$-a**.

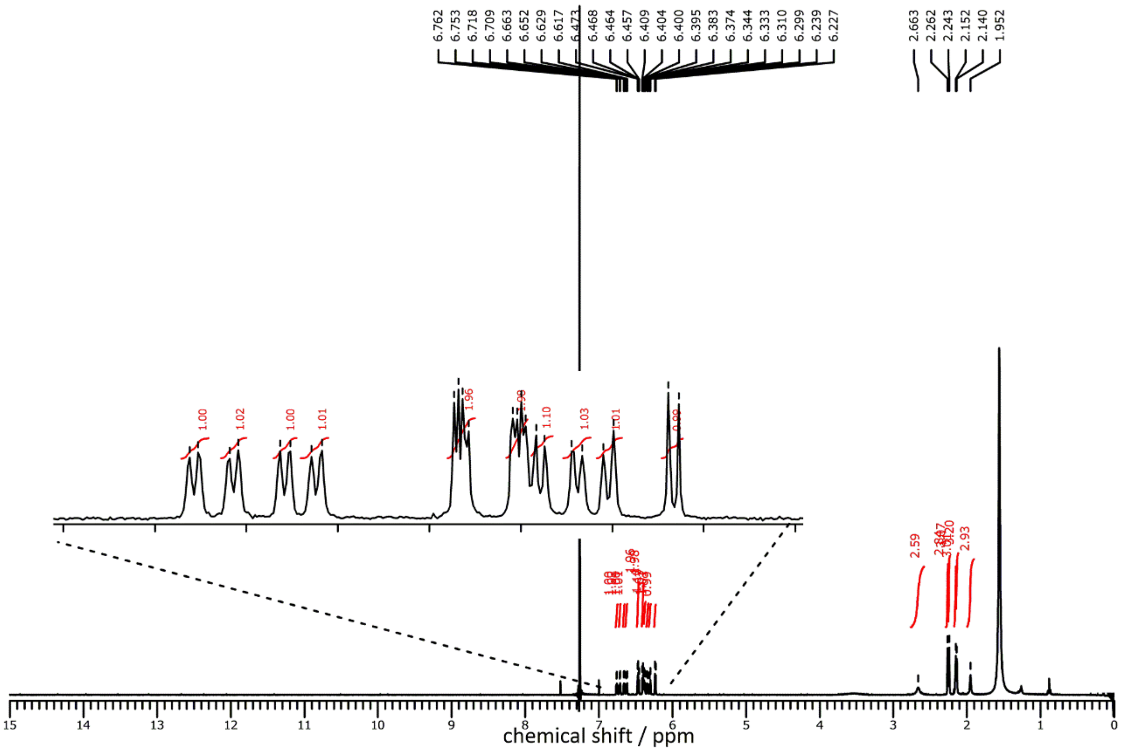

Figure 4.6. ^{1}H NMR spectrum of **$2BF_2$-a** in $CDCl_3$.

$3BF_2$-a shows six doublet peaks of pyrrolic *β*-position protons and three singlet peaks of six methyl groups (Figure 4.8). The ^{1}H NMR spectrum of **$3BF_2$-b** shows two multiplet peaks of pyrrolic *β*-position protons at 6.76 to 6.31 ppm and overlapped singlet peaks of six methyl groups (Figure 4.9). The ^{1}H NMR spectra indicate that two tri-boron complexes form higher symmetrical structures.

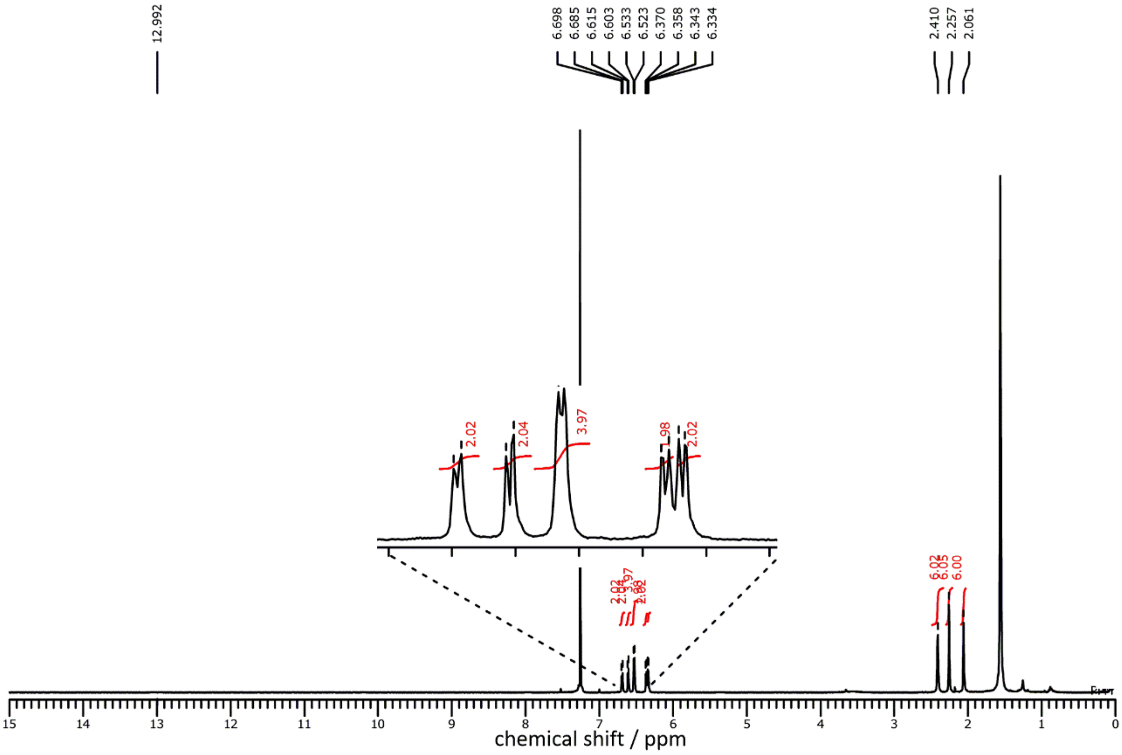

Figure 4.7. ^{1}H NMR spectrum of **$2BF_2$-b** in $CDCl_3$.

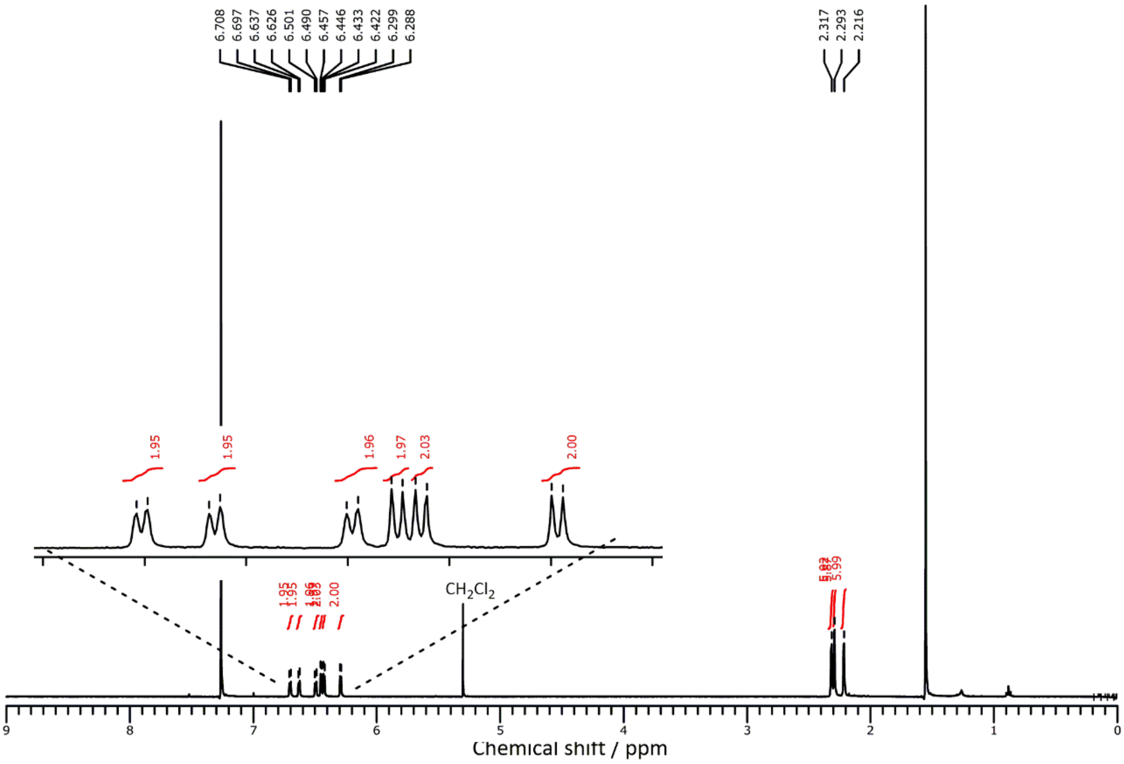

Figure 4.8. ^{1}H NMR spectrum of **$3BF_2$-a** in $CDCl_3$.

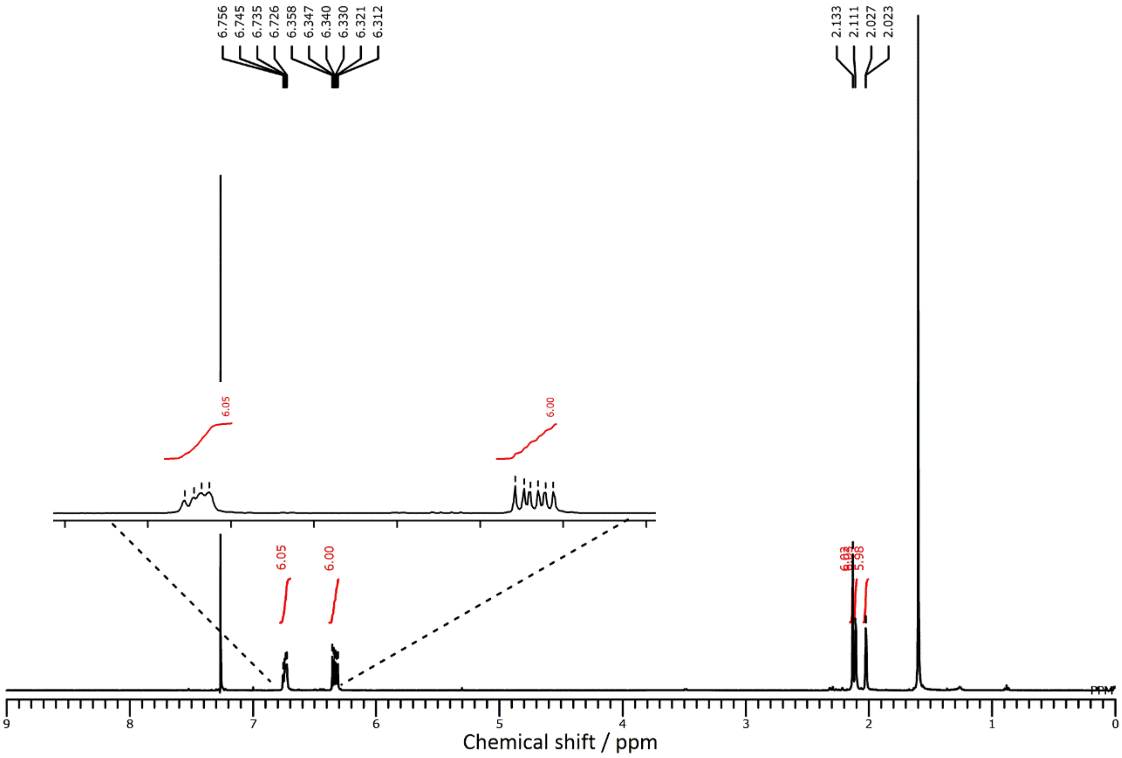

Figure 4.9. ^{1}H NMR spectrum of **3BF$_2$-b** in CDCl$_3$.

The crystal structures of the BODIPY macrocycles were revealed by X-ray diffraction analysis (Figure 4.10). Interestingly, the molecular structures of BODIPY macrocycles, **1BF$_2$**, **2BF$_2$-a**, **2BF$_2$-b**, **3BF$_2$-a** and **3BF$_2$-b**, show the different structures depending on the number of captured boron atoms in their cavity (Figure 4.10). Complexes **1BF$_2$**, **2BF$_2$-a** and **2BF$_2$-b** maintain the twisted molecular structures the same as free base **4-2**. Boron atoms are inserted into dipyrrin units one by one. First boron atom is inserted into dipyrrin unit next to the *cis*-dimethyl vinylene bridge. The second boron atom is located at the other two dipyrrin units to form complexes **2BF$_2$-a** and **2BF$_2$-b**. **2BF$_2$-b** was isolated as the main product under some reaction conditions relative to compound **2BF$_2$-a** (Scheme

4.3). The tri-boron complex **3BF$_2$-a** shows a symmetrical twisted molecular structure. Interestingly, the molecular structure of **3BF$_2$-b** shows a co-planar structure with all *trans*-dimethyl vinylene bridges. These observations indicate that of BODIPY macrocycles shows multifarious molecular structures as confirmed by NMR and X-ray crystallography. It is found that the compound **4-2** can be used as cyclic dipyrrin oligomers to form BODIPY macrocycles.

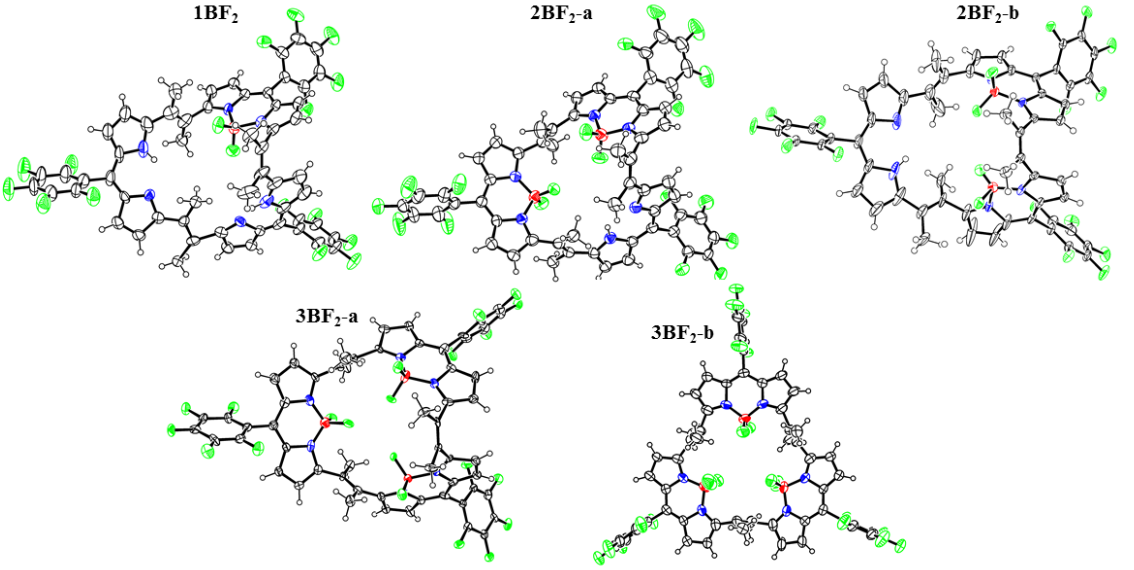

Figure 4.10. X-ray crystal structures of **1BF$_2$**, **2BF$_2$-a**, **2BF$_2$-b**, **3BF$_2$-a** and **3BF$_2$-b**. The thermal ellipsoids represent for 50% probability.

From the crystal structure of **1BF$_2$**, the dipyrrin units next to *cis*-dimethyl vinylene bridge of **4-2** is prior coordinative site compared with other the dipyrin units. To investigate the selectivity of coordination of boron atom to **4-2,** DFT calculation was carried out at B3LYP/6-31G* level with Gaussian 09[5] (Figure 4.11). The electrostatic potential of dipyrrin units next to *cis*-dimethyl vinylene bridge of **4-2** shows weaker negative potential (Figure 4.11, side view 1) than other dipyrrin units (Figure 4.11, side view 2). This means that the dipyrrin units next to *cis*-dimethyl vinylene bridge could easily generate the deprotonated species. Hence, the dipyrrin units next to *cis*-vinylene bridge show the higher reactivity than other dipyrrin unit under complexation reactions of boron atom.

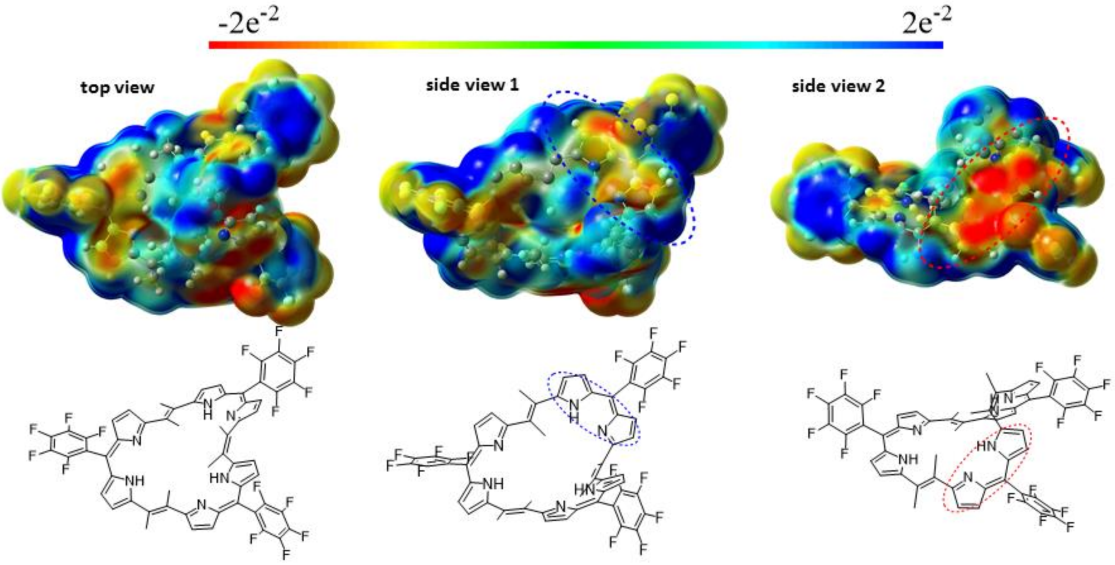

Figure 4.11. The molecular electrostatic potential surface of **4-2**, calculated at the B3LYP/6-31G* level of theory.

4-4 Redox Properties

The redox properties of free-base **4-2** and BODIPY macrocycles are measured by CV in CH_2Cl_2 with 0.1 M $TBAPF_6$ as an electrolyte. All redox potentials are shown in Figure 4.12. The free base **4-2** shows a oxidation and three reduction potentials at 0.20, –1.40, –1.55 and —1.98 V (vs. Fc/Fc^+).

The BODIPY macrocycles **$1BF_2$**, **$2BF_2$-a**, **$2BF_2$-b**, **$3BF_2$-a** and **$3BF_2$-b** show a oxidation and three reduction potentials at hexaphyrin(2.1.2.1.2.1) units. Two bis-boron complexes **$2BF_2$-a** and **$2BF_2$-b** show similar redox potentials. Besides, two tri-boron complexes **$3BF_2$-a** and **$3BF_2$-b** also show the similar redox potentials. The redox potentials of BODIPY macrocycles are positive-shifted with increasing the number of boron atoms from of 1.60 V free base **4-2** to 1.98 V of **$3BF_2$-b**.

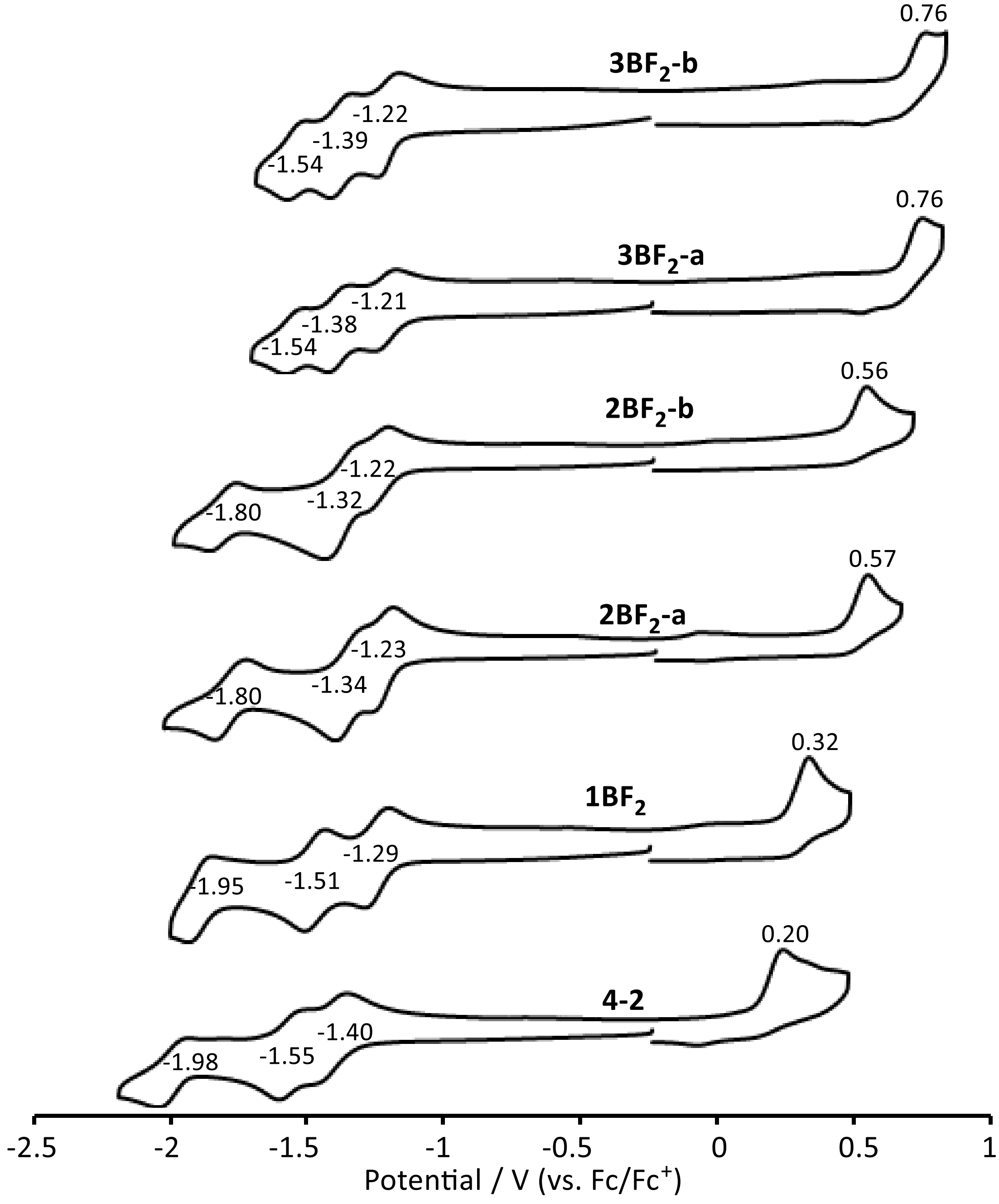

Figure 4.12. CV of **4-2**, **1BF$_2$**, **2BF$_2$-a**, **2BF$_2$-b**, **3BF$_2$-a** and **3BF$_2$-b** in CH_2Cl_2, containing 0.1 M $TBAPF_6$. Scan rate is 0.1 V s^{-1}.

4-5 Optical Properties

The absorption spectra of obtained BODIPY macrocycles are shown in Figure 4.13. Every BODIPY macrocycles show strong absorption bands around 500 nm and weak broad bands from 600 to 800 nm.

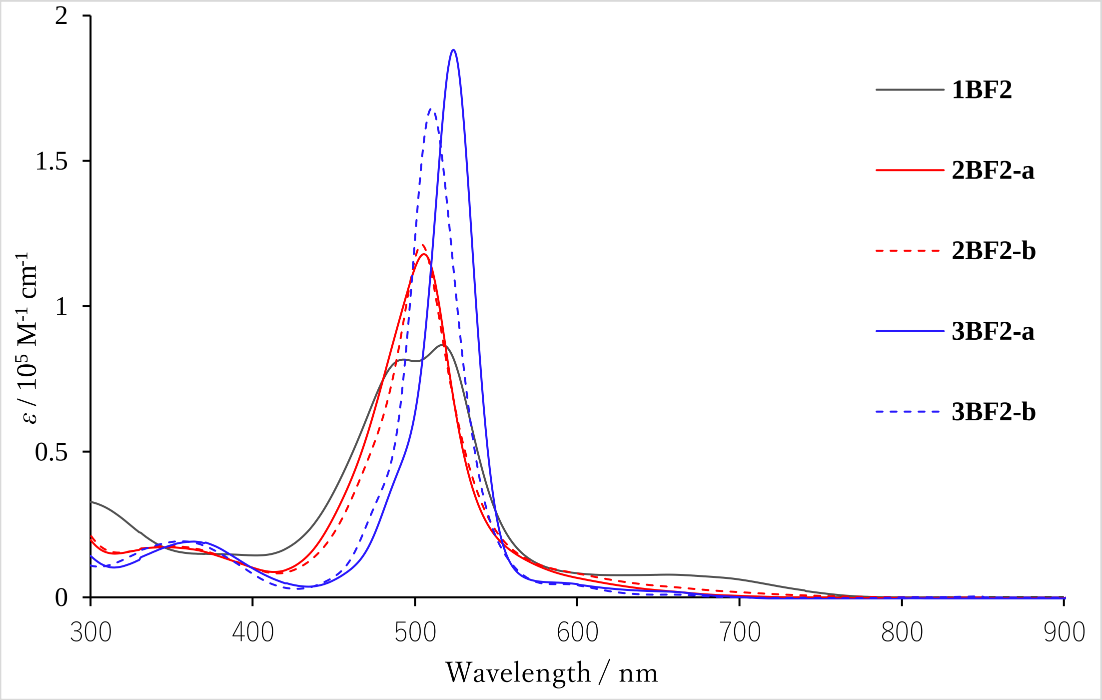

Figure 4.13. The UV-Vis absorption spectra of five BODIPY macrocycles and free base **4-2** in CH_2Cl_2.

With increasing the number of boron atoms, the strong bands are sharpened. Two bis-boron complexes **2BF$_2$-a** and **2BF$_2$-b** show very similar absorption spectra. However, two tri-boron complexes **3BF$_2$-a** and **3BF$_2$-b** show different absorption spectra. The twisted complex **3BF$_2$-a** shows strong absorption at 526 nm relative to 508 nm of co-planar **3BF$_2$-b**.

The emission spectra of **3BF$_2$-a** and **3BF$_2$-b** are shown in Figure 4.14. Two tri-boron complexes exhibit weak emissions in the red region (**3BF$_2$-a**: λ_{em} = 650 nm, Φ_F = 0.97%; **3BF$_2$-b**: λ_{em} = 650 nm, Φ_F = 1.4%). These relative fluorescence quantum yields are obtained by comparison with *meso*-tetraphenylporphyrin (quantum yield = 0.12 in CH_2Cl_2) used as a standard.[7]

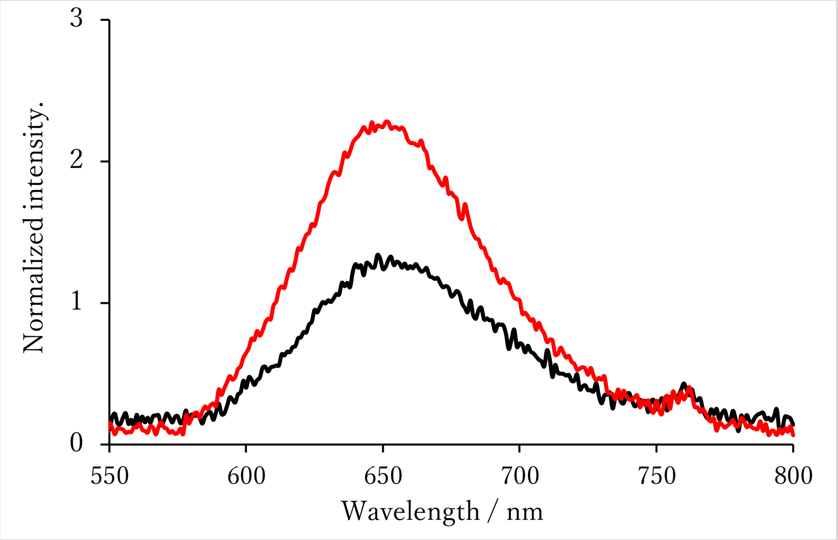

Figure 4.14. Fluorescence spectra of **3BF$_2$-a** (black line) and **3BF$_2$-b** (red line) in CH_2Cl_2. The excitation wavelength of two complexes were set at 508 nm.

The other three boron complexes, **1BF$_2$**, **2BF$_2$-a** and **2BF$_2$-b**, did not show any fluorescence..The S_0–S_1 transitions (Table 4.1) of **1BF$_2$**, **2BF$_2$-a**, **2BF2-b**, **3BF$_2$-a** and **3BF$_2$-b** were predicted by DFT and TD-DFT calculation at B3LYP/6-31G* level. The transitions of absorption of **1BF$_2$**, **2BF$_2$-a** and **2BF2-b** show clear ICT relative to **3BF$_2$-a** and **3BF$_2$-b**. The HOMO orbital of complex **2BF$_2$-a**, for example, is located at the free-base dipyrrin unit, while the LUMO orbital is mainly located at one BODIPY unit (Figure 4.15). Therefore, the calculation results suggest the presence of the ICT from the free-base dipyrrin donor units to the BDIPY accepting units of **$1BF_2$**, **$2BF_2$-a** and **$2BF_2$-b**. (Figure 4.15 - 4.16 and Table 4.1).[7]

Table 4.1 Selected TD-DFT calculated energies, oscillator strength (*f*), and major molecular orbital contribution of **$1BF_2$**, **$2BF_2$-a**, **$2BF_2$-b**, **$3BF_2$-a** and **$3BF_2$-b**.

Complexes	States	Wavelength (nm / eV)	*f*	Major Contribs
$1BF_2$	1	799.28 / 1.5512	0.0491	HOMO->LUMO
	2	537.79 / 2.3054	0.0020	HOMO->LUMO+2
$2BF_2$-a	1	766.46 / 1.6176	0.0191	HOMO->LUMO
	2	693.28 / 1.7884	0.0438	HOMO->LUMO+1
$2BF_2$-b	1	709.65 / 1.7471	0.0164	HOMO->LUMO
	2	550.70 / 2.2514	0.0088	HOMO-1->LUMO
$3BF_2$-a	1	629.04 / 1.9710	0.0248	HOMO->LUMO
	2	592.67 / 2.0919	0.0122	HOMO-1->LUMO
$3BF_2$-b	1	530.44 / 2.3374	0.0077	HOMO->LUMO
	2	506.91 / 2.4459	0.0022	HOMO->LUMO+1

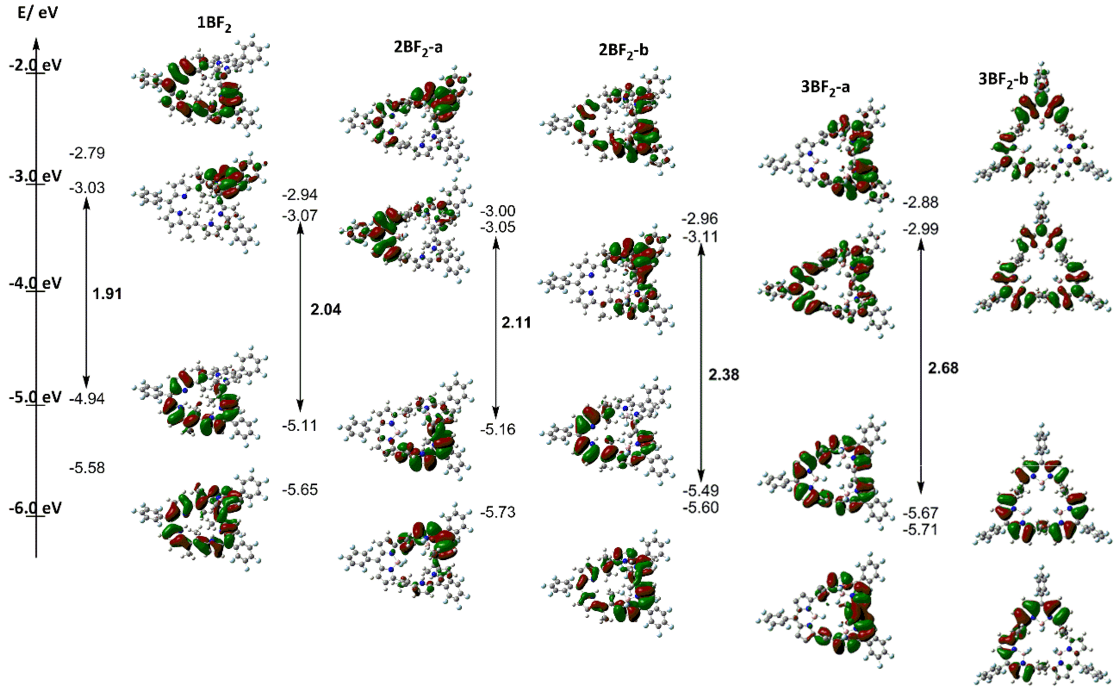

Figure 4.15. Frontier molecular orbitals and energy diagrams for the optimized structures of **1BF$_2$**, **2BF$_2$-a**, **2BF$_2$-b, 3BF$_2$-a** and **3BF$_2$-b** calculated at the B3LYP/6-31G* level of theory.

The electron density difference map (EDDM) represents the difference in electron densities upon electronic transitions.[8] Tri-boron complexes **3BF$_2$-a** and **3BF$_2$-b** shows delocated EDDMs, whereas the location of EDDMs for the lowest HOMO-LUMO transitions of **1BF$_2$**, **2BF$_2$-a** and **2BF$_2$-b** are shifted from the free base dipyrrin donor units to the BODIPY accepting units (Figure 4.16). Consistence with the predicted ICT characteristics in **1BF$_2$**, **2BF$_2$-a** and **2BF$_2$-b**, no emission spectra were observed in solution upon photoexcitation.[8]

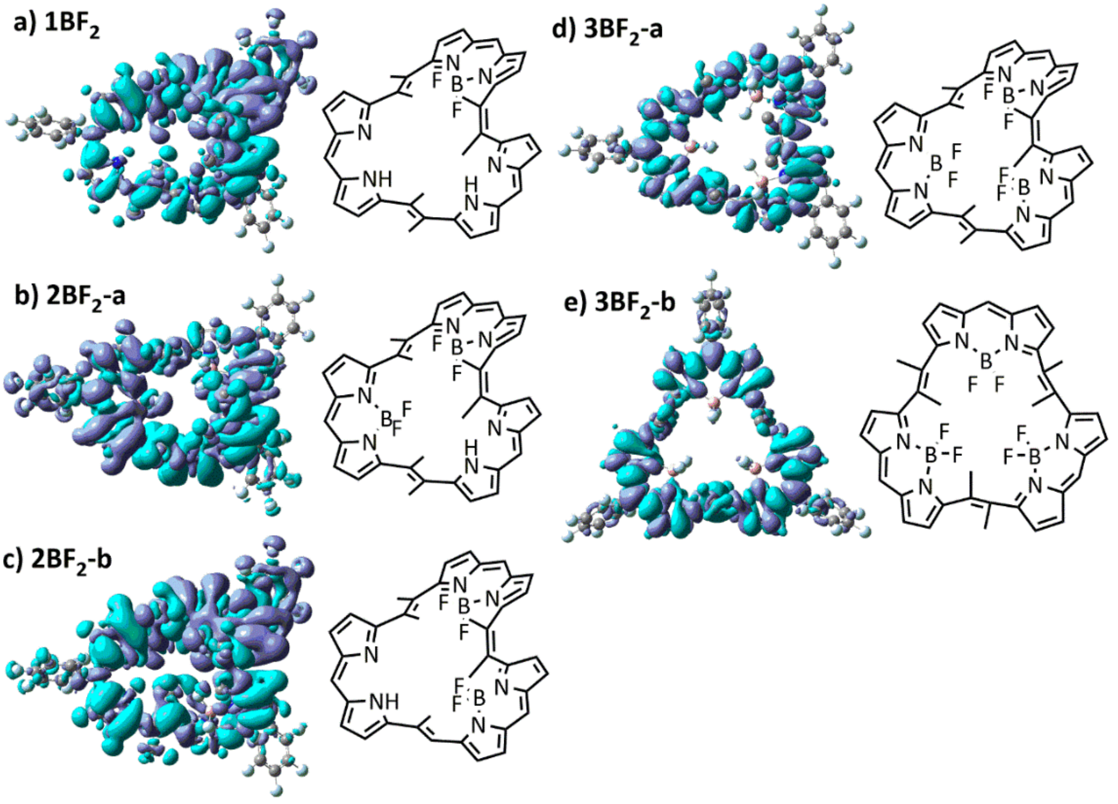

Figure 4.16. EDDMs of a) **1BF$_2$**, b) **2BF$_2$-a**, c) **2BF$_2$-b**, d) **3BF$_2$-a** and e) **3BF$_2$-b**.

4-6 Conclusion

In conclusion, three porphyrins were obtained by dimethyl vinylene-bridges linking of the dipyrrin units, whose twisted molecular structures were unambiguously determined by X-ray crystallography and ^{1}H NMR spectroscopy. After screening boron complexation reactions of hexaphyrin (2.1.2.1.2.1), **4-2** can be converted to five boron complexes, **$1BF_2$**, **$2BF_2$-a**, **$2BF_2$-b**, **$3BF_2$-a** and **$3BF_2$-b**. Therefore, **DMeDPEs** can work as useful building blocks to produce the dipyrrin oligomers for form BODIPY macrocycles.

The molecular shapes of BODIPY macrocycles are divided into two types: twisted structures as free-base **4-2** and co-planar structure. Among five boron complexes, only two tri-boron complexes with highly symmetrical conformation showed fluorescence emission. The mono-/bis-boron complexes showed no emission because of the ICT characteristic of them.

4-7 References

[1] (a) A. Loudet, K. Burgess, *Chem. Rev.*, **2007**, *107*, 4891; (b) H. Lu, J. Mack, Y. Yang, Z. Shen, *Chem. Soc. Rev.*, **2014**, *43*, 4778; (c) T. Sakida, S. Yamaguchi, H. Shinokubo, *Angew. Chem., Int. Ed.*, **2011**, *50*, 2280; (d) N. Sakamoto, C. Ikeda, T. Nabeshima, *Chem. Commun.*, **2010**, *46*, 6732; (e) Y. Hayashi, S. Yamaguchi, W. Cha, D. Kim, H. Shinokubo, *Org. Lett.*, **2011**, *13*, 2992; (f) Y. Cakmak, E. Akkaya, *Org. Lett.*, **2009**, *11*, 85; (g) A. Wakamiya, T. Murakamib, S. Yamaguchi, *Chem. Sci.*, **2013**, *4*, 1002.

[2] (a) T. Nakamura, G. Yamaguchi, T. Nabeshima, *Angew.Chem. Int. Ed.*, **2016**, *55*, 9606; (b) J. Uchida, T. Nakamura, M. Yamamura, G. Yamaguchi, T. Nabeshima, *Org. Lett.*, **2016,** *18*, 5380; (c) T. Sakida, S. Yamaguchi, H. Shinokubo, *Angew. Chem. Int. Ed.*, **2011**, *50*, 2280; (d) M. Ishida, T. Omagari, R. Hirosawa, K. Jono, Y. Sung, Y. Yasutake, H. Uno, M. Toganoh, *Angew. Chem., Int. Ed.*, **2016**, *55*, 12045.

[3] (a) J. Yadav, B. Reddy, G. Kondaji, R. Srinivasa , S. Kumar, *Tetrahedron Lett.*, **2002**, *43*, 9133; (b) T. Ono, D. Koga, Y. Hisaeda, *Chem. Lett.*, **2017**, *46*, 260.

[4] (a) M. Umetani, T. Tanaka, T. Kim, D. Kim, A. Osuka, *Angew. Chem., Int. Ed.*, **2016**, *55*, 8095; (b) Z. Yoon, A. Osuka, D. Kim. *Nat. Chem.*, **2009**, *1*, 113; (c) A. Osuka, S. Saito. *Chem. Commun.*, **2011**, *47*, 4330; (d) S. Saito, A. Osuka. *Angew. Chem., Int. Ed.*, **2011**, *50*, 4342; (4) T. Tanaka, A. Osuka. *Chem. Rev.*, **2017**, *117*, 2584.

[5] Gaussian 09, Revision B.01, M. J. Frisch, G. W. Trucks, H. B. Schlegel,G.E. Scuseria, M. A. Robb, J. R. Cheeseman, G. Scalmani, V. Barone, B. Mennucci, G. A. Petersson, H. Nakatsuji, M. Caricato, X. Li, H. P. Hratchian, A. F. Izmaylov, J. Bloino, G. Zheng, J. L. Sonnenberg, M. Hada, M. Ehara, K. Toyota, R. Fukuda, J. Hasegawa, M. Ishida, T. Nakajima, Y. Honda, O. Kitao, H. Nakai, T. Vreven, J. A. Montgomery, Jr., J. E. Peralta, F. Ogliaro, M. Bearpark, J. J. Heyd, E. Brothers, K. N. Kudin, V. N. Staroverov, T. Keith, R. Kobayashi, J. Normand, K. Raghavachari, A. Rendell, J. C. Burant, S. S. Iyengar, J. Tomasi, M. Cossi, N. Rega, J. M. Millam, M. Klene, J. E. Knox, J. B. Cross, V. Bakken, C. Adamo, J. Jaramillo, R. Gomperts, R. E. Stratmann, O. Yazyev, A. J. Austin, R. Cammi, C. Pomelli, J. W. Ochterski, R. L. Martin, K. Morokuma, V. G. Zakrzewski, G. A. Voth, P. Salvador, J. J. Dannenberg, S. Dapprich, A. D. Daniels, O. Farkas, J. B. Foresman, J. V. Ortiz, J. Cioslowski, and D. J. Fox, Gaussian, Inc., Wallingford CT, 2010.

[6] N. Sakamoto, C. Ikeda, M. Yamamura, T. Nabeshima, *Chem. Commun.,* **2012**, *48,* 4818.

[7] (a) P. Bhyrappa, M. Sankar, B. Varghese, P. Bhavana, *J. Chem. Sci.,* **2006**, *118,* 393; (b) P. Kubát, J. Mosinger, *J. Photoch. Photobio. A,* **1996**, *96,* 93.

[8] Y. Hisamune, T. Kim, K. Nishimura, M. Ishida, M. Toganoh, S. Mori, D. Kim, H. Furuta, *Chem. Eur. J.,* **2018**, *24,* 4628.

4-8 Supporting information

Spectroscopy: ^{1}H NMR and ^{19}F NMR spectra were recorded on a JNM-ECX 400 spectrometers (operating as 400 MHz for ^{1}H and 376 MHz for ^{19}F) using the residual solvent as the internal reference for ^{1}H (δ = 7.26 ppm in $CDCl_3$, δ = 5.30 ppm in CD_2Cl_2) and CF_3COOH as the external reference for ^{19}F (δ = –76.5 ppm). HR-MALDI−TOF mass spectra were recorded on a Bruker Daltonics autoflex MALDI−TOF MS spectrometer. UV-vis-NIR absorption spectra were measured with a JASCO UV/VIS/NIR Spectrophotometer V-670. Emission spectra were measured with a JASCO FP-6600 Spectrophotometer. CV and DPV measurements were conducted in a solution of 0.1 M $TBAPF_6$ in dry-dichloromethane with a scan rate of 0.1 V s^{-1} in an argon-filled cell. A glassy carbon electrode an a platinum wire were used as a working and a counter electrode, respectively. A Ag/$AgNO_3$ electrode was used as reference electrodes, which were normalized with the half-wave potential of ferrocene/ferrocenium (Fc/Fc^+) redox couple.

Materials: All solvents and chemicals were reagent grade quality, obtained commercially and used without further purification except as noted. For spectral measurements, spectral grade dichloromethane was purchased from Nakalai Tesque Co. Thin−layer chromatography (TLC), flush column chromatography, and gravity column chromatography were performed on Art. 5554 (Merck KGaA), Silica Gel 60 (Merck

KGaA), and Silica Gel 60N (Kanto Chemical Co.), respectively.

X−ray Analysis: X−ray crystallographic data for **4-1**, **4-2, 4-3, 1BF$_2$, 2BF$_2$-a**, **2BF$_2$-b, 3BF$_2$-a** and **3BF$_2$-b** were recorded at 100 K on a Rigaku CCD detector (Saturn 724) mounted on a Rigaku rotating anode X−ray generator (MicroMax−007HF) using Mo−Kα radiation from the corresponding set of confocal optics. The structures were solved by direct methods and refined on F^2 by full−matrix least−squares using the CrystalClear and SHELXS−97 and SHELXT−2014/5 programs. CCDC: 1830225, 1830228, 1830229, 1832230, 1830231, 1848201, 1830232 and 1830233 contain the supplementary crystallographic data for **4-1**, **4-2, 4-3, 1BF$_2$, 2BF$_2$-a**, **2BF$_2$-b, 3BF$_2$-a** and **3BF$_2$-b** respectively. These data can be obtained free of charge from the Cambridge Crystallographic Data Centre via www.ccdc.cam.ac.uk/data_request/cif.

Theoretical calculations: All density functional theory calculations were achieved with the Gaussian 09 program package. The geometry was fully optimized at the Becke's three-parameter hybrid functional combined with the Lee-Yang-Parr correlation functional abbreviated as the B3LYP level of density functional theory with 6-31G (d) basis set.

Synthesis of DMeDPEs

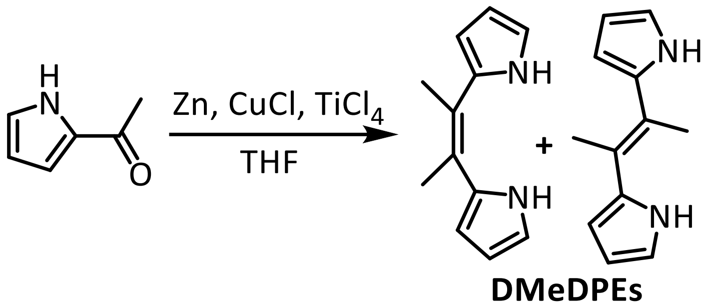

$TiCl_4$ (3.5 mL) was added dropwise to a dry THF (75 mL) solution of Zn powder (2.7 g) and CuCl (273 mg) at 0ºC under argon. The reaction mixture was refluxed for 2 hours and then 2-acetylpyrrole (600 mg, 5.5 mmol) in THF (10 mL) was added dropwise. The solution was refluxed for 2 hours until the starting material was completely consumed. The reaction was quenched with aqueous NaOAc solution. The mixture was extracted with CH_2Cl_2, the organic layer was washed with water and brine and dried over anhydrous Na_2SO_4. The solvents were removed under reduced pressure and the crude product was purified by silica-gel column chromatography (CH_2Cl_2/hexane = 3/2) to give ***Z-DMeDPE*** in 23% (120 mg, 0.6 mmol) and ***E*-DMeDPE** in 10% (51 mg, 0.3 mmol).

***Z*-DMeDPE**: ^{1}H NMR (400 MHz, $CDCl_3$, 298 K) $\delta = 7.74$ (brs, 2H, NH), 6.60 (m, 2H, pyrrole), 6.18 (m, 4H, pyrrole), 2.12 (s, 6H, methyl) ppm.

***E*-DMeDPE**: ^{1}H NMR (400 MHz, $CDCl_3$, 298 K) $\delta = 8.17$ (brs, 2H, NH), 6.81 (m, 2H, pyrrole), 6.27 (m, 2H, pyrrole), 6.24 (m, 2H, pyrrole), 2.22 (s, 6H, methyl) ppm.

Synthesis of 4-1, 4-2 and 4-3

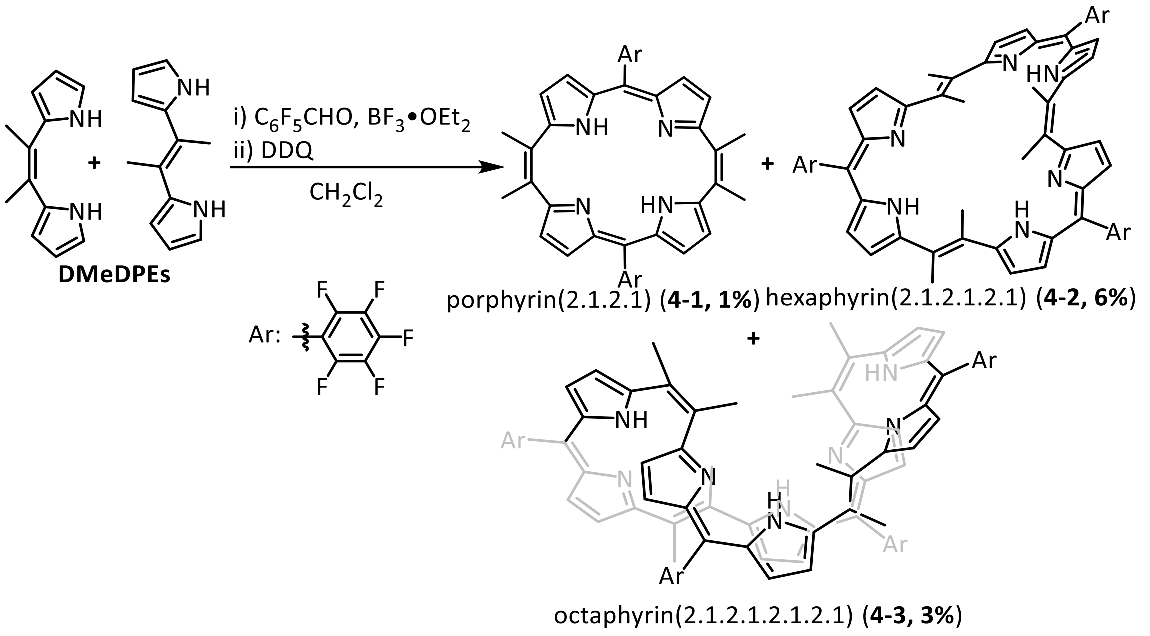

Pentafluorobenzaldehyde (196 mg, 1.0 mmol) and *Z-/E-***DMeDPEs** (186 mg, 1.0 mmol) were dissolved in 150 mL dry-CH_2Cl_2 under an argon atmosphere. The mixture was stirred for 5 min and then BF_3•Et_2O (4.3 mg, 0.03 mmol) was added. After stirring for 2 hours at room temperature, DDQ (227 mg, 1.0 mmol) was added to the mixture, which was stirred for 1 hour. After the solvent was concentrated, the residue was purified by silica gel (CH_2Cl_2) and alumina (*n*-hexane/CH_2Cl_2 = 5/1) column chromatographies. The first eluted yellow fraction was evaporated to give **Por** in 1 % (3.5 mg, 0.0048 mmol) as a deep purple solid. The second red fraction was evaporated to give **Hex** in 6 % (21.5 mg, 0.02 mmol) as a dark red solid and the third green fraction was evaporated to give **Oct** in 3 % (10.5 mg, 0.0075 mmol) as a dark red solid.

4-1: ^{1}H NMR (400 MHz, $CDCl_3$, 298 K) δ = 11.82 (brs, 2H, NH), 6.23 (d, J = 4 Hz, 4H, pyrrole), 6.12 (d, $J = 4$ Hz, 4H, pyrrole), 2.16 (s, 12H, methyl) ppm. ^{19}F NMR (376 MHz, CDCl$_3$): $\delta = -138.15$ (m, 2F, *ortho*-F), –139.28 (m, 2F, *ortho*-F), –153.04 (t, $J = 42$ Hz, 2F, *para*-F), –161.33 (m, 2F, *meta*-F), –161.55 (m, 2F, *meta*-F) ppm. HR-MALDI-MS: calcd. for $C_{38}H_{22}F_{10}N_4$: 724.1685 $[M]^+$, Found: 724.1683. UV-vis-NIR (in CH_2Cl_2) λ [nm] (ε [M^{-1} cm^{-1}]): 432 (58000).

4-2: ^{1}H NMR (400 MHz, CDCl$_3$, 298 K) $\delta = 14.14$ (brs, 1H, NH), 13.62 (brs, 1H, NH), 13.26 (brs, 1H, NH), 6.75 (d, $J = 4$ Hz, 1H, pyrrole), 6.66 (d, $J = 4$ Hz, 1H, pyrrole), 6.59 (d, $J = 4$ Hz, 1H, pyrrole), 6.51 (d, $J = 4$ Hz, 1H, pyrrole), 6.48 (d, $J = 4$ Hz, 1H, pyrrole), 6.45 (d, $J = 4$ Hz, 1H, pyrrole), 6.43 (d, $J = 4$ Hz, 1H, pyrrole), 6.39 (d, $J = 4$ Hz, 1H, pyrrole), 6.36 (d, $J = 4$ Hz, 1H, pyrrole), 6.03 (d, $J = 4$ Hz, 1H, pyrrole), 5.96 (d, $J = 4$ Hz, 1H, pyrrole), 5.56 (d, $J = 4$ Hz, 1H, pyrrole), 2.71 (s, 3H, methyl), 2.57 (s, 3H, methyl), 2.45 (s, 3H, methyl), 2.40 (s, 3H, methyl), 2.29 (s, 3H, methyl), 1.95 (s, 3H, methyl) ppm. ^{19}F NMR (376 MHz, CDCl$_3$): $\delta = -137.61$ (m, 6F, *ortho*-F), –152.80 (m, 3F, *para*-F), –161.15 (m, 6F, *meta*-F) ppm. HR-MALDI-MS: calcd. for $C_{57}H_{33}F_{15}N_6$: 1086.2527 $[M]^+$, Found: 1086.2522. UV-vis-NIR (in CH_2Cl_2) λ [nm] (ε [M^{-1} cm^{-1}]): 500 (83000).

4-3: ^{1}H NMR (400 MHz, CDCl$_3$, 298 K) $\delta = 12.49$ (brs, 4H, NH), 6.43 (s, 4H, pyrrole), 6.33 (d, $J = 4$ Hz, 4H, pyrrole), 6.23 (s, 8H, pyrrole), 2.33 (s, 12H, methyl), 2.29 (s, 12H, methyl) ppm. ^{19}F NMR (376 MHz, CDCl$_3$): δ = –137.87 (m, 8F, *ortho*-F), –152.84 (m, 4F, *para*-F), –161.21 (m, 8F, *meta*-F) ppm. HR-MALDI-MS: calcd. for $C_{76}H_{44}F_{20}N_8$: 1448.3370 [*M*]$^+$, Found: 1448.3370. UV-vis-NIR (in CH$_2$Cl$_2$) λ [nm] (ε [M^{-1} cm^{-1}]): 442 (42000), 574 (72000).

Synthesis of 1BF$_2$, 2BF$_2$-a/b and 3BF$_2$-a/b

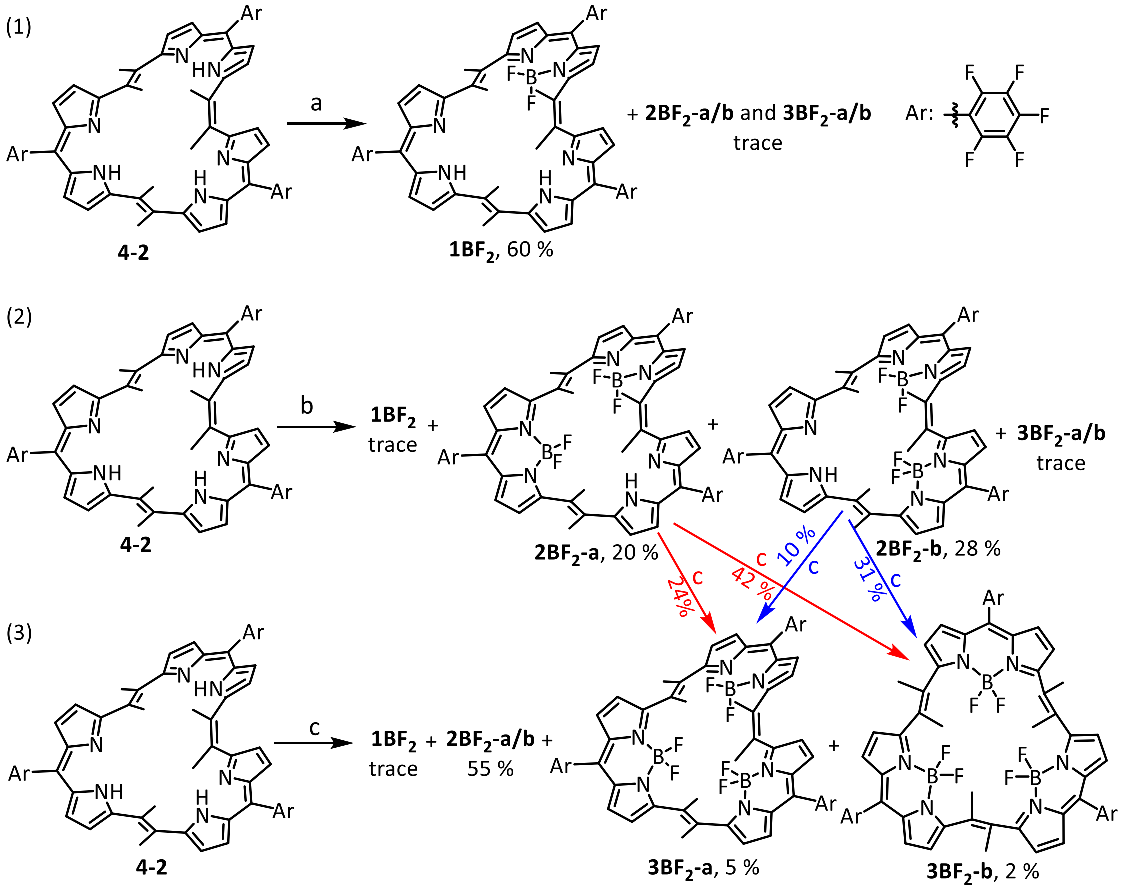

conditions: (a) 40 eq TEA, 80 eq BF$_3$.OEt$_2$, CH$_2$Cl$_2$, RT, 12 hours;
(b) 40 eq TEA, 80 eq BF$_3$.OEt$_2$, CH$_2$Cl$_2$, 40 °C, 12 hours;
(c) 40 eq TEA, 80 eq BF$_3$.OEt$_2$, toluene, 80 °C, 12 hours.

Synthesis of 1BF$_2$: To a solution of **4-2** (10.8 mg, 0.01 mmol) in dry-CH$_2$Cl$_2$ (20 mL) and TEA (40 mg, 0.4 mmol) was added BF$_3$•Et$_2$O (113 mg, 0.8 mmol) under argon. The mixture was stirred at room temperature for 12 hours. The reaction mixture was extracted with CH_2Cl_2. The organic phase was washed with aq. $NaHCO_3$ solution, water and brine, and dried over Na_2SO_4. After removal of the solvent, the resulting crude product was purified by silica gel column chromatography (hexane/CH_2Cl_2 = 3/1) to give **1BF$_2$** in 60% (6.8 mg, 0.006 mmol).

Synthesis of 2BF$_2$-a and 2BF$_2$-b: To a solution of **4-2** (11 mg, 0.01 mmol) in dry-CH_2Cl_2 (20 mL) and TEA (0.05 ml, 0.4 mmol) was added BF_3•Et_2O (0.15 ml, 1.2 mmol) under an argon atmosphere. The mixture was stirred at 40°C for 12 hours. The reaction mixture was extracted with CH_2Cl_2, then organic phase was washed with aq. $NaHCO_3$ solution, water and brine. The organic phase was dried over Na_2SO_4, then solvent was removed on a rotary evaporator under vacuum. The resulting crude product was purified by silica gel column chromatography (hexane/CH_2Cl_2 = 1.5/1) to afford **2BF$_2$-a** in 20% (2.4 mg, 0.002 mmol) and **2BF$_2$-b** in 28% (3.4 mg, 0.0028 mmol).

Synthesis of 3BF$_2$-a and 3BF$_2$-b: To a solution of **4-2** (10.8 mg, 0.01 mmol) in dry-toluene (20 mL) and TEA (0.05 ml, 0.4 mmol) was added BF_3•Et_2O (0.15 ml, 1.2 mmol) under an argon atmosphere. The mixture was stirred at 80°C for 12 hours. The reaction mixture was extracted with CH_2Cl_2, then organic phase was washed with aq. $NaHCO_3$ solution, water and brine. The organic phase was dried over Na_2SO_4, then solvent was removed on a rotary evaporator under vacuum. The resulting crude product was purified by silica gel column chromatography (hexane/CH_2Cl_2 = 1/1 to 2/3) to afford **3BF$_2$-a** in 5% (0.63 mg, 0.0005 mmol) and **3BF$_2$-b** in 2% (0.25 mg, 0.0002 mmol) and **2BF$_2$-a/b** in 55% yield.

1BF$_2$: ^{1}H NMR (400 MHz, $CDCl_3$, 298 K) δ = 13.26 (brs, 1H, NH), 13.07 (brs, 1H, NH), 6.75 (d, J = 4 Hz, 2H, pyrrole), 6.69 (d, J = 4 Hz, 1H, pyrrole), 6.65 (d, J = 4 Hz, 1H, pyrrole), 6.60 -6.59 (m, J = 4 Hz, 2H, pyrrole), 6.54 (d, J = 4 Hz, 1H, pyrrole), 6.49 (d, J = 4 Hz, 1H, pyrrole), 6.45 (d, J = 4 Hz, 1H, pyrrole), 6.28 (d, J = 4 Hz, 1H, pyrrole), 6.24 (d, J = 4 Hz, 1H, pyrrole), 6.22 (d, J = 4 Hz, 1H, pyrrole), 2.73 (s, 3H, methyl), 2.47 (s, 3H, methyl), 2.42 (s, 3H, methyl), 2.21 (s, 3H, methyl), 2.18 (s, 3H, methyl), 1.96 (s, 3H, methyl) ppm. ^{19}F NMR (376 MHz, $CDCl_3$): δ = –135.60 (m, 1F, *ortho*-F), –136.56 (m, 2F, *ortho*-F), –137.68 (m, 1F, *ortho*-F), –137.95 (m, 2F, *ortho*-F), –141.50 (brs, 2F, BF$_2$), –150.02 (t, J = 41 Hz, 1F, *para*-F), –152.46 (t, J = 42 Hz, 1F, *para*-F), –152.69 (t, J = 41 Hz, 1F, *para*-F), –159.67 (m, 2F, *meta*-F), –160.78 (m, 2F, *meta*-F), –161.15 (m, 2F, *meta*-F) ppm. HR-MALDI-MS: calcd. for $C_{57}H_{32}BF_{17}N_6$ = 1134.2510 [M]$^+$, Found: 1134.2505. UV-vis-NIR (in CH_2Cl_2) λ [nm] (ε [M^{-1} cm^{-1}]): 492 (54000), 518 (58000).

2BF$_2$-a: ^{1}H NMR (400 MHz, $CDCl_3$, 298 K) δ = 6.76 (d, J = 4 Hz, 1H, pyrrole), 6.71 (d, J = 4 Hz, 1H, pyrrole), 6.66 (d, J = 4 Hz, 1H, pyrrole), 6.62 (d, J = 4 Hz, 1H, pyrrole), 6.47 (m, 2H, pyrrole), 6.41 (m, 2H, pyrrole), 6.38 (d, J = 4 Hz, 1H, pyrrole), 6.34 (d, J =

4 Hz, 1H, pyrrole), 6.31 (d, $J = 4$ Hz, 1H, pyrrole), 6.23 (d, $J = 4$ Hz, 1H, pyrrole), 2.66 (s, 3H, methyl), 2.26 (s, 3H, methyl), 2.24 (s, 3H, methyl), 2.15(s, 3H, methyl), 2.14 (s, 3H, methyl), 1.95 (s, 3H, methyl) ppm. ^{19}F NMR (376 MHz, $CDCl_3$): $\delta = -135.14$ (m, 1F, *ortho*-F), –136.01 (m, 1F, *ortho*-F), –136.45 (m, 2F, *ortho*-F), –136.85 (m, 1F, *ortho*-F), –138.06 (m, 1F, *ortho*-F), –138.07 (brs, 1F, BF_2), –138.72 (brs, 1F, BF_2), –144.69 (brs, 1F, BF_2), –146.38 (brs, 1F, BF_2), –150.01 (t, J =42 Hz, 1F, *para*-F), –150.20 (t, $J = 42$ Hz, 1F, *para*-F), –152.86 (t, $J = 42$ Hz, 1F, *para*-F), –159.61 (m, 3F, *meta*-F), –159.95 (m, 1F, *meta*-F), –161.33 (m, 2F, *meta*-F) ppm. HR-MALDI-MS: calcd. for $C_{57}H_{31}B_2F_{19}N_6Na$ = 1205.2391 $[M+Na]^+$, Found: 1205.2391. UV-vis-NIR (in CH_2Cl_2) λ [nm] (ε [M^{-1} cm^{-1}]): 510 (114000).

2BF₂-b: ^{1}H NMR (400 MHz, $CDCl_3$, 298 K) $\delta = 6.69$ (d, $J = 4$ Hz, 2H, pyrrole), 6.61 (d, $J = 4$ Hz, 2H, pyrrole), 6.53 (d, $J = 4$ Hz,4H, pyrrole), 6.36 (d, $J = 4$ Hz, 2H, pyrrole), 6.34 (d, $J = 4$ Hz, 2H, pyrrole), 2.41 (s, 6H, methyl), 2.26 (s, 6H, methyl), 2.06 (s, 6H, methyl) ppm. ^{19}F NMR (376 MHz, $CDCl_3$, 213 K): $\delta = -133.07$ (brs, 1F, BF_2), –135.15 (m, 1F, *ortho*-F), –135.02 (m, 1F, *ortho*-F), –135.53 (m, 1F, *ortho*-F), –136.13 (m, 1F, *ortho*-F), –137.12 (m, 1F, *ortho*-F), –137.90 (m, 1F, *ortho*-F), –139.10 (brs, 1F, BF_2), –143.15 (brs, 1F, BF_2), –149.11 (t, $J = 42$ Hz, 1F, *para*-F), –149.83 (brs, 1F, BF_2), –151.55 (t, $J = 42$ Hz, 1F, *para*-F), –158.93 (m, 3F, *meta*-F), –159.83 (m, 1F, *meta*-F), –160.16 (m, 2F, *meta*-F) ppm. HR-MALDI-MS: calcd. for $C_{57}H_{31}B_2F_{19}N_6Na$ = 1205.2391 [*M*+*Na*]$^+$, Found: 1205.2397. UV-vis-NIR (in CH_2Cl_2) λ [nm] (ε [M^{-1} cm^{-1}]): 500 (123000).

3BF$_2$-a: ^{1}H NMR (400 MHz, $CDCl_3$, 298 K) δ = 6.70 (d, *J* = 4 Hz, 2H, pyrrole), 6.63 (d, *J* = 4 Hz, 2H, pyrrole), 6.50 (d, *J* = 4 Hz, 2H, pyrrole), 6.45 (d, *J* = 4 Hz, 2H, pyrrole), 6.43 (d, *J* = 4 Hz, 2H, pyrrole), 6.29 (d, *J* = 4 Hz, 2H, pyrrole), 2.32 (s, 3H, methyl), 2.29 (s, 3H, methyl), 2.22 (s, 3H, methyl) ppm. ^{19}F NMR (376 MHz, $CDCl_3$): δ = –128.81 (brs, 2F, BF_2), –132.02 (brs, 1F, BF_2), –135.13 (m, 2F, *ortho*-F), –136.34 (m, 1F, *ortho*-F), –136.71 (m, 3F, *ortho*-F), –149.10 (brs, 1F, BF_2), –150.09 (t, *J* = 41 Hz, 1F, *para*-F), –150.32 (t, *J* = 43 Hz, 2F, *para*-F), –151.50 (brs, 1F, BF_2), –159.88 (m, 6F, *meta*-F) ppm. HR-MALDI-MS: calcd. for $C_{57}H_{30}B_3F_{21}N_6Na$ = 1253.2393 [*M*+*Na*]$^+$, Found: 1253.2399. UV-vis-NIR (in CH_2Cl_2) λ [nm] (ε [M^{-1} cm^{-1}]): 525 (187000).

3BF$_2$-b: ^{1}H NMR (400 MHz, $CDCl_3$, 298 K) δ = 6.76 – 6.73 (m, 6H, pyrrole), 6.36 – 6.31 (m, 6H, pyrrole), 2.13 (s, 6H, methyl), 2.11 (s, 6H, methyl), 2.03 (s, 3H, methyl), 2.02 (s, 3H, methyl) ppm. ^{19}F NMR (376 MHz, $CDCl_3$): δ = –136.37 (m, 6F, *ortho*-F), –139.86 (m, 2F, BF_2), –143.61 (brs, 2F, BF_2), –147.17 (brs, 2F, BF_2), –150.10 (m, 3F, *para*-F), –159.64 (m, 6F, *meta*-F) ppm. HR-MALDI-MS: calcd. for $C_{57}H_{30}B_3F_{21}N_6Na$ = 1253.2393 [*M*+*Na*]$^+$, Found: 1253.2393. UV-vis-NIR (in CH_2Cl_2) λ [nm] (ε [M^{-1} cm^{-1}]): 512 (167000).

Supporting Figures

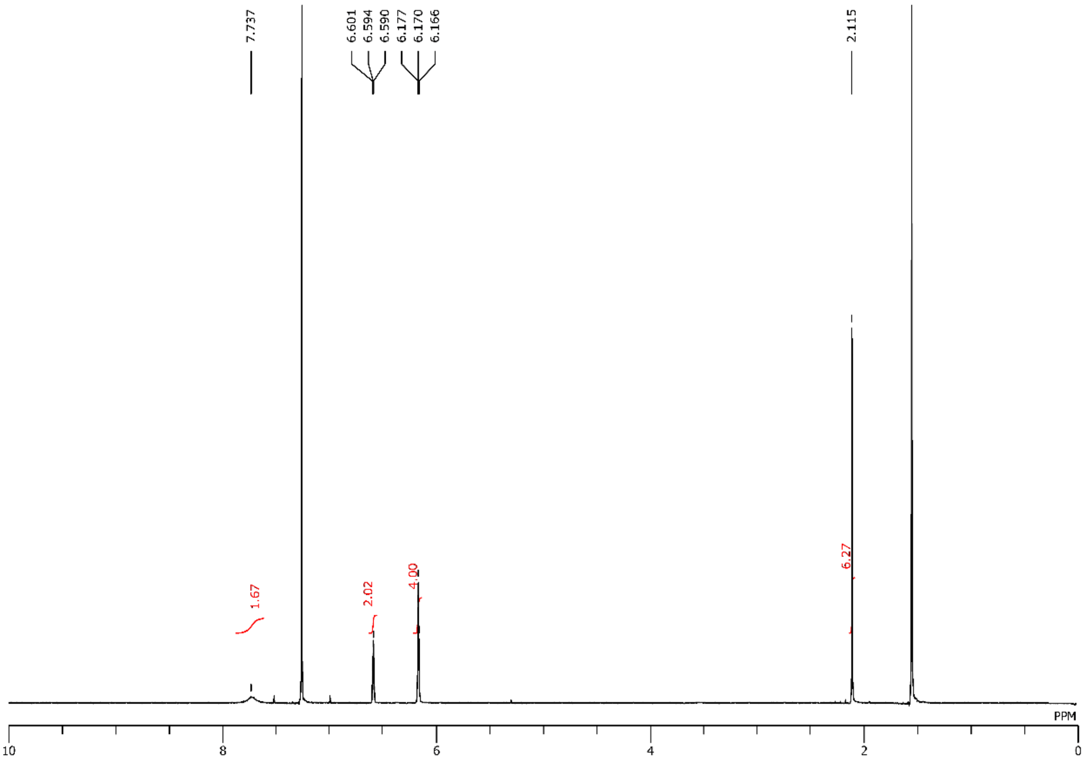

Figure S4.1. ^{1}H NMR spectrum of ***Z*-DMeDPE** in CDCl$_3$.

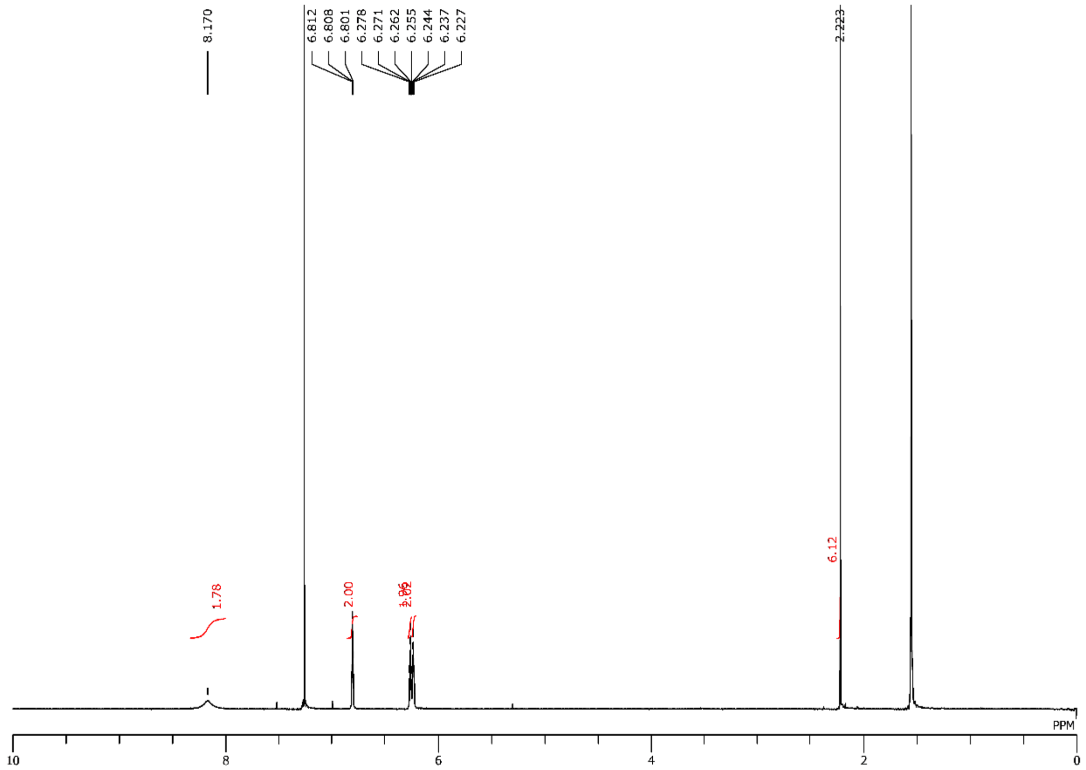

Figure S4.2. ^{1}H NMR spectrum of ***E*-DMeDPE** in CDCl$_3$.

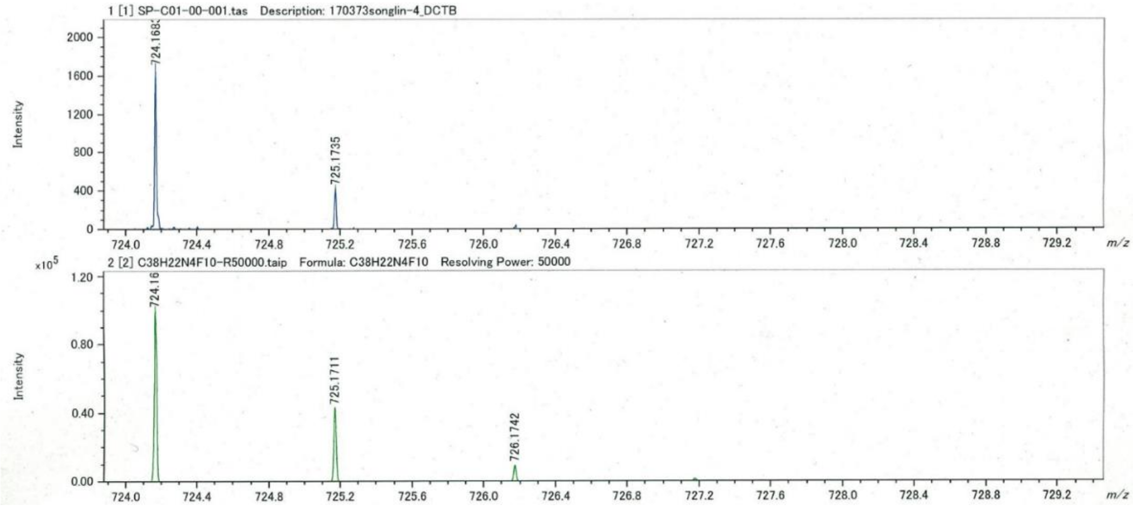

Figure S4.3. HR-MALDI-MS spectrum of **4-1**.

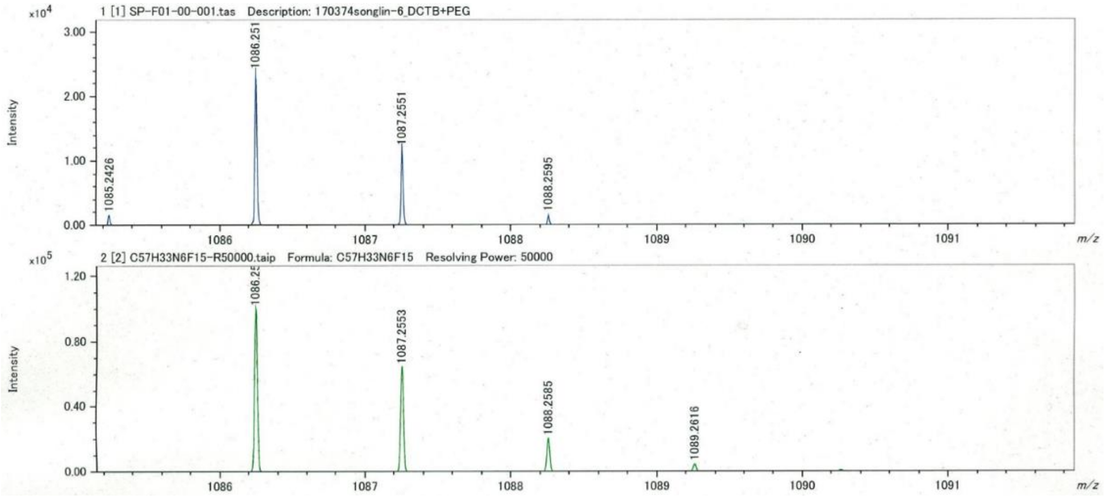

Figure S4.4. HR-MALDI-MS spectrum of **4-2**.

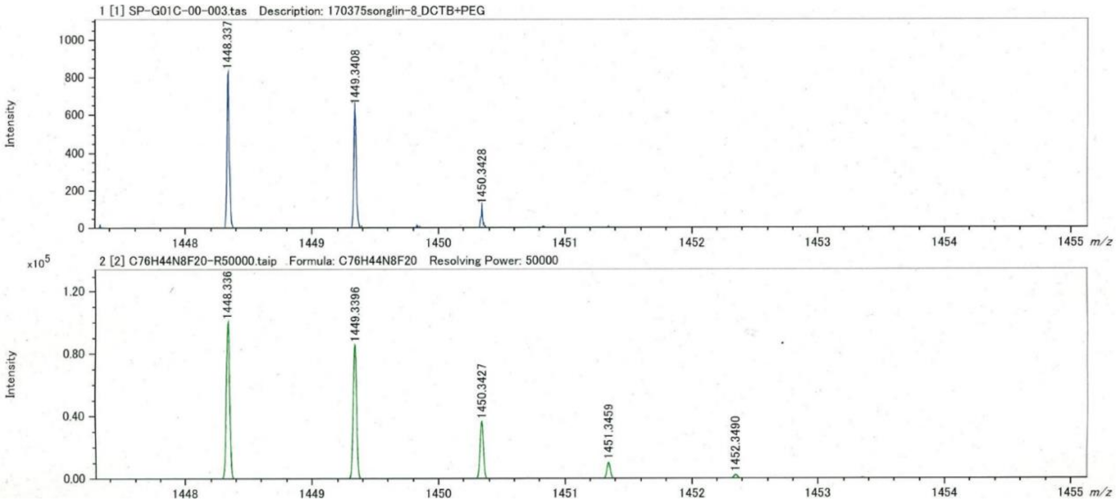

Figure S4.5. HR-MALDI-MS spectrum of **4-3**.

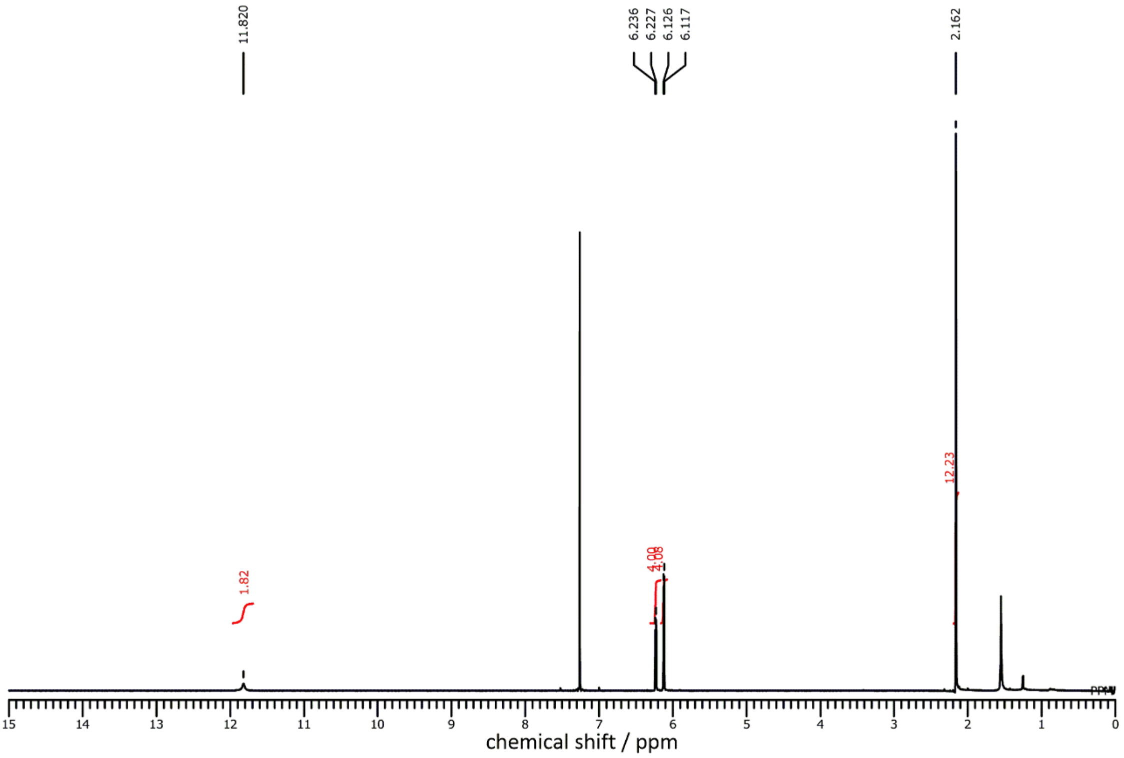

Figure S4.6. ^{1}H NMR spectrum of **4-1** in $CDCl_3$.

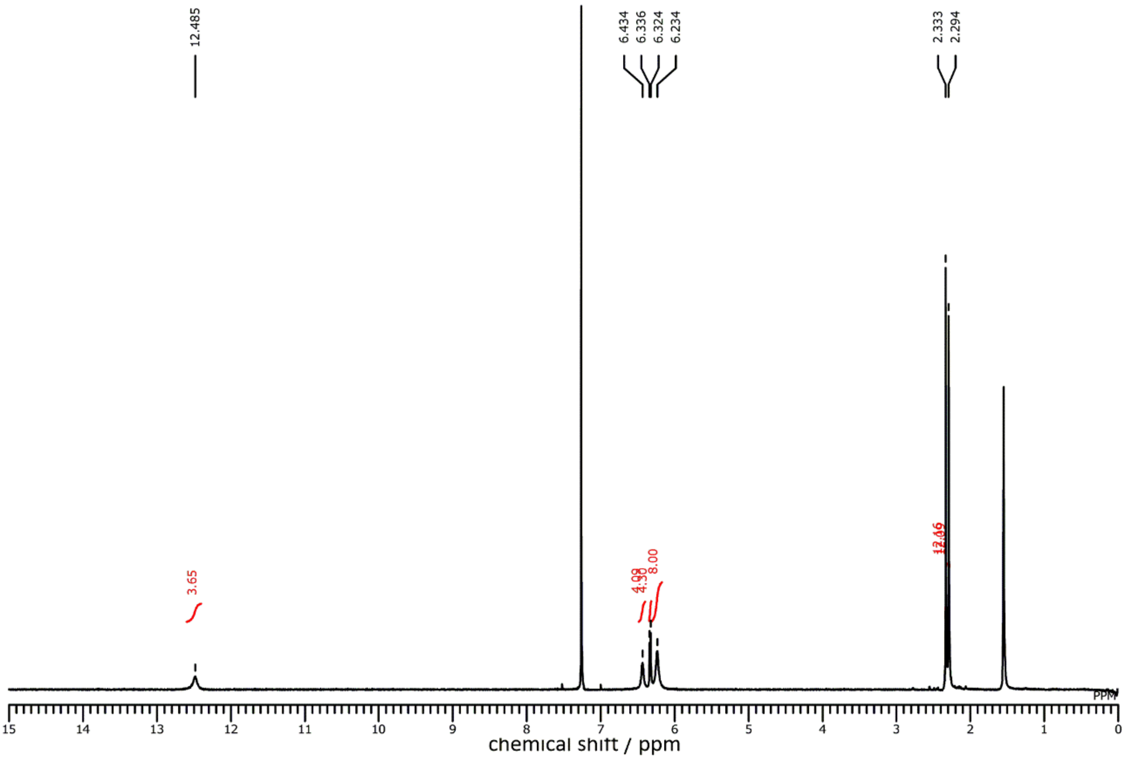

Figure S4.7. ^{1}H NMR spectrum of **4-3** in $CDCl_3$.

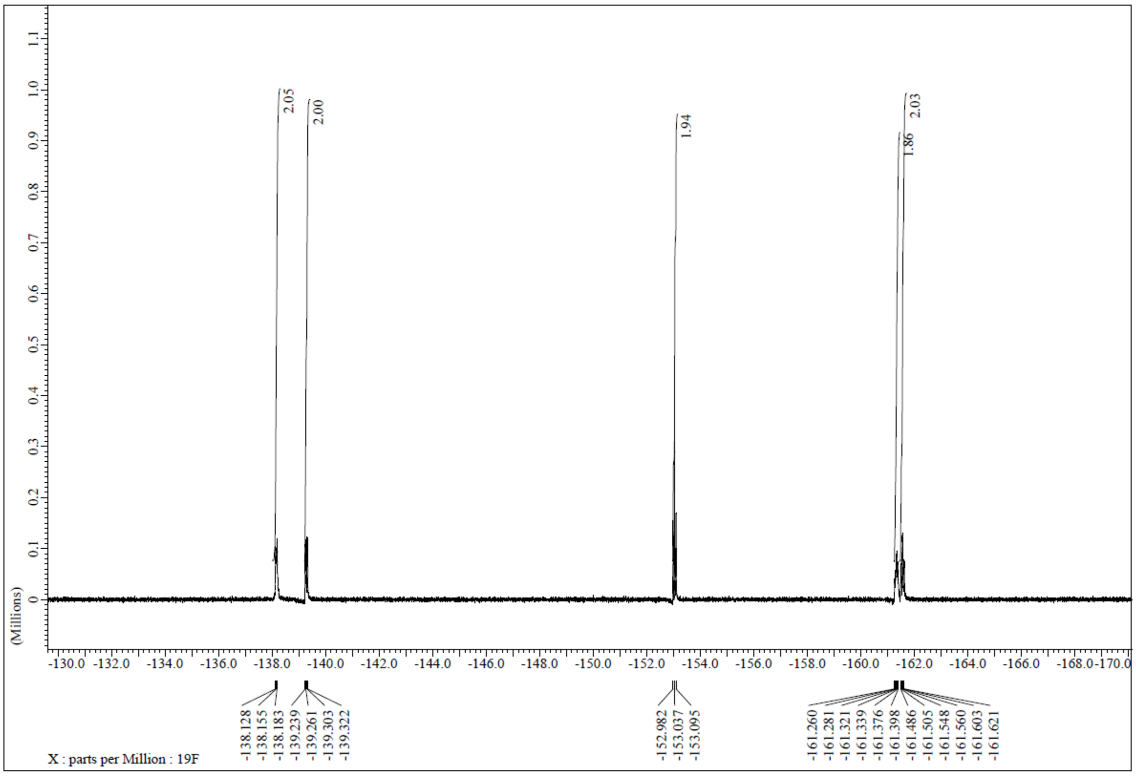

Figure S4.8. ^{19}F NMR spectrum of **4-1** in $CDCl_3$.

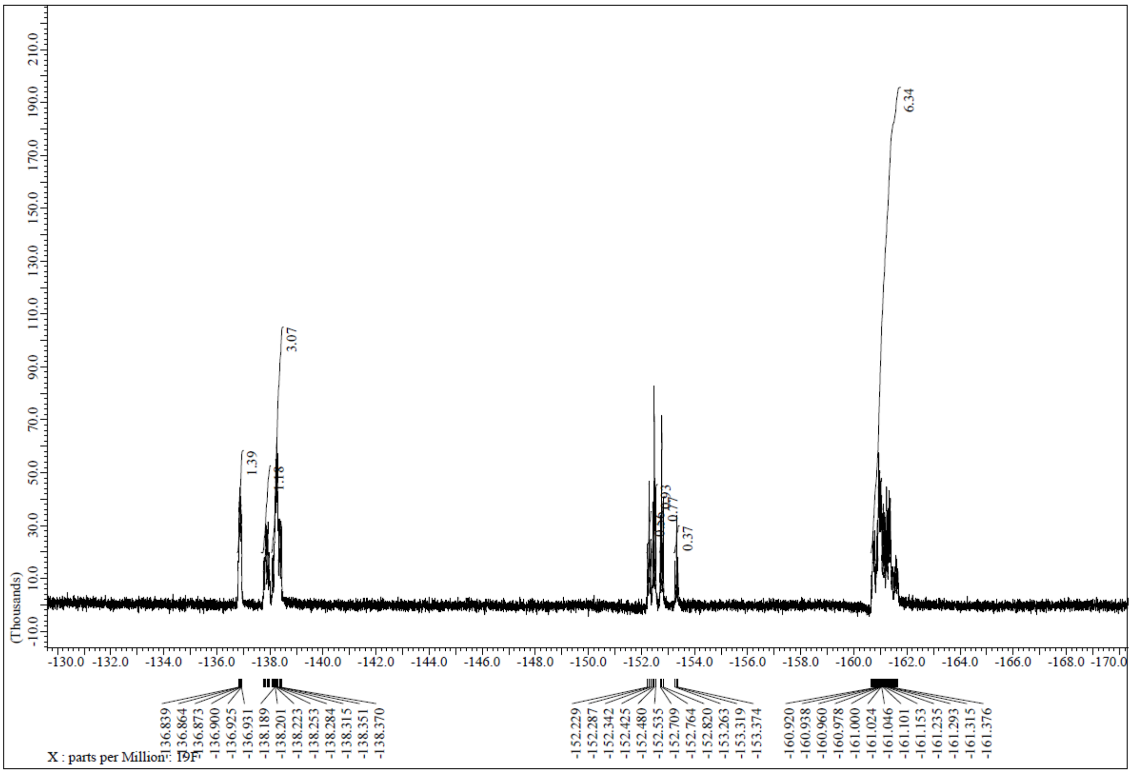

Figure S4.9. ^{19}F NMR spectrum of **4-2** in $CDCl_3$.

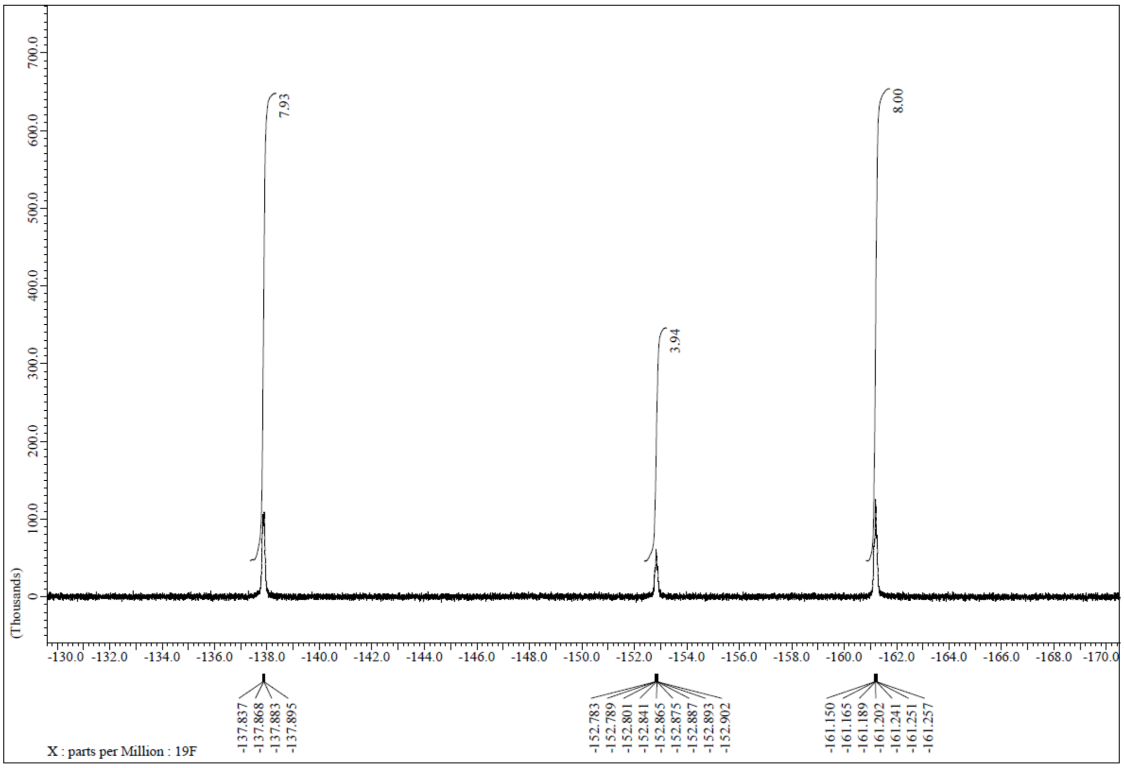

Figure S4.10. ^{19}F NMR spectrum of **4-3** in $CDCl_3$.

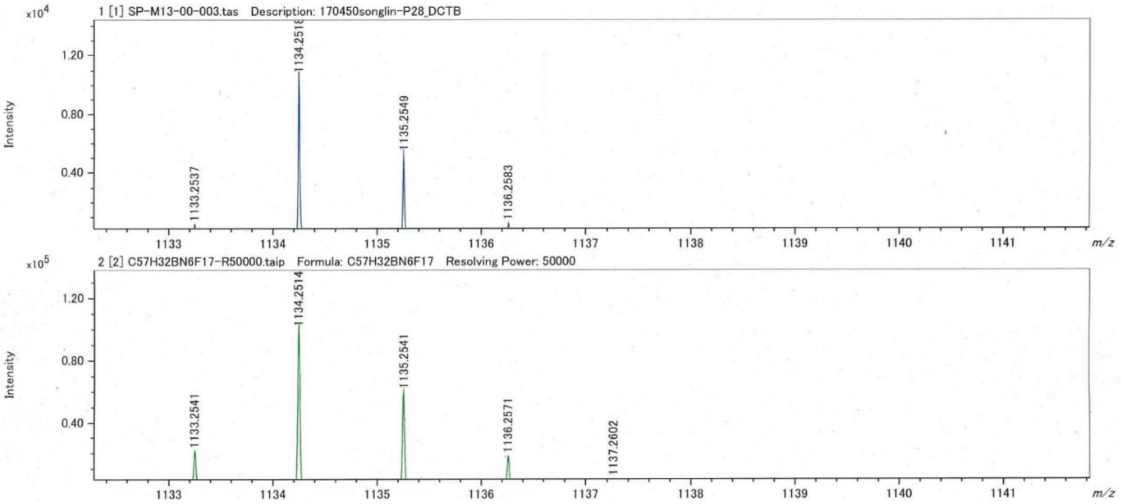

Figure S4.11. HR-MALDI-MS spectrum of **1BF$_2$**.

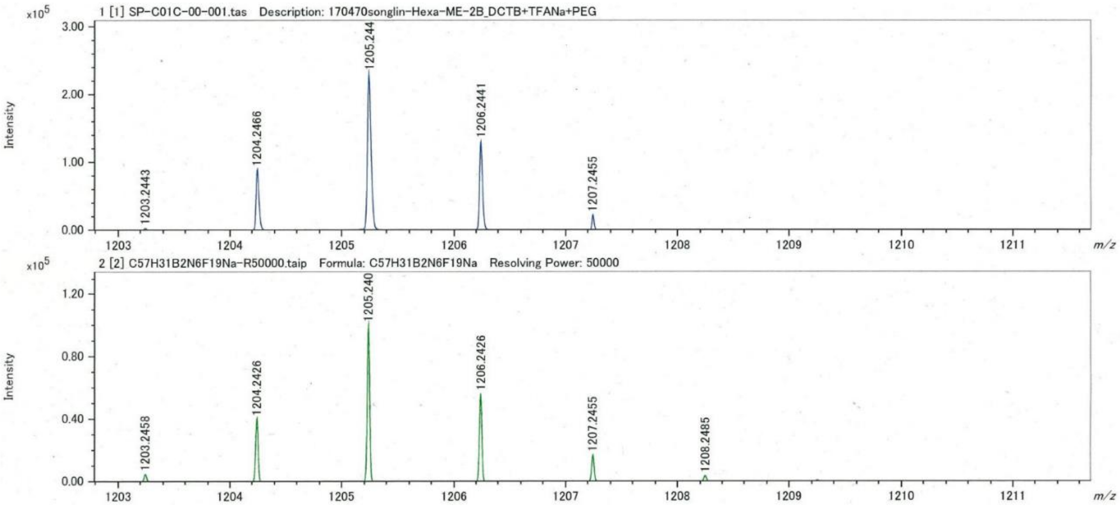

Figure S4.12. HR-MALDI-MS spectrum of **2BF$_2$-a**.

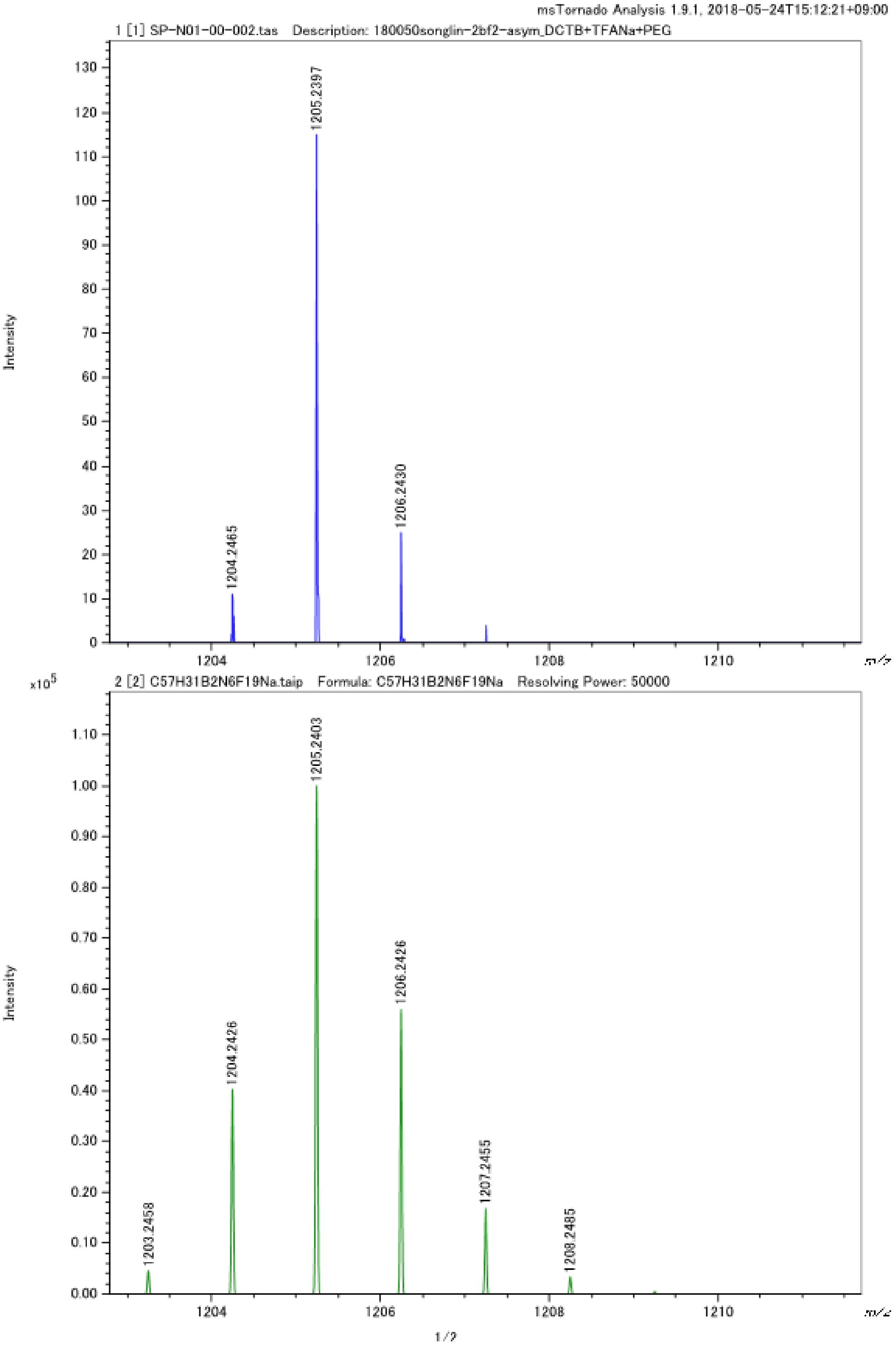

Figure S4.13. HR-MALDI-MS spectrum of **$2BF_2$-b**.

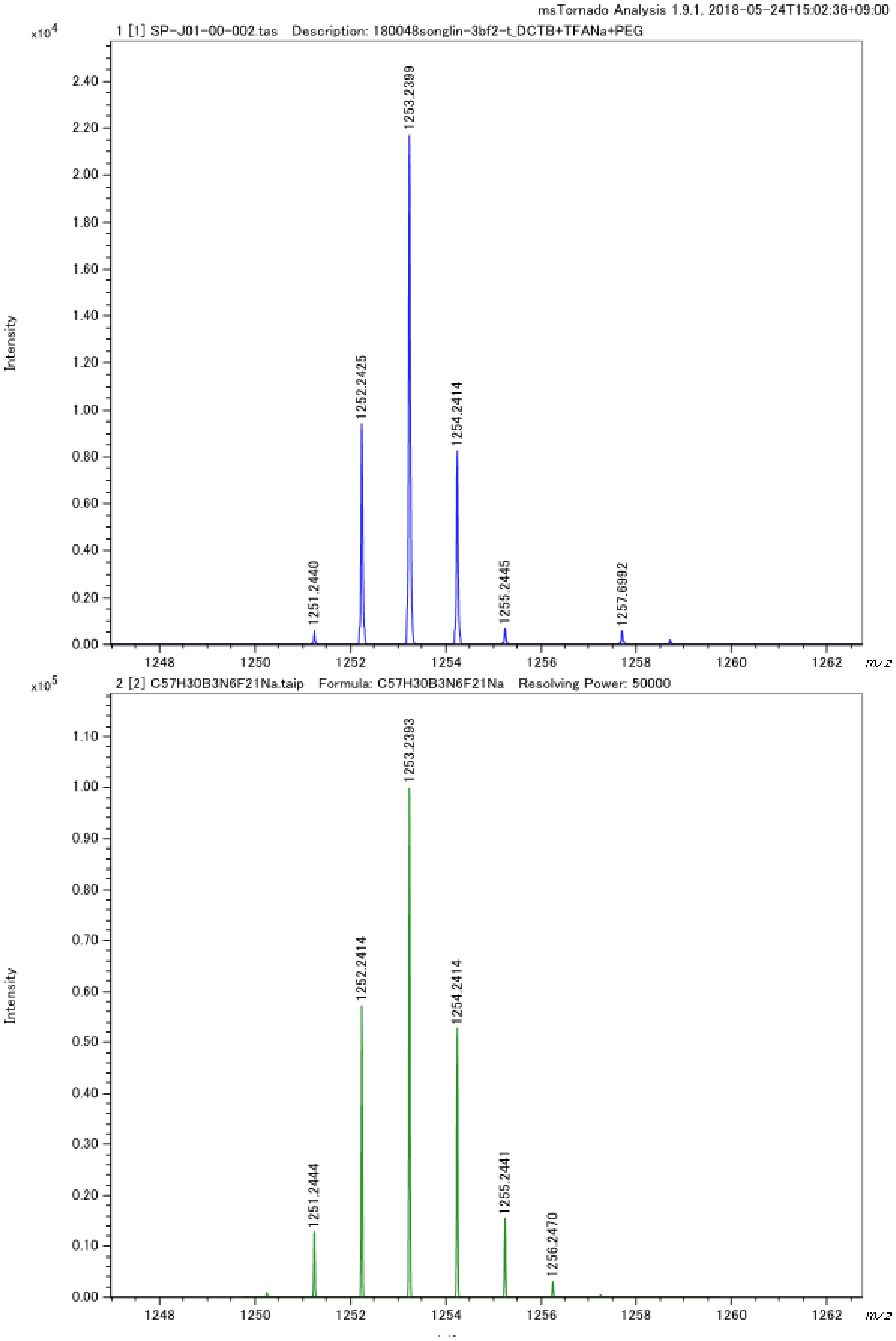

Figure S4.14. HR-MALDI-MS spectrum of **3BF$_2$-a**.

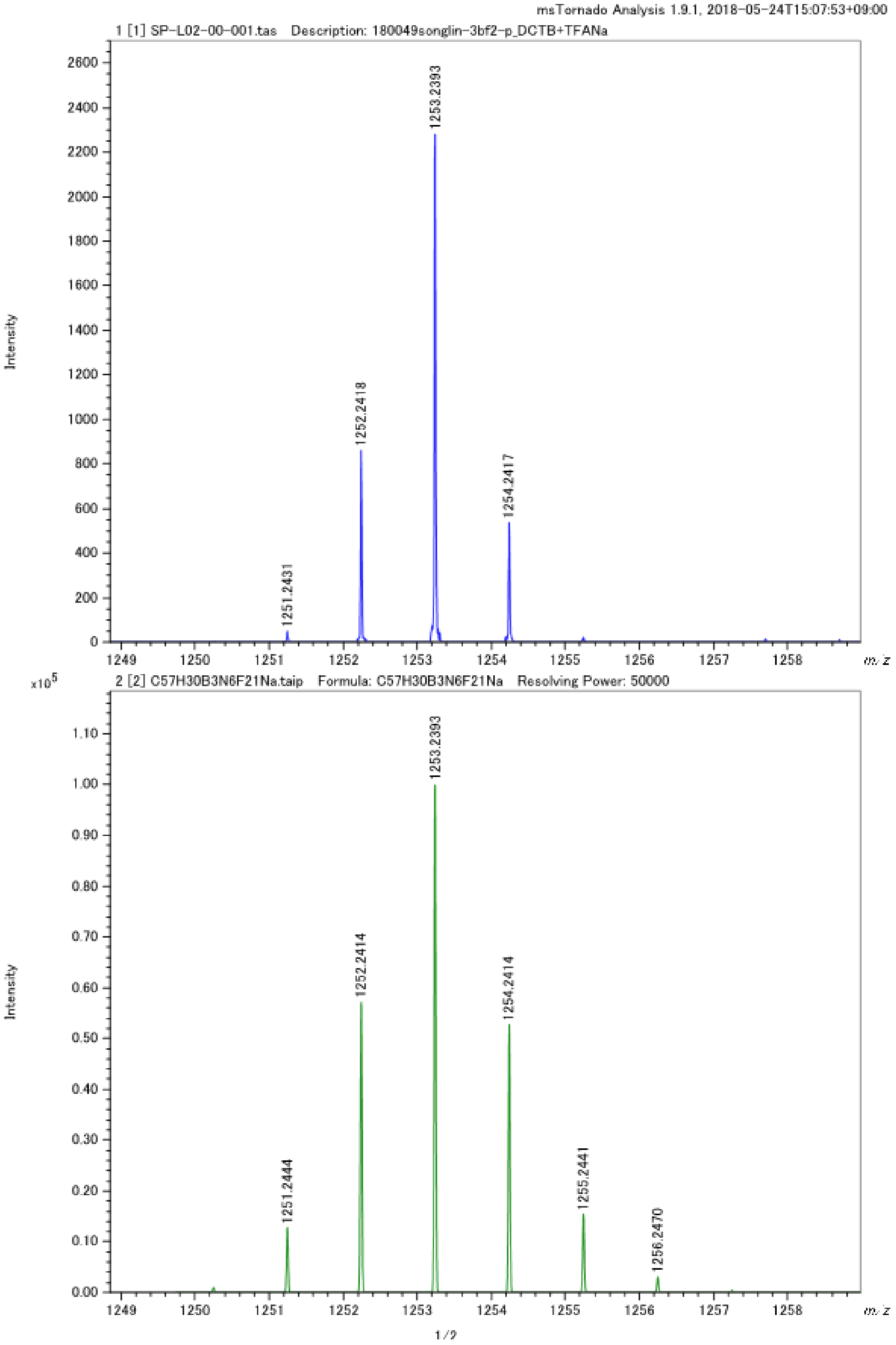

Figure S4.15. HR-MALDI-MS spectrum of **$3BF_2$-b**.

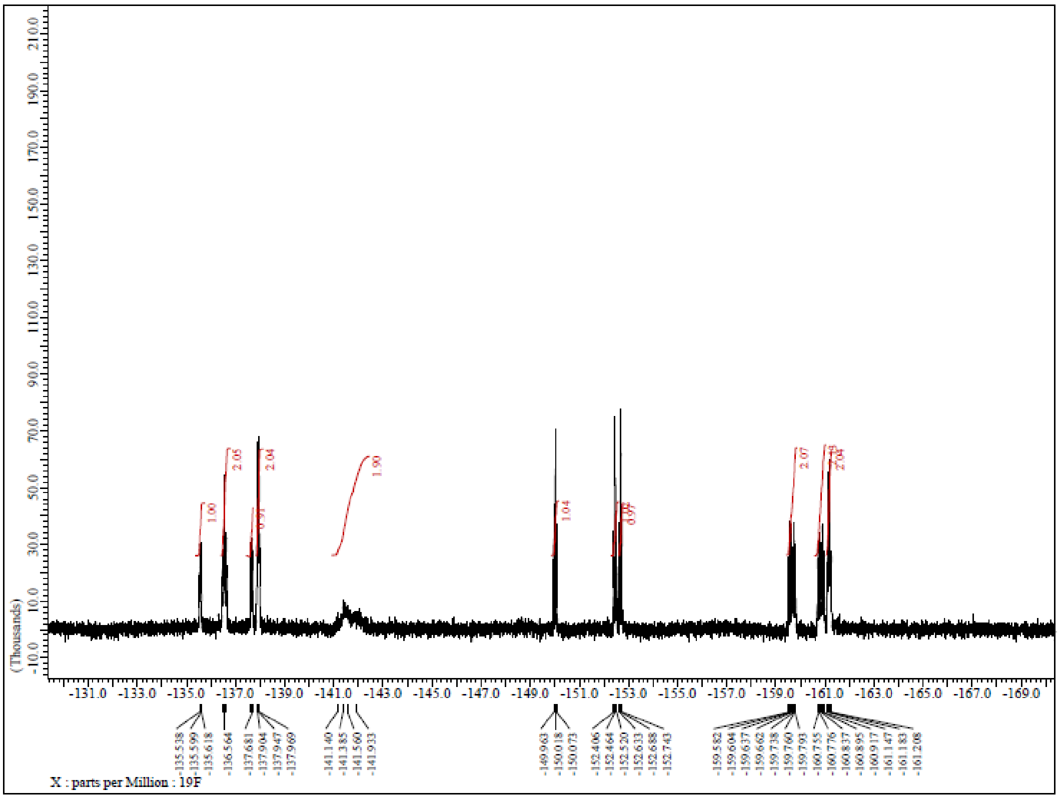

Figure S4.16. ^{19}F NMR spectrum of **1BF$_2$** in CDCl$_3$.

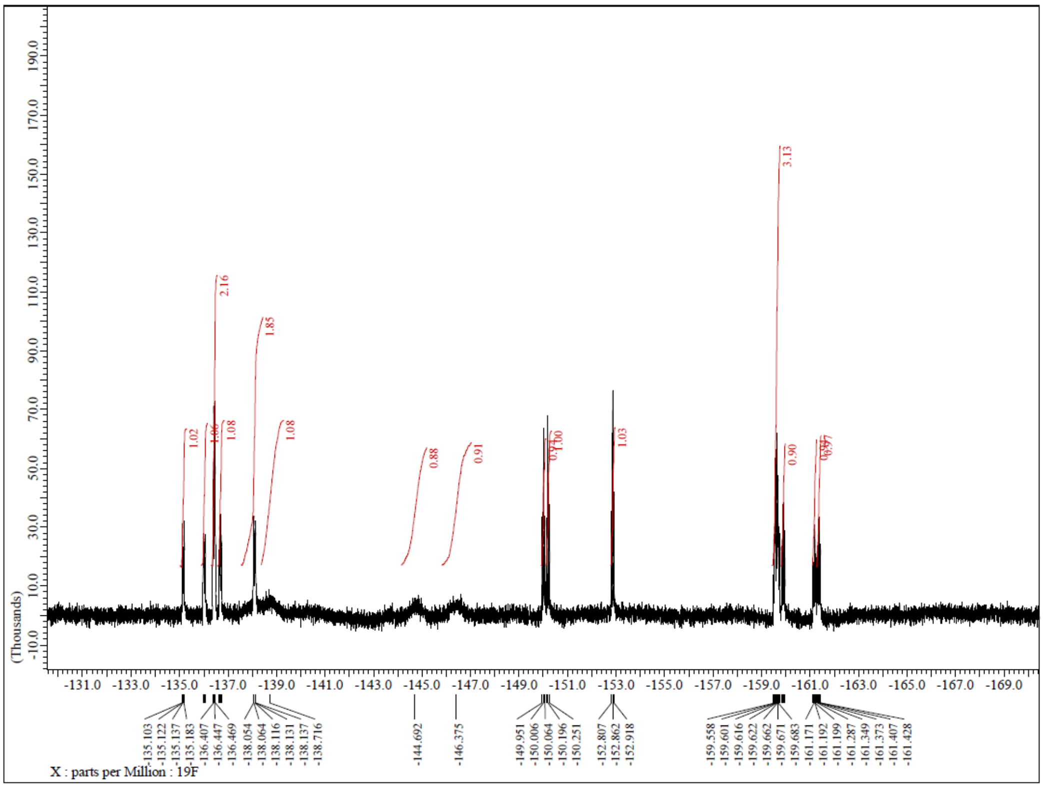

Figure S4.17. ^{19}F NMR spectrum of **2BF$_2$-a** in CDCl$_3$.

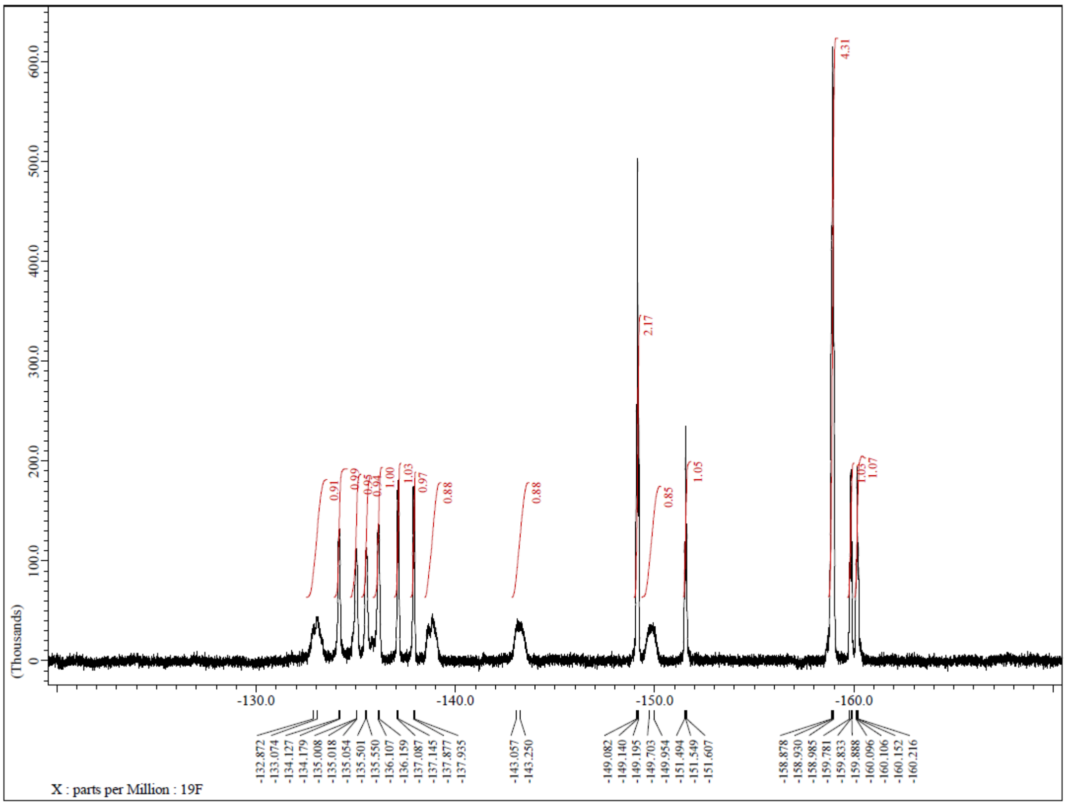

Figure S4.18. ^{19}F NMR spectrum of **$2BF_2$-b** in $CDCl_3$ at 213K..

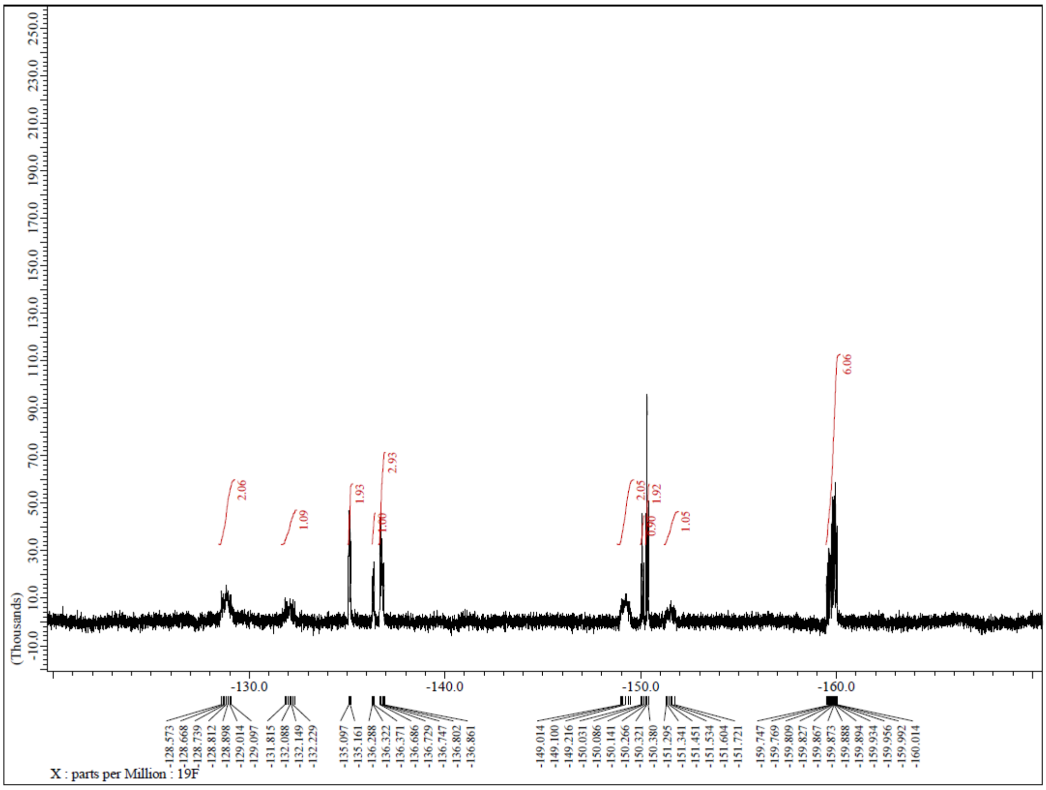

Figure S4.19. ^{19}F NMR spectrum of **$3BF_2$-a** in $CDCl_3$.

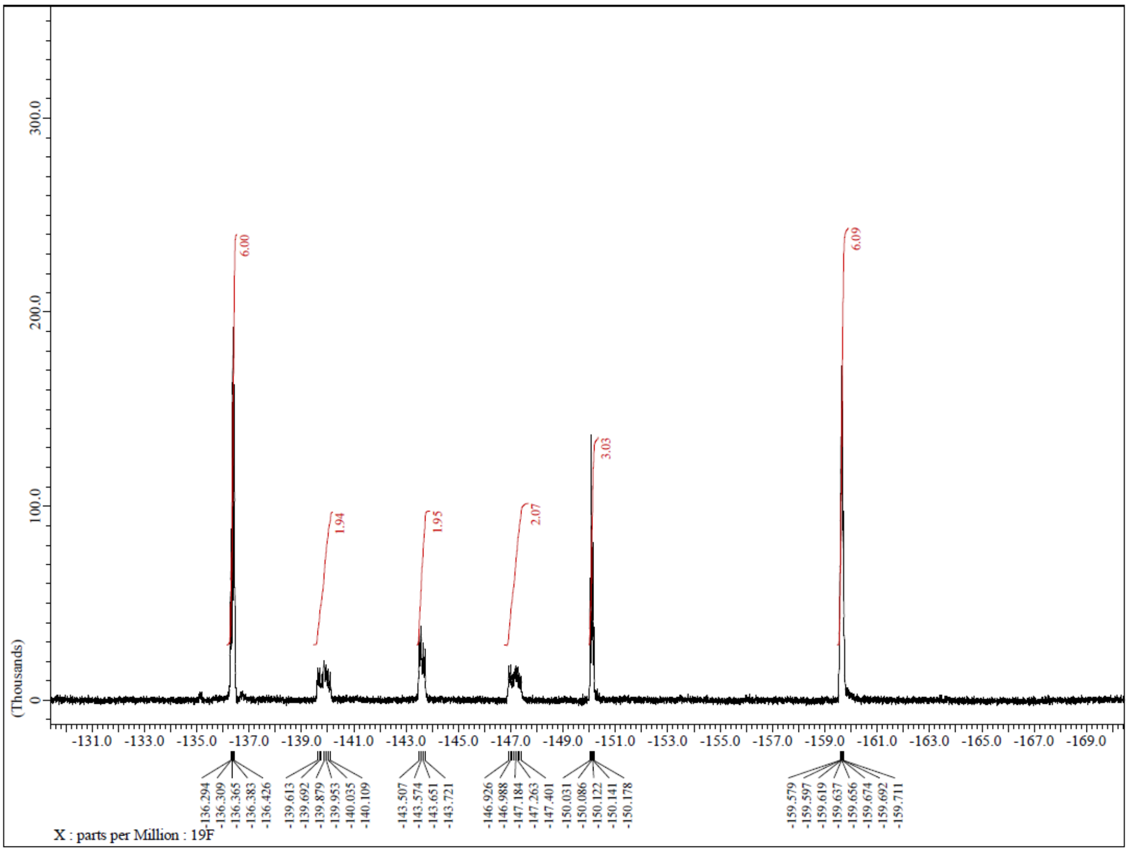

Figure S4.20. ^{19}F NMR spectrum of **3BF$_2$-b** in CDCl$_3$.

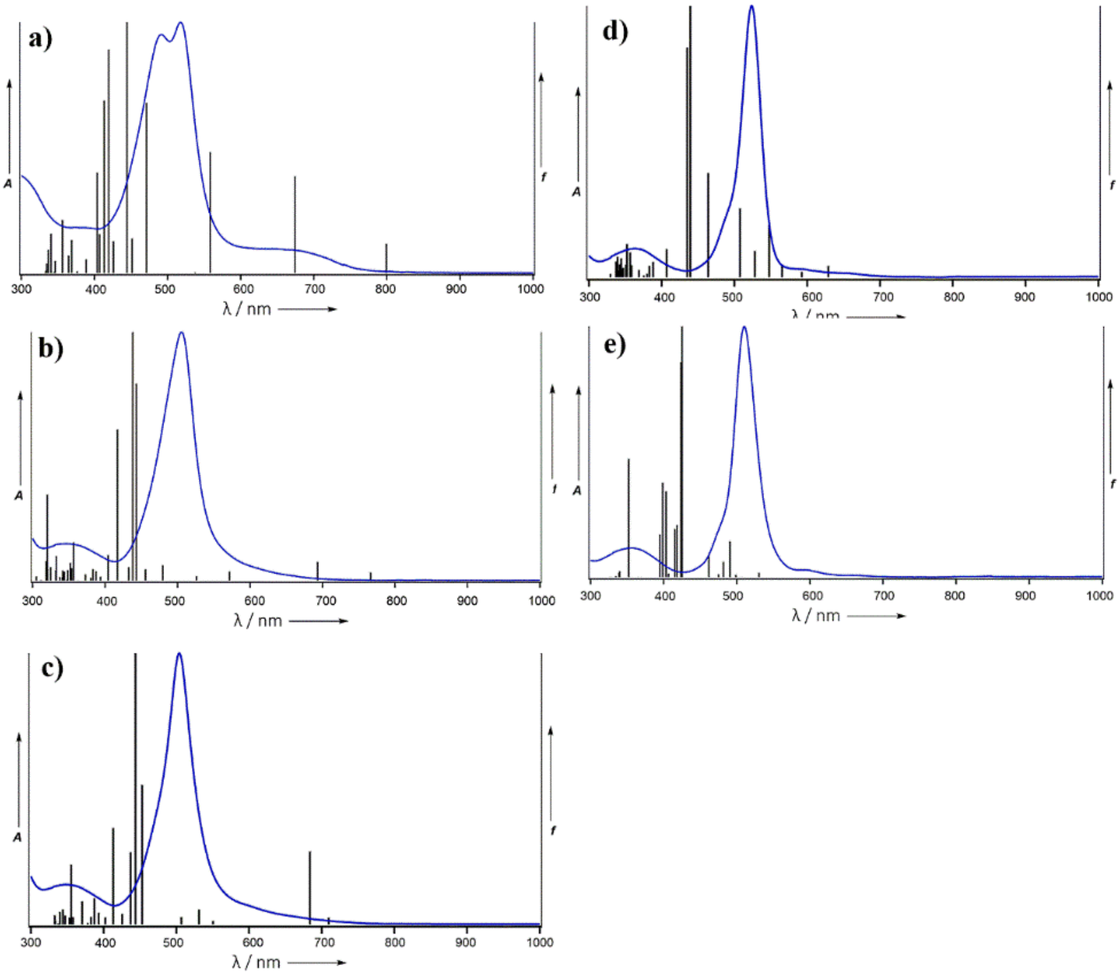

Figure S4.21. Simulated absorption spectra with TD-DFT of a) **1BF$_2$**, b) **2BF$_2$-a**, c) **2BF$_2$-b**, d) **3BF$_2$-a** and 4) **3BF$_2$-b.**

Table S4.1. Crystal data and structure refinement of 4-1.

Empirical formula	$C_{38}H_{22}F_{10}N_4$	
Formula weight	724.60	
Temperature	103 K	
Wavelength	0.71075 Å	
Crystal system	Monoclinic	
Space group	$P2_1$/c(#14)	
Unit cell dimensions	a = 17.4510(4) Å	
	b = 19.8253(4) Å	β = 91.195(6)°
	c = 10.1920(2) Å	
Volume	3525.35(13) $Å^3$	
Z	4	
Density (calculated)	1.365 g/cm^3	
Absorption coefficient	1.183 cm^{-1}	
F(000)	1472.00	
Crystal size	0.130 x 0.020 x 0.20 mm^3	
Theta range for data collection	3.113 to 25.350°.	
Index ranges	$-41 \leq h \leq 41$, $-23 \leq k \leq 23$, $-25 \leq l \leq 25$	
Reflections collected	49001	
Independent reflections	6443 [R(int) = 0.0692]	
Completeness to theta = 25.242°	99.6 %	
Max. and min. transmission	0.998 and 0.801	
Refinement method	Full-matrix least-squares on F^2	
Data / restraints / parameters	6443 / 473 / 113.62	

Goodness-of-fit on F^2	1.018
Final R indices [$I > 2\delta(I)$]	$R_1 = 0.0446$
R indices (all data)	$wR_2 = 0.0944$
Largest diff. peak and hole	0.23 and -0.21 e.Å^{-3}

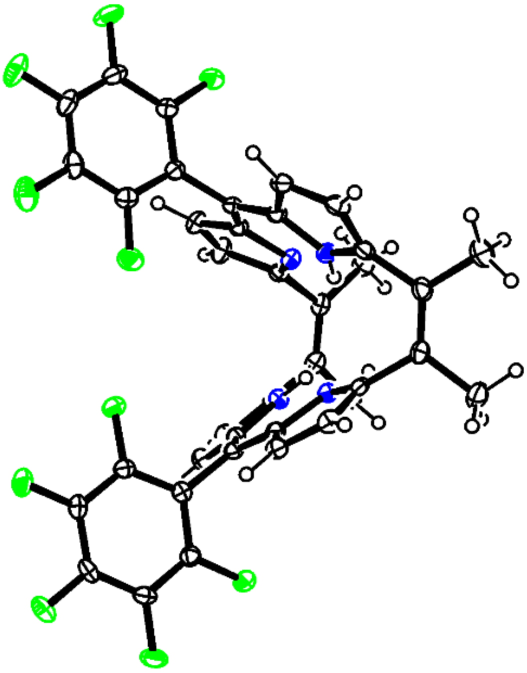

Figure S4.22. Crystal structure of **4-1**. The thermal ellipsoids represent for 50% probability.

Table S4.2. Crystal data and structure refinement of 4-2.

Empirical formula	$C_{57}H_{33}F_{15}N_6$	
Formula weight	1086.90	
Temperature	103 K	
Wavelength	0.71075 Å	
Crystal system	Monoclinic	
Space group	$P2_1/c$(#14)	
Unit cell dimensions	a = 10.0477(2) Å	
	b = 18.2174(5) Å	β = 99.059(7)°.
	c = 28.7465(7) Å	
Volume	5196.2(2) $Å^3$	
Z	4	
Density (calculated)	1.389 g/cm^3	
Absorption coefficient	1.204 cm^{-1}	
$F(000)$	2208	
Crystal size	0.050 x 0.040 x 0.030 mm^3	
Theta range for data collection	3.113 to 25.350°.	
Index ranges	$-41 \leq h \leq 41$, $-23 \leq k \leq 23$, $-25 \leq l \leq 25$	
Reflections collected	64768	
Independent reflections	8541 [R(int) =0.0929]	
Completeness to theta = 25.242°	99.6 %	
Max. and min. transmission	0.996 and 0.665	
Refinement method	Full-matrix least-squares on F^2	
Data / restraints / parameters	8541 / 709 / 12.05	

Goodness-of-fit on F^2	1.031
Final R indices [$I > 2\delta(I)$]	$R_1 = 0.0571$
R indices (all data)	$wR_2 = 0.1387$
Largest diff. peak and hole	0.32 and -0.28 e.Å^{-3}

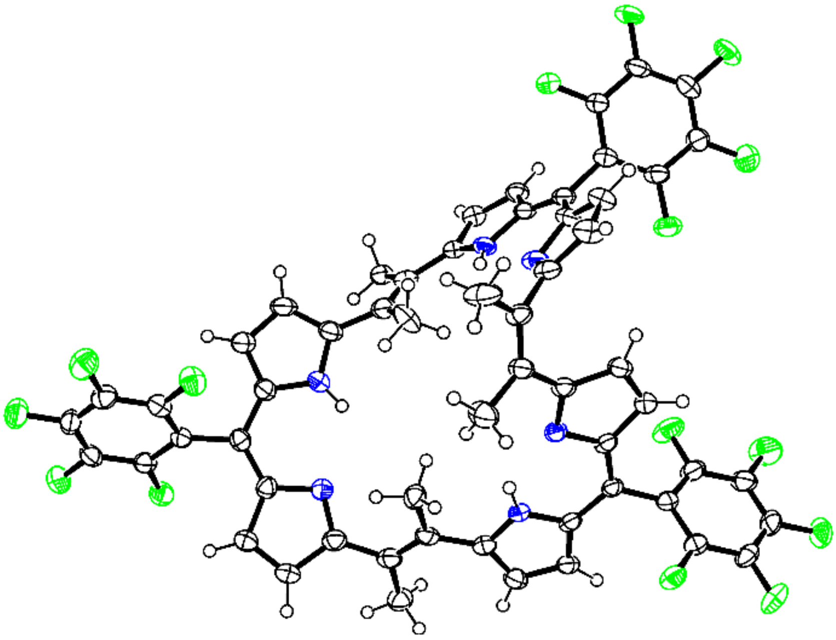

Figure S4.23. Crystal structure of **4-2**. The thermal ellipsoids represent for 50% probability.

Table S4.3. Crystal data and structure refinement of 4-3.

Empirical formula	$C_{90}H_{60}F_{20}N_8$	
Formula weight	1633.49	
Temperature	103 K	
Wavelength	0.71075 Å	
Crystal system	Monoclinic	
Space group	$P2_1/c$(#14)	
Unit cell dimensions	a = 9.2800(7) Å	
	b = 34.913(3) Å	β = 97.438(7)°.
	c = 23.6880(18) Å	
Volume	7610.1(10) $Å^3$	
Z	4	
Density (calculated)	1.426 g/cm^3	
Absorption coefficient	1.186 cm^{-1}	
F(000)	3344.00	
Crystal size	0.260 x 0.30 x 0.020 mm^3	
Theta range for data collection	3.113 to 25.350°.	
Index ranges	$-41 \leq h \leq 41$, $-23 \leq k \leq 23$, $-25 \leq l \leq 25$	
Reflections collected	94248	
Independent reflections	12440 [R(int) = 0.3660]	
Completeness to theta = 25.242°	99.6 %	
Max. and min. transmission	0.998 and 0.356	
Refinement method	Full-matrix least-squares on F^2	
Data / restraints / parameters	12440 / 1073 / 11.59	

Goodness-of-fit on F^2	1.005
Final R indices $[I > 2\delta(I)]$	$R_1 = 0.1115$
R indices (all data)	$wR_2 = 0.3187$
Largest diff. peak and hole	0.42 and -0.31 e.Å^{-3}

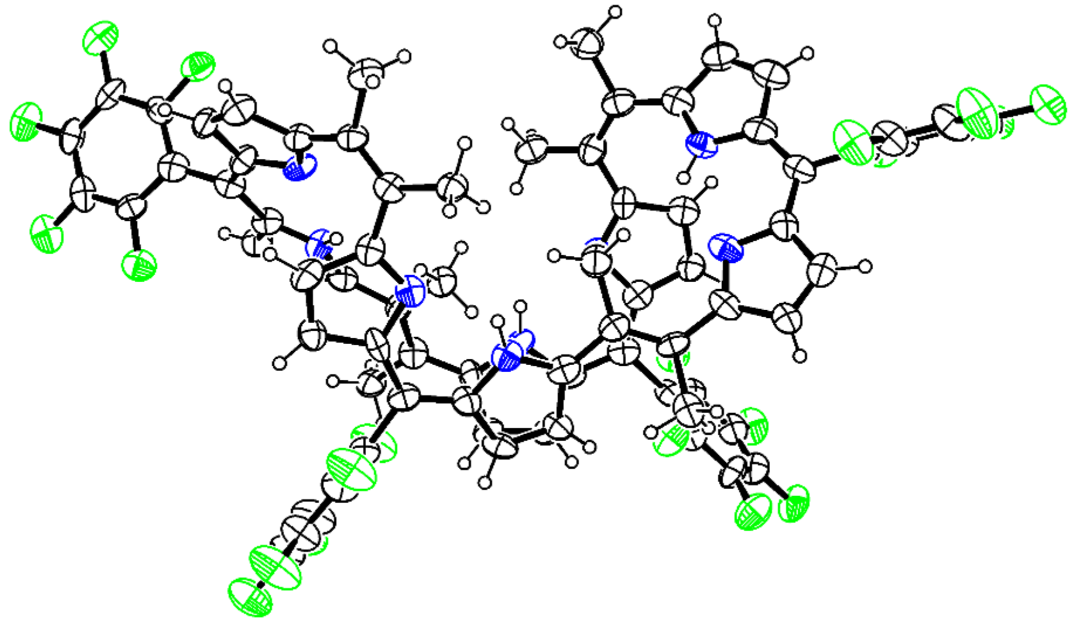

Figure S4.24. Crystal structure of **4-3**. The thermal ellipsoids represent for 50% probability.

Table S4.4. Crystal data and structure refinement of $1BF_2$.

Empirical formula	$C_{57}H_{32}BF_{17}N_6$	
Formula weight	1134.69	
Temperature	90 K	
Wavelength	0.71073Å	
Crystal system	Triclinic	
Space group	*P*-1	
Unit cell dimensions	a = 13.267(2) Å	α = 104.422(3)°.
	b = 15.334(3) Å	β = 109.003(3)°.
	c = 16.490(3) Å	γ = 99.003(3)°.
Volume	2966.7(9) $Å^3$	
Z	2	
Density (calculated)	1.270 mg/m^3	
Absorption coefficient	0.113 mm^{-1}	
F(000)	1148	
Crystal size	0.300 x 0.100 x 0.020 mm^3	
Theta range for data collection	1.631 to 24.000°.	
Index ranges	$-15 <= h <= 15, -11 <= k <= 17, -18 <= l <= 18$	
Reflections collected	125837	
Independent reflections	11291 [*R*(int) = 0.1164]	
Completeness to theta = 24.000°	99.2 %	
Absorption correction	Semi-empirical from equivalents	
Max. and min. transmission	0.975 and 0.497	

Refinement method	Full-matrix least-squares on F^2
Data / restraints / parameters	11291 / 911 / 12.39
Goodness-of-fit on F^2	1.285
Final R indices [I>2sigma(I)]	$R_1 = 0.1228$, $wR_2 = 0.3267$
R indices (all data)	$R_1 = 0.1434$
Extinction coefficient	*n/a*
Largest diff. peak and hole	1.71 and -0.70 e.Å^{-3}

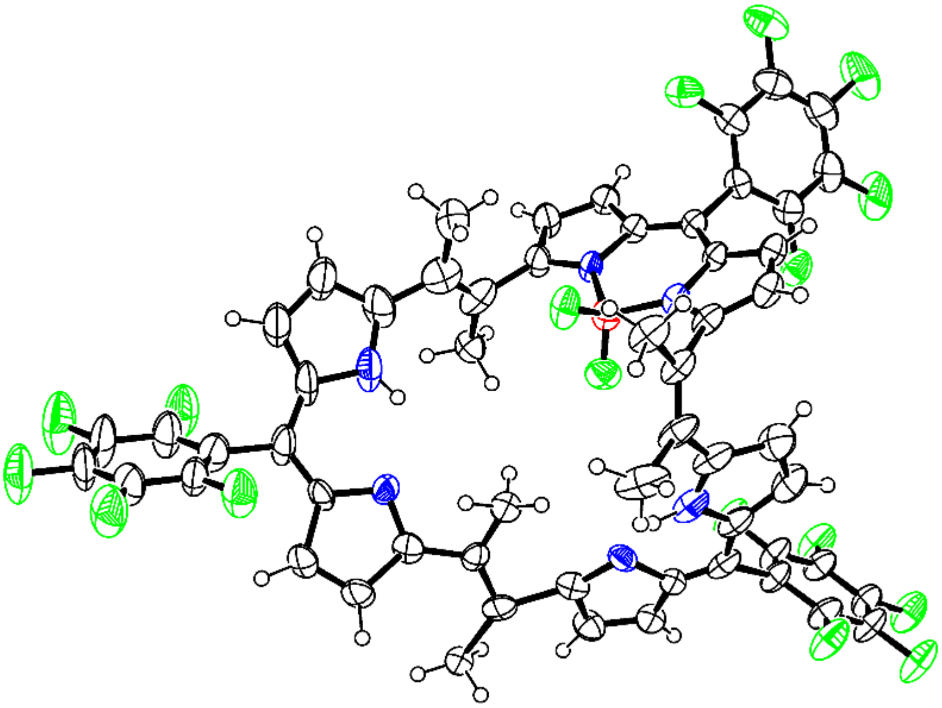

Figure S4.25. Crystal structure of **1BF2**. The thermal ellipsoids represent for 50% probability.

Table S4.5. Crystal data and structure refinement of $2BF_2$-a.

Empirical formula	$C_{57}H_{31}B_2F_{19}N_6$	
Formula weight	1182.50	
Temperature	103 K	
Wavelength	0.71075 Å	
Crystal system	monoclinic	
Space group	$P2_1/c$(#14)	
Unit cell dimensions	a = 14.1364(9) Å	
	b = 30.887(2) Å	β = 103.727(7)°.
	c = 11.9832(8) Å	
Volume	5082.7(6) Å^3	
Z	4	
Density (calculated)	1.545 g/cm^3	
Absorption coefficient	1.403 cm^{-1}	
F(000)	2384.00	
Crystal size	0.200 x 0.100 x 0.010 mm^3	
Theta range for data collection	3.113 to 25.350°.	
Index ranges	$-41 \leq h \leq 41$, $-23 \leq k \leq 23$, $-25 \leq l \leq 25$	
Reflections collected	68779	
Independent reflections	9295 [R(int) = 0.1627]	
Completeness to theta = 25.242°	99.6 %	
Max. and min. transmission	0.999 and 0.212	
Refinement method	Full-matrix least-squares on F^2	
Data / restraints / parameters	9295 / 763 / 12.18	

Goodness-of-fit on F^2	1.043
Final R indices $[I > 2\delta(I)]$	$R_1 = 0.0976$
R indices (all data)	$wR_2 = 0.2668$
Largest diff. peak and hole	0.28 and -0.26 e.Å^{-3}

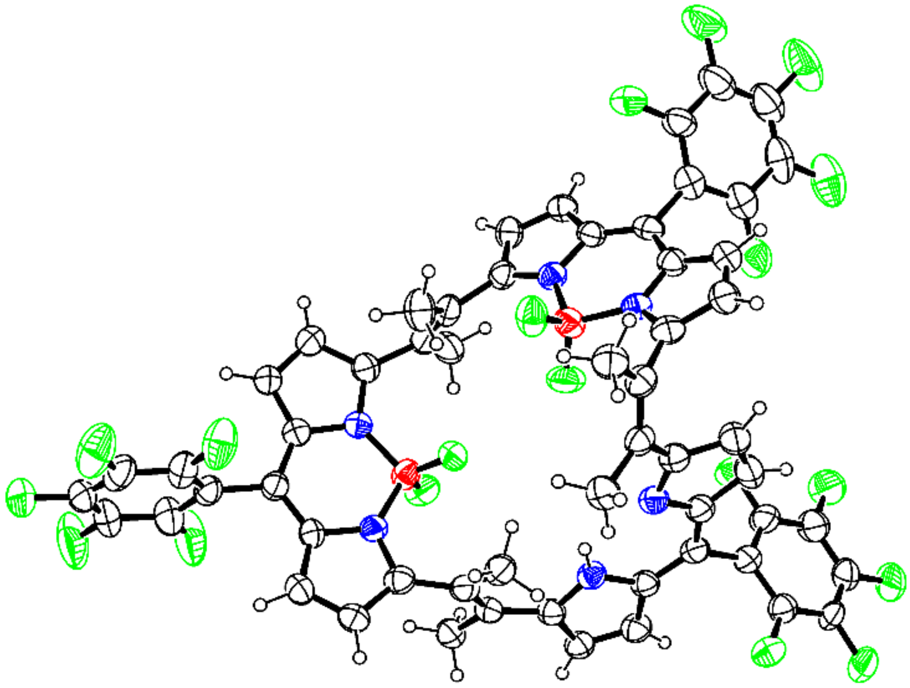

Figure S4.26. Crystal structure of **2BF$_2$-a**. The thermal ellipsoids represent for 50% probability.

Table S4.6. Crystal data and structure refinement of 2BF_2-b.

Empirical formula	$C_{66}H_{31}B_2F_{19}N_6$	
Formula weight	1290.59	
Temperature	90 K	
Wavelength	0.71073 Å	
Crystal system	Triclinic	
Space group	*P*-1	
Unit cell dimensions	a = 11.7169(7) Å	α = 95.7087(11)°.
	b = 14.6385(9) Å	β = 97.4311(12)°.
	c = 18.5296(11) Å	γ = 105.6457(11)°.
Volume	3004.5(3) $Å^3$	
Z	2	
Density (calculated)	1.427 Mg/m^3	
Absorption coefficient	0.126 mm^{-1}	
F(000)	1300	
Crystal size	0.300 x 0.300 x 0.300 mm^3	
Theta range for data collection	1.983 to 27.939°.	
Index ranges	$-15 <= h <= 12$, $-19 <= k <= 19$, $-16 <= l <= 24$	
Reflections collected	20417	
Independent reflections	14252 [*R*(int) = 0.0186]	
Completeness to theta = 25.242°	99.3 %	
Absorption correction	Semi-empirical from equivalents	
Max. and min. transmission	0.963 and 0.907	

Refinement method	Full-matrix least-squares on F^2
Data / restraints / parameters	14252 / 2 / 940
Goodness-of-fit on F^2	1.319
Final R indices [I>2sigma(I)]	R_1 = 0.0745, wR_2 = 0.2031
R indices (all data)	R_1 = 0.1111, wR_2 = 0.2281
Extinction coefficient	*n/a*
Largest diff. peak and hole	1.050 and -0.659 e.Å^{-3}

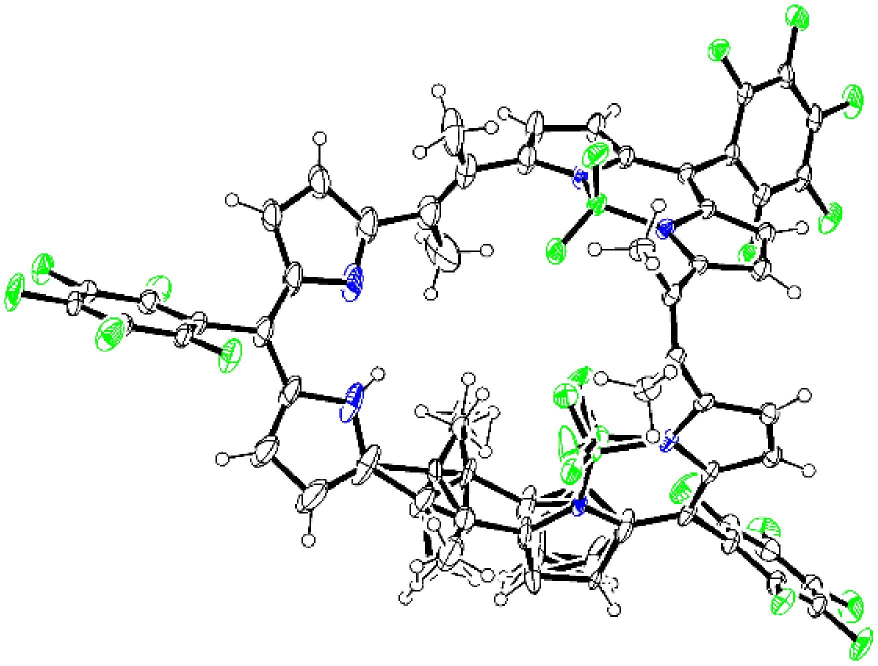

Figure S4.27. Crystal structure of **2BF$_2$-b**. The thermal ellipsoids represent for 50% probability.

Table S4.7. Crystal data and structure refinement of $3BF_2$-a.

Empirical Formula	$C_{60}H_{32}B_3Cl_9F_{21}N_6$
Formula Weight	1587.43
Crystal Color, Habit	purple, prism
Crystal Dimensions	0.120 x 0.050 x 0.050 mm
Crystal System	trigonal
Lattice Type	Primitive
Lattice Parameters	a = 26.8942(12) Å
	c = 15.0541(3) Å
	V = 9429.8(6) $Å^3$
Space Group	*P3c1*
Z value	6
Dcalc	1.677 g/cm^3
F(000)	4746.00
μ(MoKα)	5.103 cm^{-1}
Diffractometer	R-AXIS RAPID
Radiation	MoKα (λ = 0.71075 Å)
	multi-layer mirror monochromated
Voltage, Current	50 kV, 24 mA
Temperature	-170.0°C
Detector Aperture	460.0 x 256.0 mm
Data Images	192 exposures
ω oscillation Range (χ = 45.0, ϕ = 0.0)	130.0 - 190.0°
Exposure Rate	110.0 sec./°

ω oscillation Range (χ = 45.0, ϕ = 210.0)	0.0 - 162.0°
Exposure Rate	110.0 sec./°
ω oscillation Range (χ = 45.0, ϕ = 105.0)	0.0 - 162.0°
Exposure Rate	110.0 sec./°
Detector Position	127.40 mm
Pixel Size	0.100 mm
2θmax	50.7°
No. of Reflections Measured	Total: 125837
	Unique: 11291 (Rint = 0.1164)
	Parsons quotients (Flack x parameter): 3095
Corrections	Lorentz-polarization Absorption
	(trans. factors: 0.497 - 0.975)
Structure Solution	Direct Methods (SHELXT Version 2014/5)
Refinement	Full-matrix least-squares on F^2
Function Minimized	Σ w $(Fo^2 - Fc^2)^2$
Least Squares Weights	w = 1/ [$\sigma^2(Fo^2)$ + $(0.2000. P)^2$
	+ 0.0000. P]
	where P = $(Max(Fo^2,0) + 2Fc^2)/3$
2θmax cutoff	50.7°
Anomalous Dispersion	All non-hydrogen atoms
No. Observations (All reflections)	11291
No. Variables	911
Reflection/Parameter Ratio	12.39
Residuals: R_1 ($I > 2.00\sigma(I)$)	0.1228

Residuals: R (All reflections)	0.1434
Residuals: wR_2 (All reflections)	0.3267
Goodness of Fit Indicator	1.285
Flack parameter (Parsons' quotients = 3095)	0.20(3)
Max Shift/Error in Final Cycle	0.001
Maximum peak in Final Diff. Map	1.71 e.Å^3
Minimum peak in Final Diff. Map	-0.70 e.Å^3

Table S4.8. Crystal data and structure refinement of 3BF$_2$-b.

Empirical formula	$C_{60}H_{33}B_3Cl_9F_{21}N_6$
Formula weight	1588.40
Temperature	90 K
Wavelength	0.71073 Å
Crystal system	Hexagonal
Space group	$P6_3/m$
Unit cell dimensions	a = 20.714(3) Å
	c = 9.1709(12) Å
Volume	3407.7(10) Å^3
Z	2
Density (calculated)	1.548 mg/m^3
Absorption coefficient	0.471 mm^{-1}
F(000)	1584
Crystal size	0.200 x 0.100 x 0.050 mm^3
Theta range for data collection	1.966 to 24.976°.
Index ranges	$-24 <= h <= 21, -24 <= k <= 20, -10 <= l$

<= 10

Reflections collected	17971
Independent reflections	2124 [R(int) = 0.0673]
Completeness to theta = 24.976°	99.8 %
Absorption correction	Semi-empirical from equivalents
Max. and min. transmission	0.977 and 0.846
Refinement method	Full-matrix least-squares on F^2
Data / restraints / parameters	2124 / 10 / 247
Goodness-of-fit on F^2	1.402
Final R indices [I>2sigma(I)]	R_1 = 0.1103, wR_2 = 0.3207
R indices (all data)	R_1 = 0.1610, wR_2 = 0.3787
Extinction coefficient	*n/a*
Largest diff. peak and hole	0.922 and -0.620 e.Å^{-3}

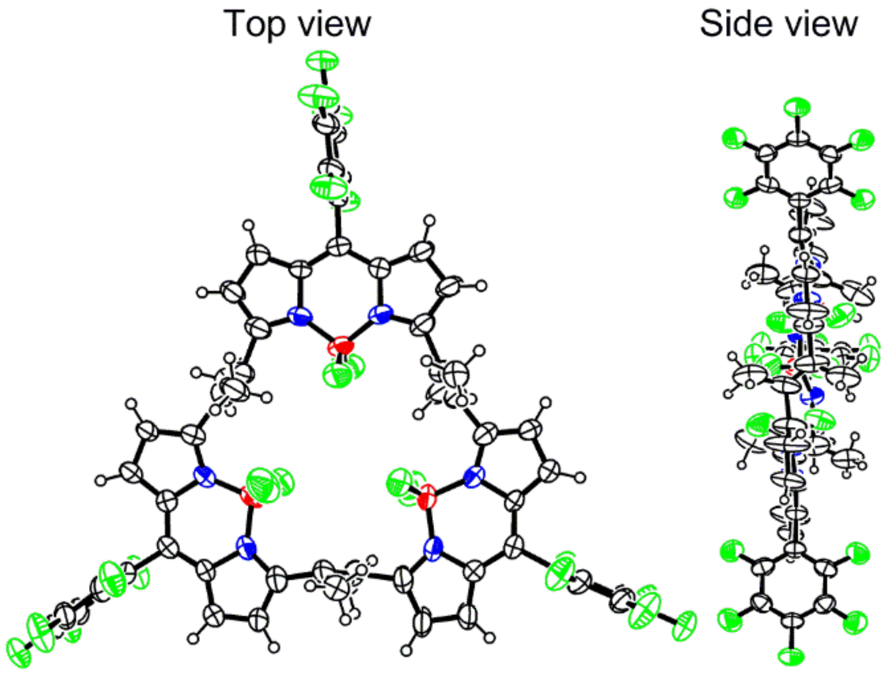

Figure S4.29. Crystal structure of **3BF$_2$-b**. The thermal ellipsoids represent for 50% probability.

Chapter 5

Porphyrin(2.1.2.1)-Based Nanobelts

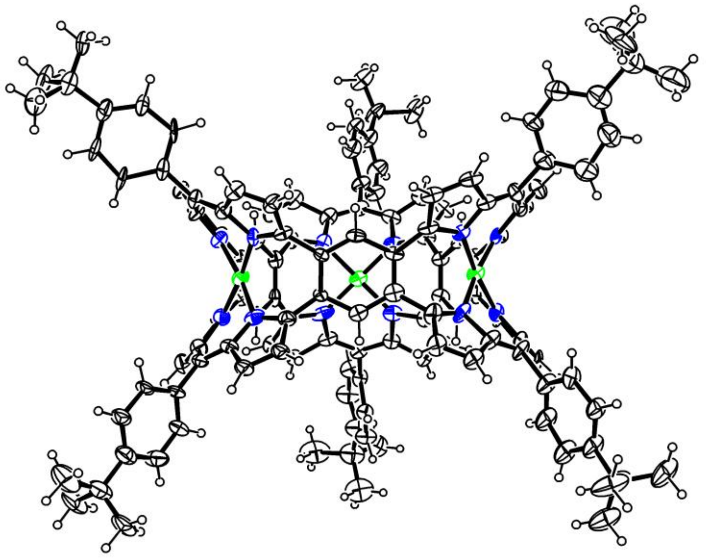

In this Chapter, the synthesis, characterization and binding ability of porphyrin(2.1.2.1)-based nanobelt are described.

5-1 Introduction

More than 30 years have passed since the discovery of C_{60} in 1985. The modern nanocarbon chemistry started at that time (Figure 5.1).[1a] The single-walled carbon nanotube (**SWNT**) as 1D nanocarbon has been attracting great attentions because of unique structures, remarkable physical and chemical properties, such as high mechanical strength, coherent electron transport, excellent thermal properties and self-assembly property.[1c]

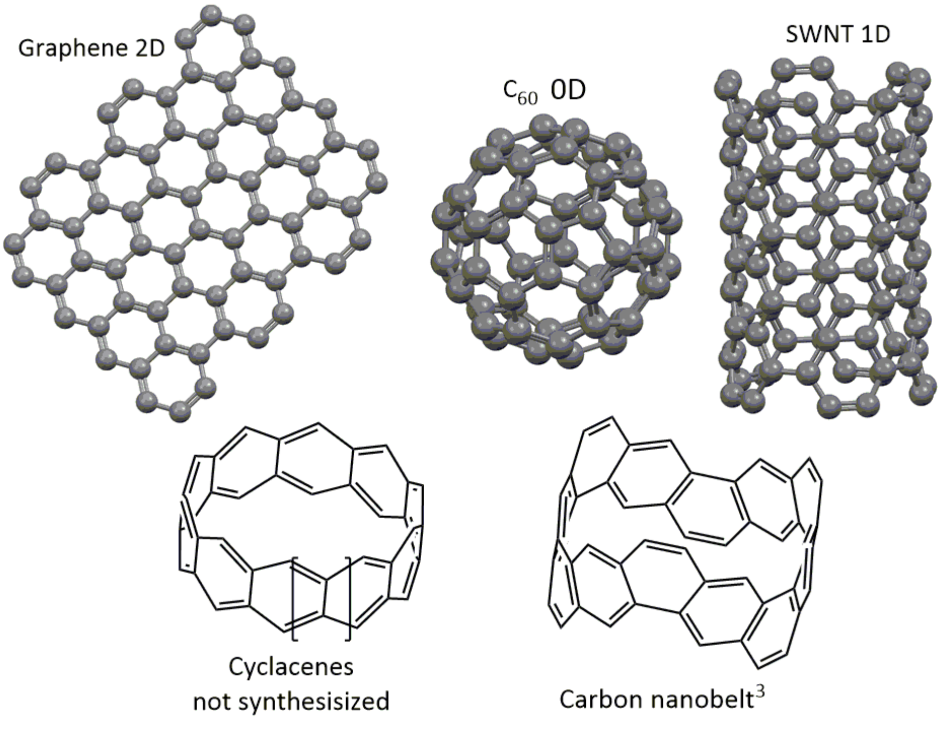

Figure 5.1. Nanocarbons.

As a fragment of **SWNT**, the belt-shaped compounds comprised of benzene rings has attracted extensively attentions in organic chemistry for the last decade.[1c,1d] The belt-shaped compounds are important platforms for exploration of bent aromatic molecules. The twisted aromatic compounds are expected to display novel electronic properties referred to the normal planar aromatic molecules.[2] In 2017, Itami and co-workers reported the first carbon nanobelt by multi-step Witting reactions and Ni catalyzed aryl-aryl coupling reaction (Figure 5.1).[3]

Porphyrin is a representative compound with planar molecular structure and aromatic property. It can act as building units for constructing porphyrin nanorings, nanotube, nanobarrel and Ruassian Doll.[4] These cyclic porphyrins oligomers have some interesting properties.[4] The reported porphyrin nanotube has 3D π-conjugation. Porphyrin nanobarrel show nice C_{60} binding ability in its cavity. However, the porphyrin nanobelt has not been reported yet. Recently, an arch-shaped molecule, dibenzoporphyrin(2.1.2.1), was developed by our group.[5] 1,2-Di(pyrrol-2-ly)benzene reacted with various aldehydes in presence of acid to generate dibenzoporphyrin(2.1.2.1). Dibenzoporphyrin(2.1.2.1) and its metal complexes show arch-shaped molecular structures. In this context, it was expected that arch-shaped dibenzoporphyrin(2.1.2.1) could produce a porphyrin(2.1.2.1) nanobelt.

In this Chapter, the synthesis of porphyrin(2.1.2.1) nanobelts was developed by simple one-pot condensation reaction from 1,2,4,5-tetra(pyrrol-2-ly)benzene (**TPB**) and benzaldehyde derivative under acidic conditions. This condensation reaction gave porphyrin(2.1.2.1) nanobelt in acceptable yield and with very nice repeatability. The X-ray crystallography reveals that porphyrin(2.1.2.1) nanobelts form C_{3h}-symmetric structure comprising large binding surface. The details of synthesis, optical and electrochemical properties, crystal structure, DFT calculation and C_{60} binding ability of porphyrin nanobelts will be presented.

5-2 Synthesis

The detailed synthesis is shown in scheme 5.1 and supporting information. The key intermediate **TPB** is synthesized from 1,2,4,5-tetrabromobenzene and 1-(*t*-butoxycarbonyl)-pyrrole-2-boronic acid under Pd-catalysis coupling, follows by de-protection reaction under a heating condition.

The synthetic strategy of porphyrin(2.1.2.1) nanobelts involves the use of condensation and coordination reactions. Considering the purification and stability, metal complexes of porphyrin nanobelts, **NBNi$_3$** and **NBCu$_3$**, are chosen as target compounds. Treatment of **TPB** with 4-(*tert*-butyl)benzaldehyde in the presence of $BF_3•OEt_2$ as an acid catalyst in CH_2Cl_2, followed by oxidation with DDQ, then coordination with $Ni(OAc)_2•4H_2O$ and $Cu(OAc)_2•H_2O$ to afford **NBNi$_3$** and **NBCu$_3$** in 4% and 3%, respectively. The MS peak of cyclic tetramer only is detected, however, tetramer could not be isolated under this reaction condition. The HR-MALDI-MS detect corresponding molecular ion peaks of **NBNi$_3$** at $m/z = 2034.6870$ (calcd. for m/z $C_{132}H_{108}Ni_3N_{12} = 2034.6875$ $[M]^+$) and **NBCu$_3$** at $m/z = 2049.6750$ (calcd. for m/z $C_{132}H_{108}Cu_3N_{12} = 2049.6702$ $[M]^+$), indicating the formation of porphyrin(2.1.2.1) nanobelts. Two monomer porphyrin(2.1.2.1) complexes **DBPorNi** and **DBPorCu** as reference compounds are synthesized via established method (Scheme 5.1).[5]

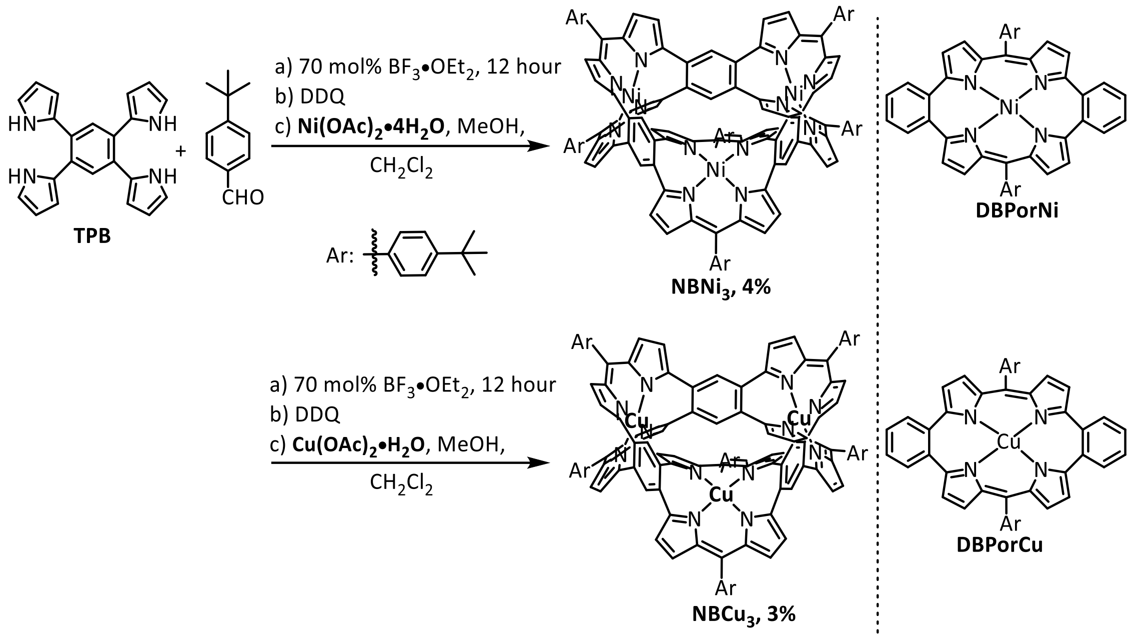

Scheme 5.1. Synthesis scheme of **NBNi3** and **NBCu3**.

The key factors to determine the products are the amount of acid catalysis and reaction time. When the condensation reaction is examined with lower amount of acid catalysis (5 mol%) or shorter reaction time (2 hours or 12 hours), porphyrin monomer **PorNi** or dimer **DPorNi2** were obtained. The molecular structures of **DBPorNi** and **NBNi3** are investigated by 1D NMR spectra in CD_2Cl_2 at 298 K (Figure 5.2 - 5.4). The ^{1}H NMR spectrum of **DBPorNi** shows protons of *para*-positions of linked benzene rings at 7.47 and 7.36 ppm and, pyrrolic *β*-protons at 6.69 and 6.16 ppm as two doublet peaks (Figure 5.2).

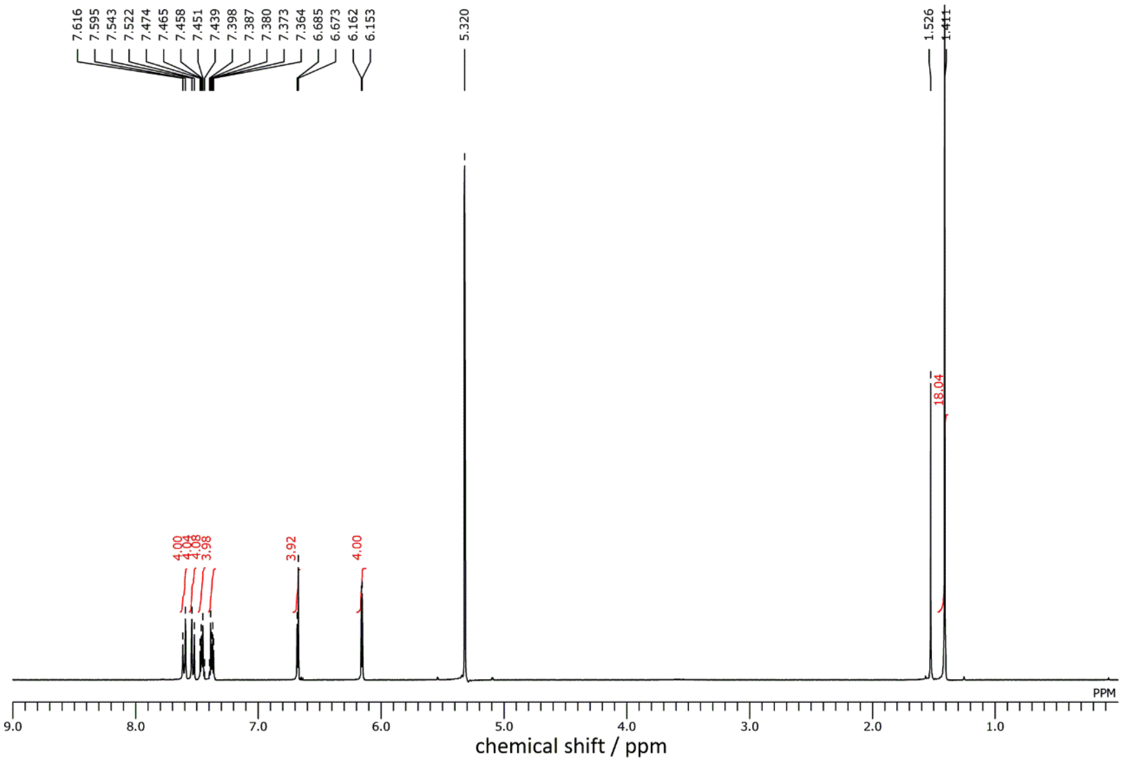

Figure 5.2. ^{1}H NMR spectrum of **DBPorNi** in CD_2Cl_2 at 298 K.

The ^{1}H NMR and NOESY spectra of **NBNi$_3$** are shown in Figure 5.3. Singlet peak at 7.46 ppm corresponds to protons of *para*-positions of linked benzene rings. . Pyrrolic *β*-protons are observed at 6.72 and 6.24 ppm as two doublet peaks (Figure 5.3). The other signals are assigned to protons of *t*-butylphenyl groups. The ^{1}H and ^{13}C NMR (Figure 5.4) spectra indicate that the **NBNi$_3$** forms a C_{3h}-symmetric structure in solution. Considering ^{1}H NMR spectra of **DBPorNi** and **NBNi$_3$**, the finding is that π-electron of benzene linkages between porphyrin(2.1.2.1) units are localized without mutual interaction of porphyrin(2.1.2.1) units.

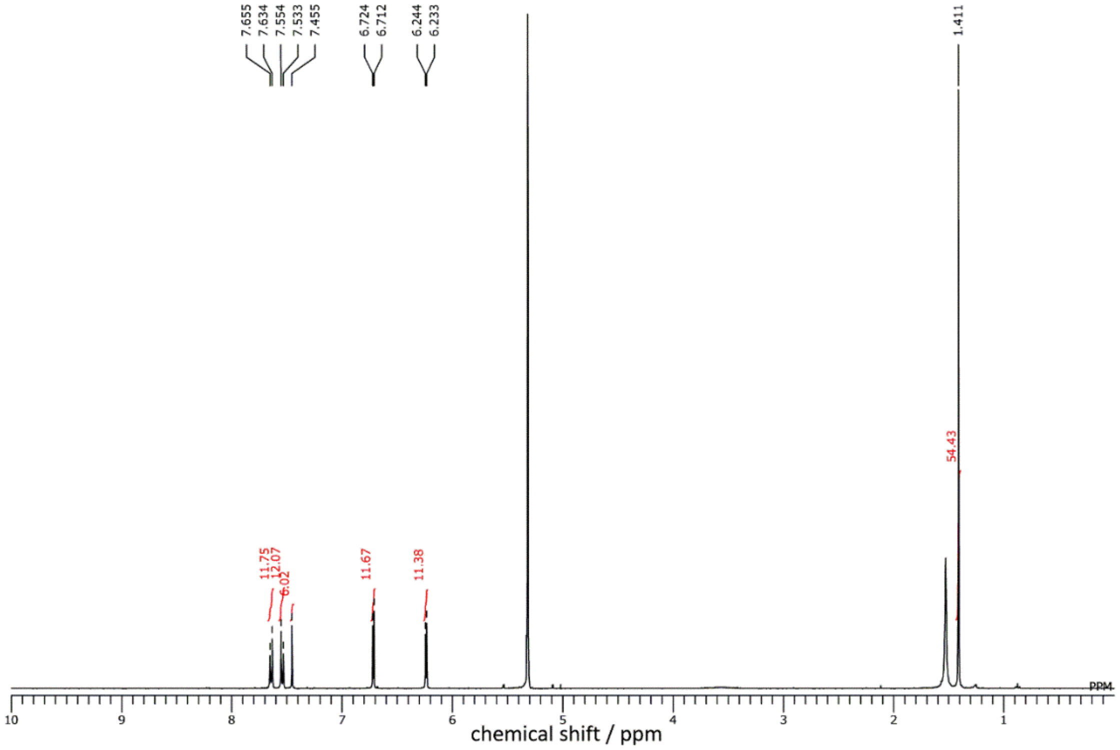

Figure 5.3. ^{1}H NMR spectrum of **NBNi$_3$** in CD_2Cl_2 at 298 K.

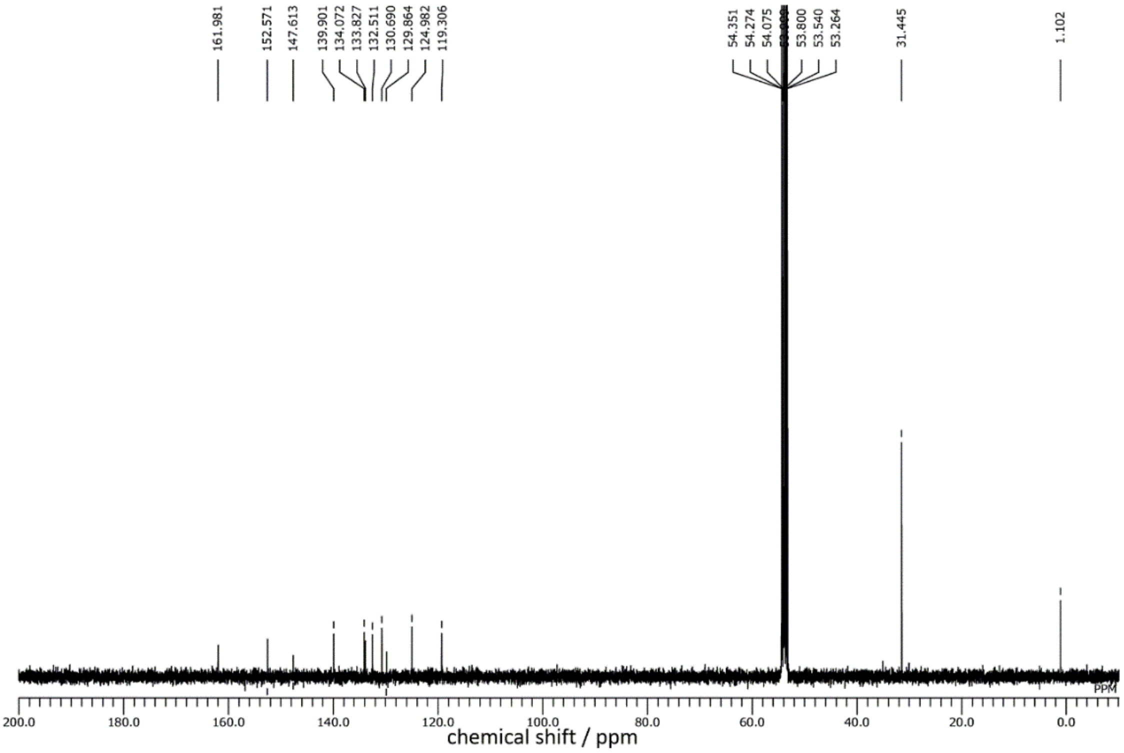

Figure 5.4. ^{13}C NMR spectrum of **NBNi$_3$** in CD_2Cl_2 at 298 K.

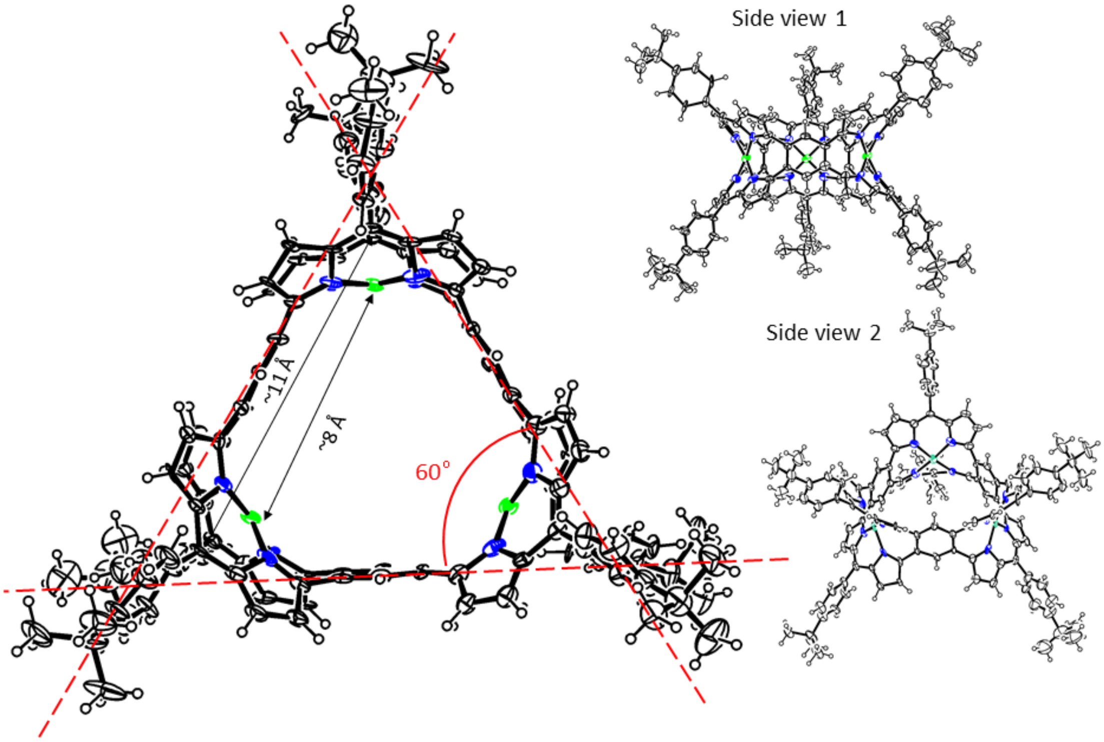

Figure 5.5. Crystal structure, selected distances and angles of adjacent benzene planes of **NBNi₃**. The thermal ellipsoids represent for 30% probability.

The X-ray crystallography gives the undoubtedly solid structural proof of **NBNi₃** (Figure 5.5). Porphyrin nanobelt **NBNi₃** forms a C_{3h}-symmetric cyclic structure. The bond lengths between *meso*-carbon to *meso*-carbon and Ni(II) ion to Ni(II) ion are almost 11 Å and 8 Å, respectively. The average angle of adjacent benzene planes is about 60º (Figure 5.5). These solid structure of **NBNi₃** reveals that connected porphyrin(2.1.2.1) units still take arch-shaped structures to produce the belt-shaped porphyrin nanobelts.

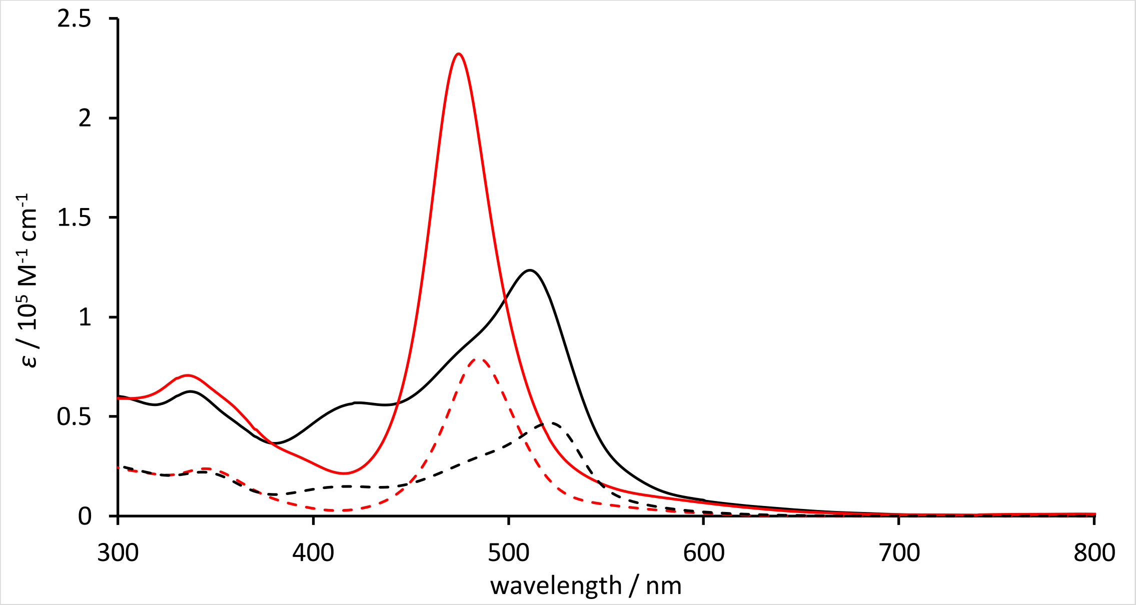

Figure 5.6. The UV-Vis absorption spectra of **DBPorCu** (red dash line), **DBPorNi** (black dash line)**,** **$NBCu_3$** (red solid line) and **$NBNi_3$** (black solid line) in CH_2Cl_2.

The optical properties of **$NBNi_3$**, **$NBCu_3$**, **DBPorCu** and **DBPorNi** were investigated by absorption spectra in CH_2Cl_2 (Figure 5.6). All compounds display broad absorption bands. The absorption of **$NBNi_3$** shows broad bands at 348, 424 and 512 nm. **$NBCu_3$** exhibits blue-shifted and sharpened absorption peaks at 345 and 474 nm. Nanobelts show similar-shaped with three times as high as molar absorption coefficiency of the monomer porphyrins **DBPorCu**. The absorption characteristics indicate that benzene rings with localized π-electron and each porphyrin unit do not have mutual interactions.

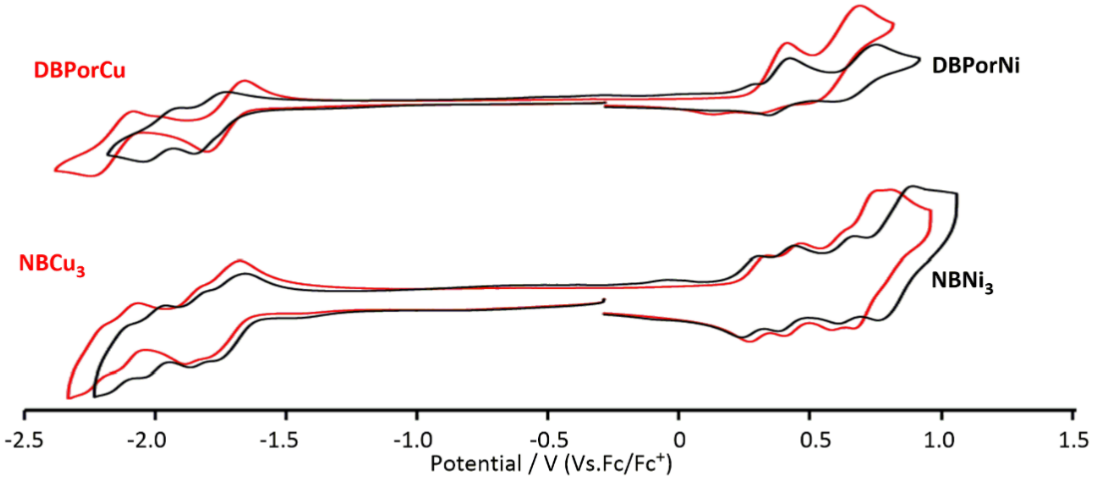

Figure 5.7. CV of **DBPorNi**, **DBPorCu**, **NBNi$_3$** and **NBCu$_3$** in CH_2Cl_2 containing 0.1 M $^nBu_4NPF_6$. Scan rate is 0.1 V s^{-1}.

Table. 5.1. Oxidation (Ox) and reduction (Red) potentials (V, Vs.Fc/Fc$^+$) of **DBPorNi**, **DBPorCu**, **NBNi$_3$** and **NBCu$_3$** in CH_2Cl_2.

Compounds	Red^4	Red^3	Red^2	Red^1	Ox^1	Ox^2	Ox^3	Ox^4
DBPorNi			-1.93	-1.75	0.38	0.70		
DBPorCu			-2.12	-1.70	0.35	0.62		
NBNi$_3$	-2.13	-1.98	-1.80	-1.70	0.31	0.45	0.68	0.88
NBCu$_3$	-2.19	-2.07	-1.79	-1.68	0.32	0.43	0.62	0.76

The redox properties of **DBPorNi**, **DBPorCu**, **NBNi$_3$** and **NBCu$_3$** were investigated by CV in CH_2Cl_2 with 0.1 M $^nBu_4NPF_6$ as an electrolyte (Figure 5.7 and Table 5.1). Unfortunately, **PorNi** and **DPorNi$_2$** could not be obtained stable redox waves because they have redox active pyrrole moieties, which might conduct the polymerizations or uncontrollable side reactions under the measurement conditions. Two monomer porphyrin complexes **DBPorNi** and **DBPorCu** both show two oxidation and two reduction potentials at porphyrin(2.1.2.1) units. Compound **DBPorNi** exhibits two oxidation potentials at 0.38 and 0.70 V, and two reduction potentials at –1.75 and –1.93 V (vs Fc/Fc^{+}). Compound **DBPorCu** exhibits two oxidation potentials at 0.35 and 0.62 V, and two reduction potentials at –1.70 and –2.12 V (vs Fc/Fc^{+}).

Interestingly, **NBNi$_3$** and **NBCu$_3$** exhibit similar redox properties with four reversible oxidation potentials and four reversible reduction potentials. These eight reversible oxidation and reduction potentials indicate that porphyrin(2.1.2.1) nanobelts have multi-electrons donating and storage abilities considering as a result of larger molecular skeletons.[4i]

Molecular orbital calculations were examined at the B3LYP/6-31G(d) level with Gaussian 09.[6] The monometic porphyrin(2.1.2.1) **DBPorNi** have non-generated HOMO and LUMO levels. On the other hand, **NBNi$_3$** exhibits HOMO and generated HOMO–1 to HOMO–3 and two set of three generated LUMO to LUMO+2 and LUMO+3 to LUMO+5. This electronic property of **NBNi$_3$** contributes the multi-electrons donating and accepting properties.

5-3 Binding Ability with Fullerene

The molecular design of C_{60} receptors is an interesting and growing research field because of the functions of C_{60}.[4b,7] The X-ray crystallography revealed that porphyrin(2.1.2.1) nanobelt has a large binding surface, which might catch C_{60} to form host-guest complex.

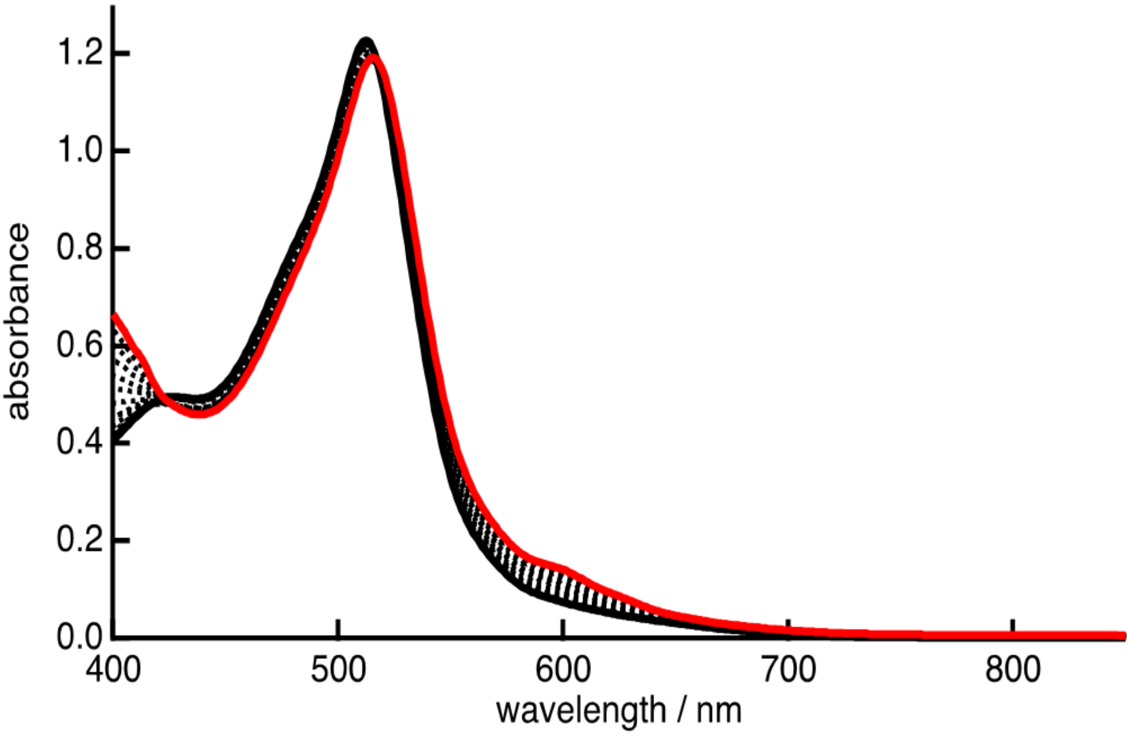

Figure 5.8. The UV-vis absorption spectra of **NBNi**$_3$ (8.8 μM) in toluene in the presence of various equivalent of [C_{60}] (from 0 eq. black line to 9 eq. red line).

The complex formation of the **NBNi**$_3$ and C_{60} is indicated by titration using the UV-vis absorption spectra in toluene (Figure 5.8). With increasing of [C_{60}], the absorption band at 512 nm of **NBNi**$_3$ is red-shifted to 516 nm. The feature of absorption spectral is similar to those of other porphyrin–C_{60} complexes.[4b,7f, 7g, 8b] This binding progress is analyzed with the Hill equation and Job's plot (Figure 5.9 - 5.12).[8,9]

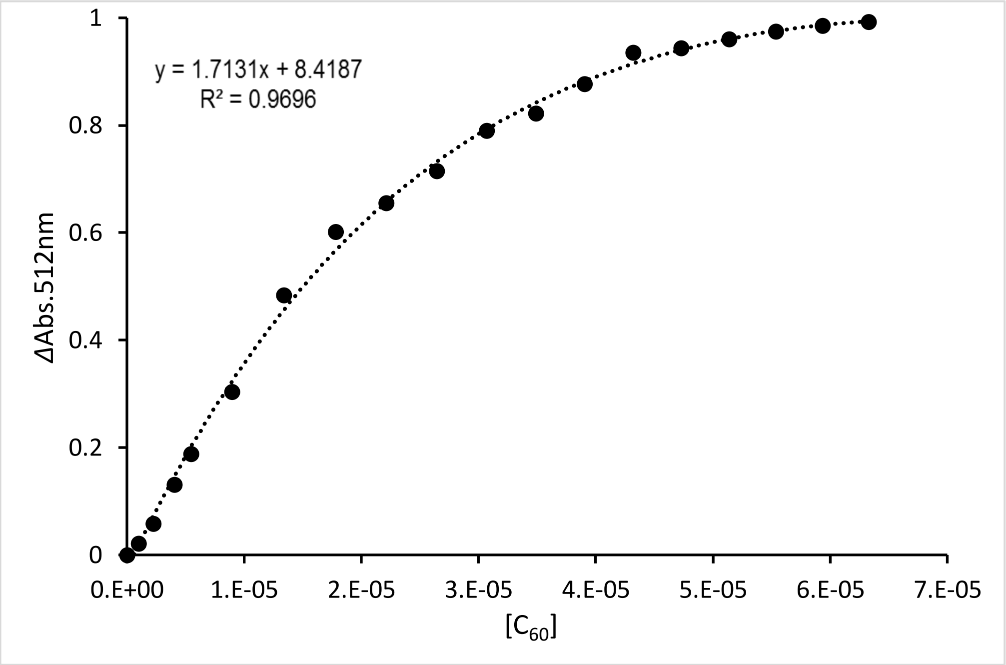

Figure 5.9. Hill plot of ΔAbs at 512 nm versus [C_{60}].

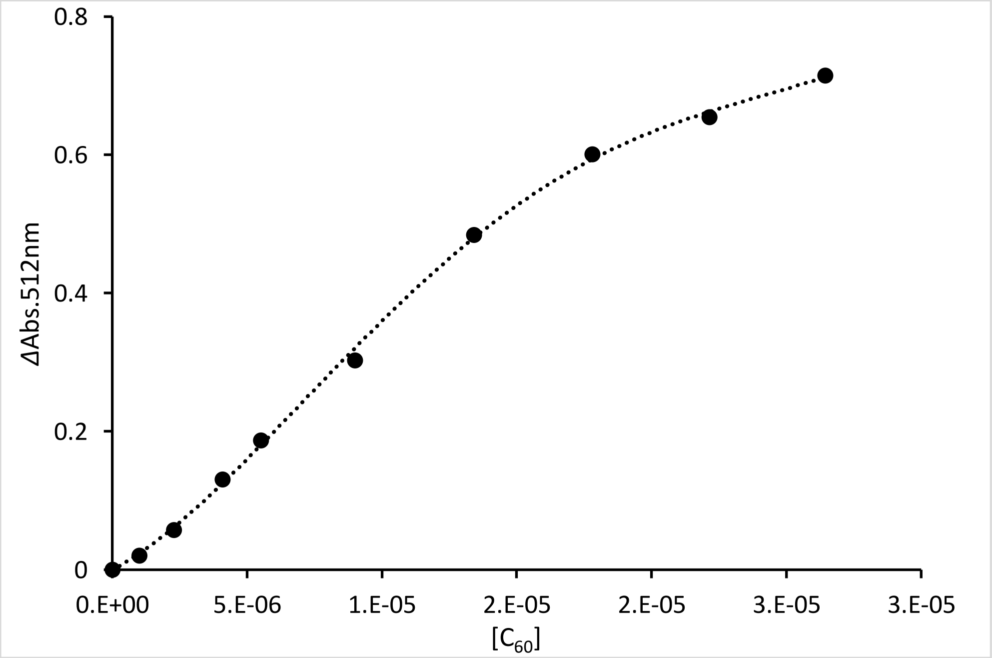

Figure 5.10. The sigmoidal line versus [C_{60}].

Hill equation is $\log(y/(1-y)) + n\log[C_{60}] = \log K$, where K and n are the association constant and Hill coefficient, respectively. $y = (Abs_{\mathrm{obs}} - Abs_0)/(Abs_\infty - Abs_0)$, where Abs_0, Abs_∞ is Abs_{obs} at $C_{60} = 0$ and infinite, respectively. The Hill equation gave the $\log K = 8.4$ and $n = 1.7$ (Figure 5.9). These results indicate that **NBNi$_3$** captures two C_{60} molecules in the formation of a host-guest complex **2C$_{60}$@NBNi$_3$**. The Hill coefficient is $n = 1.7$, which supports the view that the binding of C_{60} to **NBNi$_3$** is taking place cooperatively.[10]

The Hill's plot also shows the sigmoidal feature, suggesting that **NBNi$_3$** allosterically captures the C_{60} during the binding progress (Figure 5.10). The allosteric effect of binding progress is evaluated by DFT calculation. The free binding surface of **C$_{60}$@NBNi$_3$** was enlarged relative to **NBNi$_3$** (Figure 5.11) because distances between protons of *para*-positions of benzene rings and distances between *β*-pyrrolic protons have lengthened. The Job's plot is obtained by plotting *Δ*Abs values at 512 nm against mole fractions of **NBNi$_3$**. The *Δ*Abs values at 512 nm shows maximum value when the mole fraction of **NBNi$_3$** is 0.33, therefore, the Job's plot also supports 1:2 binding pattern of complex **2C$_{60}$@ NBNi$_3$** (Figure 5.12).[7b, 8]

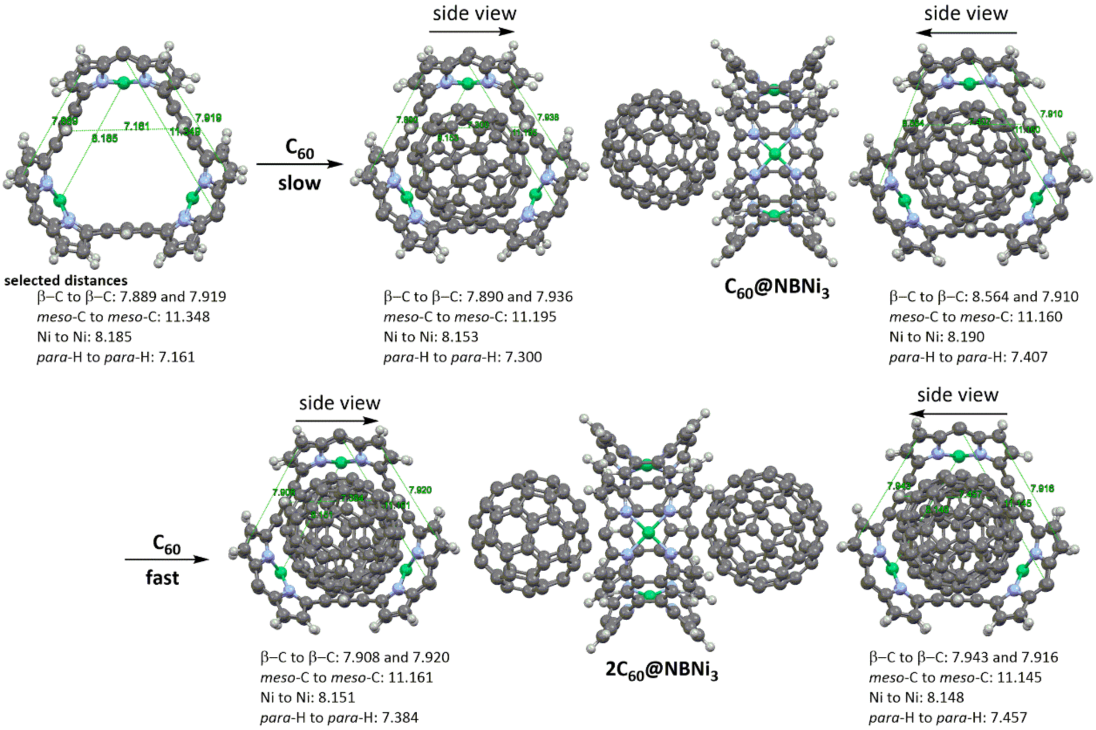

Figure 5.11. All optimized structures of **$NBNi_3$**, **C_{60}@$NBNi_3$** and **2C_{60}@$NBNi_3$** calculated at the B3LYP/6-31G* level of theory. Aryl groups are omitted for clarity. Selected distances are gave in Å.

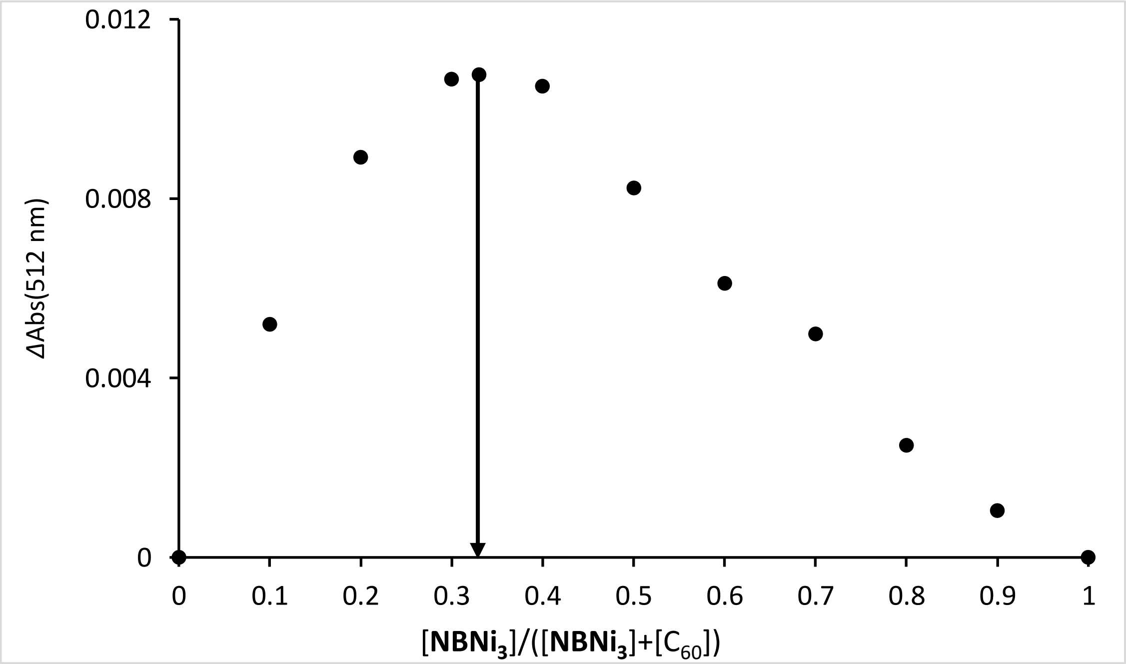

Figure 5.12. Job's plot for **2C_{60}@$NBNi_3$** complex formation.

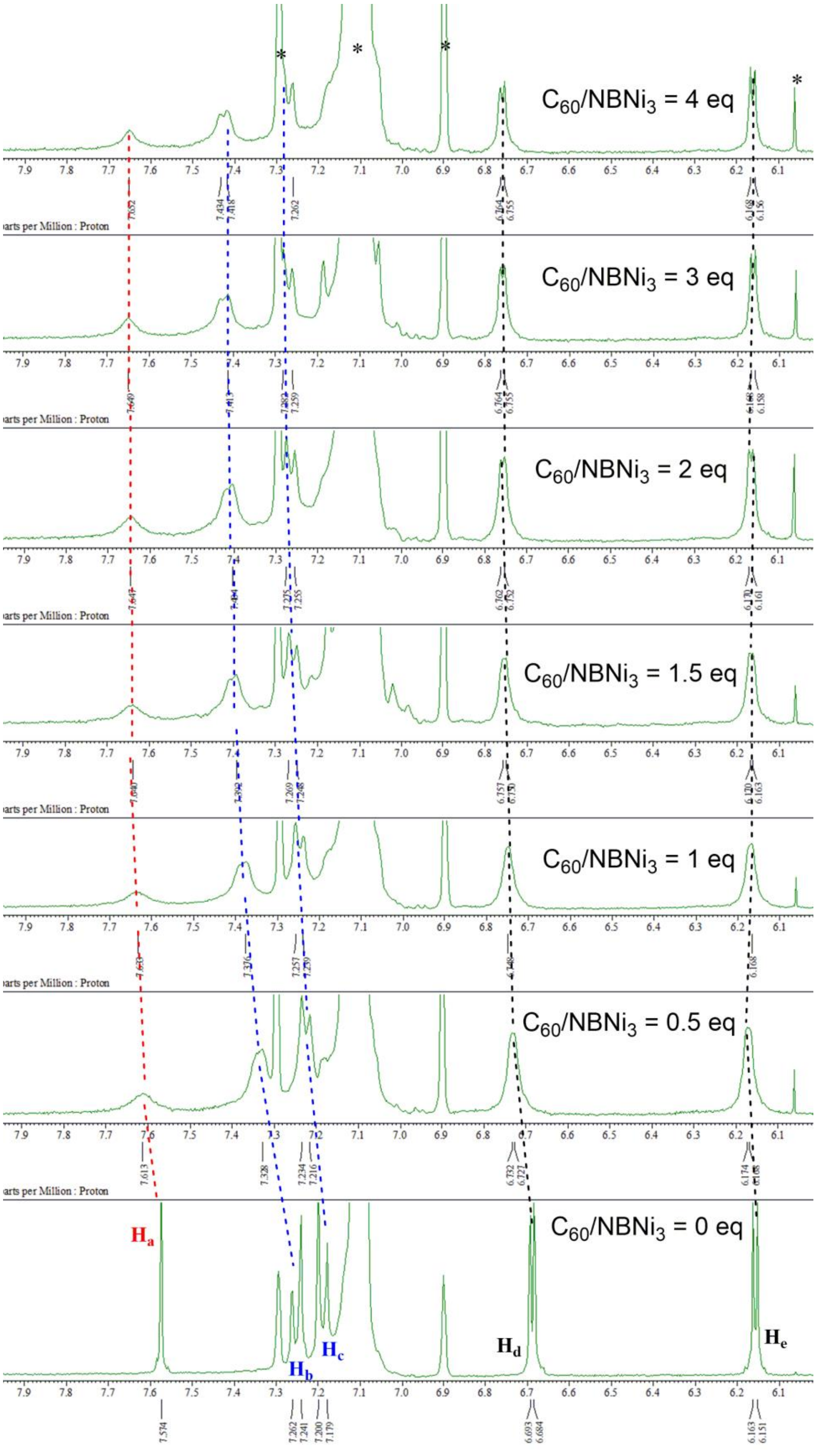

Figure 5.13 ^{1}H NMR titration spectra of **NBNi₃** with C_{60} in benzene-d_6 at 25°C.

To investigate the stoichiometry between **NBNi$_3$** and fullerene, ^{1}H NMR titration is examined in benzene-*d$_6$* at 298 K. The resonance signals of the benzene rings protons and *meso*-aryl protons are shifted downfield in the addition of C_{60} from 0 eq. to 2 eq (Figure 5.13).[8b] As shown in Figure 5.14, plots of chemical shift changes $\Delta\delta$ versus $[C_{60}]/[\mathbf{NBNi_3}]$ has a clear inflection point at $[C_{60}]/[\mathbf{NBNi_3}]$ = 2. This value support the result of UV titration.

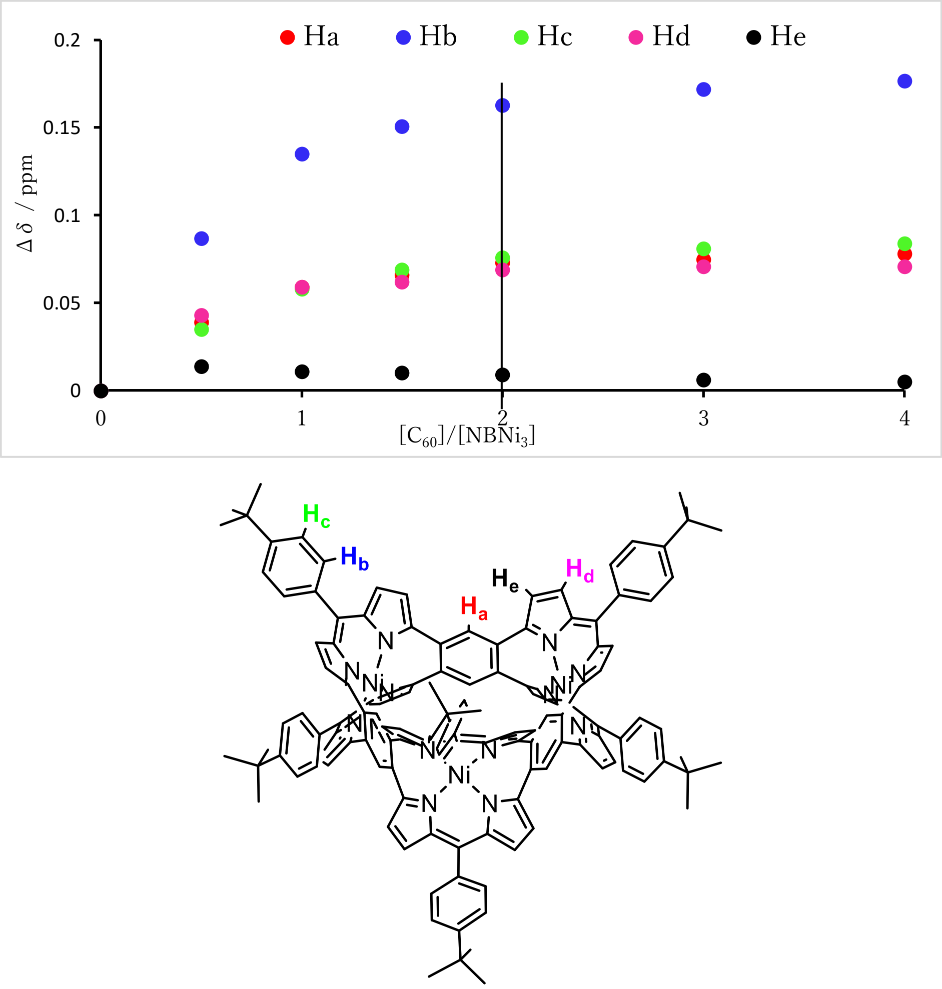

Figure 5.14. Plots of chemical shift changes of protons versus $[C_{60}]/[\mathbf{NBNi_3}]$ in benzene-*d$_6$* at 298 K and selected protons of **NBNi$_3$**.

The optimized structure of **$2C_{60}$@$NBNi_3$** is calculated by DFT at the B3LYP/6-31G* level with Gaussian 09[6]. The optimized structure shows the distances between protons of benzene rings and *meso*-aryl groups of host **$NBNi_3$** to the nearest center of six-/five-member rings of guests C_{60} molecules (Figure 5.15). The distances between benzene rings protons H^a and *meso*-aryl protons H^b to C_{60} are 3.215 Å and 3.318 Å, these distance are slightly shorter than the sum of van der Waals radii (3.4 Å), suggesting the CH-π interactions to form the **$2C_{60}$@$NBNi_3$** complex.[6h] Besides, the binding energy of **$2C_{60}$@$NBNi_3$** complex is –12.90 kcal/mol (Figure 5.16).

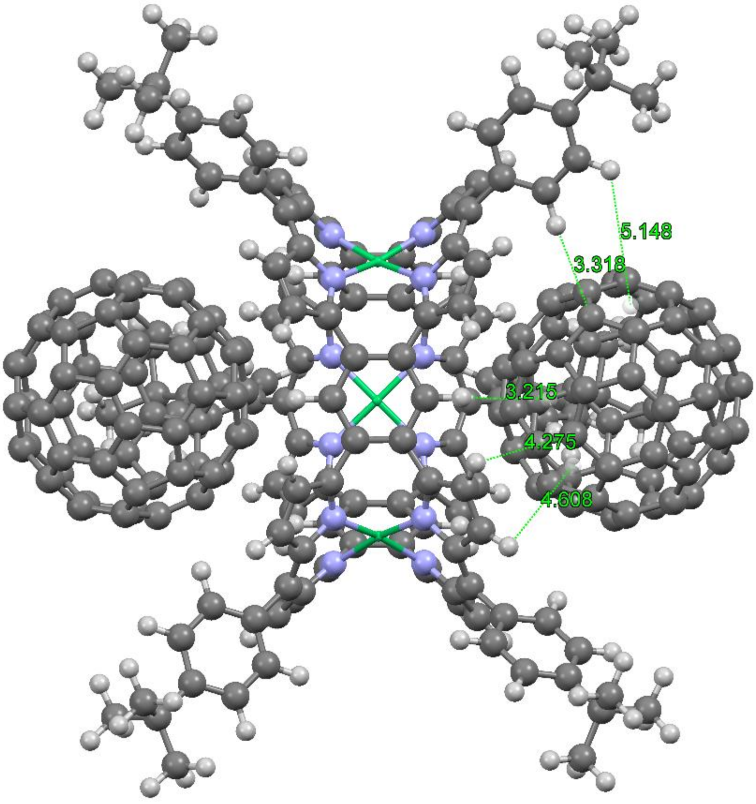

Figure 5.15. Minimum-energy geometry of **$2C_{60}$@$NBNi_3$** calculated at the B3LYP/6-31G* level of theory. Selected distances are given in Å.

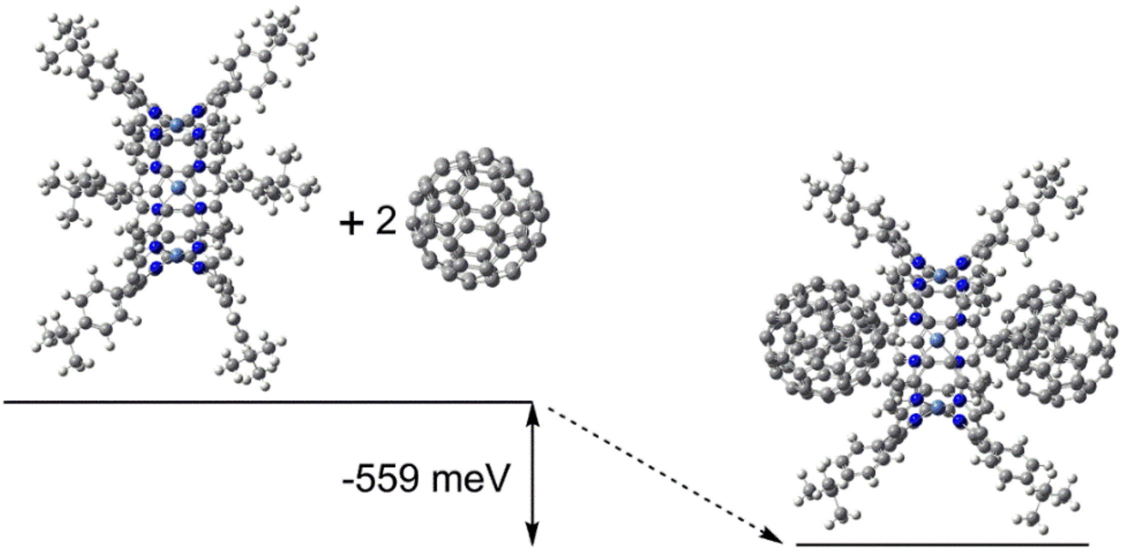

Figure 5.16. Binding energy of **$2C_{60}$@$NBNi_3$** calculated at the B3LYP/6-31G* level of theory.

5-4 Conclusion

An effective synthetic method of porphyrin(2.1.2.1) nanobelts was successfully developed. The X-ray crystallography reveals that porphyrin nanobelt forms the C_{3h}-symmetric structure comprising larger binding surface. The UV and NMR titration reveal that the **NBNi$_3$** can catch two C_{60} molecules to form host-guest complex that indicates strong capacity of porphyrin nanobelt in supramolecular chemistry. According to DFT calculation, the binding ability with C_{60} was supported by double concave shape, large exposed π-surface and CH-π interaction. In addition, porphyrin(2.1.2.1) nanobelts have multi-electrons donating and storage abilities.

5-5 References

[1] (a) H. W. Kroto, J. R. Heath, S. C. O'Brien, R. F. Curl, R. E. Smalley, *Nature,* **1985**, *318*, 162; (b) S. Iijima, *Nature,* **1991**, *354,* 56; (c) S. Reich, C. Thomsen, J. Maultzsch, Carbon Nanotubes: Basic Concepts and Physical Properties; Wiley-VCH: Weinheim, Germany, **2004**, 215; (d) K. Tahara, Y. Tobe, *Chem. Rev.,* **2006**, *106,* 5274; (c) D. Eisenberg, R. Shenhar, M. Rabinovitz, *Chem. Soc. Rev.,* **2010**, *39,* 2879.

[2] (a) P. Parkinson, D. V. Kondratuk, C. Menelaou, J. Q. Gong, H. L. Anderson, L. M. Herz, *J. Phys. Chem. Lett.,* **2014**, *5,* 4356; (b) D. V. Kondratuk, L. M. A. Perdigão, A. M. S. Esmail, J. N. O`Shen, P H. Beton, H. L. Anderson, *Nat. Chem.,* **2015**, *7,* 317; (c) S. Richert, J. Cremers, I. Kuprov, M. D. Peeks, H. L. Anderson, C. R. Timmel, *Nat. Comm.,* **2017**, *8*, 14842; (d) M. D. Peeks, C. E. Tait, P. Neuhaus, G. M. Fischer, M. Hoffmann, R. Haver, A. Cnossen, J. R. Harmer, C. R. Timmer, H. L. Anderson, *J. Am. Chem. Soc.,* **2017**, *139,* 10461; (e) M. D. Peeks, T. D. W. Claridge, H. L. Anderson, *Nature,* **2017**, *541*, 200.

[3] G. Povie, Y. Segawa, T. Nishihara, Y. Miyauchi, K. Itami, *Science,* **2017**, *356,* 172.

[4] (a) J. Song, N. Ararani, H. Shinokubo, A. Osuka, *Chem. Eur. J.,* **2010**, *16,* 13320; (b) J. Song, N. Ararani, H. Shinokubo, A. Osuka, *J. Am. Chem. Soc.,* **2010**, *132,* 16356; (c) M. C. O`Sullivan, J. K. Sprafke, D. V. Kondratuk, C. Rinfray, T. D.W. Claridge, A. Saywell, M. O. Blunt, J. N. O`Shea, P. H. Beton, M. Malfois, H. L. Anderson, *Nature,*

2011*, 469*, 72; (d) H. Jiang, T. Tanaka, H. Mori, K. H. Park, D. Kim, A. Osuka, *J. Am. Chem. Soc.,* **2015***, 137,* 2219; (e) M. Rickhaus, A. V. Jentzsch, L. Tejerina, I. Grübner, M. Jirasek, T. D. W. Claridge, H. L. Anderson, *J. Am. Chem. Soc.,* **2017***, 139,* 16502; (f) P. Neuhaus, A. Cnossen, J.Q. Gong, L.M. Herz, H. L. Anderson, *Angew. Chem. Int. Ed.,* **2015***, 54,* 7344; (g) M. D. Peeks, T. D. W. Claridge, H. L. Anderson, *Nature,* **2017***, 541*, 200.

[5] D. Kuzuhara, W. Fulukawa, A. Kitashiro, N. Aratani, H. Yamada, *Chem. Eur. J.,* **2016***, 22,* 10671.

[6] Gaussian 09, Revision B.01, M. J. Frisch, G. W. Trucks, H. B. Schlegel, G. E. Scuseria, M. A. Robb, J. R. Cheeseman, G. Scalmani, V. Barone, B. Mennucci, G. A. Petersson, H. Nakatsuji, M. Caricato, X. Li, H. P. Hratchian, A. F. Izmaylov, J. Bloino, G. Zheng, J. L. Sonnenberg, M. Hada, M. Ehara, K. Toyota, R. Fukuda, J. Hasegawa, M. Ishida, T. Nakajima, Y. Honda, O. Kitao, H. Nakai, T. Vreven, J. A. Montgomery, Jr., J. E. Peralta, F. Ogliaro, M. Bearpark, J. J. Heyd, E. Brothers, K. N. Kudin, V. N. Staroverov, T. Keith, R. Kobayashi, J. Normand, K. Raghavachari, A. Rendell, J. C. Burant, S. S. Iyengar, J. Tomasi, M. Cossi, N. Rega, J. M. Millam, M. Klene, J. E. Knox, J. B. Cross, V. Bakken, C. Adamo, J. Jaramillo, R. Gomperts, R. E. Stratmann, O. Yazyev, A. J. Austin, R. Cammi, C. Pomelli, J. W. Ochterski, R. L. Martin, K. Morokuma, V. G. Zakrzewski, G. A. Voth,

P. Salvador, J. J. Dannenberg, S. Dapprich, A. D. Daniels, O. Farkas, J. B. Foresman, J. V. Ortiz, J. Cioslowski, D. J. Fox, Gaussian, Inc., Wallingford CT, 2010.

[7] (a) B. W. Smith, M. Monthious, D E. Luzzi, *Nature,* **1998***, 396*, 323; (b) S. Bandow, M. Takizawa, H. Kato, T. Okazaki, H. Shinohara, S. Iijima, *Chem. Phys. Lett.,* **2001***, 347*, 23; (c) T. Kawase, H. Kurata, *Chem. Rev.,* **2006***, 106,* 5250; (d) G. Gil-Ramırez, S. D. Karlen, A. Shundo, K. Porfyrakis, Y. Ito, G. A. D. Briggs, J. J. L. Morton, H. L. Anderson, *Org. Lett.,* **2010***, 12,* 3544; (e) A. Takai, M. Chkounda, A. Eggenspiller, C. P. Gros, M. Lachkar, J.M. Barbe, S. Fukuzumi, *J. Am. Chem. Soc.,* **2010***, 132,* 4477; (f) H. Nobukuni, Y. Shimazaki, F. Tani, Y. Naruta, *Angew. Chem., Int. Ed.,* **2007***, 46,* 8975; (g) X. S. Ke, T. Kim, F. T. Brewster II, V. M. Lynch, D. Kim, JL. Sessler, *J. Am. Chem. Soc.,* **2017***, 139,* 4627.

[8] (a) B. Perlmutter-Hayman, *Acc. Chem. Res.,* **1986***, 19,* 90; (b) J. Song, N. Ararani, H. Shinokubo, A. Osuka, *Chem. Sci.,* **2011***, 2,* 748; (c) Y. Saegusa, T. Ishizuka, T. Kojima, S. Mori, M. Kawano, T. Kojima, *Chem. Eur. J.,* **2015***, 21,* 5302.

[9] E. J. Olson, P. Bühlmann, *J. Org. Chem.,* **2011***, 76,* 8406.

[10] (a) H. Sato, K. Tashiro, H. Shinmori, A. Osuka, Y. Murata, K. Komatsu, T. Aida, *J. Am. Chem. Soc.,* **2017**, *139*, 13086; (b) Y. Kubo, A. Sugasaki, M. Ikeda, K. Sugiyasu, K. Sonoda, A. Ikeda, M. Takeuchi, S. Shinkai *Org. Lett.,* **2002***, 4,* 925.

5-6 Supporting Information

Spectroscopy. ^{1}H NMR spectrum was recorded on a JNM-ECX 400 and JNM-ECA 600 spectrometers using the residual solvent as the internal reference for ^{1}H (δ = 5.30 ppm in CD_2Cl_2, δ = 7.16 ppm in benzene-*d*$_6$) and ^{13}C (δ = 53.84 ppm in CD_2Cl_2). HR-MALDI-TOF mass spectra were recorded on a Bruker Daltonics autoflex MALDI-TOF MS spectrometer. UV-vis absorption spectra were measured with a JASCO UV/VIS/NIR Spectrophotometer V-670. CV and DPV measurements were conducted in a solution of 0.1 M $TBAPF_6$ in dry-dichloromethane with a scan rate of 0.1 V s^{-1} in an argon-filled cell. A glassy carbon electrode and a platinum wire were used as a working and a counter electrode, respectively. A $Ag/AgNO_3$ electrode was used as reference electrodes, which were normalized with the half-wave potential of ferrocene/ferrocenium (Fc/Fc^+) redox couple.

Materials. All solvents and chemicals were reagent grade quality, obtained commercially and used without further purification except as noted. For spectral measurements, spectral grade dichloromethane was purchased from Nacalai Tesque Co. Thin−layer chromatography (TLC), flush and gravity column chromatographies were performed on Art. 5554 (Merck KGaA), Silica Gel 60 (Merck KGaA) and Silica Gel 60N (Kanto Chemical Co.), respectively.

X-ray Analysis. X-ray crystallographic data for **PorNi** and **NBNi$_3$** were recorded at 90 K on a Bruker APEX II X-Ray diffractometer equipped with a large area CCD detector by using graphite monochromated Mo-Kα radiation (λ = 0.71073 Å). The structure was solved by direct methods and refined on F^2 by full−matrix least−squares using the SHELXL-97.[S1] CCDC: 1827024, 1822773, contains the supplementary crystallographic datas for **PorNi** and **NBNi$_3$**. These data can be obtained free of charge from the Cambridge Crystallographic Data Centre via www.ccdc.cam.ac.uk-/data_request/cif.

Theoretical calculations. All density functional theory calculations were achieved with the Gaussian 09 program package. The geometries of **DBPorNi, NBNi$_3$**, **C$_{60}$@NBNi$_3$** and **2C$_{60}$@NBNi$_3$** were optimized at the Becke's three-parameter hybrid functional combined with the Lee-Yang-Parr correlation functional abbreviated as the B3LYP level of density functional theory with 6-31* basis set.

Synthesis of TPB(Boc)$_4$

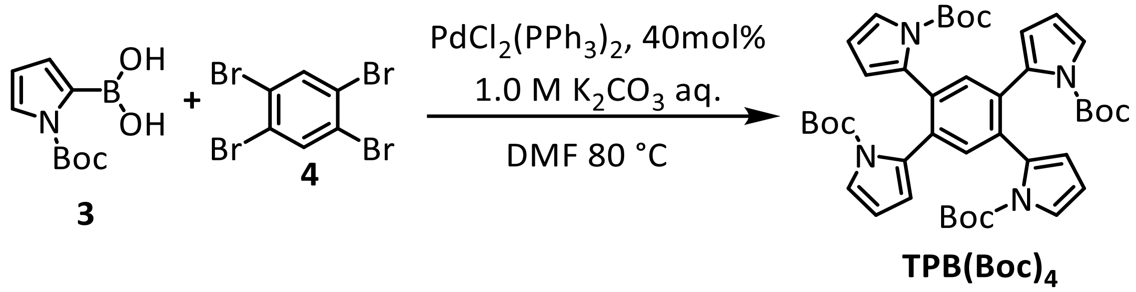

Compounds **4** (311 mg, 0.80 mmol) and **3** (844 mg, 4 mmol) were added to a mixture of DMF (20 mL) and (4 mL) 1.0 M K_2CO_3 aq.. The resulting reaction mixture was bubbled with argon for 5 min. The $PdCl_2(PPh_3)_2$ (40 mol%, 234 mg, 0.32 mmol) was added to reaction solution. The reaction mixture was stirred at 80 °C for 12 hours. The reaction mixture was extracted with EtOAc. The combined organic phase was washed with water and brine, then dried over Na_2SO_4. The crude was purified by silica gel column chromatography (*n*-hexane: EtOAc = 10 :1) to afford crude product. After removal of solvent, the obtained solid was washed with *n*-hexane to afford compound **TPB(Boc)$_4$** as white powder in 40 % yield (236.1 mg, 0.32 mmol).

^{1}H NMR (400 MHz, CD_2Cl_2) δ = 7.23 (s, 2H, benzene), 7.15 (m, 4H, pyrrole), 6.08 (m, 4H, pyrrole), 5.98 (m, 4H, pyrrole), 1.41 (s, 36H, Boc) ppm. ^{13}C NMR (100 MHz, CD_2Cl_2) δ = 148.929, 133.597, 133.199, 132.205, 121.846, 115.006, 110.262, 83.577, 27.895 ppm. HR-MALDI-MS: calcd. for $C_{42}H_{50}N_4O_8$: 738.3629 $[M]^+$, Found: 761.3517.

Synthesis of TPB

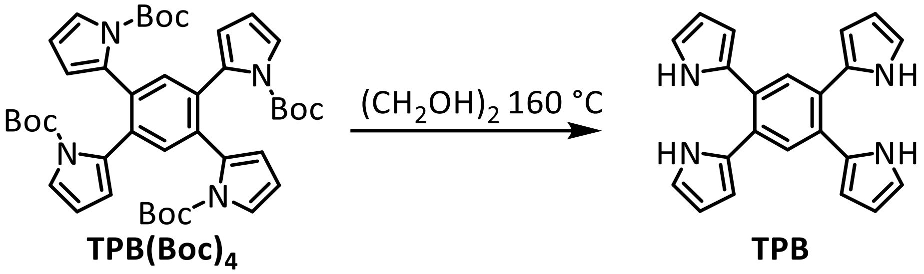

TPB(Boc)$_4$ (200 mg, 0.27 mmol) and $(CH_2OH)_2$ (30 mL) were added into a 100 mL flask, and then the reaction mixture was bubbled with argon for 5 min. The reaction mixture was heated at 160 °C for 1 hour under argon atmosphere. The reaction mixture was extracted with CH_2Cl_2. The combined organic phase was washed with water and brine, then dried over Na_2SO_4. Evaporation of the organic solvent, the obtained solid was washed with *n*-hexane to afford **TPB** as a pale-white solid in 90% (82.2 mg, 0.24 mmol).

^{1}H NMR (400 MHz, CD_2Cl_2) δ = 8.12 (s, 4H, NH), 7.59 (s, 2H, benzene), 6.75 (m, 4H, pyrrole), 6.37 (m, 4H, pyrrole), 6.23 (m, 4H, pyrrole) ppm. ^{13}C NMR (100 MHz, CD_2Cl_2) δ = 130.950, 130.675, 129.527, 119.183, 109.390, 108.549 ppm. HR-MALDI-MS: calcd. for $C_{22}H_{18}N_4$: 338.1531 $[M]^+$, Found: 338.1522.

Synthesis of PorNi, DPorNi$_2$ and NBNi$_3$

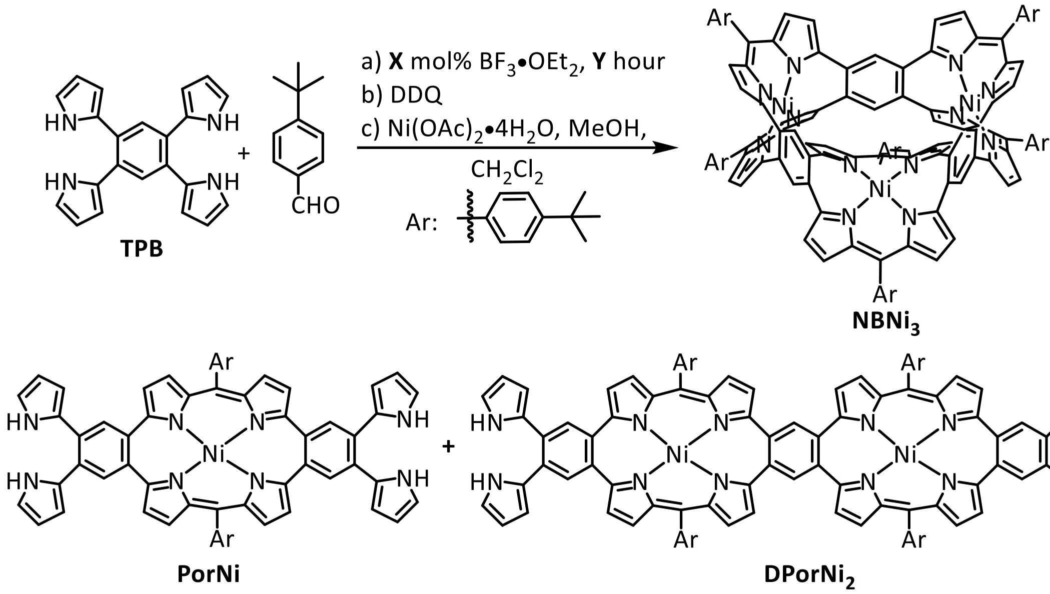

X. mol%	**Y.** hour	**PorNi**	**DPorNi$_2$**	**NBNi$_3$**
5	2	10%	trace	X
5	12	trace	2%	X
70	12	X	X	4%

A solution of **TPB** (36 mg, 0.11 mmol) and 4-(*tert*-butyl)benzaldehyde (36 mg, 0.22 mmol) in dry CH_2Cl_2 (100 ml) was bubbled with argon for 5 min, and then BF_3•OEt_2 (**X** mol%) was added to reaction mixture. The reaction mixture was stirred for **Y** hours under an argon atmosphere in the dark. DDQ (49 mg, 0.22 mmol) was added to the reaction mixture, which was stirred for 1 hour. Then saturated $Ni(OAc)_2$•$4H_2O$ in 5 mL MeOH was added to mixture which was stirred for next 4 hours. After removal of the solvent, the residue was purified by silica gel column chromatography (CH_2Cl_2/*n*-hexane = 1/3 to 1/1). The yellow-red was evaporated to give crude product. The crude products was recrystallized by $CHCl_3$/MeOH to give pure compound.

PorNi (5.5 mg, 0.0054 mmol): ^{1}H NMR (400 MHz, CD_2Cl_2) δ = 8.04 (brs, 4H, NH), 7.54 (d, J = 8 Hz, 4H, aryl), 7.47 (d, J = 12 Hz, 4H, aryl), 7.41 (s, 4H, benzene), 6.67 (m, 4H, pyrrole), 6.637 (d, J = 4 Hz, 4H, pyrrole), 6.30 (m, 4H, pyrrole), 6.15 (m, 8H, pyrrole), 1.34 (s, 18H, *tert*-butyl) ppm. ^{13}C NMR (100 MHz, CD_2Cl_2) δ = 161.614, 152.494, 147.416, 139.504, 134.057, 132.526, 132.159, 131.134, 130.874, 130.690, 130.369, 124.952, 119.566, 118.770, 109.528, 109.054, 35.040, 31.445 ppm. HR-MALDI-MS: calcd. for $C_{66}H_{54}NiN_8$: 1016.3825 [*M*]$^+$, Found: 1016.3819. UV-Vis (in CH_2Cl_2) λ [nm] (ε [$M^{-1}cm^{-1}$]): 321 (46200), 405 (19600) and 537 (50600).

DPorNi₂ (1.2 mg, 0.0007 mmol): ^{1}H NMR (400 MHz, CD_2Cl_2) δ = 8.01 (brs, 4H, NH), 7.52 (d, J = 8 Hz, 8H, aryl), 7.45 (d, J = 8 Hz, 8H, aryl), 7.40 (s, 4H, benzene), 7.33 (s, 2H, benzene), 6.64 (m, 8H, pyrrole), 6.59 (d, J = 8 Hz, 4H, pyrrole), 6.28 (m, 4H, pyrrole), 6.14 (m, 12H, pyrrole), 1.33 (s, 36H, *tert*-butyl) ppm. ^{13}C NMR (100 MHz, CD_2Cl_2) δ = 161.66, 161.01, 151.93, 146.75, 139.35, 133.97, 133.40, 132.34, 132.28, 132.12, 130.71, 130.52, 130.43, 130.37, 124.51, 119.30, 118.79, 118.58, 109.27, 108.73, 34.87, 31.48 ppm. HR-MALDI-MS: calcd. for $C_{110}H_{90}Ni_2N_{12}$: 1694.6118 [*M*]$^+$, Found: 1694.6094. UV-Vis (in CH_2Cl_2) λ [nm] (ε [$M^{-1}cm^{-1}$]): 316 (45800), 402 (24200) and 558 (85200).

NBNi₃ (2.90 mg, 0.0014 mmol): ^{1}H NMR (400 MHz, CD_2Cl_2) δ = 7.65 (d, J = 8 Hz, 12H, aryl), 7.54 (d, *J* = 8 Hz, 12H, aryl), 7.46 (s, 6H, benzene), 6.72 (d, *J* = 4 Hz, 12H, pyrrole), 6.24 (d, *J* = 4 Hz, 12H, pyrrole), 1.41 (s, 54H, *tert*-butyl) ppm. ^{13}C NMR (100 MHz, CD_2Cl_2) δ = 161.981, 152.571, 147.613, 139.901, 134.072, 133.827, 132.511, 130.690, 129.864, 124.982, 119.306, 31.445, 1.102 ppm. HR-MALDI-MS: calcd. for $C_{132}H_{108}Ni_3N_{12}$: 2034.6875 $[M]^+$, Found: 2034.6870. UV-Vis (in CH_2Cl_2) λ [nm] (ε $[M^{-1}cm^{-1}]$): 348 (62400), 424 (56600) and 512 (123300).

Synthesis of $NBCu_3$

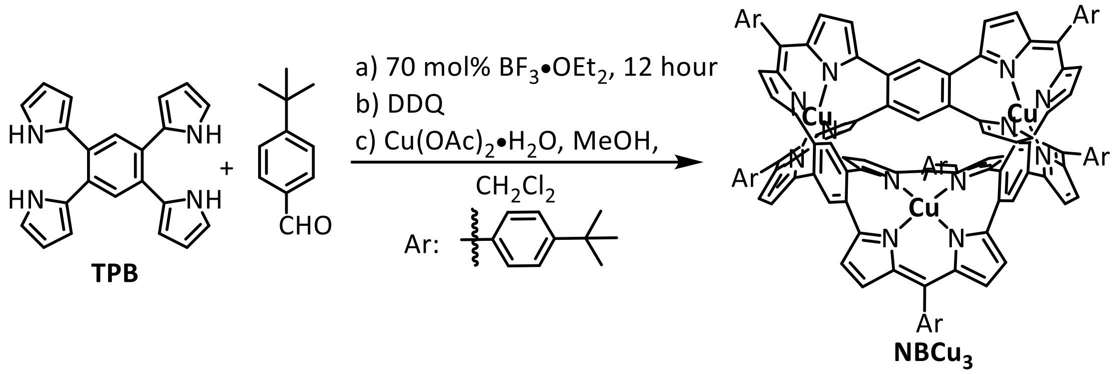

A solution of **TPB** (36 mg, 0.11 mmol) and 4-(*tert*-butyl)benzaldehyde (36 mg, 0.22 mmol) in dry-CH_2Cl_2 (100 ml) was bubbled with argon for 5 minutes, then BF_3•OEt_2 (0.077 mmol, 10.9 mg) was added to reaction mixture. The reaction mixture was stirred for 12 hours under an argon atmosphere and protect from light. DDQ (49 mg, 0.22 mmol) was added to the reaction mixture, which was stirred for 1 hour. Then excess amount of $Cu(OAc)_2$•H_2O in 5 mL MeOH was added to mixture. The mixture was stirred for 4 hours. After the solvent was concentrated, the residue was purified by silica gel column chromatography (CH_2Cl_2/*n*-hexane = 1/3). The first red-yellow fraction was collected to afford crude solid. The crude solid was recrystallized by $CHCl_3$/MeOH to give **NBCu$_3$** as a deep green solid in 3 % (2.2 mg, 0.0011 mmol).

HR-MALDI-MS: calcd. for $C_{132}H_{108}Cu_3N_{12}$: 2049.6702 $[M]^+$, Found: 2049.6750. UV-Vis (in CH_2Cl_2) λ [nm] (ε [$M^{-1}cm^{-1}$]): 345 (67000) and 474 (232000).

Synthesis of DBPor[S2]

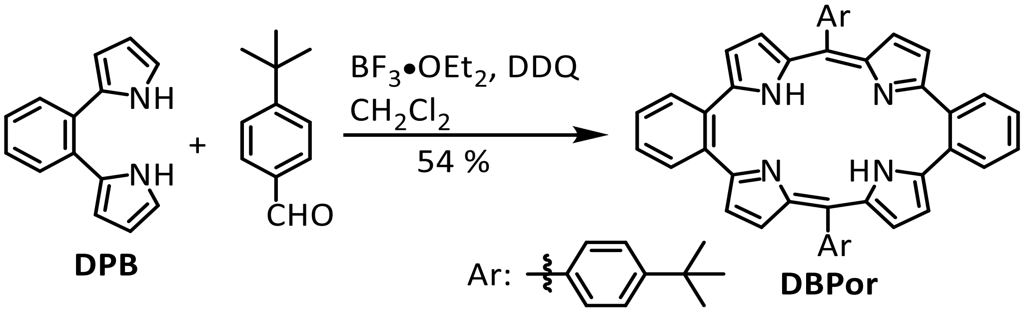

A solution of **DPB** (110 mg, 0.53 mmol) and 4-(*tert*-butyl)benzaldehyde (86 mg, 0.53 mmol) in dry-CH_2Cl_2 (50 ml) was bubbled with argon for 5 min, then BF_3•OEt_2 (3 mol%, 0.67 mg, 0.016 mmol) was added into reaction mixture. The reaction mixture was stirred for 3 hours under an argon atmosphere in the dark. DDQ (120 mg, 0.53 mmol) was added to the reaction mixture, which was stirred for 2 hour. After removal of the solvent, the residue was purified by alumina column (CH_2Cl_2) and silica gel column chromatographies (CH_2Cl_2/MeOH = 20/1). The first red fraction was evaporated to give crude product. The crude product was recrystallized from $CHCl_3$/MeOH to give **DBPor** in 54% (100.3 mg, 0.14 mmol).

^{1}H NMR (400 MHz, CD_2Cl_2) δ = 12.26 (brs, 2H, NH), 7.45 (d, J = 4 Hz, 8H, phenyl), 7.43 (d, J = 4 Hz, 8H, benzene), 6.57 (d, J = 4 Hz, 4H, pyrrole), 6.31 (d, J = 4 Hz, 4H, pyrrole), 1.38 (s, 18H, *tert*-butyl) ppm. ^{13}C NMR (100 MHz, CD_2Cl_2) δ = 155.77, 152.69, 142.70, 141.29, 134.96, 134.70, 131.56, 129.80, 129.45, 128.36, 124.83, 118.95, 35.01, 31.40 ppm. HR-MALDI-MS: calcd. for $C_{50}H_{42}NiN_4$: 700.3566 [M]$^+$, Found: 700.3588.

Synthesis of DBPorCu

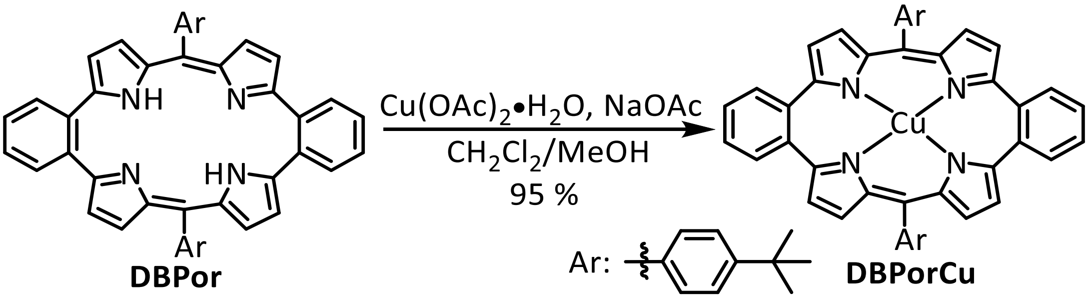

Cu(OAc)$_2$•H$_2$O (172 mg, 0.86 mmol) and NaOAc (70 mg, 0.86 mmol) were added to a solution of **DBPor** (60 mg. 0.09 mmol) in 40 mL of methanol/chloroform (1/4) mixture. The reaction mixture was stirred for 12 hours at room temperature. After removal of the solvent, the residue was purified by silica gel column chromatography (*n*-hexane/CH_2Cl_2 = 3/1) to give **DBPorCu** as xxx solid in 95% (61 mg, 0.08 mmol).

HR-MALDI-MS: calcd. for $C_{50}H_{42}CuN_4$: 761.2705 [M]$^+$, Found: 761.2700. UV-Vis (in CH_2Cl_2) λ [nm] (ε [M^{-1}cm^{-1}]): 350 (21400), 484 (77600).

Synthesis of DBPorNi

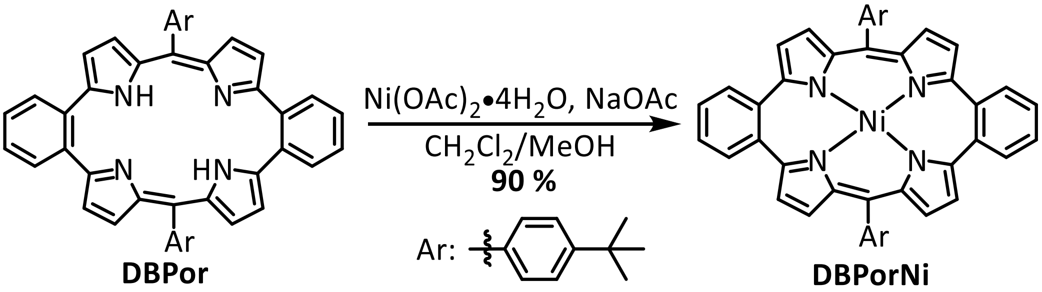

$Ni(OAc)_2$•$4H_2O$ (63 mg, 0.29 mmol) and NaOAc (24 mg, 0.29 mmol) were added to a solution of **DBPor** (20 mg. 0.03 mmol) in 40 mL of methanol/chloroform (1/4) mixture. The reaction mixture was stirred for 3 hours at room temperature. After removal of the solvent, the residue was purified by silica gel column chromatography (*n*-hexane/CH_2Cl_2 = 3/1) to give **DBPorNi** as xxx solid in 95% (61 mg, 0.080 mmol).

^{1}H NMR (400 MHz, CD_2Cl_2) δ = 7.61 (d, J = 8 Hz, 4H, phenyl), 7.53 (d, J = 8 Hz, 4H, phenyl), 7.46 (m, 4H, benzene), 7.38 (m, 4H, benzene), 6.68 (d, J = 8 Hz, 4H, pyrrole), 6.16 (d, J = 4 Hz, 4H, pyrrole), 1.41 (s, 18H, *tert*-butyl) ppm. ^{13}C NMR (100 MHz, CD_2Cl_2) δ = 162.27, 152.40, 147.45, 139.35, 134.42, 133.41, 132.42, 130.66, 129.86, 128.93, 124.91, 118.88, 35.03, 31.45 ppm. HR-MALDI-MS: calcd. for $C_{50}H_{42}NiN_4$: 756.2763 $[M]^+$, Found: 756.2758. UV-Vis (in CH_2Cl_2) λ [nm] (ε [$M^{-1}cm^{-1}$]): 351 (20900), 522 (45700).

Supporting Figures

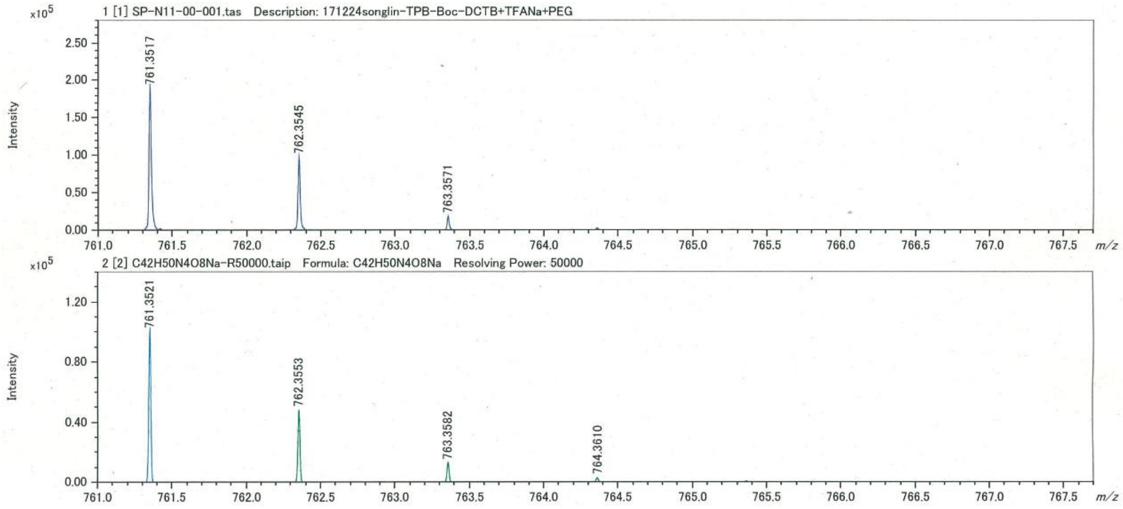

Figure S5.1. HR-MALDI-MS spectrum of **TPB(Boc)$_4$**.

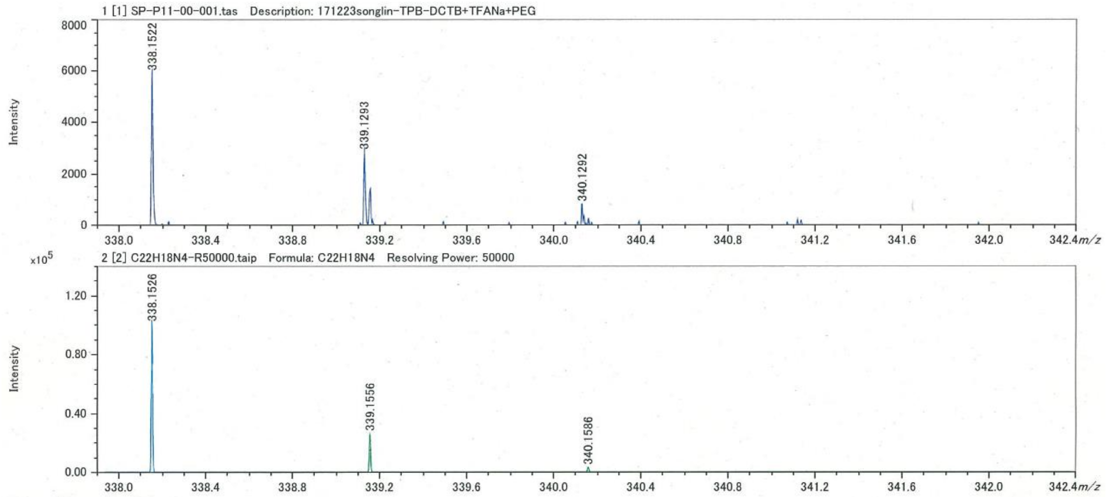

Figure S5.2. HR-MALDI-MS spectrum of **TPB**.

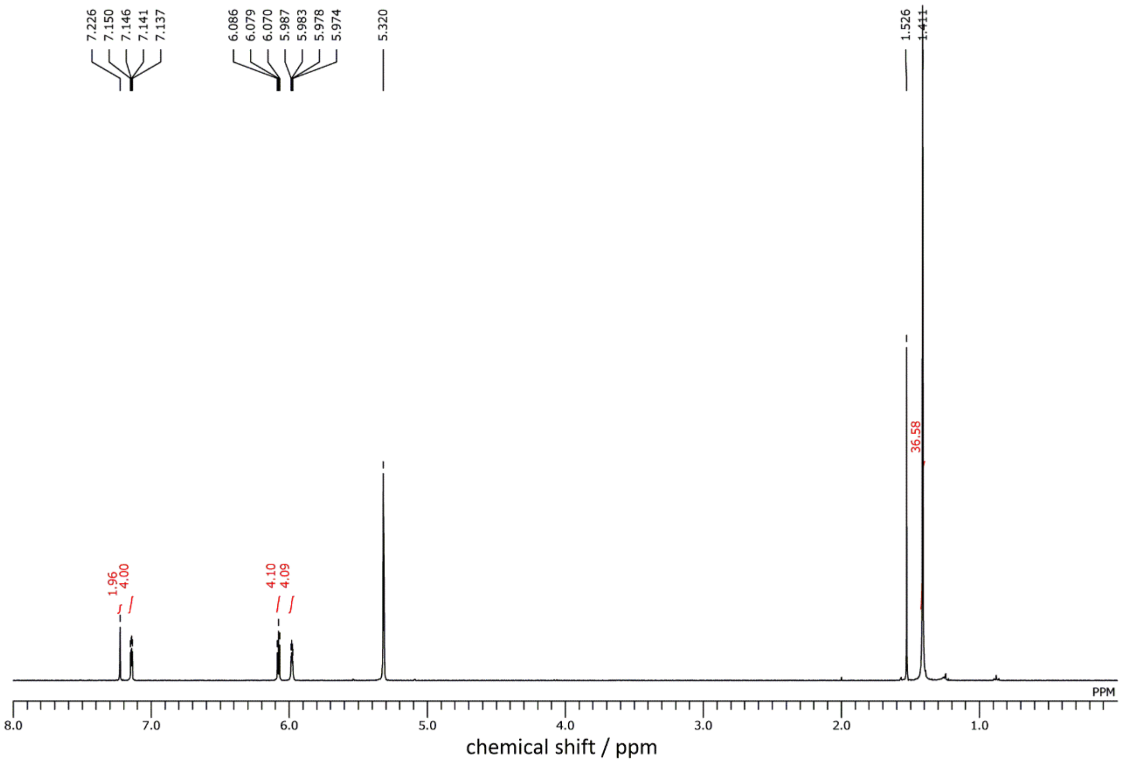

Figure S5.3. ^{1}H NMR spectrum of **TPB(Boc)$_4$** in CD_2Cl_2.

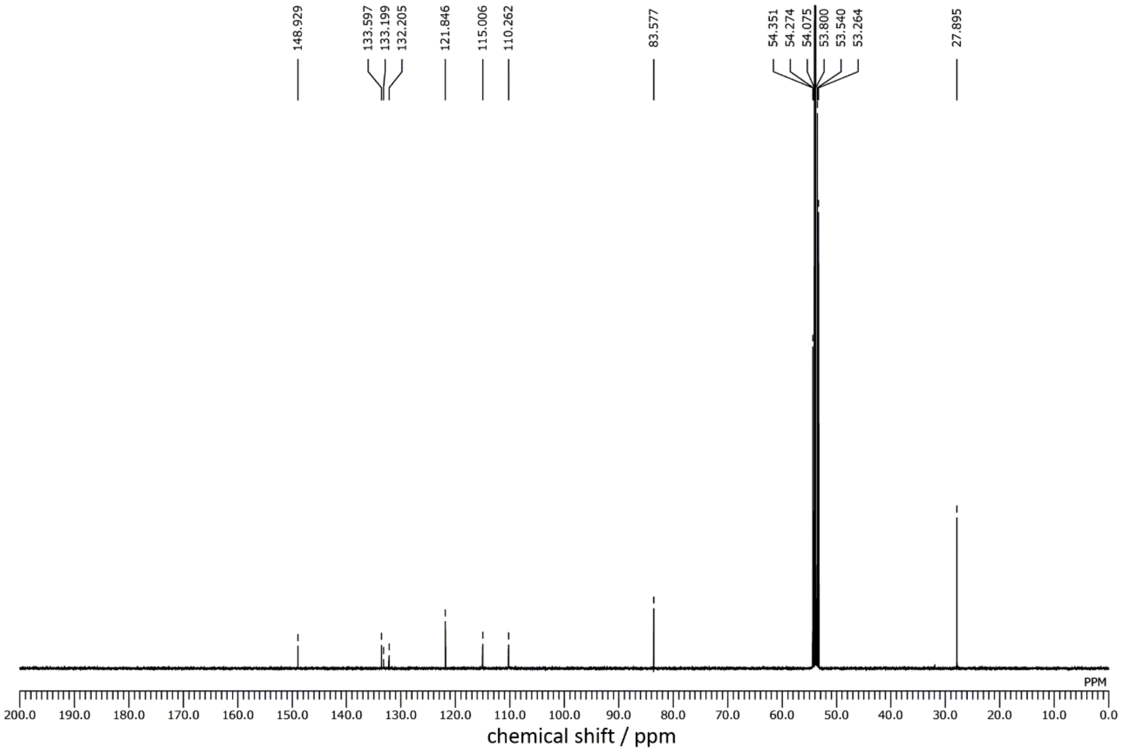

Figure S5.4. ^{13}C NMR spectrum of **TPB(Boc)$_4$** in CD_2Cl_2.

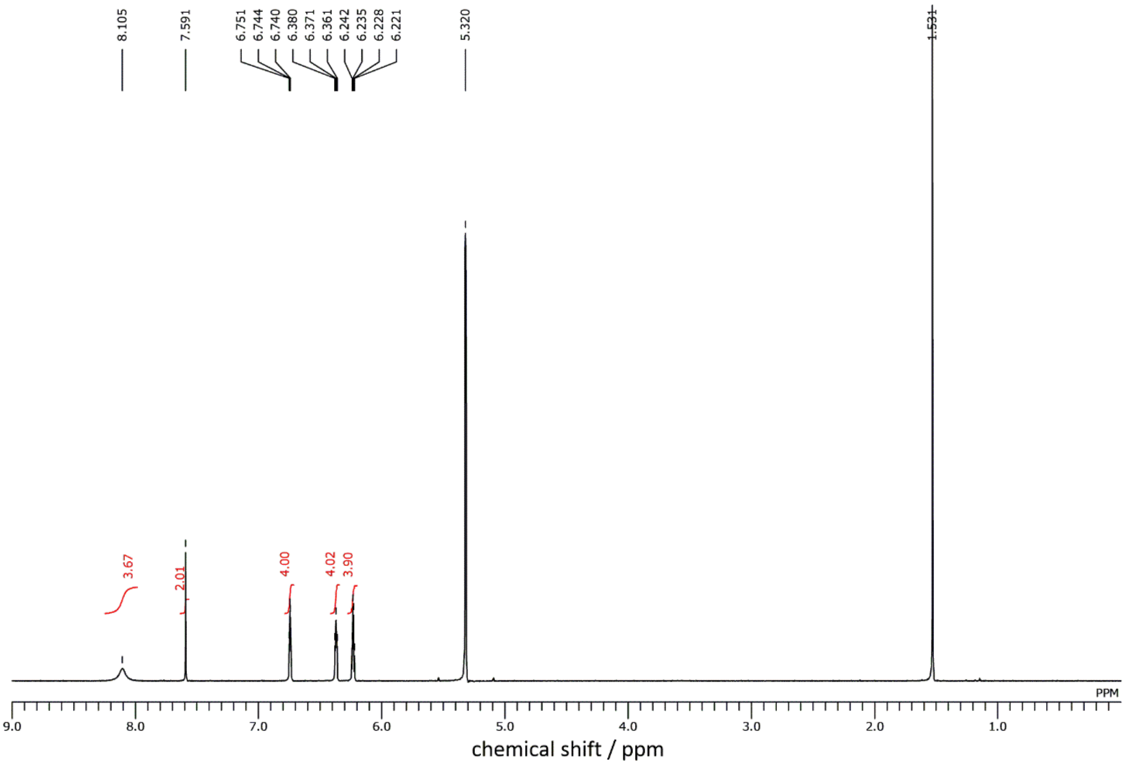

Figure S5.5. ^{1}H NMR spectrum of **TPB** in CD_2Cl_2.

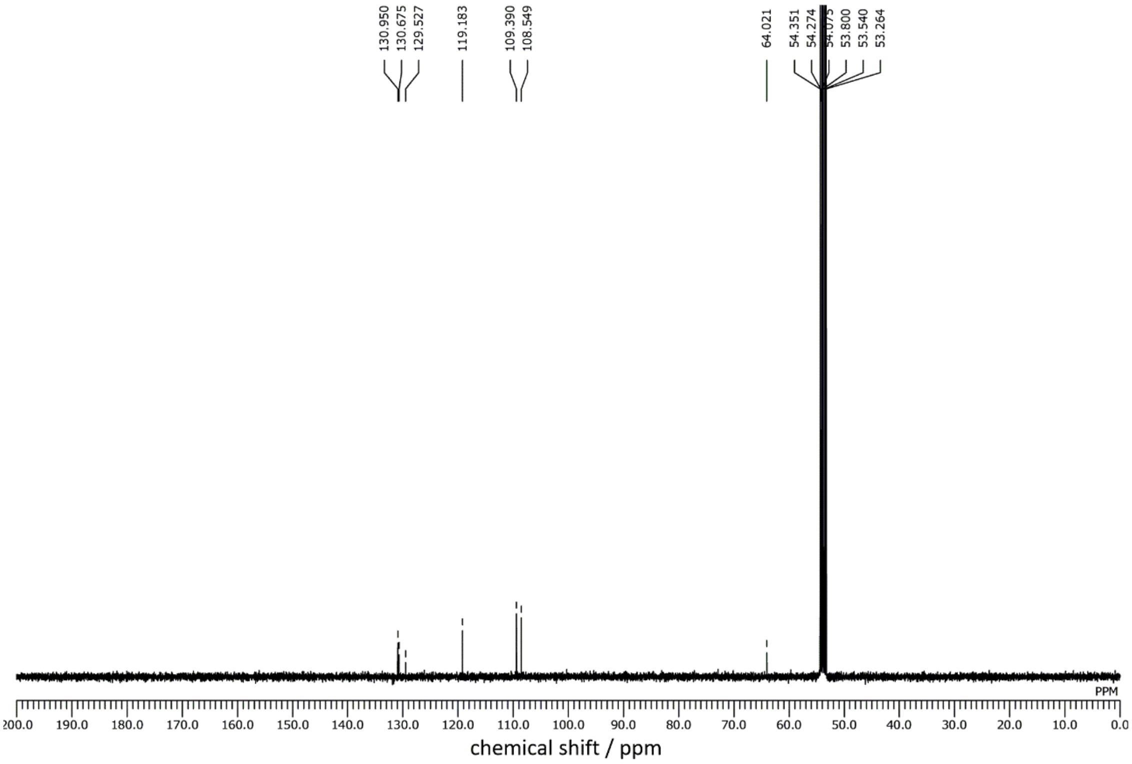

Figure S5.6. ^{13}C NMR spectrum of **TPB** in CD_2Cl_2.

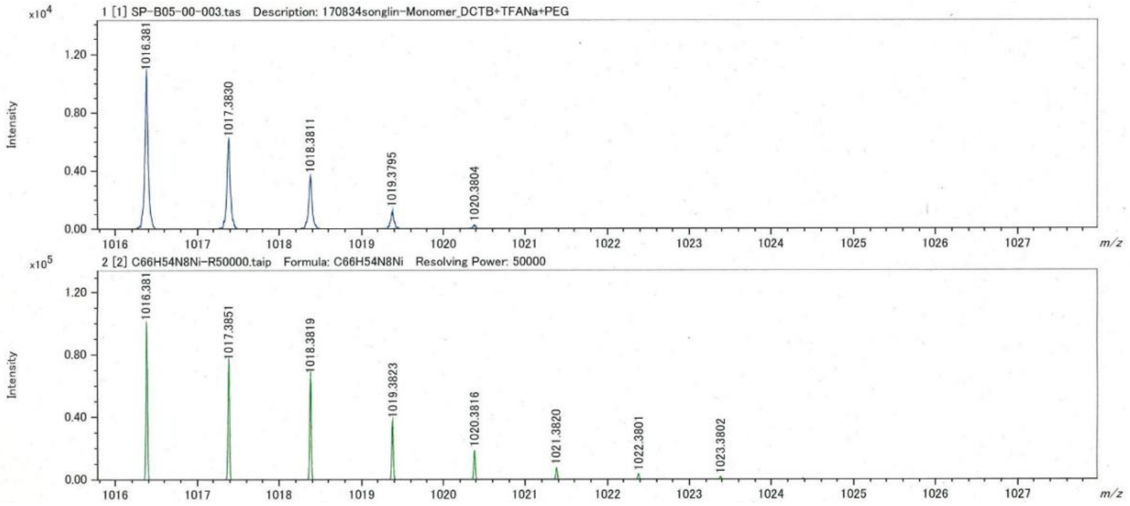

Figure S5.7. HR-MALDI-MS spectrum of **PorNi**.

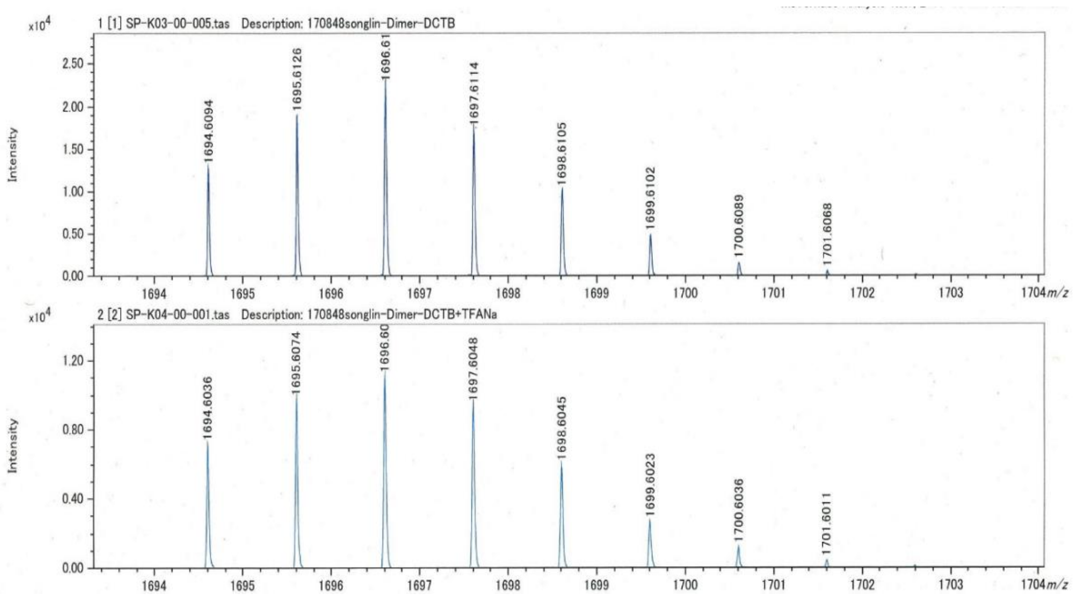

Figure S5.8. HR-MALDI-MS spectrum of **DPorNi$_2$**.

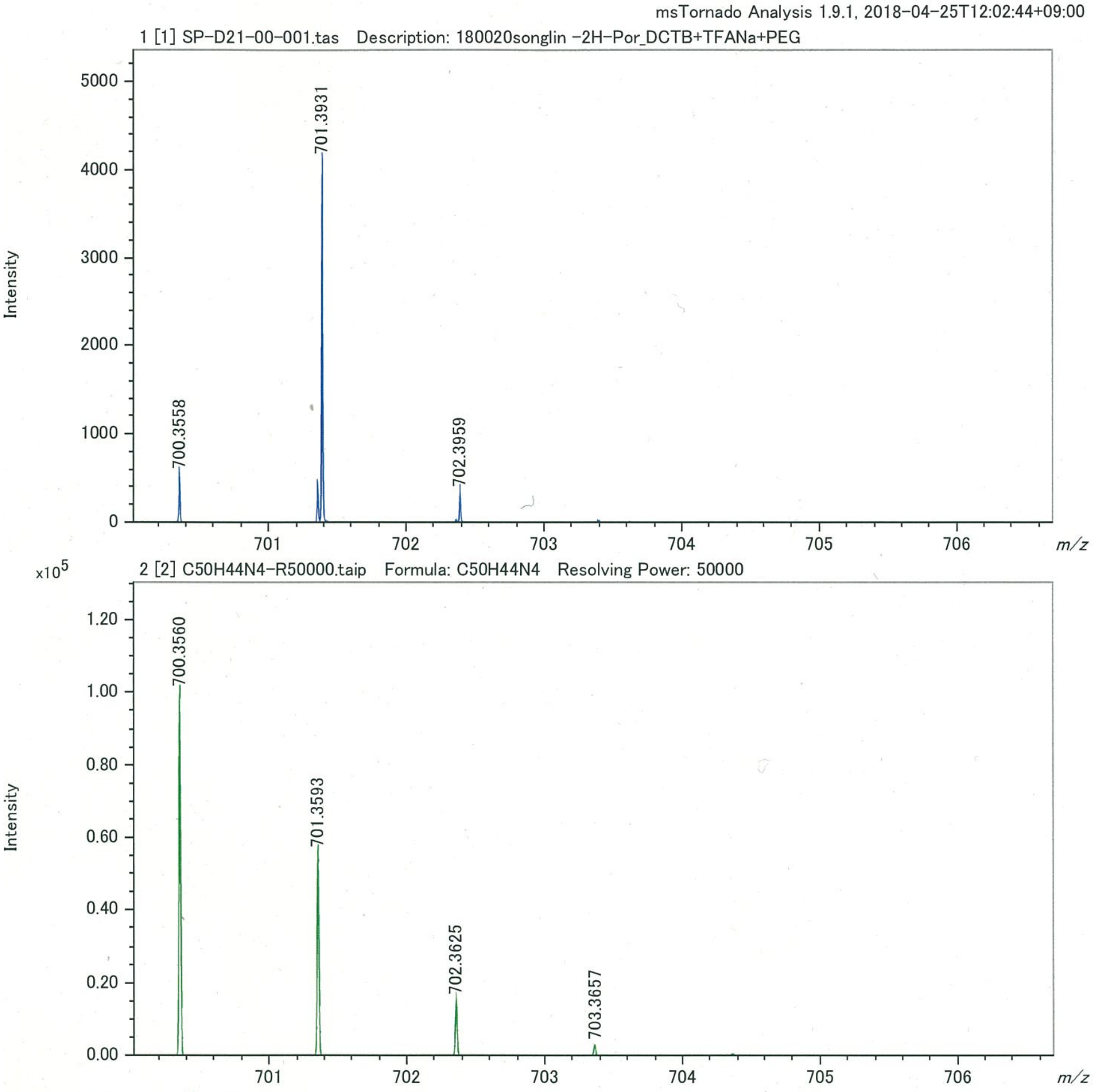

Figure S5.9. HR-MALDI-MS spectrum of **DBPor**.

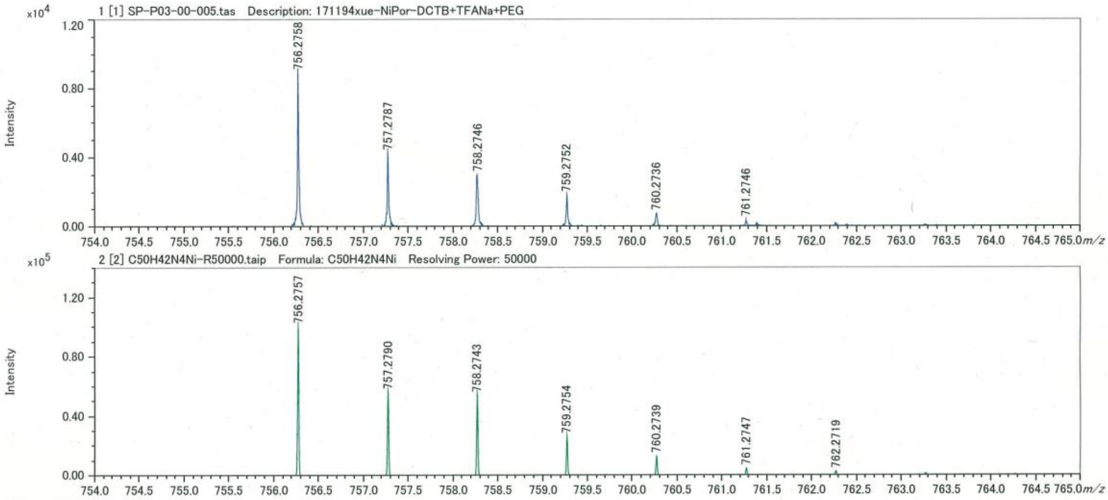

Figure S5.10. HR-MALDI-MS spectrum of **DBPorNi**.

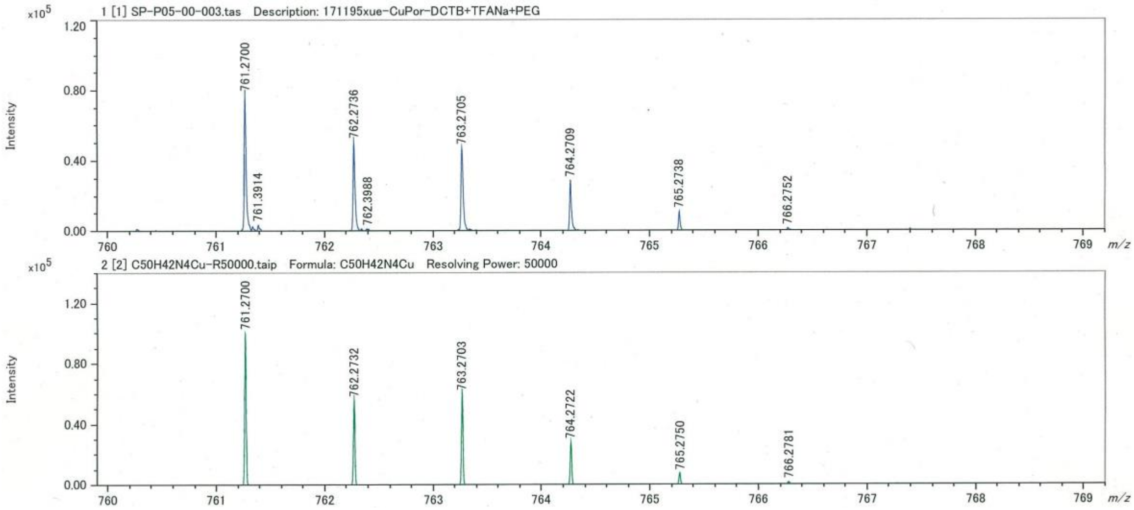

Figure S5.11. HR-MALDI-MS spectrum of **DBPorCu**.

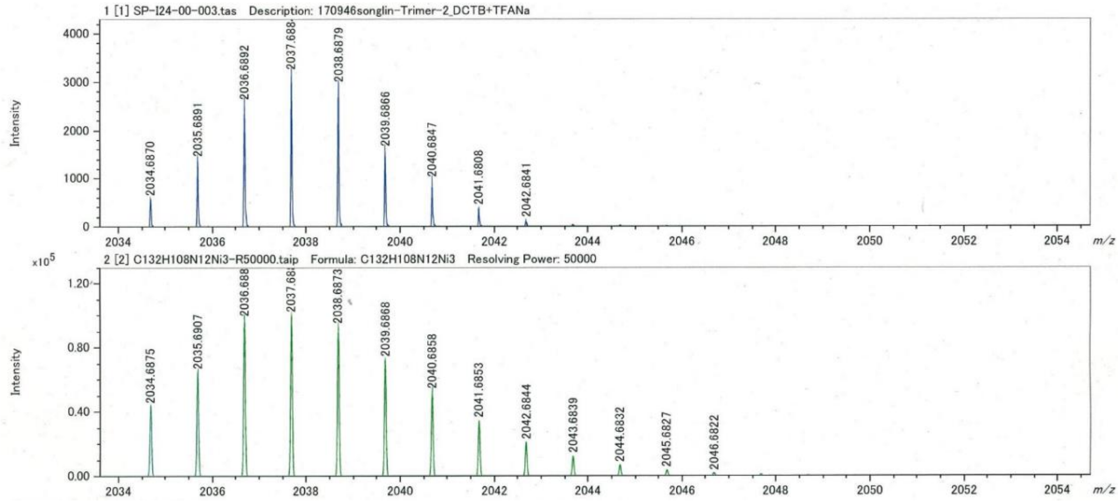

Figure S5.12. HR-MALDI-MS spectrum of **NBNi$_3$**.

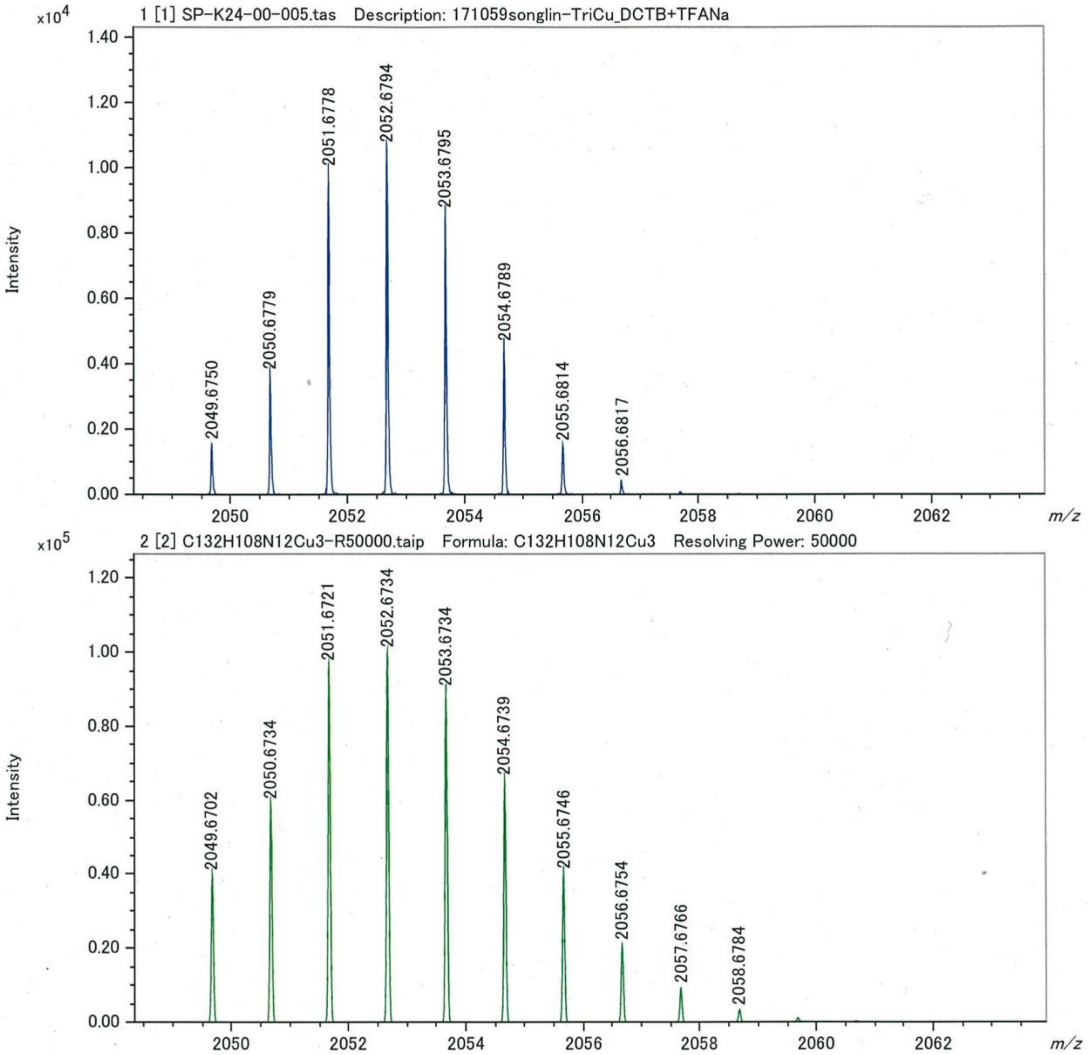

Figure S5.13. HR-MALDI-MS spectrum of **NBCu$_3$**.

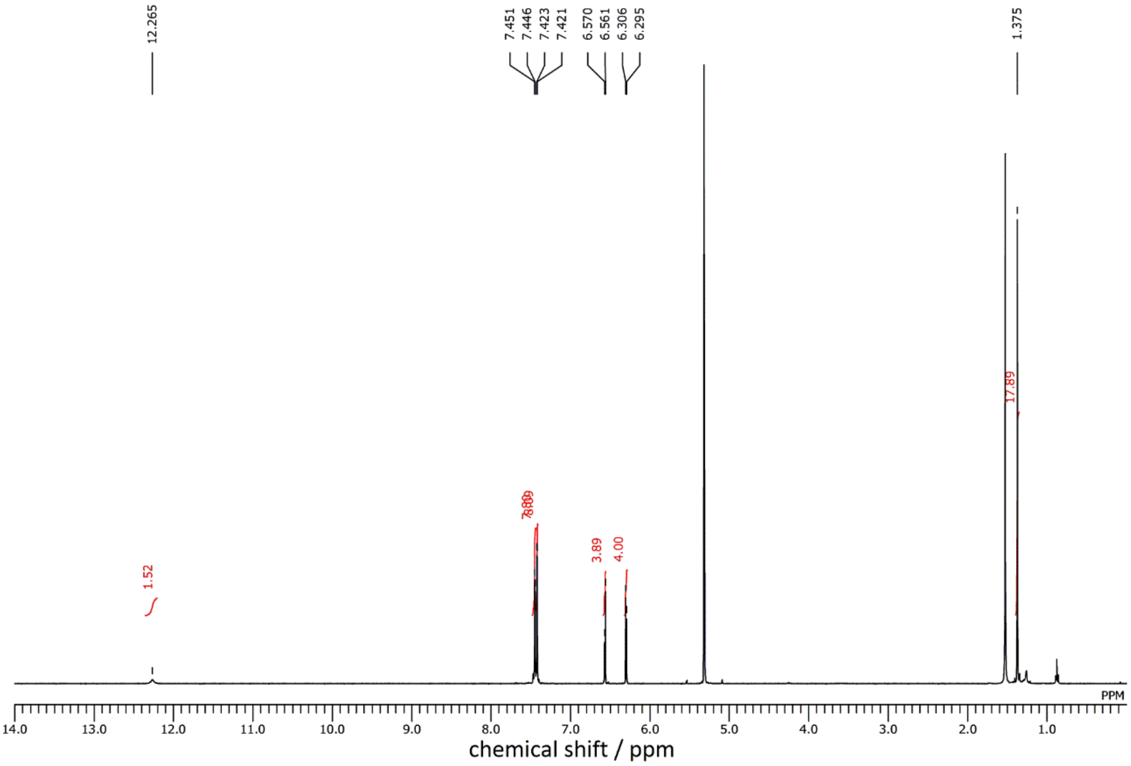

Figure S5.14. ^{1}H NMR spectrum of **DBPor** in CD_2Cl_2.

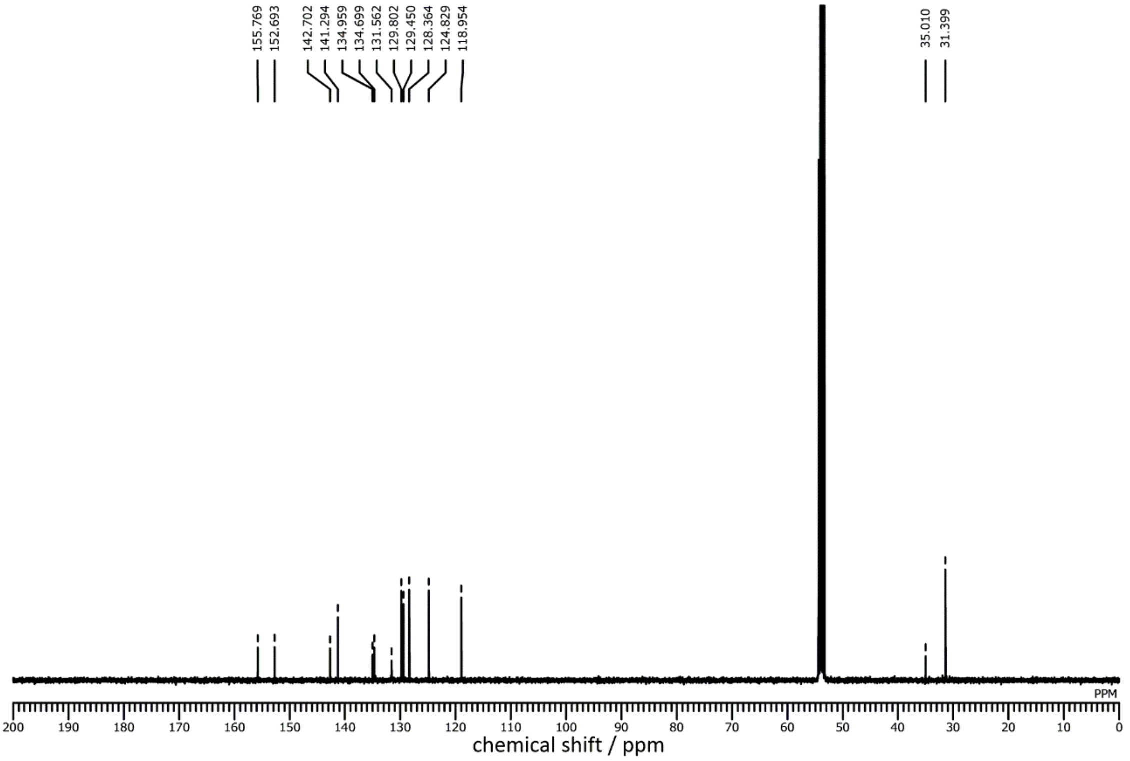

Figure S5.15. ^{13}C NMR spectrum of **DBPor** in CD_2Cl_2.

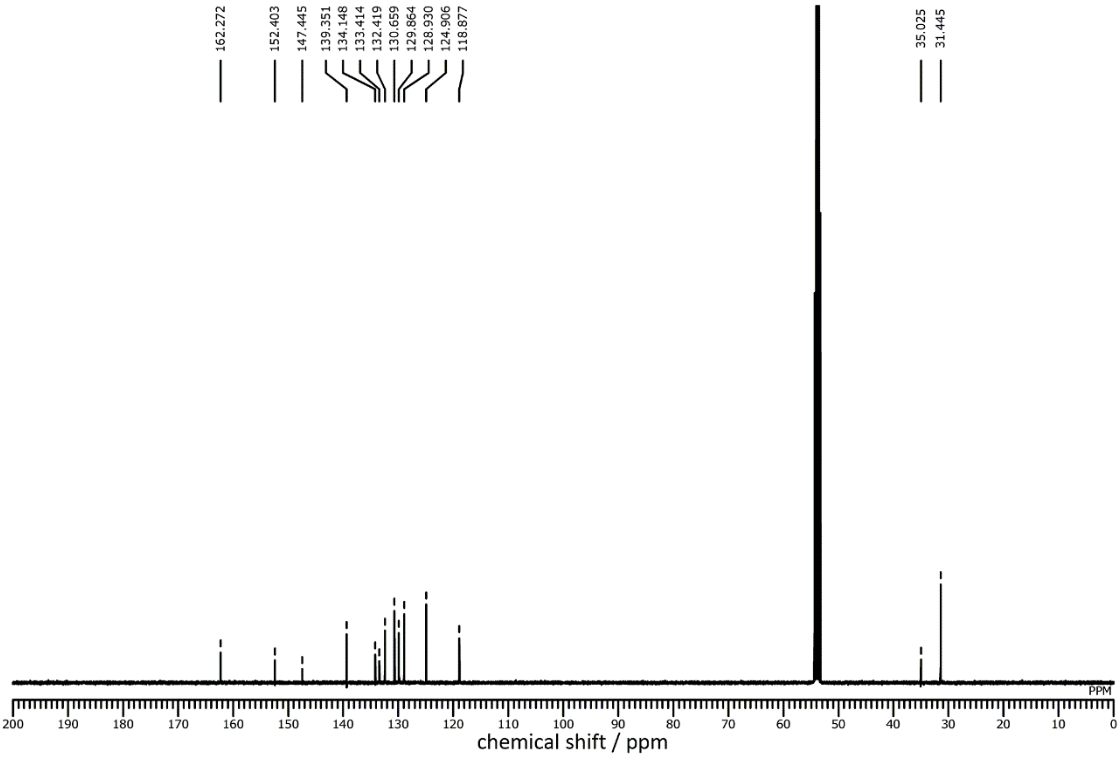

Figure S5.16. ^{13}C NMR spectrum of **DBPorNi** in CD_2Cl_2.

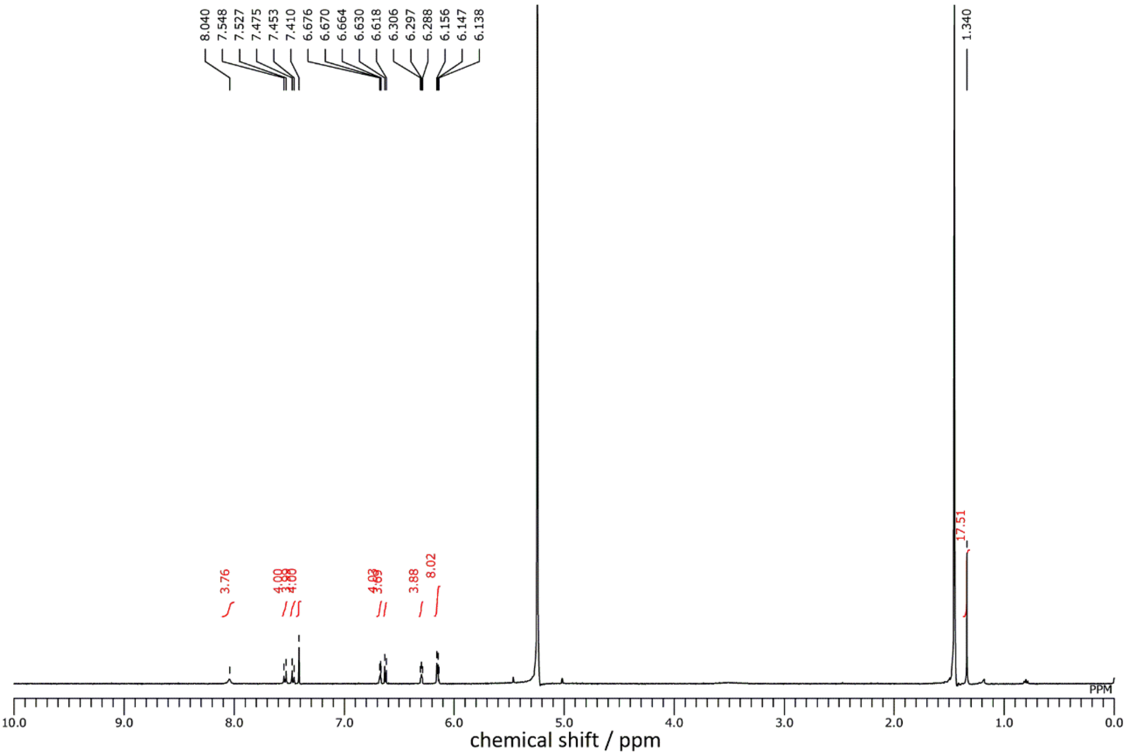

Figure S5.17. ^{1}H NMR spectrum of **PorNi** in CD_2Cl_2.

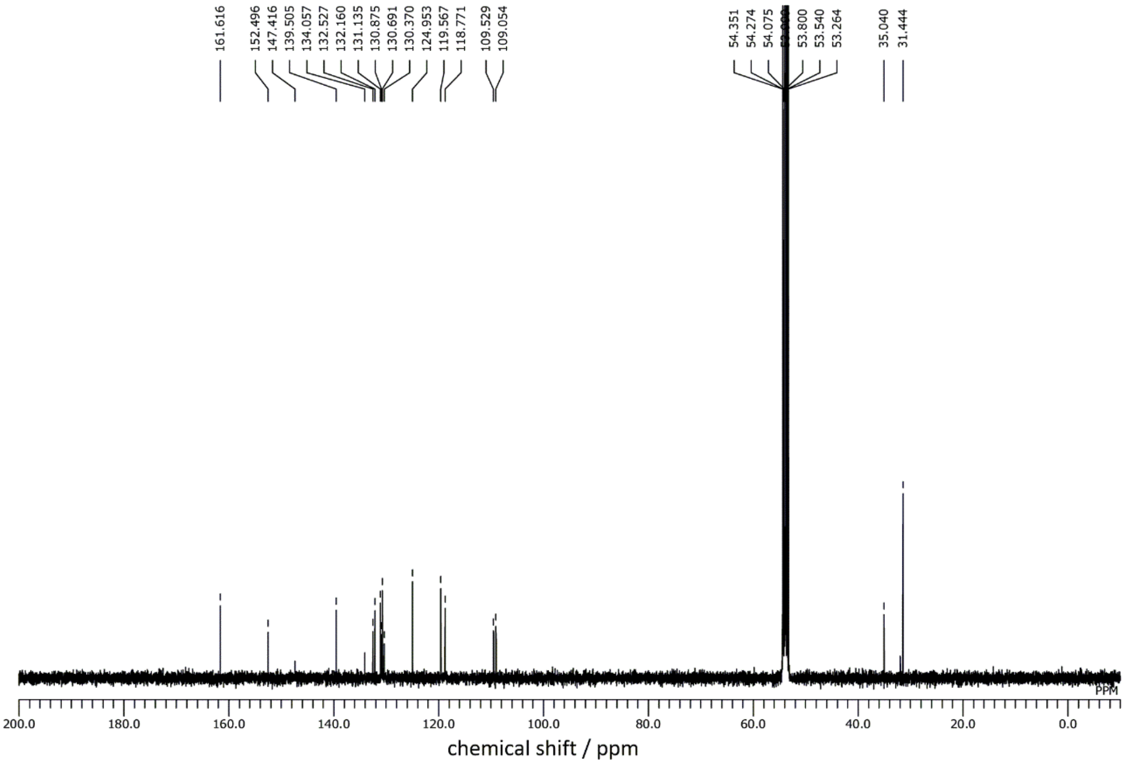

Figure S5.18. ^{13}C NMR spectrum of **PorNi** in CD_2Cl_2 at 298 K.

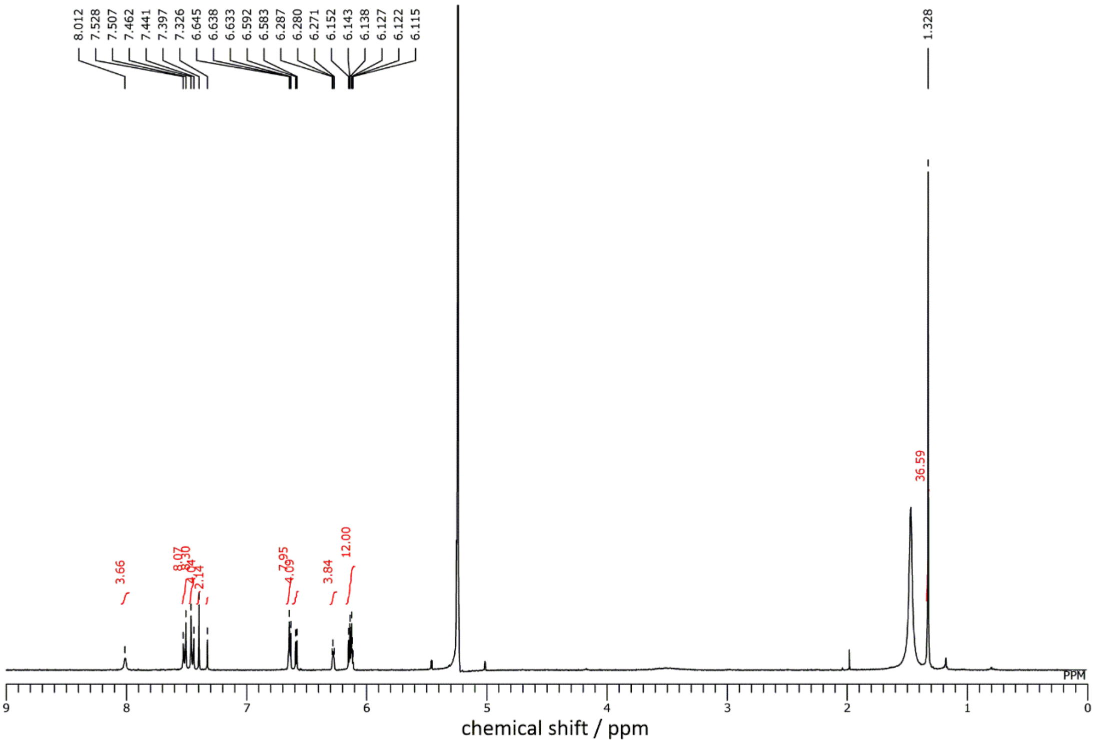

Figure S5.19. ^{1}H NMR spectrum of **DPorNi$_2$** in CD_2Cl_2.

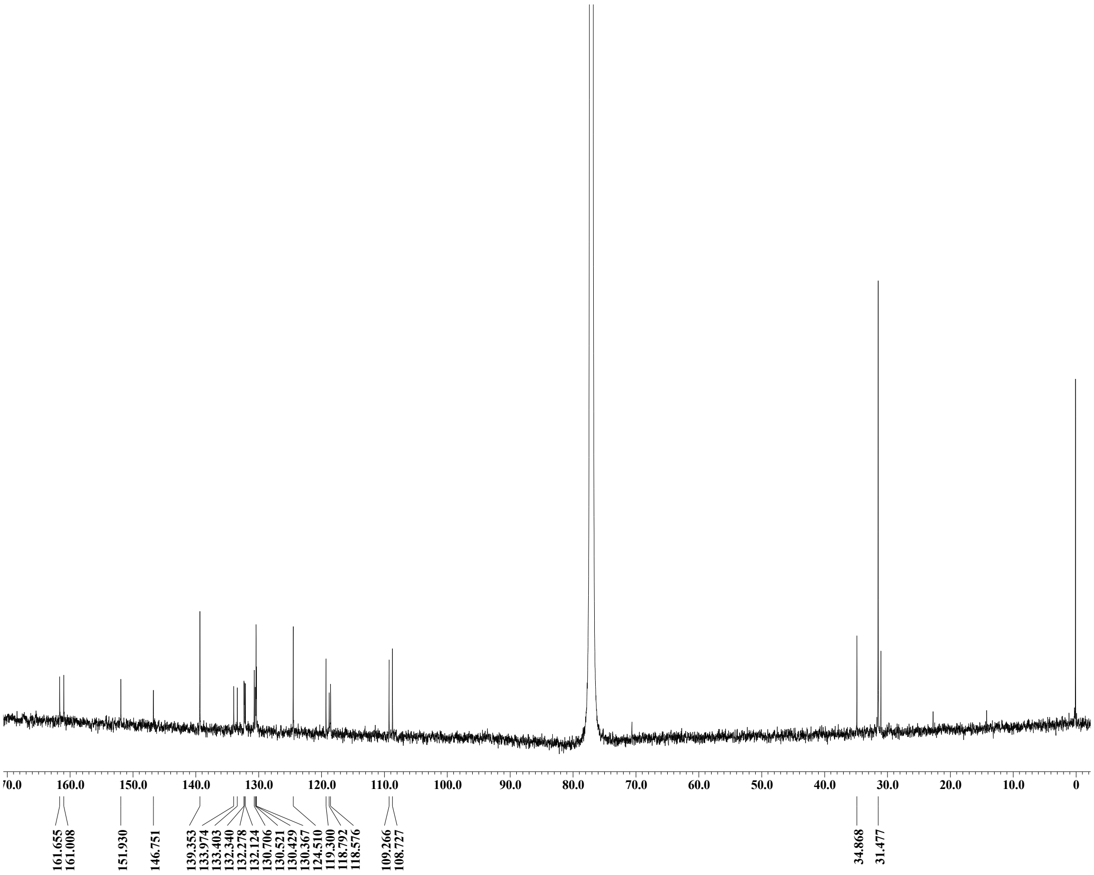

Figure S5.20. ^{13}C NMR spectrum of **DPorNi$_2$** in CD_2Cl_2 at 298 K.

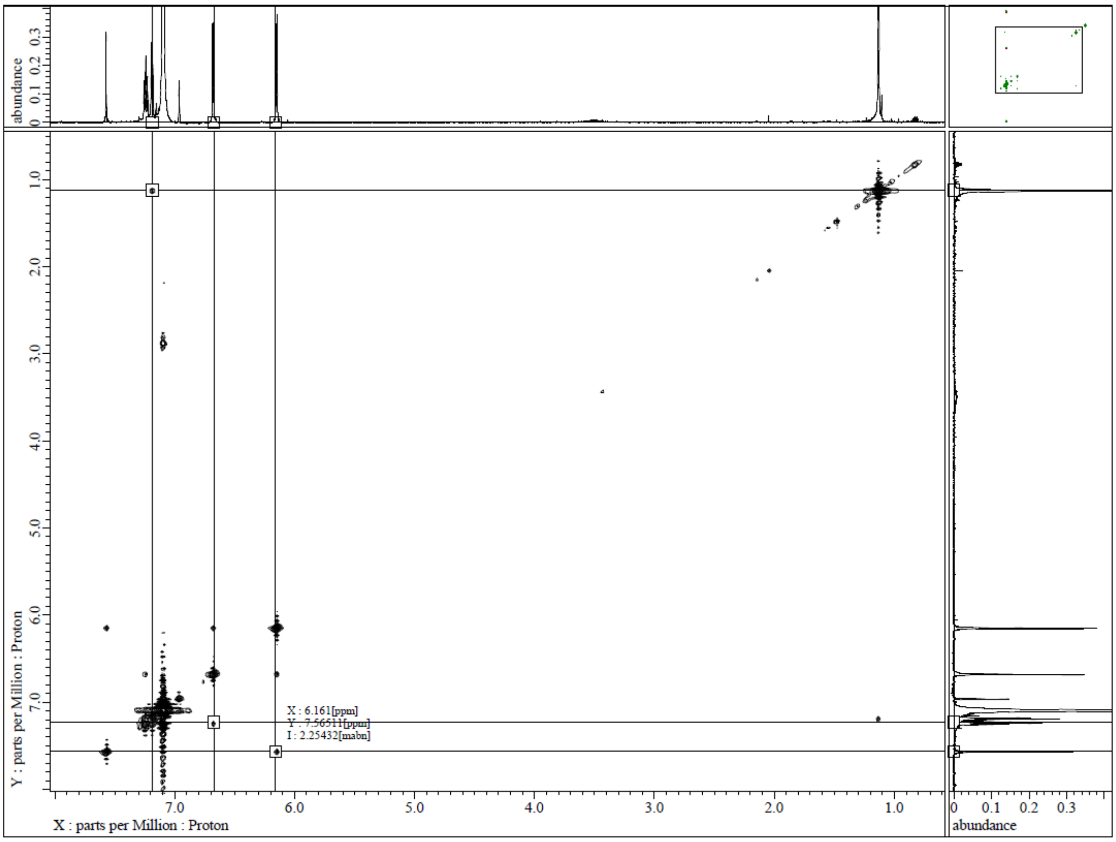

Figure S5.21. NOESY spectrum of **NBNi$_3$** in benzene-d_6 at 298 K.

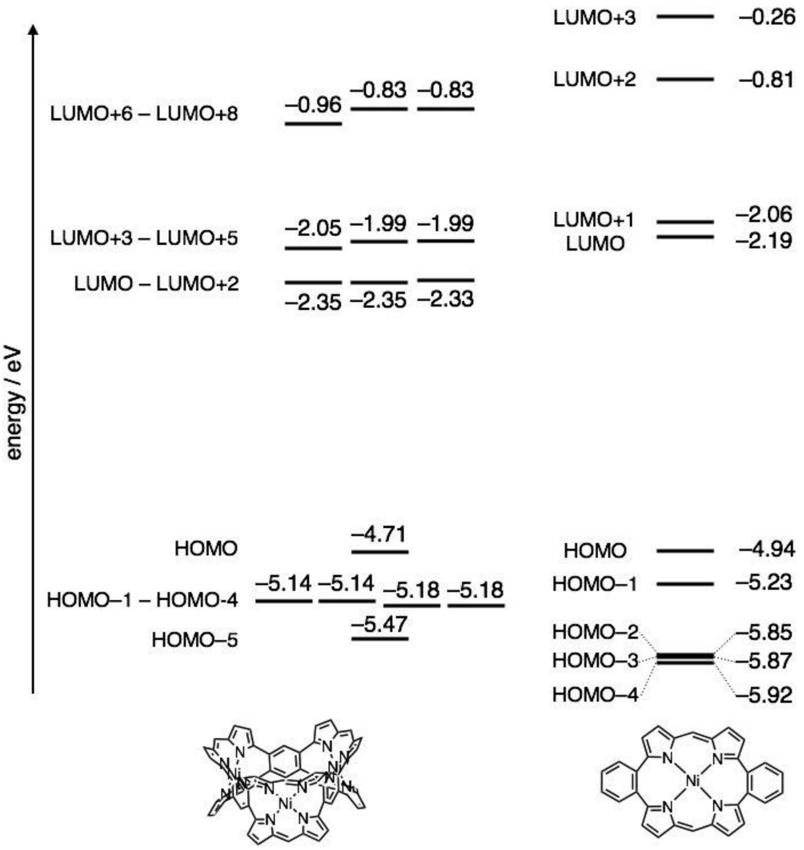

Figure S5.22. Energy diagrams of **DBPorNi** and **NBNi$_3$**.

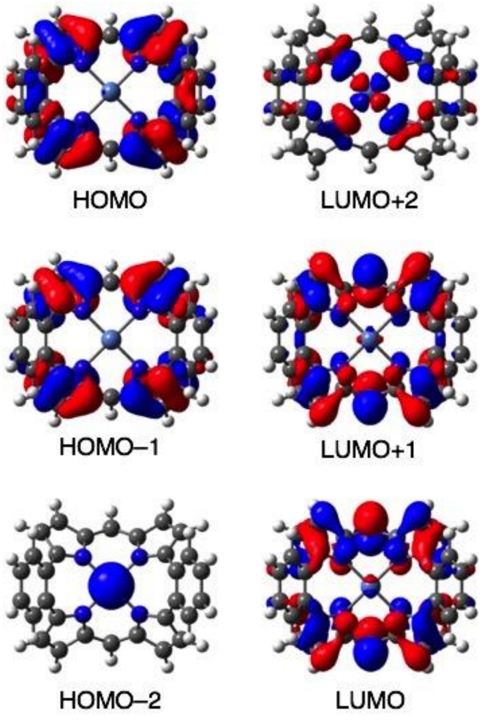

Figure S5.23. Selected molecular orbitals of **DBPorNi**.

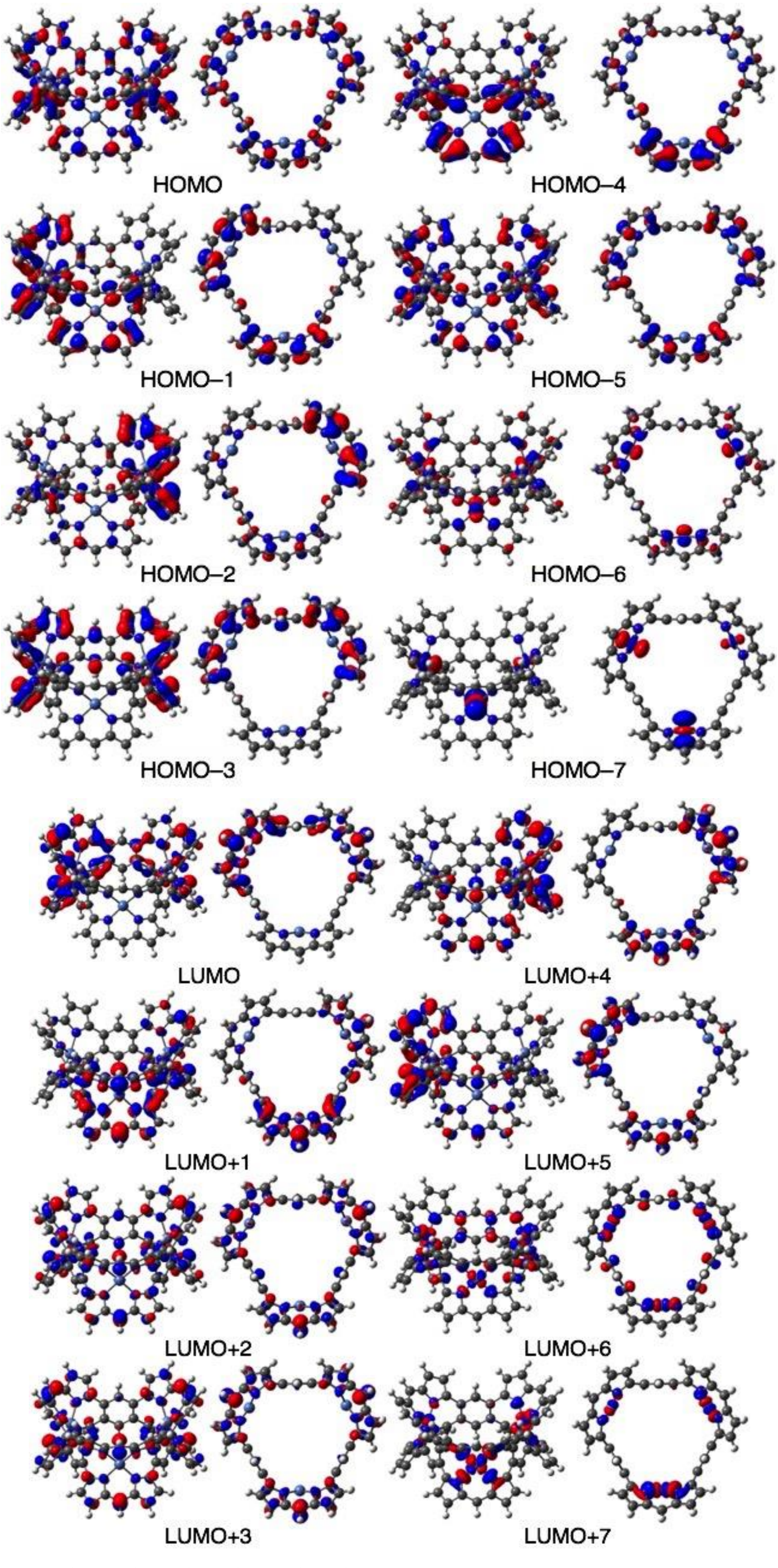

Figure S5.24. Selected molecular orbitals of **NBNi₃**.

Table S5.1. Crystal data and structure refinement of PorNi.

Empirical formula	$C_{68}H_{56}C_{l6}N_{8}Ni$	
Formula weight	1256.61	
Temperature	103(2) K	
Wavelength	0.71075 Å	
Crystal system	Triclinic	
Space group	*P*-1	
Unit cell dimensions	a = 12.8399(3) Å	α = 114.713(3)°.
	b = 15.5721(3) Å	β = 105.687(7)°.
	c = 18.5627(12) Å	γ = 95.108(6)°.
Volume	3158.2(3) $Å^3$	
Z	2	
Density (calculated)	1.321 Mg/m^3	
Absorption coefficient	0.609 mm^{-1}	
F(000)	1300	
Crystal size	0.200 x 0.080 x 0.060 mm^3	
Theta range for data collection	2.520 to 25.350°.	
Index ranges	$-15 <= h <= 15$, $-18 <= k <= 18$, $-22 <= l <= 22$	
Reflections collected	43461	
Independent reflections	11561 [*R*(int) = 0.0537]	
Completeness to theta = 25.242°	99.8 %	
Absorption correction	Semi-empirical from equivalents	
Max. and min. transmission	0.964 and 0.616	

Refinement method	Full-matrix least-squares on F^2
Data / restraints / parameters	11561 / 0 / 782
Goodness-of-fit on F^2	1.116
Final *R* indices [I>2sigma(I)]	$R_1 = 0.0669$, $wR_2 = 0.1755$
R indices (all data)	$R_1 = 0.0778$, $wR_2 = 0.1828$
Extinction coefficient	*n/a*
Largest diff. peak and hole	1.219 and -0.950 e.Å^{-3}

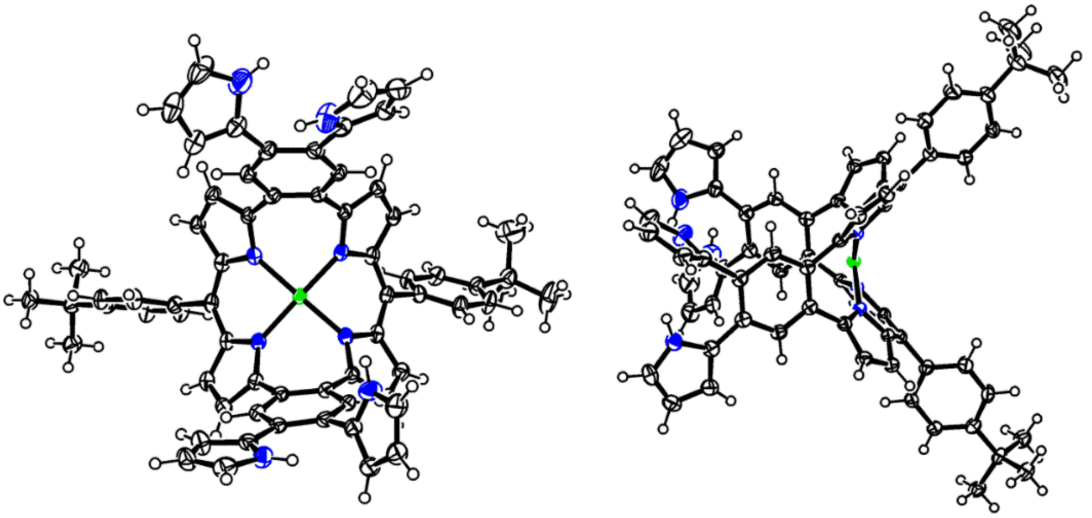

Figure S5.25. Crystal structure of **PorNi**. The thermal ellipsoids represent for 50% probability.

Table S5.2. Crystal data and structure refinement of $NBNi_3$.

Empirical formula	$C_{132}H_{108}N_{12}Ni_3$	
Formula weight	2038.43	
Temperature	90 K	
Wavelength	0.71073 Å	
Crystal system	Monoclinic	
Space group	$P2_1/n$	
Unit cell dimensions	a = 31.3781(9) Å	
	b = 26.0328(16) Å	β = 103.146(4)°
	c = 37.1161(12) Å	
Volume	29524(2) $Å^3$	
Z	8	
Density (calculated)	0.917 Mg/m^3	
Absorption coefficient	0.421 mm^{-1}	
$F(000)$	8544	
Crystal size	0.200 x 0.100 x 0.050 mm^3	
Theta range for data collection	1.538 to 21.400°.	
Index ranges	$-32 <= h <= 32, -26 <= k <= 21, -38 <= l <= 38$	
Reflections collected	100819	
Independent reflections	33273 [R(int) = 0.2495]	
Completeness to theta = 21.400°	99.4 %	
Absorption correction	None	
Refinement method	Full-matrix least-squares on F^2	

Data / restraints / parameters	33273 / 2260 / 2620
Goodness-of-fit on F^2	1.149
Final R indices [I>2sigma(I)]	R_1 = 0.1734, wR_2 = 0.3933
R indices (all data)	R_1 = 0.2640, wR_2 = 0.4493
Extinction coefficient	*n/a*
Largest diff. peak and hole	1.366 and -0.575 e.Å^{-3}

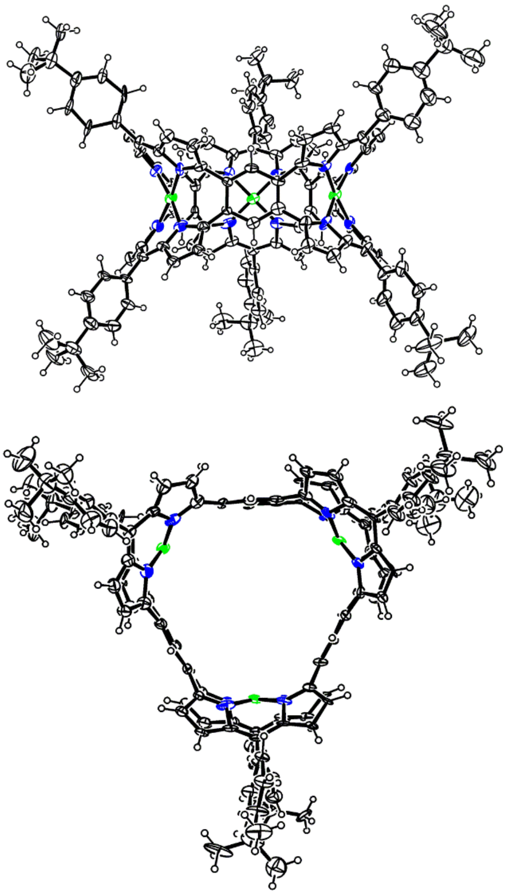

Figure S5.26. Crystal structure of **NBNi$_3$**, (a) side view, (b) up view. The thermal ellipsoids represent for 40% probability.

Reference

[S1] G. M. Sheldrick, *Acta Cryst.*, **2008**, *A64*, 112.

[S2] D. Kuzuhara, W. Fulukawa, A. Kitashiro, N. Aratani, H. Yamada, *Chem. Eur. J.*, **2016**, *22,* 10671.

Chapter 6

Conclusions and Prospect

This dissertation focuses on constructing novel porphyrins with various vinylene-bridges and porphyrin(2.1.2.1)-based nanobelts by simple acid-catalyzed condensation reaction to explore molecular structures, aromaticity, optical and electronic properties, coordination behavior and supramolecular assembly.

In Chapter 2, two type porphyrins with diphenyl vinylene-bridges and their metal complexes were obtained. The contracted porphyrin **2-1** produces the sandwich-type iridium complex **2-2**. The cod ring is transformed from 1,5-cod to η^1,η^3-C_8H_{12} unit as a π-allyl ligand associated with the valence change of iridium from Ir^I to Ir^{III}. Next, the synthetic method of non-planar porphyrins with diphenyl vinylene-bridges was developed. Treatment of dipyrrolyldiphenylethene (**DPhDPE**) and C_6H_5CHO afforded three highly twisted porphyrins. These expanded porphyrins form the non-planar structures without macrocyclic aromaticity. Metalation and demetalation processes lead to transformations between non-aromatic free base **2-4** and aromatic copper complexes accompany with the *trans-/cis*-isomerization. In Chapter 3, the aromatic [30]hexaphyrin(2.1.2.1.2.1) **3-1** with vinylene-bridges was prepared by condensation reaction of 1,2-di(pyrrol-2-yl)ethane (**DPE**) and C_6H_5CHO. The protonated **3-1** forms a highly planar conformation confirmed by X-ray diffraction analysis. Compound **3-1** with three dipyrrin units and a friendly cavity size work to produce the trinuclear rhodium(l) complex **3-2**. In Chapter 4, hexaphyrin(2.1.2.1.2.1) **4-2** with dimethyl vinylene-bridges as favorable platform to form five BODIPY macrocycles by three reaction conditions. The molecular shapes of BODIPY macrocycles were divided into two types: twisted structures and co-planar structure. Among five BODIPY macrocycles, two tri-boron complexes show weak emission relative to no emission properties of mono-/bis-boron complexes. The reason may be that mono-/bis-boron complexes consist of the ICT characteristics. In Chapter 5, an efficient synthetic method of porphyrin(2.1.2.1)-based nanobelts was established. The X-ray crystallography revealed that porphyrin(2.1.2.1)-based nanobelt forms an hourglass-shaped C_{3h}-symmteric structure consisting with arch-shaped porphyrin(2.1.2.1) moieties and benzene linkages. This hourglass-shaped structure conducts as an effective C_{60} receptor to be 1:2 stoichiometric complex investigated by UV-vis and NMR titrations. Porphyrin(2.1.2.1)-based nanobelt shows multi-electrons donating and accepting abilities indicating that nanobelt can stabilize multi-cationic and anionic states.

One of the main findings of investigative projects is that 1,2-di(pyrrol-2-yl)ethene derivate can work as powerful building blocks to form various expanded porphyrins with different molecular structures and electronic properties. The obtained porphyrins, which can be seen as multi-dipyrrin ligands, work to form metal complexes with various conformations and electronic properties. The next finding is that **TPB** can produce porphyrin-based nanobelt.

The author has faith in that the findings of projects that will be useful for constructing expanded porphyrins with other linked bridges between dipyrrin units to investigate optical and electronic properties, molecular structures and coordination ability. In porphyrin(2.1.2.1)-based nanobelt project, the finding can open the window of preparing porphyrin(2.1.2.1)-based nanobelts with larger macrocyclic cavity and their metal complexes to explore the functional properties and potential applications (Scheme 6.1).

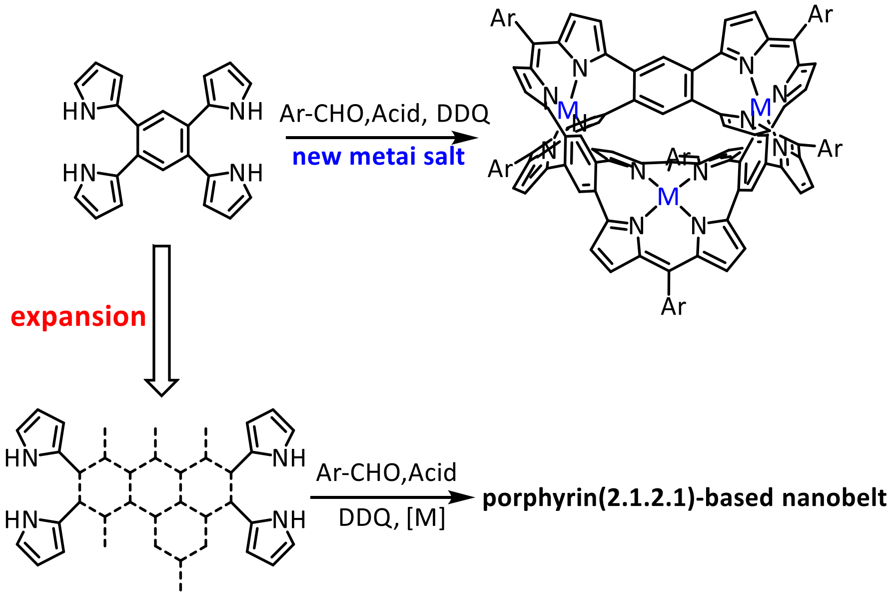

Scheme 6.1 Synthetic scheme of new porphyrin(2.1.2.1)-based nanobelts.

Achievements

List of Papers

1. Synthesis and Characterization of an Iridium Triphyrin Complex

   Songlin Xue, Daiki Kuzuhara, Naoki Aratani, Hiroko Yamada.

   Inorg. Chem., **2016**, *55,* 10106–10109.

2. [30]Hexaphyrin(2.1.2.1.2.1) as Aromatic Planar Ligand and its Trinuclear Rhodium(I) Complex

   Songlin Xue, Daiki Kuzuhara, Naoki Aratani, Hiroko Yamada.

   Inorg. Chem., 10.1021/acs.inorgchem.8b00977.

3. Control of Aromaticity and *cis-/trans* Isomeric Structure of Non-Planar Hexaphyrin(2.1.2.1.2.1) and Metal Complexes

   Songlin Xue, Daiki Kuzuhara, Naoki Aratani, Hiroko Yamada.

   To be submitted.

4. Porphyrin(2.1.2.1) nanobelt: Synthesis and Binding Ability with Fullerene

   Songlin Xue, Daiki Kuzuhara, Naoki Aratani, Hiroko Yamada.

   To be submitted.

List of Presentations

1. Porphyrin(2.1.2.1) Nanobelts

   Songlin Xue, Daiki Kuzuhara, Naoki Aratani, Hiroko Yamada.

   The 10st International Conference on Porphyrins and Phthalocyanines, Munich, Germany, 2018/07.

2. One-Step Synthesis of Porphyrin(2.1.2.1) Nanobelt.

   Songlin Xue, Daiki Kuzuhara, Naoki Aratani, Hiroko Yamada.

   The 98st Annual Meeting of Chemical Society of Japan, Chiba, Japan, 2018/03.

3. Synthesis of [30]Hexaphyrin(2.1.2.1.2.1)s with Different Conformations on Ethylene Bridges.

   Songlin Xue, Daiki Kuzuhara, Naoki Aratani, Hiroko Yamada.

   The 17st International Symposium on Novel Aromatic Compounds, New York, USA, 2017/07.

4. Synthesis and Metalation of Highly Bent Skeletons of Hexaphyrin(2.1.2.1.2.1) and Porphyrin(2.1.2.1)

   Songlin Xue, Daiki Kuzuhara, Naoki Aratani, Hiroko Yamada.

   The 27st Symposium on Physical Organic Chemistry, Hiroshima, Japan, 2016/09.

Acknowledgements

This dissertation deals with the studies accomplished by the author under direction of Prof. Hiroko Yamada at Nara Institute of Science and Technology, Japan.

The author would like to express sincere gratitude to Prof. Hiroko Yamada and Associate Prof. Naoki Aratani for excellent guidance and constant encouragement throughout Ph.D. study. Their guidance helped the author in all the time of research work and writing of papers and this dissertation. The author also would like to thank the members of supervisor committee: Prof. Shun Hirota (Laboratory for Supramolecular Science) and Associate Prof. Takuya Nakashima (Laboratory for Photonic Molecular Science) for their insightful comments.

The author greatly appreciates to Dr. Daiki Kuzuhara (Assistant Prof., Faculty of Science and Engineering, Iwate University). Without fruitful and efficient comments of research projects from Dr. Daiki Kuzuhara, it would not be possible to conduct research work of doctoral course. The author also would like to appreciate Assistant Prof. Mitsuharu Suzuki and Assistant Prof. Hironobu Hayashi for useful advices.

The author also grateful to Prof. Gwénaël Rapenne in Centre d’Élaboration de Matériaux et d’Etudes Structurales (01/2017-02/2017, CEMES-CNRS, France) for giving the author an excellent Lab-stay in his laboratory.

The author would like to thank Ms. Yoshiko Nishikawa, Mr. Fumio Asanoma and Mr. Shouhei Katao in NAIST for measuring and analyzing of high-resolution mass spectrometry, NMR spectra and single-crystal structure analysis, respectively.

The author appreciates staff and lab mates of Prof. Yamada group for giving kind and useful assistance. It made author accustomed to new Lab. and for all the fun in the past three years.

The author would like to thank the financial support from NAIST and Japanese Government Scholarship from The Ministry of Education, Culture, Sports, Science, and Technology.

Finally, the author would like to thank his family for their unselfish love.

Songlin Xue

July-11-2018